Galactic archaeology with ages based on chemical clocks

UNIVERSITÀ
DEGLI STUDI
FIRENZE

DOTTORATO DI RICERCA IN FISICA E ASTRONOMIA

CICLO XXXIII

COORDINATORE Prof. Raffaello D'Alessandro

Galactic Archaeology with ages based on chemical clocks

Settore Scientifico Disciplinare FIS/05

Dottorando
Dott.ssa Giada Casali
Giada Casali
(firma)

Tutori
Dott.ssa Laura Magrini
Laura Magrini
(firma)

Prof.ssa Stefania Salvadori
Stefania Salvadori
(firma)

Coordinatore
Prof. Raffaello D'Alessandro
Raffaello D'Alessandro
(firma)

Anni 2017/2020

CONTENTS

ABSTRACT

Like traditional archaeology, which studies the human history by investigating the remnants of past civilizations, Galactic archaeology traces the history of our Galaxy observing its stellar population. In fact, the chemical composition of the stellar atmospheres preserve the information of the gas from which stars formed. Our Galaxy is the best place where Galactic archaeology can be applied, since its stellar populations can be resolved. Moreover, stars of different ages can be studied in detail, obtaining for them, photometric, astrometric and spectroscopic data. We are living in a privileged epoch for Galactic archaeology, thanks to the launch in 2013 of the *Gaia* satellite, which is providing parallaxes and proper motions for more than two billions stars. In addition, numerous large spectroscopic surveys were recently conceived: some of them are already completed, as RAVE, Gaia-ESO, APOGEE-1, other still ongoing, as APOGEE-2, GALAH, LAMOST and other planned for the next future, as WEAVE, 4MOST, MSE and MOONs. These surveys are providing powerful databases of stellar parameters, chemical abundances and radial velocities.

The overarching aim of this Thesis is to provide additional empirical methods to measure stellar ages. The determination of stellar ages is indeed one of most difficult tasks of the Galactic archaeology, because they cannot be directly measured, unlike other stellar properties such as mass, distance and chemical composition. The most commonly adopted technique to infer stellar ages is the isochrone fitting, based on the comparison of observational quantities (magnitude and colours) to theoretical models.

Recently, other methods have been proposed, such as stellar activity, lithium depletion boundary, gyrochronology and asteroseismology. The first two methods can be just applied to young stars, gyrochronology is so far poorly calibrated for old stars, and asteroseismology works with stars having an outer convective envelope, such as giant stars or solar-like stars. In this framework, a new technique based on calibration of tight relations between age and particular chemical abundance ratios, the so-called chemical clocks, is providing interesting results. The relations between those ratios (e.g. [C/N], [Y/Mg]) and stellar ages, calibrated on stars with well-known ages (e.g., star clusters or solar-twins stars), allow us to derive ages of large sample of stars. To derive these relations, I have used data from *Gaia*, from the spectroscopic surveys Gaia-ESO and APOGEE and data-sets of high-resolution ($R \sim 115,000$) spectra. The spectra were collected with HARPS and HARPS-N spectrographs, mounted respectively at the ESO 3.6 m telescope in Chile and at the Telescopio Nazionale Galileo (TNG) in La Palma, Spain.

The present Thesis is composed of three main projects, published in the scientific journal *Astronomy & Astrophysics*: Casali et al. (2019, A&A, 629, A62), Casali et al. (2020b, A&A, 639, A127) and Casali et al. (2020a, A&A, 643, A12). In summary, the projects are:

- **Stellar dating using [C/N] as a chemical clock.** I derived an empirical relation between stellar ages and the [C/N] ratio in red giant branch stars. The value of this ratio depends, indeed, to the initial mass. During the red giant branch phase, the penetration of convective envelope towards inner regions brings up C and N to the surface,

in different quantities depending on the stellar mass, and thus producing a variation in the surface chemical composition. Since in a given evolutionary phase, there is a direct relation between mass and age, [C/N] can be used as an age tracer for giant stars. I calibrated an empirical relation between [C/N] and stellar ages, using red giant stars belonging to open clusters (observed in Gaia-ESO and APOGEE surveys), whose ages are determined from a global isochrone fitting of the cluster sequence. A first application of this relation was to calculate the ages of a large sample of red giant stars in the Galactic disc, finding a clear age separation between the two components of the disc: the thin and thick stellar populations. In particular, the youngest stars are present in the thin disc: their ages become older with increasing α-element content and with decreasing metallicity. In addition, the typical age of the thin-disc stars decreases in the inner part of the disc at low height on the Galactic plane and towards the outskirts. This means that the stars in the inner disc represent the later phases of the Galactic evolution, while the decreasing age towards the outskirts confirms an inside-out formation of the disc. Moreover, I compared the [C/N]-ages of open clusters to theoretical predictions and to the asteroseismologic age of a sample of field giant stars. In both cases, I found a good agreement.

- **Stellar dating using chemical clocks affected by chemical evolution.** In this work, I investigated relations between abundance ratios, composed by pairs of elements modified in opposite way by chemical evolution, and stellar ages. These pairs are usually composed by elements produced in short time-scales as α-elements (e.g. Mg, Ca, Si, Ti) and elements with a delayed production, as slow-process neutron-capture elements (e.g. Y, Sm, Sr). I analysed a sample of high-resolution HARPS spectra of solar twin stars, deriving with a differential spectral analysis with respect to the Sun, stellar parameters, chemical abundances, and ages. This technique allows us to minimise the systematic errors due to the model atmospheres, reducing the uncertainties on the stellar parameters and chemical abundances. I obtained empirical relations between age and 17 different chemical clocks, taking into account also the metallicity dependence. Using open clusters, located at different Galactocentric distances, I validated these relations, finding that their applicability is limited to the Solar neighbourhood. Namely, the ages derived from chemical clocks cannot reproduce the literature age of open clusters in the inner disc. In addition, by comparing the open cluster data-set with Galactic chemical evolution models, the theoretical s-process yields present in the literature are not able to reproduce the abundances of star clusters in the inner regions. To reproduce them, a reduced production at high metallicity of s-process yield by a factor of ten is required. The reasons should be sought in different star formation history of different portions of the Galactic disc. Indeed, star formation history produces variation in the shape of the linear relation between abundance ratios and stellar ages. Finally, I applied the dating relation to the Gaia-ESO field stars, located in the solar neighbourhood, in order to derive their ages. The ages derived with this relation confirm the dichotomy in age between the thin and thick disc seen in the previous project.

- **Chemical trends in the Galactic disc through the SPA observing program.** In the framework of the Stellar Population Astrophysics (SPA) observing program at the TNG telescope, I presented observations and spectroscopic analysis (HARPS-N spec-

tra) of four little studied open clusters located in the solar neighbourhood, namely Collinder 350, Gulliver 51, NGC 7044, and Ruprecht 171. I placed the four clusters in the framework of the Galactic chemical evolution, comparing their metallicity and abundance with the radial distributions of large samples of clusters observed in the spectroscopic surveys. The four clusters follow the general properties of the Galactic disc. I also derived the abundances of C and Li, which are compared with theoretical models, showing the need to use rotation-induced mixing models to better explain their abundances.

The Thesis is structured as follows:

- in Chapter 1, I present the Milky Way's structure, discussing its main components: bulge, halo, thin and thick disc; and its main stellar populations: open and globular clusters. Then, I introduce the Milky Way's formation scenarios and its chemical evolution, with a special focus on the nucleosynthesis sites where the elements heavier than lithium are produced.
- in Chapter 2, I show the main large spectroscopic surveys and the *Gaia* mission. I discuss the sky coverage, target selection and analysis strategy for the surveys used in this Thesis: Gaia-ESO and APOGEE.
- in Chapter 3, I discuss some methods for the determination of stellar ages, including isochrone fitting and chemical clocks, the main topic of this Thesis.
- Chapter 4, 5 and 6 show my three projects.
- Finally, I summarise and give my conclusions in Chapter 7.
- Moreover, in Appendix A I describe the spectral analysis based on the equivalent width measurement and the differential line-by-line analysis. I give some details on the software used in the projects to measure the equivalent width and to derive atmospheric parameters and chemical abundances from high-resolution spectra.

1

THE MILKY WAY

Galactic Archaeology is a branch of astrophysics that studies the formation and evolution of our Galaxy, the Milky Way. One of main aims of the Galactic Archaeology is the study of the properties of resolved stellar populations. Stars are indeed the major constituents of the baryonic galactic components, and also the main actors of the Galactic chemical evolution, since they are the main producers of elements heavier than He. They return part of them in the interstellar medium (ISM) in the final phases of their evolution, while the remaining elements are locked in stellar remnants as white dwarfs, neutron stars and black holes. The elements dispersed in the ISM become constituent of a new generation of stars. This recycle is responsible for the evolution of the Galactic chemical composition. Therefore, stars act as fossils, preserving – for most elements – the chemical composition of their parent gas clouds, giving information on the ISM composition at the time they were born. Thus, studying stars of different ages, we can investigate the whole chemical evolution.

In this framework, the study of the Milky Way plays a fundamental role, since it is the best environment in which we can determine chemical and kinematic properties of individual stars, from faint dwarfs to supergiants, allowing us to derive the whole formation history. In particular, the oldest components provide us with unique insights into how galaxies form and evolve in the first billion years, the so-called near field cosmology.

In this Chapter, I give a general introduction on the Milky Way, starting from the structure of its main components: the halo, the thick disc, the thin disc, and the bulge. Finally, I present a possible scenario for its formation and chemical evolution.

1.1. GALACTIC STRUCTURE

The Milky Way is classified as a barred spiral galaxy Sb, and it is located in a cluster of galaxies called Local Group. It is composed by three main structures (see, e.g. Sparke & Gallagher, 2007; Schneider, 2015): a disc, a spherical halo and a central bulge (see Fig. 1.1). The Sun is located in the Galactic disc, at 8.3 kpc from the Galactic centre, in one of its spiral arms (Eisenhauer et al., 2005).

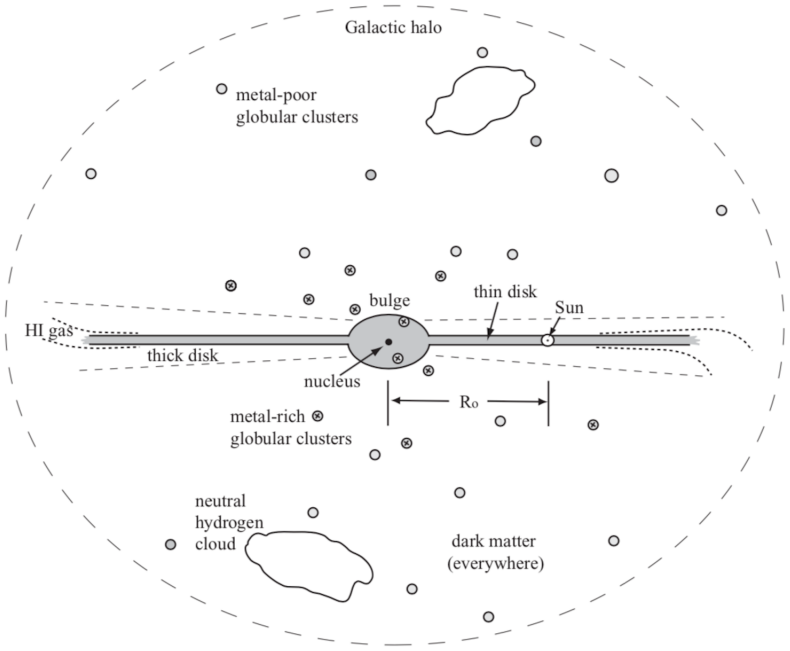

Fig. 1.1: A schematic side view of the Milky Way from Sparke & Gallagher (2007).

1.1.1. THE GALACTIC BULGE

The Galactic bulge is the central component of the Milky Way with a typical scale-length of ~ 1 kpc (Sparke & Gallagher, 2007). It is a massive component comprising about a quarter of the Galactic stellar mass, i.e. $M = 2.0 \pm 0.3 \cdot 10^{10}\, M_{\odot}$ (Valenti et al., 2013). Due to the presence of dust and gas towards the centre of the Galaxy, the bulge is better studied in the near-IR than in the optical. The observations of the COBE satellite (Dwek et al., 1995) revealed a peanut-shaped bar in the bulge (McWilliam & Zoccali, 2010; Nataf et al., 2010). In particular, Hill et al. (2011) by observing bulge red clump stars concluded that their metallicity distribution is doubled-peaked, with one peak at [Fe/H]$= -0.30$ dex and the other one at [Fe/H][1]$= +0.32$ dex. They called these two populations metal poor and metal rich. More recently, Schultheis et al. (2017) with the APOGEE data (Zasowski et al., 2013, 2017; Majewski et al., 2011, 2017) and Rojas-Arriagada et al. (2017) with the Gaia-ESO data (Gilmore et al., 2012; Randich et al., 2013) concluded that the metallicity distribution function in the bulge is bimodal. Zoccali et al. (2017) confirmed that the metal poor population is more concentrated towards the centre of the Bulge. Later, Bensby et al. (2017) found a more complex multi-modal metallicity distribution, with at least four peaks. These peaks correspond to different star formation episodes occurred 12, 8, 6 and 3 Gyr ago. Although most bulge stars are older than 10 Gyr (Valenti et al., 2013; Barbuy et al., 2018; Renzini et al., 2018), there is also a young stellar component.

At its centre there is a dense nucleus of stars (central star cluster) and a black hole with a mass of $M_{BH} \approx 4 \cdot 10^{6} M_{\odot}$ (Genzel et al., 2003; Gennaro et al., 2010). Bulge stars have larger random velocities, but follow a general rotation around the centre of the Galaxy.

[1] $[\mathrm{Fe/H}] = \log(n_{\mathrm{Fe}}/n_{\mathrm{H}})_{\star} - \log(n_{\mathrm{Fe}}/n_{\mathrm{H}})_{\odot}$ with n the number of atoms of Fe and H.

1.1.2. THE GALACTIC HALO

The halo is a spherical structure surrounding the Galactic disc and bulge. The stellar halo includes about 1% of the Galactic stellar content ($M = 4 - 7 \cdot 10^8 M_\odot$, Bland-Hawthorn & Gerhard, 2016), consisting of about 150 globular clusters (see Sect. 1.1.4 for more details) and field stars with a high velocity component perpendicular to the Galactic plane. Stars in the halo are metal-poor, with a peak of the metallicity distribution around [Fe/H]~ -1.6 dex and an extension up to -3 dex (Ryan & Norris, 1991; Helmi, 2008), and α-enhanced[2] (Wheeler et al., 1989; Nissen et al., 1994; Carretta et al., 2000). Moreover, they do not have any organised rotation around the centre of the Galaxy, but they follow random directions with eccentric orbits.

Hartwick (1987) found a duality in the spatial distribution of halo stars: a flattened inner component and a more spherical outer one. Further studies confirmed the presence of this duality, showing a prograde rotation for the inner component with a high α content and a mean metallicity of [Fe/H]~ -1.6 dex; and a retrograde rotation for the outer component with a less content of α-elements and a mean metallicity of [Fe/H]~ -2.2 dex (Carollo et al., 2007; Nissen & Schuster, 2010; Hayes et al., 2018). These two components imply a different formation: in situ for the high-α stars and via accretion for the low-α stars. Moreover, the halo continues to accrete matter in the form of dwarf galaxies which are then tidally disrupted in the gravitational field (Belokurov et al., 2006). A possible remnant of a past merger, Gaia-Enceladus (Helmi et al., 2018; Belokurov et al., 2018; Koppelman et al., 2019), was discovered thanks to *Gaia* data. This merger, occurred approximately 10 Gyr ago, likely heated up the gas in the dark matter halo (Chaplin et al., 2020), preventing the star formation in the disc (Vincenzo et al., 2019). This event might explain the quenching period after the thick disc formation (Bovy et al., 2016; Khoperskov et al., 2018).

1.1.3. THE GALACTIC DISC: THICK AND THIN COMPONENTS

The main stellar component of the Milky Way is its disc with a stellar mass of $M = 4 \pm 1 \cdot 10^{10} M_\odot$ (Bland-Hawthorn & Gerhard, 2016). This component represents the main Galactic structure studied in the present work.

Distribution of stars The Galactic disc has a radial extension of about 15 kpc. The disc can be divided in two main components: the *thin disc*, with a typical height in the range 220-450 pc (Ojha, 2001; Reid, 1993; Gould et al., 1996; Jurić et al., 2008) and typical length of 2.6 ± 0.5 kpc (Jurić et al., 2008; Bland-Hawthorn & Gerhard, 2016); and the *thick disc*, with a height of about 900 pc (Jurić et al., 2008) and typical length of 2.0 ± 0.2 kpc (Bovy et al., 2012; Bland-Hawthorn & Gerhard, 2016). The former contains $\sim 95\%$ of stars, the latter $\sim 5\%$, although recent works indicate that the thick disc can be more massive (e.g. Pouliasis et al., 2017). The gas and dust components are located in the disc with a scale height of about 100 pc.

The density n of stars in the disc drops towards the outer regions following a proportional relation as $n(R) \propto e^{-R/h_R}$, where R is the radius and h_R is the scale length of the disc. Whereas, the stellar density in the direction perpendicular to the Galactic disc is approximately described by $n(z) \propto e^{-|z|/h_z}$ where h_z is the scale-height that specifies the thickness

[2] α-elements are all the elements produced by adding α-particles, i.e. O, Ne, Mg, Si, S, Ca etc.

of the respective component (Schneider, 2015).

The two exponential laws describing the radial and vertical distributions of stars can be combined together, giving a density distribution of the total stellar population (per spectral type s, or age):

$$n(R,z,s) = n_0 \left(e^{-|z|/h_{thin}} + 0.02 e^{-|z|/h_{thick}} \right) e^{-R/h_R} \tag{1.1}$$

where $h_{thin} \sim 300$ pc is the scale-height of the thin disc (Jurić et al., 2008), $h_{thick} \sim 1$ kpc is the scale-height of the thick disc (Sparke & Gallagher, 2007) and h_R is the scale-length of the disc, typically in the range of 2.5 kpc $\lesssim h_R \lesssim$ 4.5 kpc (Sparke & Gallagher, 2007).

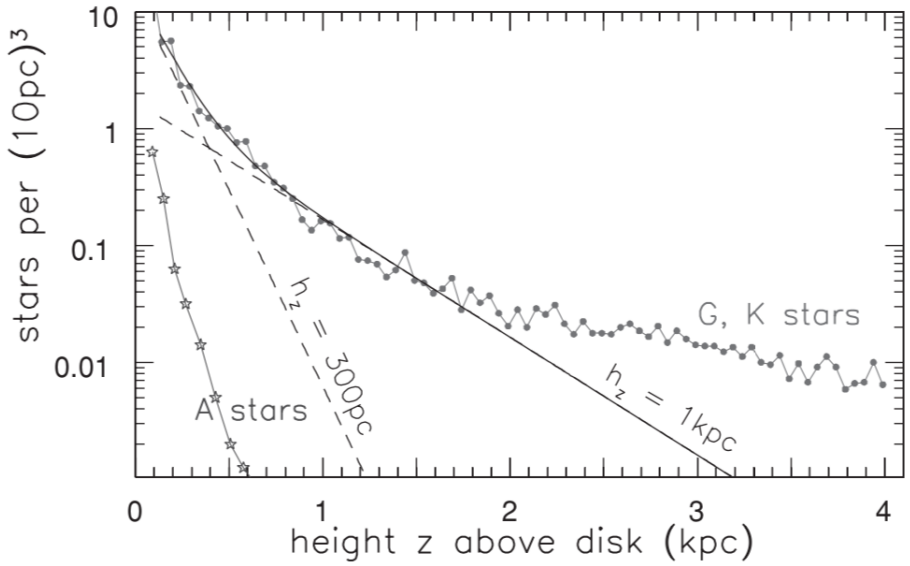

Fig. 1.2: The vertical density distribution. The dashed lines show $n(z) \propto e^{(-z/300\text{pc})}$ (thin disc) and $n(z) \propto e^{(-z/1\text{kpc})}$ (thick disc), respectively. The solid curve is their sum. The curve with the star symbols represents the density distribution of A dwarfs, while the curve with dots represents the G, K dwarfs stars (Sparke & Gallagher, 2007).

In the vertical direction, the thick disc dominates at high z with respect to the thin disc. The vertical density distribution for both discs and for their sum is shown in Fig 1.2 (dashed and solid lines, respectively). Moreover, this Figure displays also how old and low mass K, G[3] dwarf stars belong to the thin and thick discs at $z < 2$ kpc, while they belong to the halo at $z > 2$ kpc. Instead, massive and shorter-lived stars, such as the A dwarfs, are located very close to the Galactic plane, with heights above the Plane smaller than the typical height of the thin disc ($\sim$ 300 pc, Jurić et al., 2008).

The presence of two disc components in spiral galaxies is common as we can see from the Fig. 1.3. The two panels present, respectively, the thin and thick discs of the galaxy NGC 4762, where a deeper exposure reveals a thicker disk component, as extended as the thin one.

[3] The letters indicate the classification of stars based on their spectral types. The classification uses the letters O, B, A, F, G, K, M, a sequence from the hottest (O type) to the coolest (M type). See Appendix A for more details.

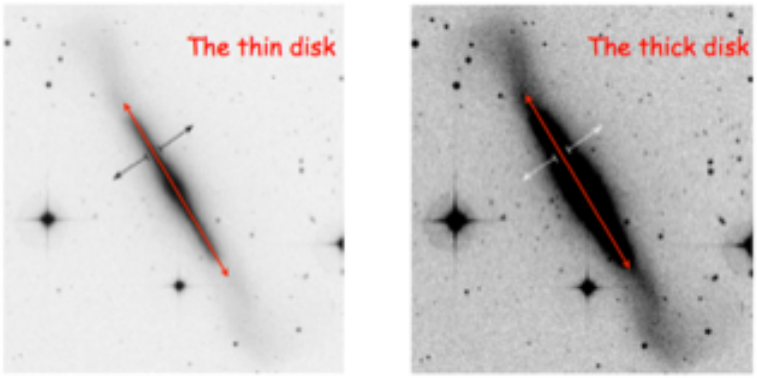

Fig. 1.3: The thin (left panel) and thick (right panel) of the spiral galaxy NGC 4762 (Tsikoudi, 1980).

Chemical composition and age of disc stars The thick disc was identified for the first time by Yoshii (1982) and Gilmore & Reid (1983). They recognised it as an overdensity of stars at large distances from the Galactic plane. However, there are also differences in the chemical composition of stars belonging to the thin and thick discs. Several observations show that thin disc stars reaches typically higher metallicities than thick disc stars (Bensby et al., 2014; Hayden et al., 2017). Moreover, the content of α-elements (Mg, Si, S, Ca, Ti) at a given metallicity is higher in the thick disc than in the thin disc. This difference in [α/Fe] has to be appointed to a different star formation history in the two components of the disc, and it is related to the different timescales for the production of α elements and iron.

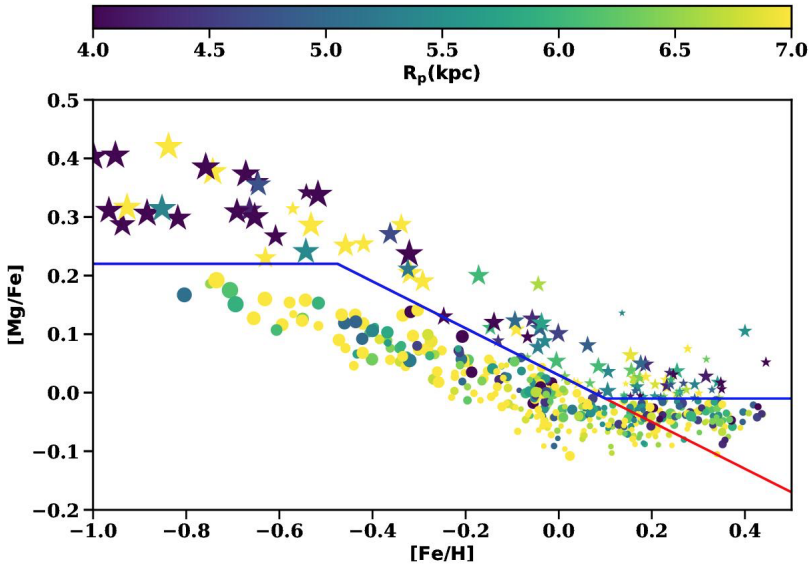

Fig. 1.4: [Mg/Fe] vs. [Fe/H] plane by Hayden et al. (2017). The blue line represents the separation between thin and thick discs: thick disc stars are marked with a star symbol, while thin disc stars with a circle symbol. The size of the symbols denotes the age of each star: the larger points are older than smaller points. Stars are colour-coded by their R_p (perigalacticon radius).

The dichotomy between thin and thick discs is shown in Fig. 1.4, in which two clear sequences in the distribution of stars in the [α/Fe] vs. [Fe/H] plane can be distinguished: one at high-[α/Fe] values and metal poor, and one at low-[α/Fe] and solar and supersolar

metallicity, which eventually merge at [Fe/H]$\sim +0.2$ dex. Moreover, the relative fraction of these two components varies with disc height z and Galactocentric radius R_{GC} (see Fig. 1.5). In the outer regions, the locus of the thin disc shifts towards lower metallicity, favouring the inside-out formation scenario (see Sect. 1.2), according to which, the outer regions are formed on longer timescales, hence the chemical enrichment has still not reached its peak, and it is lower than in the inner regions. On the other hand, the locus of thick disc appears similar in all panels in which it is observed, but it is less-populated towards the outer regions and close to the Galactic Plane (Hayden et al., 2015).

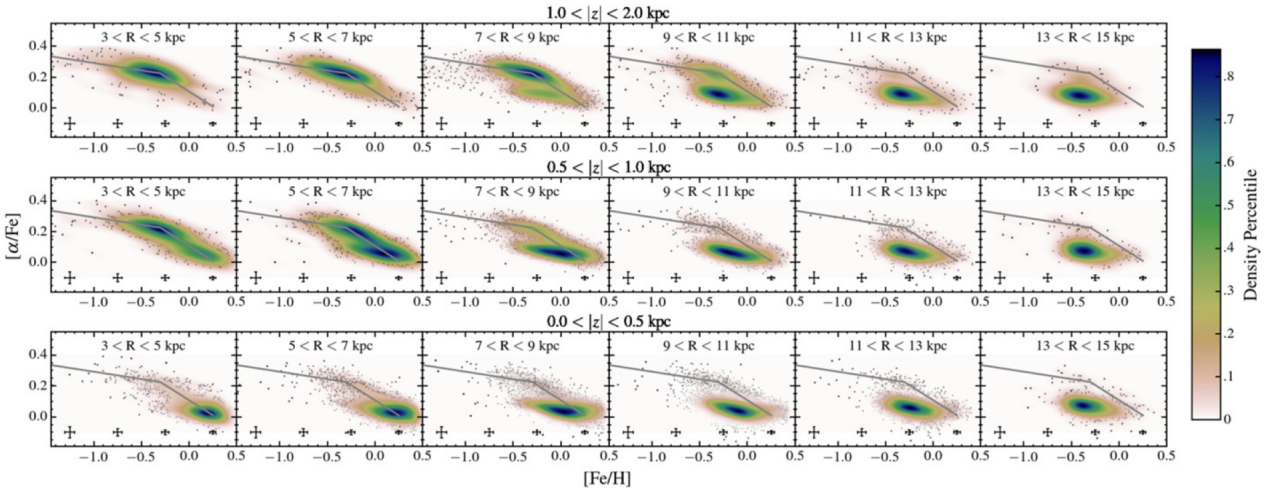

Fig. 1.5: Stellar distribution of stars in the [α/Fe] vs. [Fe/H] plane by Hayden et al. (2015).

Indeed, the Galactic disc has a dual stellar populations, chemically distinct and separated in age. In particular, the thin disc is the dominant population in the outer regions, even at large distances from the Galactic plane, and it is younger than the thick disc. In fact, the epoch where the separation between the two discs is identified is around 8 Gyr ago. This epoch coincides with the evidence for mergers between the Milky Way and another dwarf galaxy (Bensby et al., 2014).

1.1.4. STAR CLUSTERS

In the Milky Way, stars can be isolated (field stars) or grouped in clusters or associations (Lada & Lada, 2003). After the partial or total dissolution over time of star clusters, their members become part of the field populations (Fujii & Portegies Zwart, 2016; Beane et al., 2019; Hetem, 2020). The cluster disruption can be due to the interaction with the spiral arms of the Galaxy, to the two-body relaxation, or to the erosion by the tidal field (Freeman & Bland-Hawthorn, 2002). The *chemical tagging* technique aims at recovering disrupted star clusters, even after being scattered by the dissipative evolution of the disc, through the common features in the chemical composition of cluster members (Freeman & Bland-Hawthorn, 2002).

In our Galaxy, the clusters can be divided in main two groups: open clusters, usually younger and less massive, and globular ones, very old and massive. This difference is not so marked in other galaxies, such as Magellanic Clouds, where massive young clusters are observed (D'Antona et al., 2019, and references therein). In the following sections, I describe

the main features of the cluster populations, with emphasis on the open cluster population, tracers of the Galactic disc.

GLOBULAR CLUSTERS

Globular clusters (GCs) are gravitationally bound groups of stars located mainly in the Galactic halo and in the bulge. The GCs in the bulge have nearly circular orbits, while those in the halo have elongated orbits. The catalogue of Harris (1996, and the update in 2003) contains 150 members. The typical shape of a GC is spherical (for this reason, they are called "globular") and their stellar density is very high: most of the GCs are formed by about 10^5 - 10^6 stars (Stetson et al., 1996). Their ages are usually larger than 10 Gyr. Their metallicity is in the range $-2.3 <$ [Fe/H] < 0.0 dex and shows a bimodal distribution with two peaks at [Fe/H]$= -0.6$ dex and [Fe/H]$= -1.6$ dex (Zinn, 1985). They show abundance variations in several light elements, in particular there are anti-correlations between Na-O, Mg-Al, Li-Na, C-N and F-Na (Carretta et al., 2010; Gratton et al., 2012; Milone et al., 2020, 2017; Guerço et al., 2019). These anomalies mean that GCs are not exactly composed by a simple stellar population, but they are formed by at least two episodes of star formation. The two (or more) stellar generations can be distinguished by their chemistry. Several studies find that massive stars, which pollute with their eject the ISM, might be at the origin of the anomalies in the second-generation stars (Gratton et al., 2012; Nota & Charbonnel, 2016, and references therein).

In Figure 1.6, I show a typical colour-magnitude diagram (CMD), a diagram in which the stellar magnitude[4] in a given photometric band is plotted as a function of the stellar colour[5], of a globular (magenta) and open (blue) cluster. Figure 1.6 highlights the typical sequence of a GC, 47 Tuc, where the evolved stages, such as red giant branch (RGB), horizontal branch (HB) and asymptotic giant branch (AGB), are most populated. Moreover, the position of main sequence turn-off[6] (TO), the point where the main sequence is left after the exhaustion of H, is fainter than the TO of open clusters, indicating an older age with respect to the open clusters.

OPEN CLUSTERS

Open clusters (OCs) are composed by a number of stars that ranges between some hundreds to some thousands. The youngest clusters can still contain gas and dust. The process of star formation takes a shorter time compared to the lifetime of the cluster, so that all member stars are of similar age. In addition, stars in a same cluster are expected to share the same initial chemical composition, and no anti-correlations as in GCs have been observed so far (De Silva et al., 2006, 2007a,b; Reddy et al., 2012; Ting et al., 2012; Bovy, 2016). They are called "open" because they have not a clear shape and are weakly gravitationally

[4] Magnitude is a logarithmic measurement of the radiative flux of an object measured in a specific wavelength or band A with respect to the flux of a reference source: $m_A - m_{ref} = -2.5\log(F_A/F_{ref})$. The magnitude m observed from Earth is called the apparent magnitude. An absolute magnitude M is then defined as the magnitude at a distance of 10 parsecs (1 pc = 3.26 light years) from Earth.

[5] Colour is the difference in magnitude between two distinct bands.

[6] The main sequence is a region in the CMD where stars burn hydrogen in helium in the stellar core, while the turn off is the point where stars finish the H-burning in the core and they evolve towards the sub-giant branch sequence.

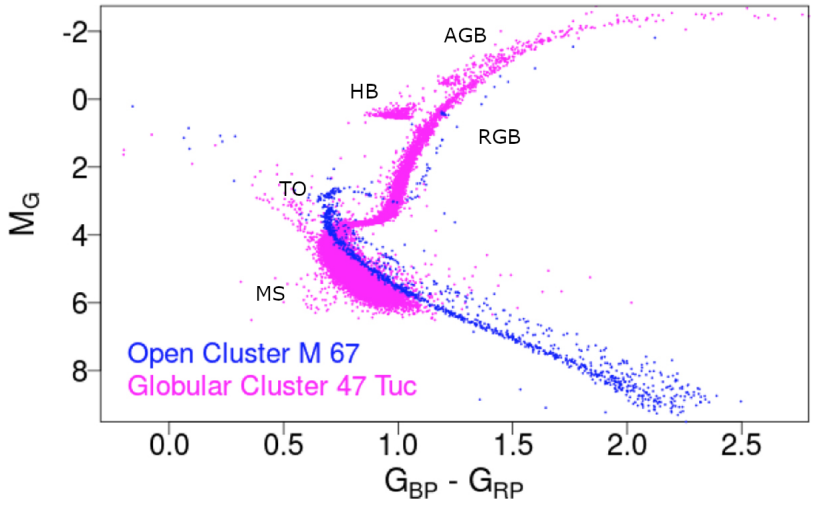

Fig. 1.6: Comparison between the CMDs of 47 Tuc (Age=12.75 Gyr, [Fe/H]=−0.72), a globular cluster (magenta dots), and M 67 (Age=3.47 Gyr, [Fe/H] = 0.03), one of the oldest open clusters (blue dots). Figure from Gaia Collaboration et al. (2018a).

bound. For this reason, some of them are going to disperse over time (Lada & Lada, 2003; Beane et al., 2019; Hetem, 2020).

Unlike GCs, OCs have a CMD with less populated evolved evolutionary stages and a TO brighter than in GCs. This means that OCs are, on average, younger than GCs. We can see this difference comparing the CMD of a globular and an open cluster in Fig. 1.6.

The first catalogues of open clusters, reporting their sky coordinates and some distances, were those of Melotte (1915), Trumpler (1930) and Collinder (1931). Modern catalogues provide more information of clusters, as their age, photometric (magnitude, reddening, etc.) and spectroscopic (metallicity, elemental abundances) parameters. The most widely-used catalogues of OCs are the catalogues of Dias et al. (2002) and of Kharchenko et al. (2013). The former is a compilation of parameters from a large number of studies obtained with different methods; the latter shows an automated characterisation of the cluster population, performed with the all-sky 2MASS photometry (Skrutskie et al., 2006).

The *Gaia* mission (Lindegren et al., 2018; Gaia Collaboration et al., 2018b; Bailer-Jones et al., 2018) has allowed us to discover and to characterise a large number of clusters in the solar neighborhood and beyond (Cantat-Gaudin et al., 2018a; Cantat-Gaudin & Anders, 2020; Cantat-Gaudin et al., 2020; Castro-Ginard et al., 2020). Recent studies, such as Castro-Ginard et al. (2020), use a machine-learning based methodology to search for overdensities in the *Gaia* DR2 and identify the open clusters using photometric information from their colour-magnitude diagrams compared with isochrones. Cantat-Gaudin et al. (2020) derive cluster parameters in a homogeneous and automatic method for ~2000 open clusters with members identified in the *Gaia* data. Their automatic searches for open clusters are driving a revolution in star cluster science, increasing the number of known open clusters so far.

Age and Spatial distribution Open clusters are mainly located in the thin disc and follow circular motions on Galactic plane around the Galactic centre. Their age ranges from 10 Myr to some Gyrs, typically much younger than the GCs.

Figure 1.7 shows how the distribution of OCs clearly follows the Galactic plane with a

dispersion of about 8 deg within a region from 4 kpc to 20 kpc from the Galactic centre. The lack of OCs out of this range (4–20 kpc) might be related to an observational bias.

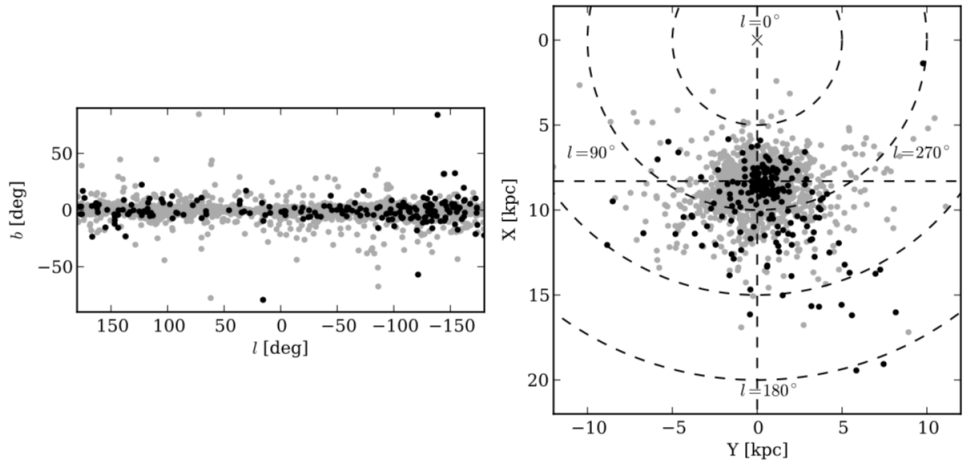

Fig. 1.7: Left panel: sky position of all 2174 OCs present in the catalogue by Dias et al. (2002) in the Galactic (l, b) coordinates. Right panel: distribution of all 1657 OCs (Dias et al., 2002) with a estimation of distance, projected on the Galactic plane. In both panels, the black points indicate clusters with available metallicity values (Figure by Cantat-Gaudin, 2015).

Old clusters exhibit a wider distribution above the Galactic plane, while younger OCs have a tighter distribution (Bonatto et al., 2006; Buckner & Froebrich, 2014). They show different scale-heights about the Galactic plane (z): about 300 pc for the older sample and about 135 pc for the younger sample (Cantat-Gaudin, 2015). Moreover, clusters in the inner disc tend to be younger than in the outer disc. The difference in age between inner and outer regions of the disc is likely due to the denser environment of the inner disc, where a cluster can be more likely disrupted early than in the outer disc. In addition, young OCs (ages <10 Myr) trace the spiral arms of the Milky Way, while older clusters have moved away from their birthplace and they have lost their originally tightly constrained spatial distribution (Dias & Lépine, 2005; Martínez-García & Puerari, 2014).

Chemical composition Open clusters have metallicity ranging $-0.8 <$ [Fe/H] < 0.5 dex with a peak at [Fe/H]= 0.0 dex (see Fig. 1.8, Chen et al., 2003). The higher number of OCs with solar metallicities ([Fe/H]= 0.0 dex) reflects the fact that most known clusters are located in the solar neighbourhood.

The relation between cluster age and their metallicity is very loose (see Bragaglia & Tosi, 2006; Carraro et al., 2007; Friel et al., 2002; Friel & Janes, 1993; Jacobson et al., 2011; Magrini et al., 2009). On the other hand, open clusters are excellent tracers of the spatial distribution of abundances and show a well-defined radial metallicity gradient (e.g. Friel et al., 2002; Jacobson et al., 2016; Casali et al., 2020a). An example of the gradient is shown in Fig. 1.9, where we see a steeper inner gradient and a flatter outer gradient, with a change in slope at R_{GC}=12 kpc. Moreover, grouping OCs into different age bins, it is possible to trace the time-evolution of the gradient (Magrini et al., 2009).

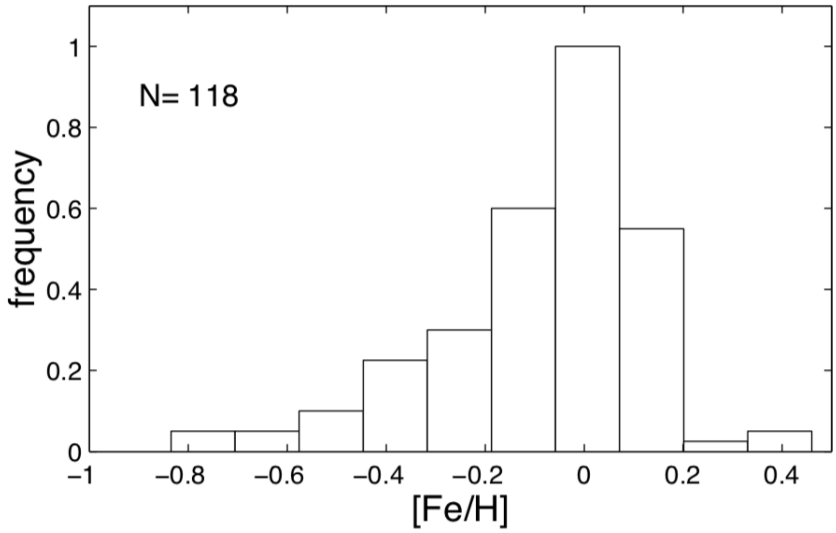

Fig. 1.8: Metallicity distribution of the Galactic open clusters (Figure by Chen et al., 2003).

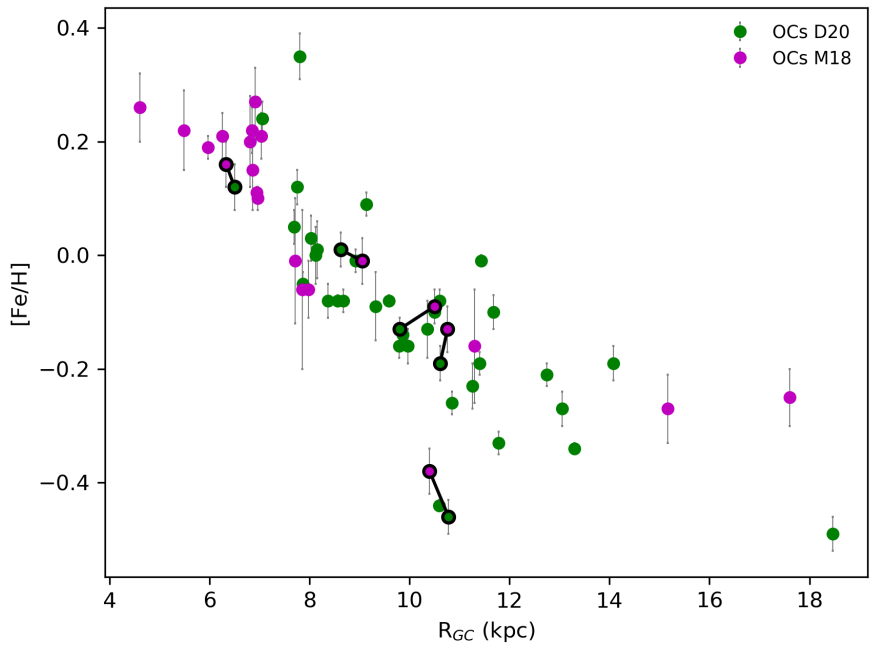

Fig. 1.9: Radial metallicity gradient using the open clusters listed by Donor et al. (2020, D20) with at least three member stars and high quality flag, and Magrini et al. (2018, M18). Clusters in common between the catalogues listed by D20 and M18 are linked with a black line.

1.2. THE FORMATION OF THE MILKY WAY

The first Galactic formation model was conceived in the 1960s by Eggen et al. (1962). According their model, the Milky Way was formed by a rapid collapse of a single spherical cloud of gas. The original gas was very poor in metals, and stars formed early in the collapse. These stars maintained the kinematic properties of the collapsing cloud, following

eccentric orbits around the centre of the Galaxy, and formed the halo and the GCs. Because of a dissipative collapse and the conservation of angular momentum, the cloud started to collapse preferentially along its rotational axis, becoming progressively flatter and forming a disc. The gas in the disc was enriched in metals produced by supernovae explosions of the early generations of halo massive stars, while the halo preserved its metallicity and kinematics.

In the following decades, new observations indicated that the Milky Way did not formed in single rapid collapse. The wide spread in metallicity and age of GCs favoured the model proposed by Searle & Zinn (1978), in which the Galactic halo formed by the aggregation of many cloud fragments, each of them evolved following an independent history and produced objects with different age and metallicity. That scenario is reinforced by recent observations of remnants of collisions of the Milky Way with other dwarf galaxies (Chaplin et al., 2020).

To reproduce the characteristics of our Galaxy, including the distribution of G-dwarf stars, a more complex scenario is required (Chiosi, 1980; Matteucci & Francois, 1989; Ferrini et al., 1994; Chiappini et al., 1997). G-dwarf stars are very old low-mass stars, still in the MS. The collapse model predicts a large number of metal-poor G-dwarfs in the solar neighbourhood, formed by pristine gas. However, the observations indicate that there are relatively few metal-poor G-dwarfs nearby the Sun. To resolve the so-called "G-dwarfs problem", a solution is to assume that the Galactic disc was less massive at the beginning of its formation and then it increased later its mass through a continuous infall of gas.

One of the most successful expressions of this scenario is the so-called "two-infall" (see Fig. 1.10 Chiappini et al., 1997; Chiappini, 2001) model. It assumes that an initial collapse formed the halo and a part of the thick disc. After an extremely efficient rate, the star formation terminates in the halo and the gas accumulates in the centre of the protogalaxy and forms the bulge. Then, a second infall event forms the thin disc, probably as a result of a merger with a small galaxy.

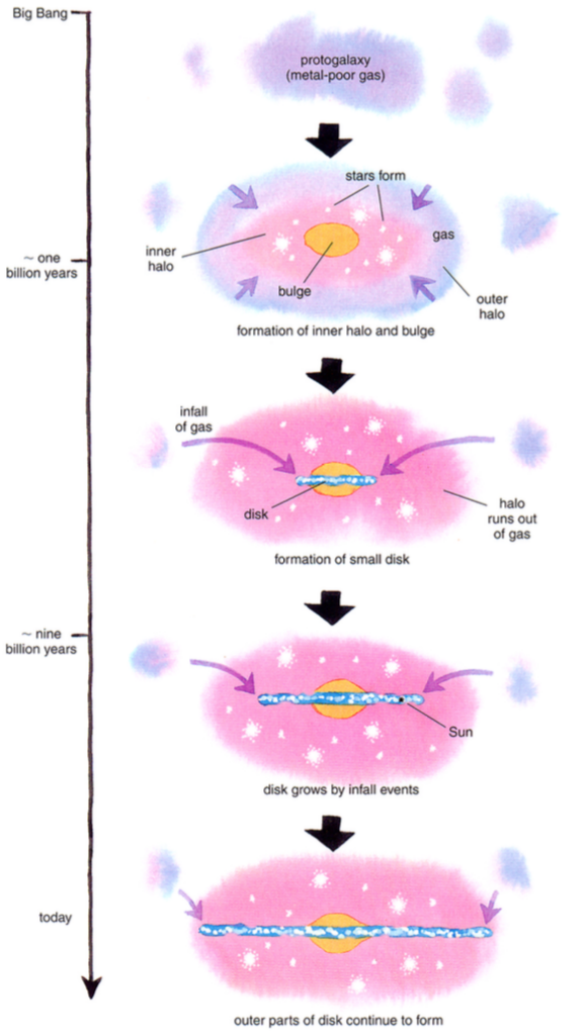

Fig. 1.10: The two-fall scenario (Chiappini, 2001).

There are many other recent studies (see, e.g. Snaith et al., 2014, 2015; Haywood et al., 2013, 2016) that have refined the scenario, as the one that predicts a separate episode for the formation of the inner Galactic disc by an early accretion of gas (inside-out scenario). Following that model, the first phase occurred with an intense star formation burst in the inner regions, while the second phase was characterised by a more quiet star formation in the outer regions, polluted by metal-poor halo

gas. A direct consequence of this scenario is a chemical discontinuity between the inner and outer regions of the Galactic disc at Galactocentric radius $R_{GC} \sim 9$ kpc (Twarog et al., 1997; Amôres et al., 2009; Lépine et al., 2014).

1.3. GALACTIC CHEMICAL EVOLUTION

The term "galactic chemical evolution" (GCE) indicates the study of how the global chemical composition of a galaxy, usually measured in its ISM, varies with time as a consequence of the star formation and of the exchange of gas through inflow and outflow episodes. There are several models describing the process of enrichment of the Milky Way: classical models, i.e. considering only the chemical evolution aspects (e.g. Ferrini et al., 1994; Chiappini et al., 1997; Chiappini, 2001; Matteucci & Recchi, 2001; Matteucci, 2014), chemodynamical-models that consider dynamical processes, as, e.g., stellar migration, gas flows, galactic fountains (e.g. Spitoni et al., 2008, 2009; Spitoni & Matteucci, 2011; Spitoni et al., 2015; Minchev et al., 2014; Kubryk et al., 2015; Prantzos, 2016), and models built in cosmological context (e.g. Gibson et al., 2013; Valentini et al., 2019). In the following sections I describe some of the main ingredients, present in all kinds of GCE.

1.3.1. THE IMF AND SFR

The star formation history (SFH) and/or the star formation rate (SFR), and the initial mass function (IMF) are important ingredients of all GCE models. These quantities regulate the number of stars in each phase of the Galactic evolution. Stars, through the ejecta of metals in the interstellar medium during the final phases of the stellar evolution, drive the enrichment of the ISM. The SFH can be expressed with the stellar birthrate function:

$$\mathscr{B}(t,m) = \psi(t)\phi(m)dtdm \tag{1.2}$$

where $\psi(t)$ and $\phi(m)$ are the SFR and IMF, respectively. This function defines the number of stars which were born in the mass interval $m, m+dm$ and in the time interval $t, t+dt$. On the most common parametrisation of the SFR is the so-called Schmidt-Kennicutt law (Schmidt, 1959; Kennicutt, 1998a,b), $\psi(t) = \nu\sigma_{gas}^{k}$, where ν is the star formation efficiency, σ_{gas} is the surface gas density and k is a index in the interval [1, 2]. The IMF is the initial mass distribution of stars at their birth. In the literature, there are several expressions of the IMF, usually computed by fitting observations in the solar neighbourhood (Kroupa et al., 1993; Scalo, 1986). The IMF is usually defined with a power law: $\phi(m) = a\,m^{-1+x}$, where a is the constant of normalisation in the interval of mass 0.1-100 $M_{\odot}$, and the mostly used value for x is 1.35 by Salpeter (1955).

1.3.2. STELLAR EVOLUTION AND NUCLEOSYNTHETIC STELLAR YIELDS

Other fundamental ingredients for the Galactic chemical evolution are the stellar yields (see, e.g. Renzini & Voli, 1981; Woosley & Weaver, 1995; Romano et al., 2010; Karakas & Lattanzio, 2014; Karakas & Lugaro, 2016), which are provided by stellar evolutionary models. Stellar yields are defined as the integral of the mass lost, in a given elements, from a star

during its entire stellar lifetime:

$$M_k = \int_0^\tau X(k) \frac{dM}{dt} dt \tag{1.3}$$

where M_k is the yield of species k (in solar masses), dM/dt is the current mass-loss rate, $X(k)$ is the current mass fraction of species k at the surface, and τ is the lifetime of the star. Indeed, the stellar yield is the amount of each element expelled into the interstellar medium over the stellar lifetime.

As shown in Fig. 1.11, elements have different cosmic origins. During the Big Bang only light elements (H, He, Li) were synthesised, while elements heavier than Li are synthesised into stars through nuclear reactions and they are restored into the ISM at the latest phases of their evolution. Some light elements, such as Li, Be and B are formed during interactions between cosmic rays. Elements up to ^{56}Fe are produced by exo-energetic nuclear reactions. For elements heavier than ^{56}Fe the nuclear fusion is inhibited and they are produced by successive capture of neutrons on lighter elements, where neutrons are transformed into protons by β-decay.

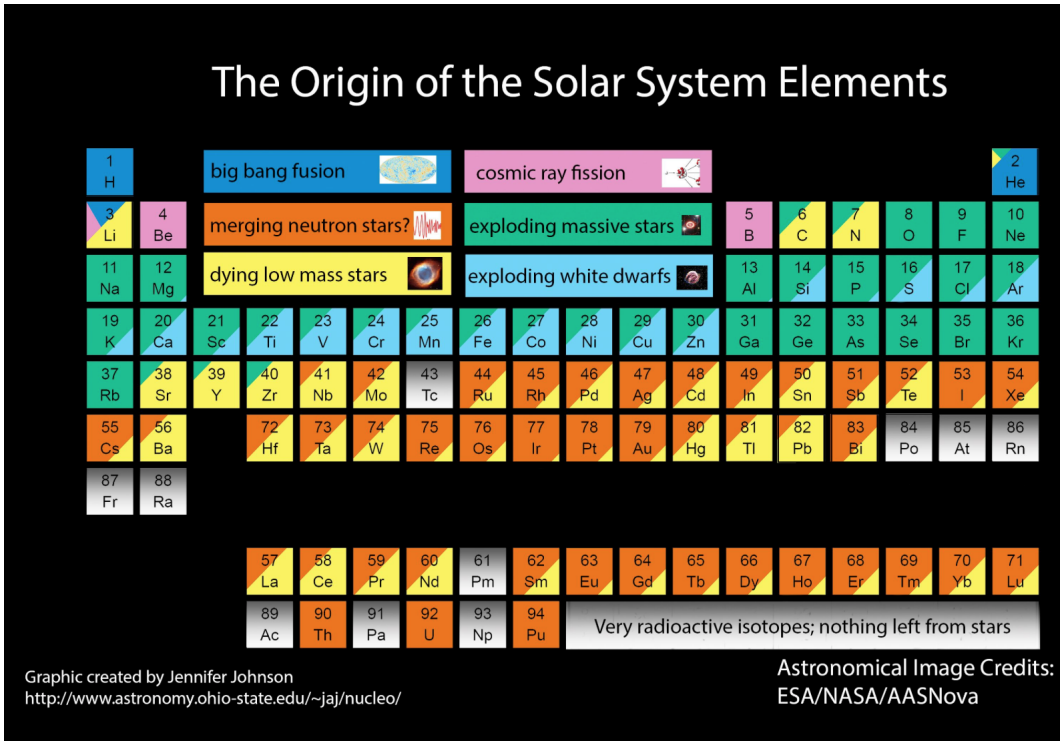

Fig. 1.11: Periodic table where the elements are colour-coded by their progenitors.

According to their mass, stars evolve in different ways, producing different amount of elements (Schwarzschild, 1958). The final phases of stellar evolution can be quiescent as in the case of low and intermediate-mass stars which end their life as white dwarfs or violent as for massive stars, evolving in core-collapse supernovae (SNe).

Massive stars ($M > 8-10M_\odot$) reach the temperature and pressure conditions necessary to synthesise elements heavier than C. They develop an onion-like structure with a central non-degenerate iron core and a series of surrounding burning shells of Si, O, Ne, C, He, H, respectively from the inner regions to outer ones. When the iron core reaches the Chandrasekhar mass limit ($M \sim 1.44M_\odot$), the star undergoes the end of its evolution. The iron

core becomes degenerate and the electron-degeneracy pressure cannot prevent the gravitational collapse. The core goes through the stage of "photo-dissociation" of iron-nuclei producing free α-particles, and then through the stage of "neutralisation". At the end, massive stars leave as remnant a neutron star or, if the neutron-degeneracy pressure cannot sustain the core, a black hole. After a lifetime of a few Myr and a core-collapse explosion, they eject in the ISM mainly elements produced through captures of α particles, such as O, Ne, Mg, Si, S, Ca and Ti, the so-called **α-elements**. However, they eject also elements with atomic number up to iron and nickel. The enrichment of the ISM can occur either through stellar wind during the "normal" evolutionary stage of a star, or at the final explosive stages when the shells are blown by shockwaves, reinforced also by high-energy neutrinos. Since the lifetime of massive stars is short on the time-scale of Galactic chemical evolution (few Myr vs several Gyr), they are the first stars to enrich the ISM.

In addition to the evolution of single stars, nucleosynthesis can happen in binary systems, composed by a CO white dwarf and a companion. This companion can be a main-sequence or red giant star which accretes material on the CO white dwarf (single-degenerate scenario), or another CO white dwarf which loses angular momentum via gravitational waves emission and collides with the companion (double-degenerate scenario). In both cases, the carbon deflagration occurs, producing a significant nucleosynthesis of chemical elements around the peak of iron. These systems explode as Type Ia SNe after reaching the Chandrasekhar mass limit, producing mainly Fe and **iron-peak elements** (e.g., Cr, Mn, Co, Ni), with a minor amount of α-elements. The binary systems that produce SNe Ia contain low-mass stars with longer evolutionary timescales (> 1 Gyr) than the timescales of massive stars SNe II progenitors (<10^{-2} Gyr) (see, e.g. Matteucci, 2014). A visual sketch of stellar evolution and of cycle of dust and gas in the Galaxy is shown in Fig. 1.12.

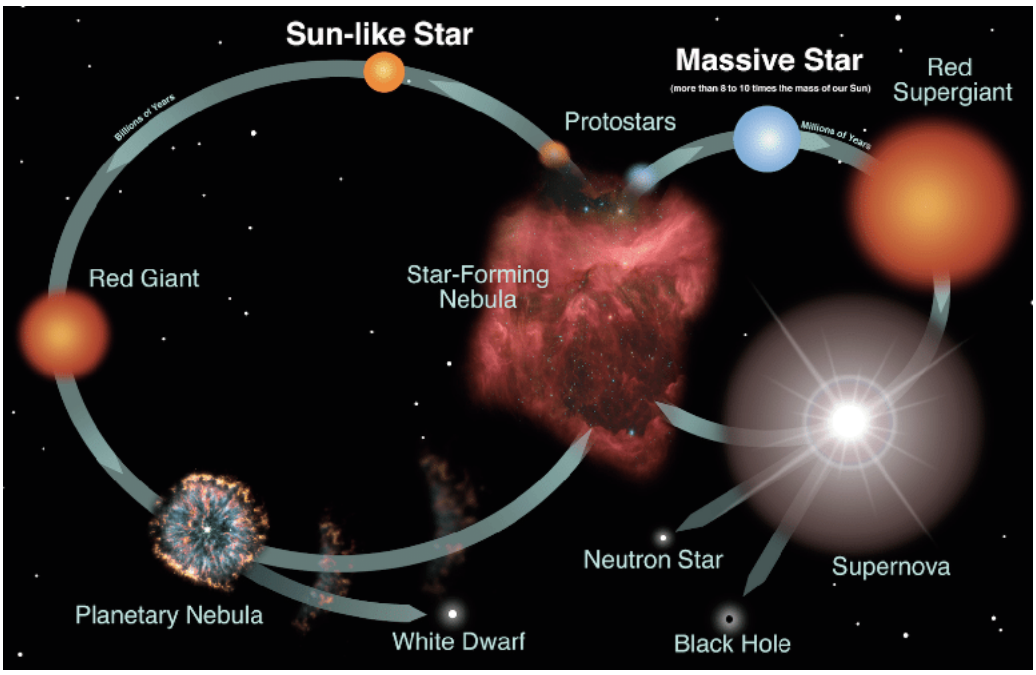

Fig. 1.12: A sketch of the life cycle of dust and gas in the Galaxy and the role of stellar evolution (Credit: NASA and the Night Sky Network).

The ratio between [α/Fe] is an important tracer of the intensity and duration of the star

formation episodes: at early epochs, the ISM was enriched by SNe II and thus their α/Fe content was higher. At later times, SNe Ia started to contribute to metal enrichment with iron, lowering the average α/Fe ratio in the ISM. There are two important features in the [α/Fe] vs [Fe/H] diagram: the location of the knee in [Fe/H] and the maximum value of the plateau [α/Fe] at low metallicity. The former is related to the star formation rate (SFR), while the latter to the fraction of massive stars in the initial mass function (IMF). Systems with a high SFR, like bulges and elliptical galaxies, have enhanced [α/Fe] at high [Fe/H], while systems with lower SFR, as the Galactic disc or even lower, as dwarf galaxies, show a reduced [α/Fe] (see Fig. 1.13).

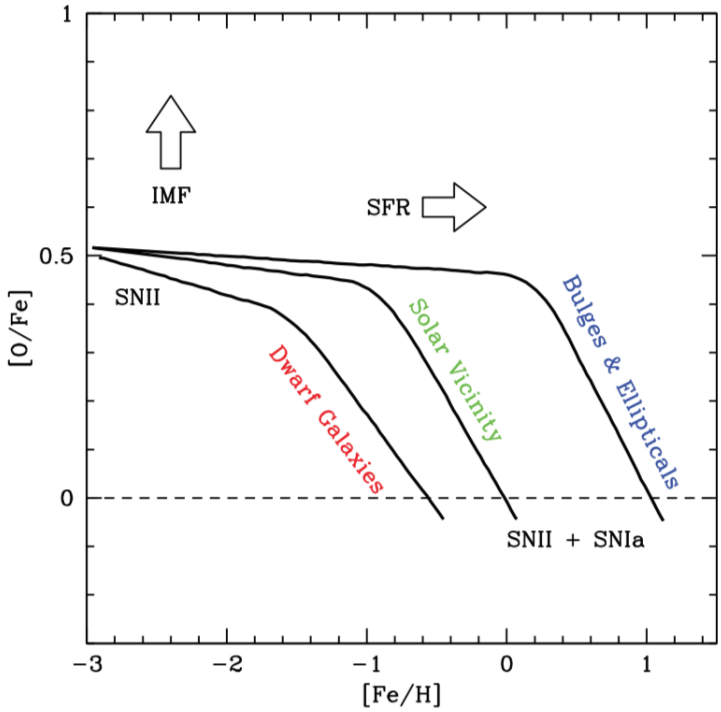

Fig. 1.13: A sketch of the predicted [O/Fe] vs. [Fe/H] relations (Matteucci & Brocato, 1990) in different systems (Figure by McWilliam, 2016).

Finally, elements with atomic number Z> 30, are produced by capture of neutrons on lighter elements, where neutrons are transformed into protons via β-decay. The **neutron-(n-) capture** processes can be divided in two channels: slow- (s-) process, if the n-capture timescale is longer than the β-decay and the density of free neutrons is 10^8 cm^{-3} (Busso et al., 1999); rapid-(r-) process, if the n-capture timescale is shorter than the β-decay and the n-density is 10^{24-28} cm^{-3} (Kratz et al., 2007).

The s-processes occur in low and intermediate mass stars during a phase of strong mass loss and thermal pulses[7] in the asymptotic giant branch (AGB) phases, corresponding to the H and He-shell burning stage (see a sketch of an AGB star in Fig. 1.14). After each thermal pulses, the outer convective envelope moves inwards, reaching internal layers contaminated by 3α nucleosynthesis and enriched in C. This mixing episode is known as third

[7] They are thermal instabilities that drive the nucleosynthesis in the two shells of inner He-burning and outer H-burning.

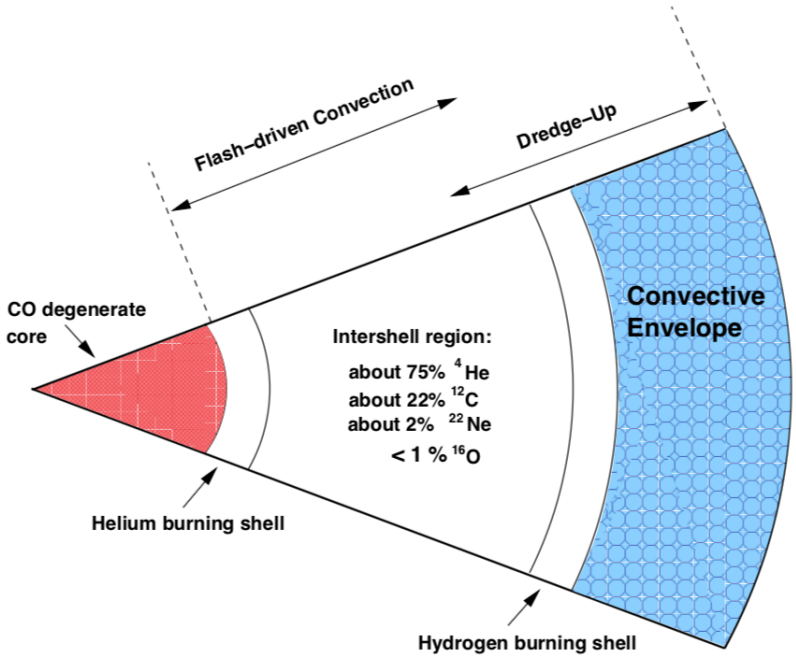

Fig. 1.14: Schematic structure of an AGB star showing the electron-degenerate core surrounded by a helium-burning shell above the core, and a hydrogen-burning shell below the deep convective envelope. The burning shells are separated by an intershell region (Karakas & Lattanzio, 2014).

dredge-up (TDU, Gallino et al., 1998; Busso et al., 1999; Sneden et al., 2008; Karakas & Lattanzio, 2014). The TDU brings C and N synthesised in the inner He-burning zone towards the intershell, where they undergo two reactions. These reactions are sources of neutrons and they are:

$$^{12}\mathrm{C(p,}\gamma)^{13}\mathrm{N}(\beta^{+}\nu)^{13}\mathrm{C}(\alpha,\mathrm{n})^{16}\mathrm{O}$$

$$^{14}\mathrm{N}(\alpha,\gamma)^{18}\mathrm{F}(\beta^{+}\nu)^{18}\mathrm{O}(\alpha,\gamma)^{22}\mathrm{Ne}(\alpha,\mathrm{n})^{25}\mathrm{Mg}$$

The first reaction occurs if the temperature exceeds $3\cdot10^{8}$ K, that is if $M > 4M_{\odot}$. The second one, instead, occurs if $M < 4M_{\odot}$. In particular, if protons belonging to the He-burning zone are mixed from the TDU into the intershell between He- and H-burning regions, they can react with the abundant ^{12}C to produce ^{13}C. A thin layer rich in ^{13}C and ^{14}N forms, known as the ^{13}C pocket (Iben & Renzini, 1982). Finally, the neutrons released in the ^{13}C pocket allow the slow neutron-captures and then the production of s-process elements. Then, these elements are ejected in the ISM through strong stellar winds with timescales from 100 Myr to few Gyr, after the end of a star as white dwarf surrounded by planetary nebula. The elements mainly produced by slow-neutron capture are Sr, Y, Zr, Ba, Ce, and La.

On the other hand, the r-processes occur in the neutrino-driven winds of core-collapse SNe II (Wanajo, 2013; Woosley & Weaver, 1995) and during the merging of neutron stars or a neutron star and a black hole (Argast et al., 2004; Surman et al., 2008; Korobkin et al., 2012). An example of r-process element is Eu, while Pr and Nd are produced by both r- and s-processes.

Due to different processes and timescales involved in their production, α-, iron-peak and n-capture elements are important markers of the timescales of the chemical evolution and formation of various stellar populations present in the Galactic disc, bulge and halo

(e.g. Chiappini et al., 1997; Gilmore et al., 1989; Haywood et al., 2013; Recio-Blanco et al., 2014). Their ratios can be also used as indicators of the stellar ages, as described in the following chapters.

2

LARGE SPECTROSCOPIC SURVEYS OPENING A NEW OBSERVATIONAL ERA

In the last decades, space- and ground-based surveys covering different wavelength bands, from gamma rays to radio bands, have brought astronomy into the *big data* era. Astronomical surveys have become a fundamental source for important scientific results in Galactic and extragalactic field.

In the present work, I focus on the observations form the *Gaia* satellite, the space mission of the European Space Agency (ESA), and on the data from the large spectroscopic surveys, in particular the Apache Point Observatory Galactic Evolution Experiment (Zasowski et al., 2013, 2017; Majewski et al., 2017, hereafter APOGEE) and the Gaia-ESO public survey (Gilmore et al., 2012; Randich et al., 2013). The combination of the astrometric data from *Gaia* with those from the spectroscopic surveys is providing a new picture of our Galaxy.

In this Chapter, I present the fundamental data-sets based on the main surveys used in this Ph.D. Thesis: *Gaia*, Gaia-ESO and APOGEE. Finally, I give a brief look at the other Galactic spectroscopic surveys.

2.1. GAIA MISSION

The *Gaia* satellite (Gaia Collaboration et al., 2016b,a; Lindegren et al., 2018; Gaia Collaboration et al., 2018b; Bailer-Jones et al., 2018) was launched on the 19 December 2013. The scientific observations of the *Gaia* mission cover three principal areas: *i)* astrometry, including the measurement of stellar positions, parallax and proper motion; *ii)* spectro-photometric data analysis; and *iii)* medium-resolution spectroscopy providing radial velocities, atmospheric parameters and chemical abundances. In its second data release (*Gaia* DR2, Gaia Collaboration et al., 2018b), *Gaia* mission has provided positions, parallaxes, proper motions, and photometry in the three bands for more than 1.3 billion sources down to $G \sim 20$ mag (see Fig. 2.1 for a sky-map from *Gaia* DR2 and Fig. 2.2 for the number of targets divided in different categories).

Gaia can measure the relative positions of the thousands of stars present simultaneously in its field of view (FoV), exploiting an astrometric field composed by 62 CCDs charge-coupled device (Boyle & Smith, 1993) and a primary mirror of $1.45 \times 0.5\,\mathrm{m}^2$.

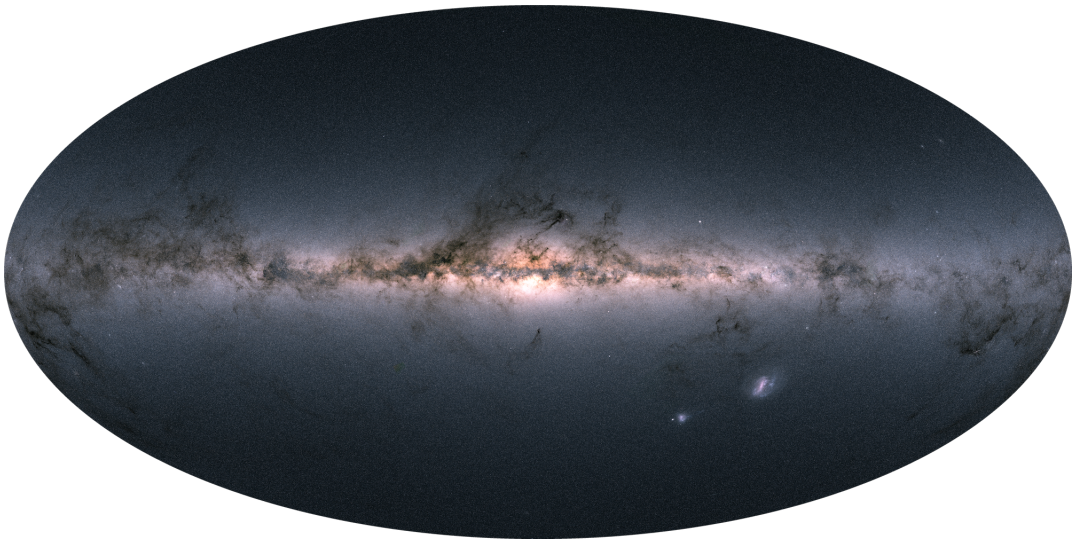

Fig. 2.1: First *Gaia* sky-map in colour. Credit: ESA/Gaia/DPAC.

Its photometric instrument consists of a broad-band white-light (G) with a wavelength coverage of 330 – 1050 nm and two low-resolution photometers: one operating in the blue wavelength range, 330 – 680 nm (BP), and the other one covering the red wavelength range, 640 – 1050 nm (RP).

Finally, its spectroscopic observations are collected with the spectroscopic instrument RVS for objects with $G < 16$ mag in the wavelength range 847 – 874 nm with a low spectral resolution of 11,500. This instrument measures the radial velocity through Doppler-shift measurements. Moreover, thanks to the RVS, *Gaia* can provide information about interstellar reddening, atmospheric parameters, and rotational velocities, for stars with $G < 12.5$ mag, and elemental abundances for stars brighter than $G \sim 11$ mag. RVS provided radial velocity for 7 million stars. In addition, the spectral range of this instrument is narrow and it permits the measurements of a few elements with large uncertainties on atmospheric parameters. For this reason, the *Gaia* mission is complemented by spectroscopic surveys.

The *Gaia* data are analysed by a large consortium of astronomers (Data Processing and Analysis Consortium, DPAC), which develops the data analysis algorithms for the astrometric, photometric and spectroscopic data. The first data release (*Gaia* DR1, Gaia Collaboration et al., 2016a) is based on observations collected between the 25 July 2014 and the 16 September 2015. This release is incomplete on the bright part ($G < 7$ mag) and has an ill-defined faint magnitude limit, which depends on celestial position. *Gaia* DR1 contains the positions and the mean G-band magnitudes for ~ 1.1 billion sources with a limit at $G \sim 20.7$ mag (Gaia Collaboration et al., 2016a). The second data release (*Gaia* DR2 Gaia Collaboration et al., 2018b) is based on observations collected between the 25 July 2014 and the 23 May 2016 and it is essentially complete between $G = 12$ and $G = 17$ mag. Although the completeness at $G < 7$ mag has improved, a fraction of stars in that range is still missing from *Gaia* DR2. Positions, parallaxes, and proper motions are given for more than 1.3 billion sources, with a limiting magnitude of $G = 21$ mag. This release provides also radial velocities for more than 7.2 million stars having $G = 4$-13 mag, BP and RP magnitudes for more than 1.38 billion sources, and effective temperatures for more than 161 million sources brighter than $G \sim 17$ mag (see Fig. 2.2).

Finally, the next *Gaia* early data release (EDR3) will be published on December 3rd

2020. This catalogue will play a central role for many astronomic fields. It will contain the full astrometric solution (positions, parallaxes and proper motions) and photometric data (brightness and color) for over 1,8 billion stars.

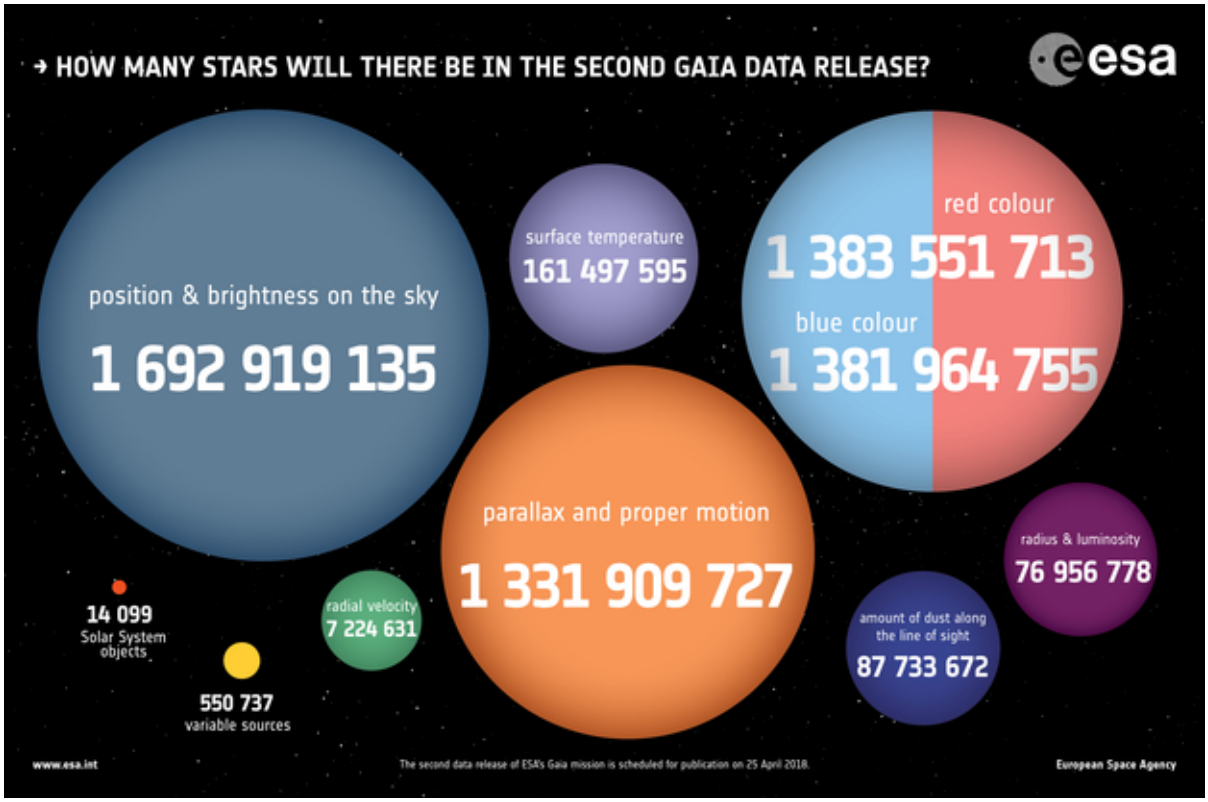

Fig. 2.2: Numbers of stars for which different parameters have been delivered in *Gaia* DR2. Credit: ESA/Gaia/DPAC.

2.2. GAIA-ESO SURVEY

The Gaia-ESO Survey (GES, Gilmore et al., 2012; Randich et al., 2013) is a large high-resolution spectroscopic survey carried on with FLAMES (Pasquini et al., 2002) mounted on the Very Large Telescope (VLT) UT-2 in Chile. FLAMES is a multi-fiber instrument composed by two different spectrographs: GIRAFFE and UVES. GIRAFFE has a spectral resolution of $R \sim 20,000$ and allows the observation of up to 130 targets at the same time; UVES has a spectral resolution of $R \sim 47,000$ and provides simultaneously observations up to 7 stars.

The aim of this ground-based survey is to provide complementary information that, combined with *Gaia* data, is offering a complete kinematic and chemical view of a sample of stars in the Milky Way. The survey benefited of about 340 nights on the VLT observing more than 10^5 stars with well-defined samples covering the bulge, the thick and thin disc and the halo component of the Milky Way, as well as a significant sample of about 80 open clusters of all ages and stellar masses. GES provides radial velocities, atmospheric parameters, [Fe/H], elemental abundances [X/H], and other additional parameters, as accretion. It allows us to address important scientific goals, such as: formation, evolution and disruption of open clusters; calibration of the complex physics that affect stellar evolution; nature

of bulge; formation, evolution and structure of the disc; kinematic and chemical distribution in the Solar neighborhood.

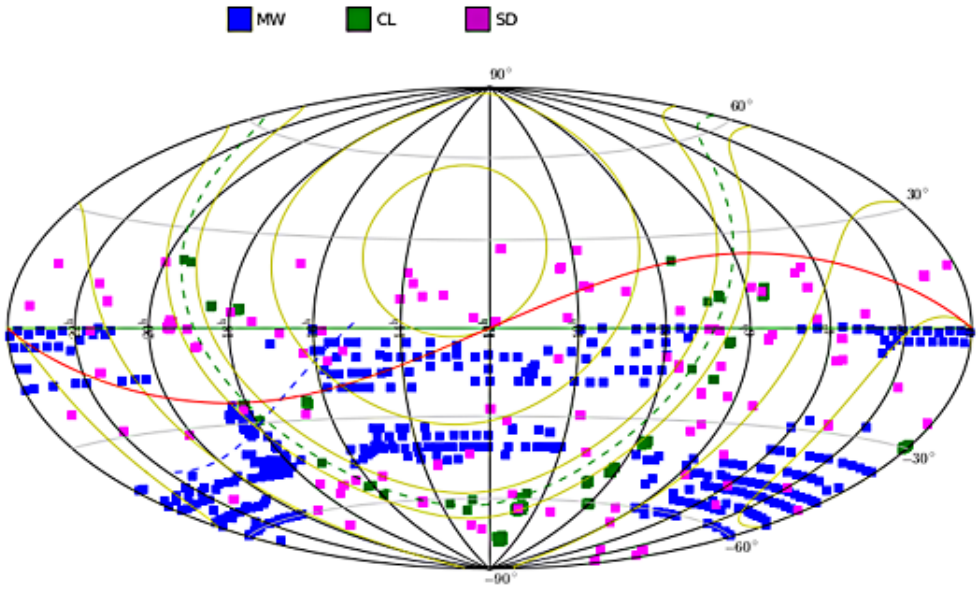

Fig. 2.3: Map of observed targets on the sky present in Gaia-ESO survey. Key: MW = Milky Way, CL = Cluster, SD = Standard. Credit: `https://www.gaia-eso.eu`

2.2.1. SKY COVERAGE AND TARGET SELECTION

GES is designed to select and observe three classes of targets in the Milky Way: field stars, candidate members of open clusters and calibration standard stars (respectively, MW, CL, SD in Fig. 2.3). The selection of field stars is described in Stonkutė et al. (2016), and it includes for the UVES sample mainly MSTO stars. The primary goal of selection strategy is to select a robust sample of field stars present in the main components of the Milky Way: thin, thick discs, bulge and halo. The target selection takes into account the magnitudes and colours of stars, based on the VHS (McMahon et al., 2013) and 2MASS (Skrutskie et al., 2006) photometry. The targets are mainly in main sequence, turn-off, and red giant branch phases.

The selection of open clusters is based on the existing database and published photometric data, as e.g., the WEBDA[1] database. GES selected as targets, clusters with excellent available photometry and astrometry and adequate membership information. Moreover, the selected open clusters range an interval of age from 1 Myr to 6 Gyr, in all phases of evolution, and in interval in Galactocentric distance R_{GC} from 4 to 20 kpc. The distributions of ages and distances for the open cluster sample present in the latest GES internal release iDR6 are shown in Fig. 2.4. For all clusters, GIRAFFE observed photometric members with I < 19 mag, with an inclusive and unbiased selection, while UVES observed high-probability member stars with V < 16.5 mag. Seven GIRAFFE setups were employed: for late-type stars HR15N/10/21, while for early-type stars (A-O) HR03/05A/06/09B/14A. UVES, instead, ob-

[1] `https://webda.physics.muni.cz`

served early-type stars with the U520 setup, centred at 520 nm, and late-type stars with the U580 setup (both setups cover a range of 200,0 nm).

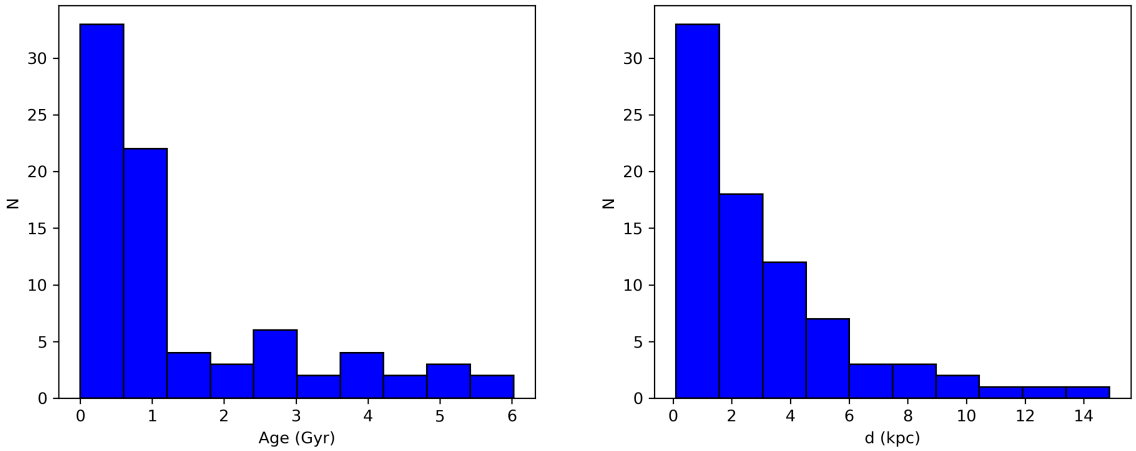

Fig. 2.4: Distribution of age and distrance from the Sun for the open cluster sample present in the latest GES internal data release iDR6.

Finally, a large sample of calibration benchmark stars is observed to allow a comparison with literature studies and with other spectroscopic surveys, but also for internal homogenisation purposes. They include radial velocity standard stars (Soubiran et al., 2013; Chubak et al., 2012); Gaia FGK benchmarks (Heiter et al., 2015b), well-studied stars with $T_{\rm eff}$ and log g derived as independently of spectroscopy as possible; well-known globular and open clusters (see Pancino et al., 2017, for more details); CoRoT ("Convection, Rotation and planetary Transits", a space mission of ESA, Michel et al., 2008) and Kepler (a space mission of NASA, Borucki et al., 2010) stars with accurate asteroseismologic log g reference values (see more details on asteroseismology in Chapter 3).

2.2.2. THE GES CONSORTIUM AND ITS ANALYSIS PHILOSOPHY

GES is led by two Co-PIs, G. Gilmore (University of Cambridge, UK) and S. Randich (INAF - Osservatorio Astrofisico di Arcetri, IT). The consortium includes more than 400 participants in over 90 institutes all over the world. The participants are distributed among 20 Working Groups (WGs), which have to manege the activities of the survey. The WGs have different tasks: target selection, telescope configuration and observations, pipeline data processing, spectral analysis, data homogenisation, science quality control, documentation and delivery of results to ESO and the building-up of a dedicated public archive. In particular, the spectral analysis is performed by four different WGs, each of them specialised in a different class of stars. Within each WG, there are several Nodes that participate to the analysis. Specifically, more than one group is expected to analyse all relevant targets of GES. This is one of the novelties introduced by GES: several groups provide results for the same spectra with different methods, allowing the unique possibility to estimate the effect of systematic errors. Finally, the results of different Nodes and different WGs are merged in a unique final set of parameters, through a process of homogenisation with the use of a set of calibrators, including *Gaia* benchmark stars, globular clusters, stars observed by the CoRoT and Kepler satellites with asteroseismic data, etc.

2.3. APOGEE SURVEY

The Apache Point Observatory Galactic Evolution Experiment (APOGEE, Zasowski et al., 2013, 2017; Majewski et al., 2017) is a large-scale high-resolution spectroscopic survey with high S/N in the near-infrared (1.6 μm, H band) that observed over 10^5 giant stars in the bulge, bar, discs, and halo of our Galaxy. It is designated to deal with the fundamental problem of galaxy formation through precision chemical and kinematic study, specifically optimised to investigate "dust-hidden" populations in the Milky Way (e.g., the bulge).

The first set of observations of the APOGEE Survey (APOGEE-1) was executed from September 2011 to July 2014 with a spectral resolution $R \sim 22,500$ on the Sloan Foundation 2.5 m Telescope of Apache Point Observatory (APO). The second instalment (APOGEE-2) has continued the data acquisition at APO until June-August 2020, adding observations with the APOGEE-South spectrograph on the Irenee du Pont 2.5m Telescope of Las Campanas Observatory (LCO). The latest data release, DR16, includes about 430,000 stars.

2.4. SKY COVERAGE AND TARGET SELECTION

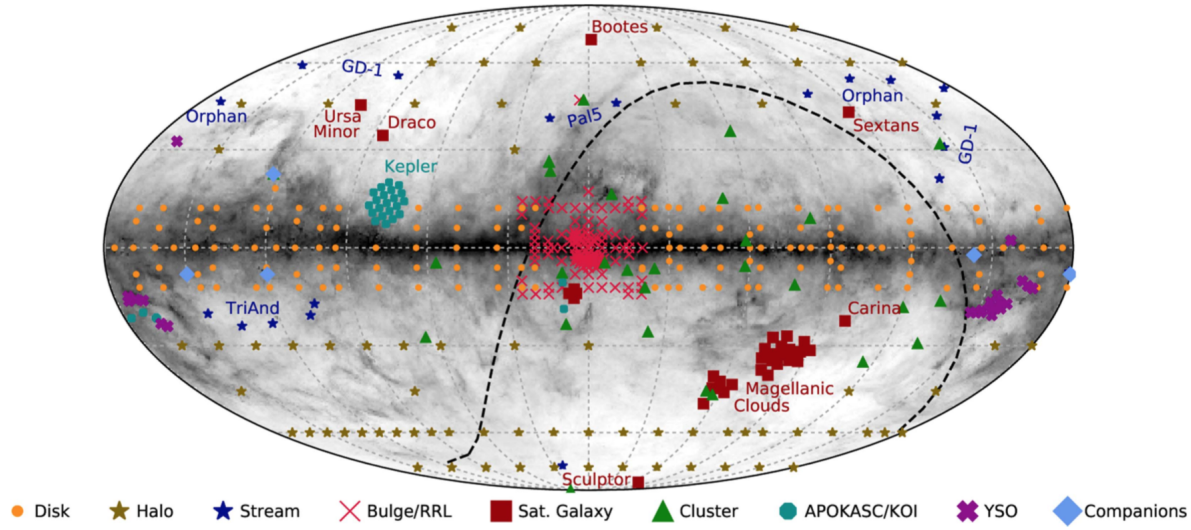

Fig. 2.5: APOGEE-2 field plan in Galactic coordinates, where the background gray scale is the integrated $E(B-V)$ map from Schlegel et al. (1998) and the dashed line indicates the approximate declination limit of -10° adopted for the Northern and Southern survey components (Zasowski et al., 2017).

The final target selection will be published by Beaton et al. (in prep.) for the APOGEE-2N field plan and Santana et al. (in prep.) for the APOGEE-2S field plan. The radial extent for the APOGEE-2N and APOGEE-2S fields are driven by the FoV of the telescopes and the declination of the field itself. The 2.5 m SDSS telescope at APO has a maximal FoV of $1^\circ.5$ in radius (APOGEE-2N), while the instrument on the 2.5 m du Pont telescope at LCO has a maximal FOV of $0^\circ.95$ in radius (APOGEE-2S). However, smaller size limits may be imposed on fields observed at high airmass, due to the high differential refraction (Zasowski et al., 2013, 2017).

APOGEE-2 has three primary categories of scientific priority for its observations: *i)* the

first priority is covered by the bulge, disc, and halo populations (e.g., red clump, RR-Lyrae stars RRL, star clusters), an asteroseismic star sample in the Kepler field (APOKASC), satellite galaxies and halo stream; *ii)* the second priority includes Kepler Objects of Interest (KOI), young star-forming clusters (YSO), K2 (Kepler's second mission, Howell et al., 2014) asteroseismic targets, substellar companions, M dwarfs and eclipsing binaries; *iii)* finally, the last priority involves observations of "ancillary" targets (see Fig. 2.5 for all of these categories).

The targets are selected starting from the 2MASS photometry (Skrutskie et al., 2006), adding the mid-IR photometry from the Spitzer-IRAC GLIMPSE (Benjamin et al., 2005; Churchwell et al., 2009) and AllWISE (Wright et al., 2010; Cutri et al., 2013) catalogues. After applying data quality limits to the photometry (Zasowski et al., 2017), the colours $(J-K_s)$ of stars were dereddened (Majewski et al., 2011). For the APOGEE-2 disc field, a dual-colour limit was used for the target selection: targets having $0.5 < (J-K_s) < 0.8$ mag and the rest with $(J-K_s) > 0.8$ mag. In some APOGEE-2 disc cohorts (groups of stars in the same field that are observed together on all of their visits), the bright limit was reduced to $H = 10$ mag to increase the number of faint, and hopefully distant, disc targets.

Star clusters are targeted by APOGEE-2 for both scientific analysis and calibration. The targeted members of star clusters are selected according to the following priorities: *i)* presence of atmospheric parameters and/or abundances from high-resolution data; *ii)* RV membership; *iii)* proper-motion membership; *iv)* location in the CMD. The largest sample of open clusters present in APOGEE DR16 is listed by Donor et al. (2020). They present a sample of 128 open clusters, whose member stars were selected using radial velocities, proper motions (from *Gaia* DR2), spatial locations, and derived metallicities.

2.4.1. ASPCAP PIPELINE

The APOGEE spectra were reduced with the pipeline ASPCAP (APOGEE Stellar Parameter and Chemical Abundances Pipeline, García Pérez et al., 2016). It works in two steps: (1) atmospheric parameters determination using a global fit over the whole spectral range; (2) elemental abundance determination using a local fit in limited spectral windows and assuming the derived atmospheric parameters. The global fit in the first step includes also the possible effects in the equation of state or in the opacity due to the variations in elemental abundance ratios. For this reason, this pipeline takes into account the variation of nine parameters: effective temperature $T_{\rm eff}$, surface gravity $\log g$, microturbulence ξ, macroturbulence, rotation $v \sin i$, overall metal abundance [M/H], α-element abundance [α/M], carbon [C/M], and nitrogen [N/M] abundances. The spectroscopic $T_{\rm eff}$ and $\log g$ for all stars have been calibrated using the photometric $T_{\rm eff}$ and asteroseismic values (and isochrones for cooler dwarfs), respectively. In the second step, ASPCAP uses the same grid of synthetic stellar spectra with the nine parameters to determine the chemical abundances. In this case, the fit is not global, but local for spectral windows that cover spectral lines of the element of interest. It permits to derive the abundances for 26 elements. They are zero-point shifted such that the median of the abundance in stars near the solar metallicity in the solar neighborhood is adjusted to be zero ([X/M] = 0).

2.5. OTHER LARGE SPECTROSCOPIC SURVEYS

In last decades, other large spectroscopic survey were built. In particular, we can mention: RAVE (Placco et al., 2017), GALAH (De Silva et al., 2015), LAMOST (Deng et al., 2012; Cui et al., 2012), and future survey-dedicated spectrographs, e.g. WEAVE (Dalton et al., 2012), 4MOST (de Jong, 2011), MOONS (Cirasuolo et al., 2011) and MSE (Bergemann et al., 2019).

RAVE (RAdial Velocity Experiment) is a magnitude-limited ($9 < I < 12$) spectroscopic survey of ~ 450,000 Galactic stars, observed with the 6dF multi-object spectrograph on the 1.23 m UK Schmidt telescope at Siding Spring in Australia. RAVE has a medium resolution of $R \sim 7500$ and covers the wavelength range of 8410 – 8795 Å. Its observations were started on 12 April 2003 and were finished on 4 April 2013.

GALAH (GALactic Archaeology with HERMES) survey is a Large Observing Program using the HERMES instrument ($R \sim 28,000$) mounted on the Anglo-Australian Telescope in the Australian Astronomical Observatory. HERMES provides simultaneous spectra for 400 objects in four wavelength bands between 470 and 790 nm. The second data release of GALAH includes precise radial velocities and abundances of 23 elements for 342,682 stars, observed between January 2014 and January 2018 (Buder et al., 2018).

LAMOST (Large Sky Area Multi-Object Fibre Spectroscopic Telescope) survey is a low-resolution survey collected by a spectrograph at the Guo Shou Jng Telescope (GSJT). It takes 4000 spectra in a single exposure with spectral resolution $R \sim 1800$ in the spectral range of 370 – 900 nm. The observations began regularly in 2012 October.

WEAVE (WHT Enhanced Area Velocity Explorer) is a new multi-object survey spectrograph for the 4.2-m William Herschel Telescope (WHT) at the Observatorio del Roque de los Muchachos (La Palma, Spain). This instrument will offer two possible spectroscopic resolutions: 5000 and 20,000 with a wavelength coverage of 366 – 606 nm (blue) and 579 – 959 nm (red) for the low-resolution mode, and 404 – 465 nm or 473 – 545 nm (blue), 595 – 685 nm (red) for the high-resolution mode. Its aim is to target about 300 open clusters. The timeline of this survey will be 5 years, from 2019 until 2024.

4MOST (4-metre Multi-Object Spectroscopic Telescope) is a fibre-fed spectroscopic survey facility on the 4-m class VISTA telescope at the Cerro Paranal Observatory in Chile. It will observe simultaneously spectra of 2400 objects with a large field-of-view. Its spectral resolution could be low or high, respectively $R \sim 4000$ and $R \sim 20,000$. Its wavelength coverage is 370 – 950 nm for low-resolution mode, and 392.6 – 435.5, 516 – 573, 610 – 679 nm for high-resolution mode. The first light date of this instrument is expected in 2022.

MOONS (Multi Object Optical and Near-infrared Spectrograph) will be a multi-objects spectrograph mounted at a Nasmyth focus at the VLT, Chile. It will consist of 1000 fibers and will cover a wavelength range of 0.6 – 1.8 μm. It will have different resolution modes covering different spectral range: $R \sim 4,000 - 6,000$ for 0.65 – 1.8 μm, $R \sim 9,000$ around the Ca II triplet, and $R \sim 20,000$ in the H-band. Observing in the near-IR, MOONS will perfectly complement the ongoing and planned surveys, including GES. The main feature of MOONS will be to observe the Galactic bulge. The start of scientific operations will expected at the end of 2020.

MSE (Maunakea Spectroscopic Explorer) is a project to transform the CFHT 3.6 m optical telescope into a 11.25 m dedicated multi-object spectroscopic facility with the capability to study up to 4,000 astronomical objects at once. The specialised technical capabilities provided by MSE will enable an enormous diversity of exciting science: stars and planets,

galaxies and cosmology, and the nature of dark matter and dark energy. The first light date of MSE is expected in 2024.

2.6. THE TARGETS FROM APOGEE AND GES USED IN THE PRESENT WORK

High-resolution spectroscopic surveys, such as APOGEE and Gaia-ESO, provide homogeneous databases of stellar parameters, chemical abundances and radial velocities of different stellar populations in the whole Milky Way. Both surveys contain large samples of star clusters, covering wide ranges in ages, distances, metallicities. For instance, the latest release of Gaia-ESO (iDR6) and APOGEE (DR16) contain more than two hundreds open clusters, while WEAVE will target about 300 open clusters. Star clusters are important tools to investigate the Galactic chemical evolution, as well as excellent calibrators for empirical relations between properties of clusters, as age, and other quantities, as abundance ratios, stellar activity, rotation.

In the present Thesis, I took advantage of the samples of open clusters from the fifth internal data release (iDR5) of Gaia-ESO and the fourteenth (DR14) data release of APOGEE[2] to build up and calibrate relations between age and abundance ratios. The spatial and metallicity distributions of the two samples of open clusters are shown in Fig. 2.6.

In addition, I determined the ages of field stars in both surveys, located mainly in the thin and thick discs, adopting the relations between abundance ratios and ages (see Chapters 3, 4 and 5). The field star sample counts about ~ 67,000 from a combined sample of APOGEE and GES and it is shown in Fig. 2.7. From the Figure, we can see that field stars are located in the extended solar neighbourhood, reaching regions towards the bulge, with higher metallicity, and towards the outskirts of the Milky Way, where the metallicity is lower.

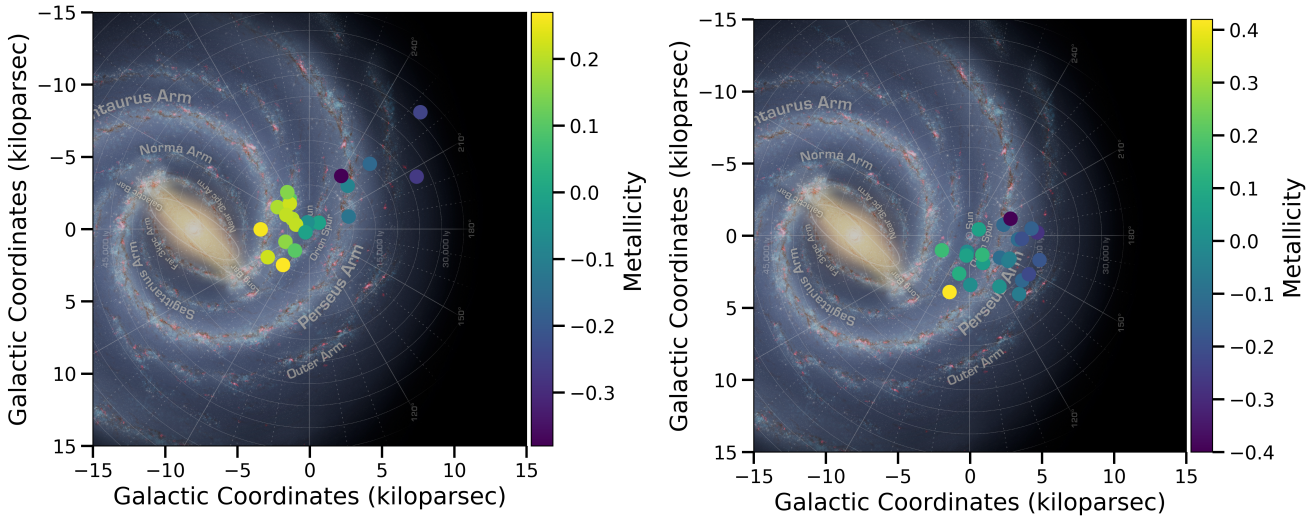

(a) (b)

Fig. 2.6: (a) Spatial distribution of open clusters present in GES iDR5, colour-coded by metallicity; (b) spatial distribution of open clusters present in APOGEE DR14, colour-coded by metallicity.

[2] The latest releases available during my Thesis work

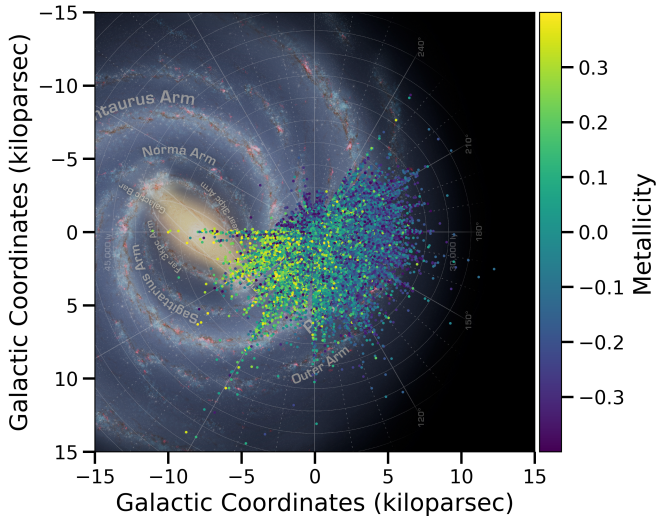

Fig. 2.7: Sample of field stars present in APOGEE and GES surveys. This sample is employed in the Chapter 4.

3

DETERMINATION OF STELLAR AGES

As said in the previous Chapters, Galactic archaeology is living in a *golden age* thanks to *Gaia* satellite and the large spectroscopic surveys, which, combined, are providing a new multi-dimensional view of the structure of our Galaxy. In Fig. 3.1, we show how the data from *Gaia* and Gaia-ESO can be combined to give a multi-dimensional view of the Milky Way.

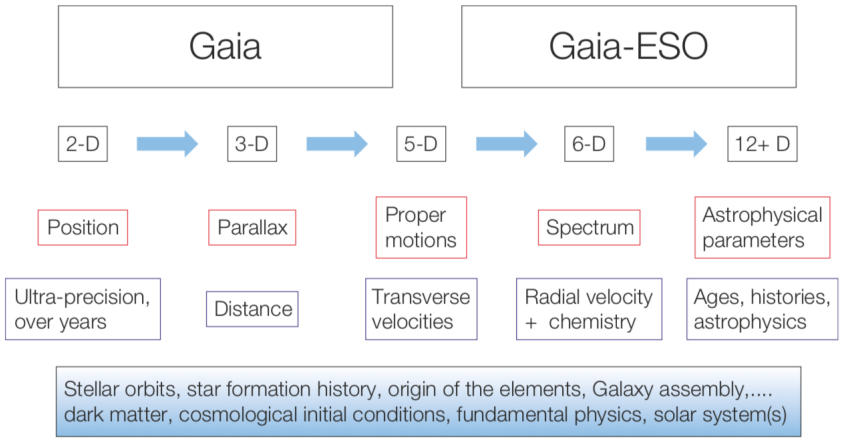

Fig. 3.1: A diagrammatic representation of the outputs of the Gaia and Gaia-ESO surveys (Gilmore et al., 2012).

A further essential ingredient to complete the Galactic puzzle is the determination of the ages of individual stars, which allows us to trace back the star formation history and to investigate the Galactic structure in previous epochs. Moreover, the age distribution of stellar populations provides fundamental constraints to the formation scenarios of our Galaxy. The determination of stellar ages is, however, one of the most difficult tasks of astrophysics, because ages cannot be directly measured, but they have to be inferred through the comparison between observable quantities and theoretical models.

For this reason, it is important to look for observable quantities which can be related to stellar ages, once calibrated on samples of objects with well-known ages. The basic requirements for these observable quantities are, e.g., discussed in Barnes (2007): calibration on

benchmark samples, well-known uncertainties, relation between age-indicators and stellar age that should be easily invertible, and finally when the relation is applied to a coeval sample of stars, it should give consistent ages.

In this Chapter, I discuss the main techniques adopted to determine the stellar age, focusing mainly on chemical clocks and their calibrators, which are used in the following projects.

3.1. STANDARD METHOD: ISOCHRONE FITTING

The most commonly-used technique to estimate the stellar ages is to compare quantities related to observations with the results of stellar evolution models. This comparison, called isochrone[1] fitting, can be made on several planes, using directly observed quantities (magnitudes and colours) or derived quantities such as surface gravities, $\log g$, and effective temperatures, $T_{\rm eff}$. Given a set of calculated models and varying their properties, it is possible to achieve the best overall match to the observations and, then, infer the stellar age.

Isochrones fitting works very well for star clusters, composed by many coeval and chemically homogeneous stars along the whole evolutionary sequence in the colour-magnitude diagram. This method provides better results in regions of the planes where isochrones have a good separation, mainly close to the main sequence turn-off (TO), as we can see from the Fig. 3.2. Indeed, in order to infer the cluster age, isochrone fitting uses the position of the TO as an age indicator, a point that becomes redder and dimmer for increasing age. Once a star reaches the TO, the evolution is rapid, and so the luminosity of this point becomes an age diagnostic. The comparison involves the observed TO brightness and the appropriate theoretical isochrones. On the other hand, isochrones of different ages almost overlap on the red giant branch[2] (RGB) and on the lower main sequence. Therefore, small uncertainties on $T_{\rm eff}$ and $\log g$ or on magnitude and colour correspond to large uncertainties on the derived stellar age (see Fig. 3.3).

The isochrone fitting depends basically on comparing observed data collected in a vector q (total metallicity [M/H], $\log T_{\rm eff}$, magnitude M_V) with theoretical values obtained from stellar models, where age (τ), initial stellar mass (m) and initial chemical composition (Z) are free parameters, summarised in another vector p. The age determination can thus be understood as direct numerical inversion of the function $q(\tau, Z, m)$, and in particular the calculation of $\tau(q)$. The function $q(\tau, Z, m)$ is in practice realised by numerical interpolation in a set of isochrones. In the past, the best isochrone passing through the observed point was not found by numerical interpolation, but by a visual one, and the corresponding age was assigned to the star.

Recently, many groups applied the Bayesian method to the isochrone-fitting age determination (see, e.g. Lin et al., 2018; Queiroz et al., 2018). In this case, the parameters τ, Z, m are regarded as random variables of a probability density function. They are obtained by finding the maximum of this function, using as weights [M/H], $\log T_{\rm eff}$ and M_V or $\log g$ (Jørgensen & Lindegren, 2005). Moreover, it also calculates the confidence intervals for

[1] A curve in the Hertzsprung-Russell (HR) diagram, the theoretical counterpart of the CMD, which connects the points belonging to different evolutionary tracks of stars being part of the same stellar population at the same time and with the same chemical composition, but with different initial masses.

[2] H-burning phase in a shell around the stellar core.

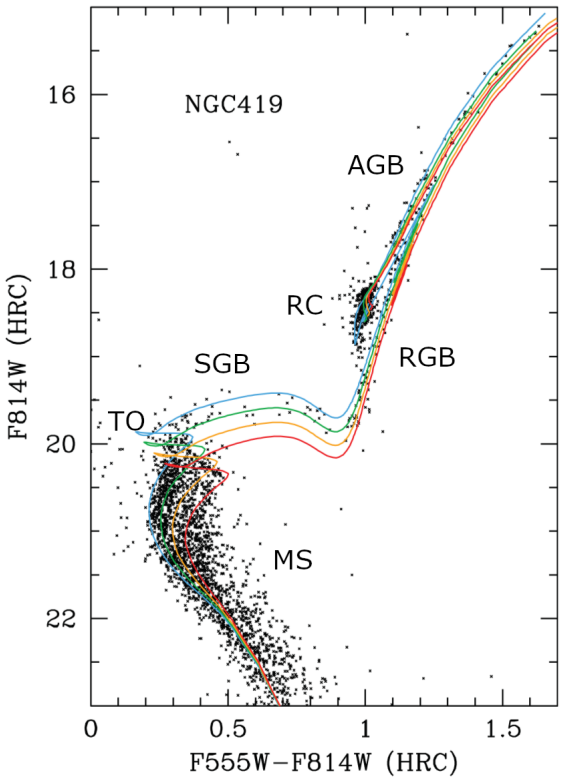

Fig. 3.2: A colour-magnitude diagram for the cluster NGC 419 of the Small Magellanic Cloud, compared with PARSEC (Bressan et al., 2012) isochrones of different age. The isochrones are for metallicity Z = 0.004 and log(age/yr) = 9.15, 9.20, 9.25, 9.30. The magnitude $F814W$ and colour $F555W - F814W$ come from the photometry obtained with the HRC camera of HST telescope. The labels MS, TO, SGB, RGB, RC and AGB represent the main evolutionary sequences: main sequence, turn off, sub-giant branch, red giant branch, red clump and asymptotic giant branch, respectively. Figure by Bressan et al. (2012).

these parameters, that fall inside the [M/H], $\log T_{\rm eff}$ and M_V (or $\log g$) space covered by the uncertainties on them (see Fig. 3.4).

3.1.1. THEORETICAL UNCERTAINTIES ON ISOCHRONE MODELS

Several uncertainties on theoretical models and their calibrations, as well as observational effects, limit the accuracy of the age determination. Moreover, different sets of isochrones – Pisa (Tognelli et al., 2018; Dell'Omodarme et al., 2012), PARSEC (Bressan et al., 2012), Yonsei-Yale (Spada et al., 2017), etc. – use different initial values and can be used spanning a large range of stellar ages. The uncertainties on the theoretical models are due to several aspects (see Degl'Innocenti, 2009; Tognelli et al., 2011; Valle et al., 2013a,b, for more details):

- the initial chemical composition, where the abundances are expressed in mass fraction (X for H, Y for He and Z for metals). Each element directly enters the model calculation via physical processes (nuclear reaction rates, opacity, equation of state, diffusion, etc.), and thus, their abundances impact the structure of the star. However, we do not have direct observations of the internal stellar composition, since the observations provide only the present-time surface abundances, not initial abundances nor inner abundances. Moreover, theoretical models often assume solar abundance ratios $(X_i/Z) = (X_i/Z)_\odot$, where X_i is the abundance of a given element i, and [M/H] =

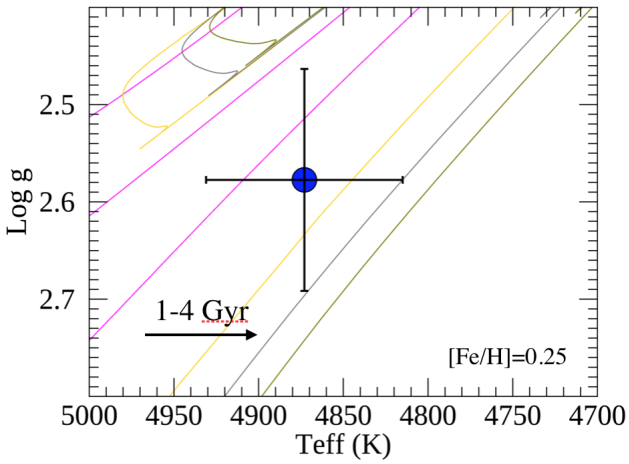

Fig. 3.3: A log g–$T_{\rm eff}$ diagram for an individual star, compared with Pisa isochrones of different age with metallicity [Fe/H]=0.25 dex.

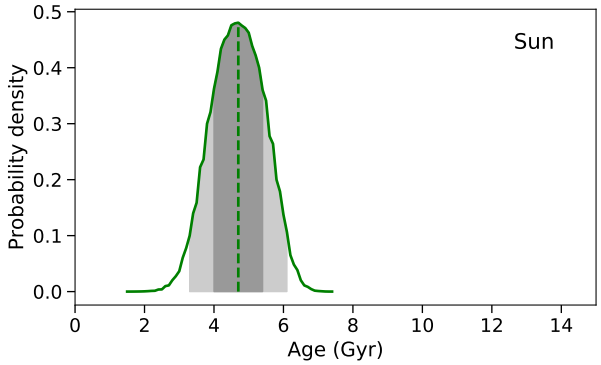

Fig. 3.4: An example of age determination using the Bayesian method (through the Python code q2). In Figure: the probability density distribution for the age of Sun, where the peak is the most probable age estimate. The two grey regions indicate the confidence intervals at 68% and 95%.

$\log(Z/X) - \log(Z/X)_\odot$, with $[{\rm M/H}] = [{\rm Fe/H}] + \log(0.638 \cdot 10^{[\alpha/{\rm Fe}]} + 0.362)$, or scaled abundance ratios on the basis of mean trends, e.g., in the Galactic disc.

- the initial helium abundance Y, which cannot be obtained from the observations. To evaluate the initial helium content, we can only use an indirect method following the relation among the helium and metals abundances in the star and the primordial He: $Y = Y_P + (\Delta Y/\Delta Z)\cdot Z$, where Y_P is the cosmological helium abundance, $\Delta Y/\Delta Z$ is the Galactic helium-to-metal enrichment ratio and Z is the metal abundance. The main uncertainty is due to our limited knowledge of $\Delta Y/\Delta Z$ (5.3 ± 1.4 in Gennaro et al., 2010, 3 ± 2 in Pagel & Portinari, 1998). A variation of initial He abundance affects the TO luminosity, shifting the theoretical TO location towards the blue, and thus changing the age estimate.

- efficiency of physical mechanisms such as diffusion and convection. The diffusion is a transport mechanism of the matter which consists in a net movement of atoms or molecules, due to the concentration, pressure gradients and radiative forces. It might vary the position of the TO and consequently it might affect the age estimate.

The convection, instead, is a mechanism of energy transport that involves motions of the matter on the large scale in the stellar interior. Under certain conditions given by the Schwarzschild[3] criterion, the convection occurs: the hot matter rises to the outer layers, where it cools and falls down as colder material. A given convective element might continue to rise over the limit boundary under which the Schwarzschild criterion is valid, because its non-negligible velocity. This process is called overshooting. In the stellar convective core, the overshooting carries fuel in the nuclear fusion regions, extending the lifetime of the star in the main sequence and changing the age.

- inputs physics such as opacity and cross section of the nuclear reactions. The opacity is distinguished in radiative and conductive. The former represents the ability of the stellar material to absorb the radiation thanks to interactions between photons and matter. The latter is related to the electron conductive transport that becomes dominant in the dense degenerate regions in the stellar interiors due to the electronic degeneracy.

Finally, the relations necessary to translate the theoretical quantities in the models (luminosity and effective temperature) to the observable ones (magnitude, colours) generate other additional sources of uncertainties in the final age determination.

3.2. OTHER METHODS

During the latest years, several groups have been investigating the use of other methods to estimate stellar ages, as, for instance, the lithium-depletion boundary, asteroseismology, gyrochronology, stellar activity and chemical clocks (see, e.g. Soderblom et al., 2014, for a recent review).

3.2.1. LITHIUM-DEPLETION BOUNDARY

The lithium-depletion boundary (LDB) method uses the abundance of lithium, a light element burned in stellar interiors at the temperatures $\sim 2.5 \cdot 10^6$ K, to estimate the ages of open clusters in the range from 20 to 200 Myr. In this age range, the location of the Li depletion is related to the stellar mass, since the more massive and luminous pre-main sequence stars destroy their Li before the lower-mass and lower-luminosity stars that still contain their original Li content. The luminosity at the transition between these two regimes is known as the LDB (see the box in Fig. 3.5). It divides stars at low luminosities retaining all their initial Li and those at higher luminosities with total Li depletion. The LDB depends on the masses of stars that are reaching the Li burning temperature, and thus consequently to the age of the cluster. The LDB technique is limited by constraints due to the measurement of the Li I line at 6708 Å in cool and faint stars where the Li depletion happens. Indeed, it is necessary to have a spectral resolution higher than at least 30 000 and a good signal-to-noise ratio. Moreover, this technique depends on the stellar evolutionary predictions.

[3] The Schwarzschild criterion is $\Delta_{rad} > \Delta_{ad}$, where Δ_{rad} is the radiative temperature gradient of the environment if the convection is not present and Δ_{ad} is the adiabatic temperature gradient (i.e. that of the convective bubble assuming the adiabatic approximation).

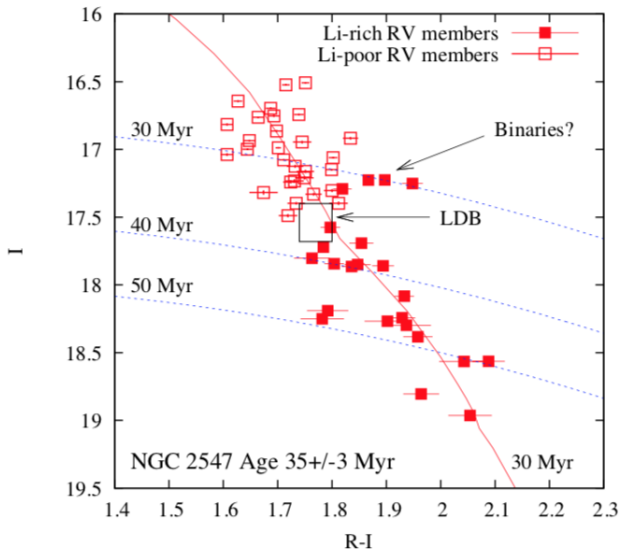

Fig. 3.5: The colour-magnitude diagram of NGC 2547, where the location of the LDB is indicated. The plot shows three dashed loci of constant luminosity, corresponding to LDB ages of 30, 40 and 50 Myr. The solid locus is an isochrone at 30 Myr. The squares represent cluster members (Soderblom et al., 2014).

3.2.2. ASTEROSEISMOLOGY

The term asteroseismology indicates the study of internal structure and dynamics of stars from small oscillations observed on their surface. They are produced by waves travelling inside the star which interfere constructively with themselves giving rise to resonant modes (see, e.g. Ulrich, 1986; Lebreton & Montalbán, 2009; Soderblom, 2010; Davies & Miglio, 2016; Bellinger et al., 2016). The waves that produce these oscillations in a star can be classified in two categories: acoustic waves, the so-called pressure (p-) modes, and internal gravity waves, called also g-modes (e.g. Houdek et al., 1999; Samadi & Goupil, 2001; Samadi et al., 2001).

In Fig. 3.6, the left panel displays how p and g modes propagate in the stellar structure, while the right panel shows a power spectrum density of p-modes from which it is possible to derive the density, the sound speed or the internal rotation rate by inversion of the frequencies. Moreover, these frequencies give access to information on the solar properties such as the age, helium content and depth of the outer convective envelope. Pulsating stars are observed in each region of the HR diagram and their pulsations may be excited by different mechanisms, in a large range of amplitudes. However, ages from asteroseismology can be obtained for solar-type and red giant stars, since to observe stellar pulsation it is necessary to have the convective layer near to the stellar surface. Comparing the oscillation spectrum with predictions of stellar models, the age and mass of a star can be determined (Lebreton & Montalbán, 2009). In this approach, large grids of stellar models are interpolated and the mass and age of the model that best matches the observations provide the age and mass for the given star. However, ages from oscillation spectra are limited by the number of stars observed by dedicated space telescopes (e.g. CoRoT, Kepler missions, Michel et al., 2008; Borucki et al., 2010), but they will increase in the next decades thanks to new dedicated space missions, as, e.g. TESS (Stassun et al., 2018) and PLATO (Rauer et al., 2014). In Fig. 3.7 I show the Kiel diagram of the stars observed by the Kepler satellite, highlighting

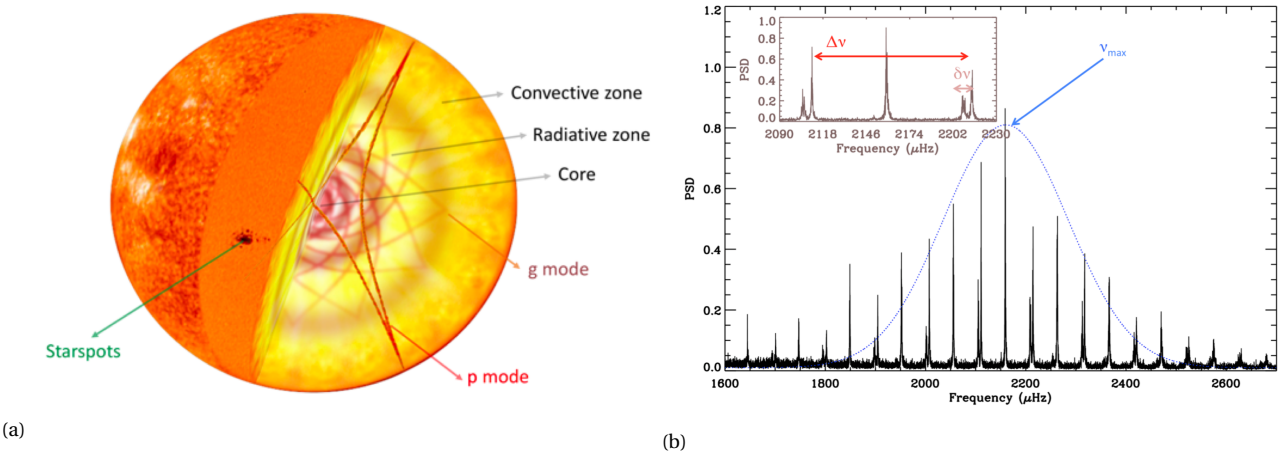

(a) (b)

Fig. 3.6: (a) Structure of a typical 1 $M_\odot$ main-sequence solar-like pulsating star where the p- and g- modes are propagating. The structure of the star is divided in two main regions: the inner radiative zone (including the core) and the external convective zone. (b) Power spectrum density PSD (in arbitrary units) of 16 Cyg A. The blue dotted line represents the Gaussian fit to obtain the frequency at maximum power: ν_{max}. The inset is an enlargement showing the large frequency separation, $\Delta\nu$, between two consecutive modes of angular degree $\ell = 0$ and the small frequency separation $\delta\nu_{0,2}$. Figures by García & Ballot (2019).

the stars where pulsations were measured (figure from García & Ballot, 2019).

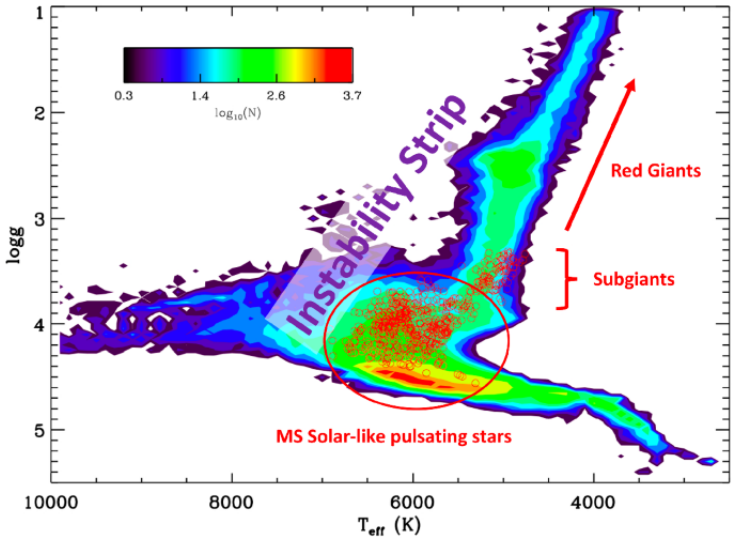

Fig. 3.7: Kiel diagram, log g as a function of $T_{\rm eff}$, colour coded by the logarithm of the number of the stars, N, observed by Kepler (Mathur et al., 2017). Open red circles locate MS and sub-giant stars where pulsations have been measured by Kepler (Chaplin et al., 2014). Figure by García & Ballot (2019).

3.2.3. GYROCHRONOLOGY AND STELLAR ACTIVITY

Gyrochronology and stellar activity are additional methods adopted to estimate stellar ages (Barnes, 2007; Soderblom, 2010). They are both empirical techniques, based on observed relations between a measurable property and age. So they are not dependent on theoretical evolutionary models as the previous ones. However, since the ages of the calibrators, usually star clusters, are obtained via isochrone fitting, there is a secondary dependence on

the theoretical evolutionary models also on ages determined from these empirical methods. These methods are based on the variation with time of the rotation period and of the non-thermal emissions that arise in the upper atmospheres of stars, respectively. These variations are due to the decrease with time of the magnetic field in main sequence stars, for the presence of a convective zone. The convection and rotation interact to create complex motions, in which the gas is ionized and it becomes a conductor. These motions can reinforce and amplify the magnetic field, and lead to an angular momentum loss. This effect manifests in different forms: a variation in the rotational period or a deposit of non-thermal energy into the chromosphere and corona. As a consequence, the rotational velocity and stellar activity decreases with time, and thus we can establish relations between rotation period or non-thermal emission and age, using proper calibrators (we can see an example in Fig. 3.8 for both cases).

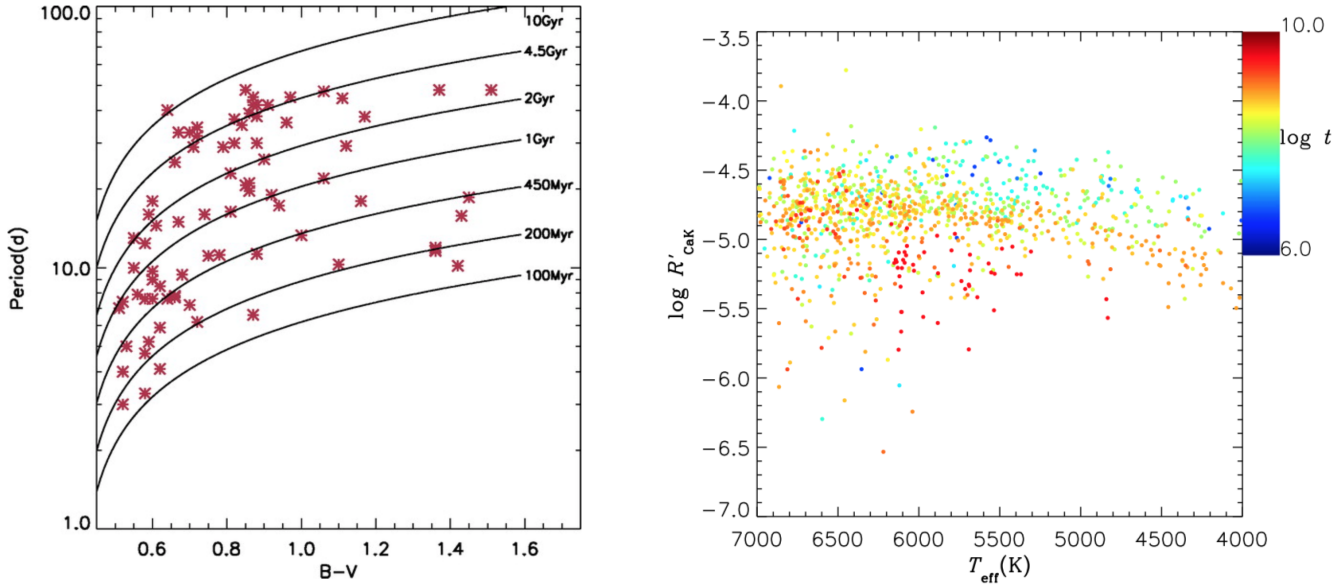

(a) (b)

Fig. 3.8: (a) A period-colour diagram for field stars by Pizzolato et al. (2003), where the lines correspond to rotational isochrones with ages marked in the plot (Barnes, 2007). (b) log R'_{CaK} vs. T_{eff} for star members of more than 90 open clusters in the LAMOST survey, colour-coded by age (Zhang et al., 2019).

The rotational period is calculated starting from precise photometry, while the activity can be observed in the cores of very strong absorption features such as H_α, the Mg II h and k lines, the Ca II H and K lines, or the Ca II infrared triplet. For the stellar activity, some indexes are used such as log R'_{CaK}, the ratio of the flux in the core of Ca II K line to bolometric flux (σT_{eff}^4), where the photospheric contribution is removed ($'$). Moreover, the stellar activity is better observed at wavelengths where the photosphere is weak or suppressed, such as in x-rays, ultraviolet, or in the radio regime.

The Large Synoptic Survey Telescope[4] (LSST, now called Vera Rubin Observatory, LSST Science Collaboration et al., 2009) is a 8.4 m telescope currently under construction in Chile. LSST will cover about 18,000 deg^2 of the southern sky with 6 filters in its main survey,

[4] https://www.lsst.org; LSST red book: https://www.lsst.org/sites/default/files/docs/sciencebook/SB_6.pdf

with about 825 visits to each spot. It will be able to measure rotation periods of: 250 Myr solar analogues between 1 and 20 kpc; older solar analogues at a shorter distance, because of their smaller photometric variations (LSST will measure periods for 5 Gyr solar analogues over a distance range from 1 to 8 kpc); lower mass M dwarfs, which are significantly fainter but also much more numerous, out to 500 pc for stars as old as 5 Gyrs. Measuring photometric rotation periods for thousands of field stars in a variety of Galactic environments, LSST will enable gyrochronology relations to map out the SFH of the Galactic disc over the past 1-2.5 Gyrs, and as far back as 5 Gyrs for brighter stars within the extended solar neighborhood.

3.2.4. CHEMICAL CLOCKS

We can also infer stellar ages through the so-called chemical clocks, i.e. abundances ratios (e.g., [Y/Mg] or [C/N]), which show a clear dependence on stellar ages. Chemical clocks, calibrated with stars with well-known ages (see Sect. 3.3 for more details), allow us to derive ages of large sample of stars through empirical relationships such as Age = a $\cdot$ [X_1/X_2] + b, where [X_1/X_2] is a chemical clock. These ratios can be distinguished in two different families: those based on elements produced through different nucleosynthesis channels with different time scales, and those based on elements modified by stellar evolution and dependent on stellar mass.

Abundance ratios dependent on chemical evolution They are based on pairs of elements, produced with a different contribution of SNe Type II on short time scales and SNe Type Ia or asymptotic giant branch (AGB) stars on longer time scales. Their chemical composition does not change in consequence of the mixing processes in the stellar surfaces. This means that their present abundance is the same as in the time of their formation.

The global effect of the Galactic chemical evolution produces increasing (or decreasing) trends of the abundance ratios over Fe with age, as we can see in Fig. 3.9: [X/Fe] with X a *s*-element (e.g. Y) has a negative slope due to the delayed production of Y from low-mass AGB stars with respect to the early contribution of SNe Ia and SNe II that produce iron; [X/Fe] with X an α-element (e.g. Mg) shows a positive trend in agreement with the production of α-elements with shorter timescale with respect to iron; [X/Fe] with X a iron-peak element (e.g. Ni) has a light positive slope, consistent within the errors with a null slope that reflects the same mechanisms of production of Ni and iron. Ratios of elements with opposite behaviours with respect to stellar age (see e.g. [Mg/Fe] and [Y/Fe] in Fig. 3.9, decreasing and increasing, respectively, with stellar age) show a strong dependence on age. Examples of their dependence on age are shown in Fig. 3.10, where the dots are solar twin stars (stars within $\pm$100 K in $T_{\rm eff}$ and $\pm$0.1 dex in log g and [Fe/H] from solar values) and the red line is the linear fit Age = a $\cdot$ [Y/Mg] (or [Y/Al]) + b.

The first work exploring the relation [s/α]-age was da Silva et al. (2012). More recently, Nissen (2015) and Nissen et al. (2017) found that the abundance ratios [Y/Mg] and [Y/Al] are good age indicators in the case of solar twins stars, as confirmed by other works (Spina et al., 2016; Tucci Maia et al., 2016; Spina et al., 2018b; Delgado Mena et al., 2019; Casali et al., 2020b). Feltzing et al. (2017), Delgado Mena et al. (2019) and Casali et al. (2020b) showed that including stars of different metallicities reveals a secondary dependence in these relations on metallicity.

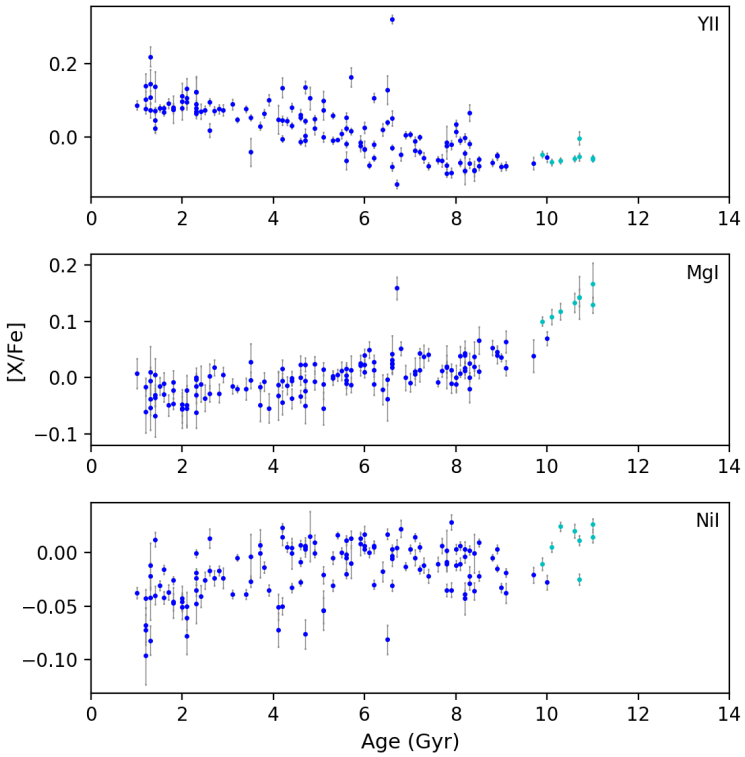

Fig. 3.9: [X/Fe]-age trends for α- (MgI), iron-peak (NiI) and s- (YII) elements in $-0.1 <$ [Fe/H] $< +0.1$. Blue stars belong to the thin disc, cyan stars to the thick disc.

Abundance ratios dependent on stellar evolution They are composed by pairs of elements modified in opposite way by stellar evolution, as, e.g., the [C/N] ratio. During the RGB phase, the penetration of convective envelope towards inner regions brings up previously processed materials to the surface, in particular C and N (products of the CNO-cycle in main sequence stars). The phase in which the convection reaches its maximum penetration is called first dredge-up (FDU, hereafter). The mixing processes produce a variation in the chemical composition of the stellar surface. The depth reached by convective envelope and the amounts of C and N brought to the surface depend on stellar mass, thus on the age (age and mass are related in RGB phase – as in any other evolutionary phase – in first approximation). This means that [C/N] ratio in evolved stars can be used as an age proxy (Salaris et al., 2015; Masseron & Gilmore, 2015; Casali et al., 2019). Carbon and nitrogen have been expected to be good indicators of stellar masses and, therefore of ages, since Masseron & Gilmore (2015), Salaris et al. (2015) and Martig et al. (2016). Lagarde et al. (2019) discussed the limits and applicability of this technique, through population synthesis models.

3.3. AGE CALIBRATORS: STAR CLUSTERS AND SOLAR TWINS

To calibrate empirical relations between ages and chemical clocks, it is necessary to have a pool of reliable benchmark stars whose ages are well-determined, typically with the isochrone fitting. These *calibrators* are usually star clusters and solar twin stars. To this end, I used

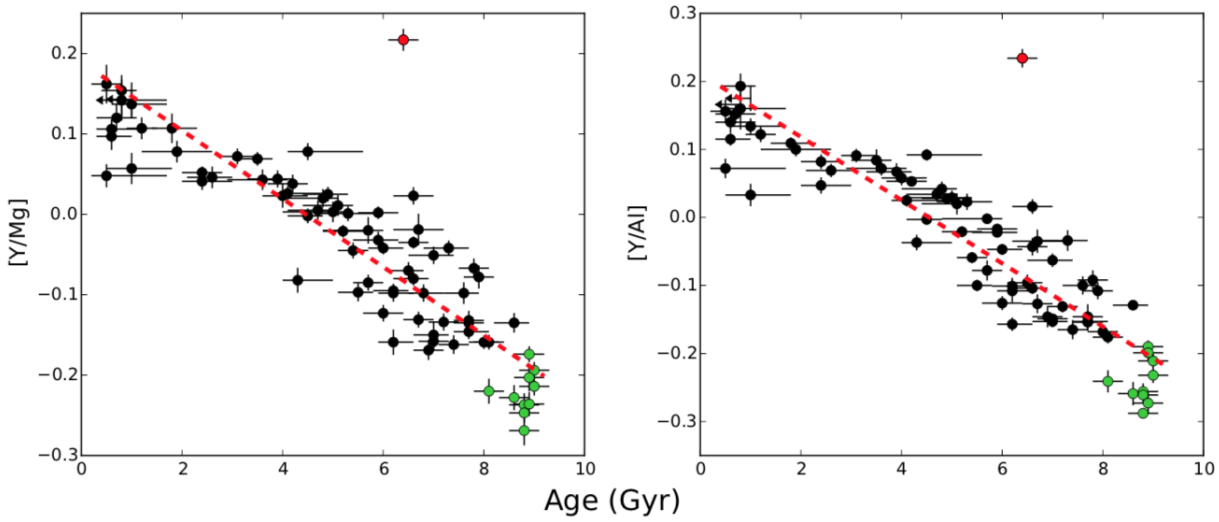

Fig. 3.10: [Y/Mg] and [Y/Al] as a function of stellar age. The black circles represent the thin disc stars, while the green ones the thick disc population. The red circle is a chemically anomalous star. The red dashed lines correspond to the linear fitting (Spina et al., 2018b).

the open clusters in the project present in the Chapter 4, and solar-twins in the Chapter 5.

Calibrating the ages of young and intermediate-age populations with open clusters The Milky Way disc contains a large number of open clusters, with ages ranging from few Myr to several Gyr (Randich et al., 2013; Bailer-Jones et al., 2018; Holtzman et al., 2015; De Silva et al., 2015; Deng et al., 2012, see also Chapter 1). Since clusters are composed by coeval and chemically homogeneous stars, their ages can be measured with higher accuracy than those of field stars. Thereby, they are powerful tools to calibrate relationships between stellar ages and properties of stars. Typical uncertainties on the ages from isochrone fitting of open clusters are ~ 0.2 Gyr (e.g Magrini et al., 2018), while of field stars[5] (Mints & Hekker, 2017, 2018, e.g.) are ~ 1.6 Gyr. The latter are much larger due to the intrinsic difficulty in comparing a single point with an isochrone grid. Although the distances measured with *Gaia* have improved our knowledge of the ages of field stars, their uncertainties remain larger than those of stars in clusters. On the other hand, the *Gaia* data have improved and made the age scale of the clusters homogeneous. Recently, Cantat-Gaudin et al. (2020) have used the deep and homogeneous *Gaia* photometry to estimate the distance, age, and interstellar reddening for about 2000 open clusters identified with the astrometry present in the second data release of *Gaia* mission (DR2, Gaia Collaboration et al., 2018b). Their large and homogeneous cluster catalogue, with all clusters on the same age scale, provides a database of accurate cluster ages. In Fig. 3.11 we show the distribution of open clusters pre- and with *Gaia* in bins of age.

Exploring the oldest ages with Globular clusters Globular clusters populating the halo of our Galaxy are among the oldest objects of the Milky Way. Their abundances are about one-hundredth or less of the Solar ones, suggesting that they are composed by less chemically processed gas. Being among the oldest known astronomical objects, their age estimate

[5] `http://www2.mps.mpg.de/homes/mints/unidam.html`

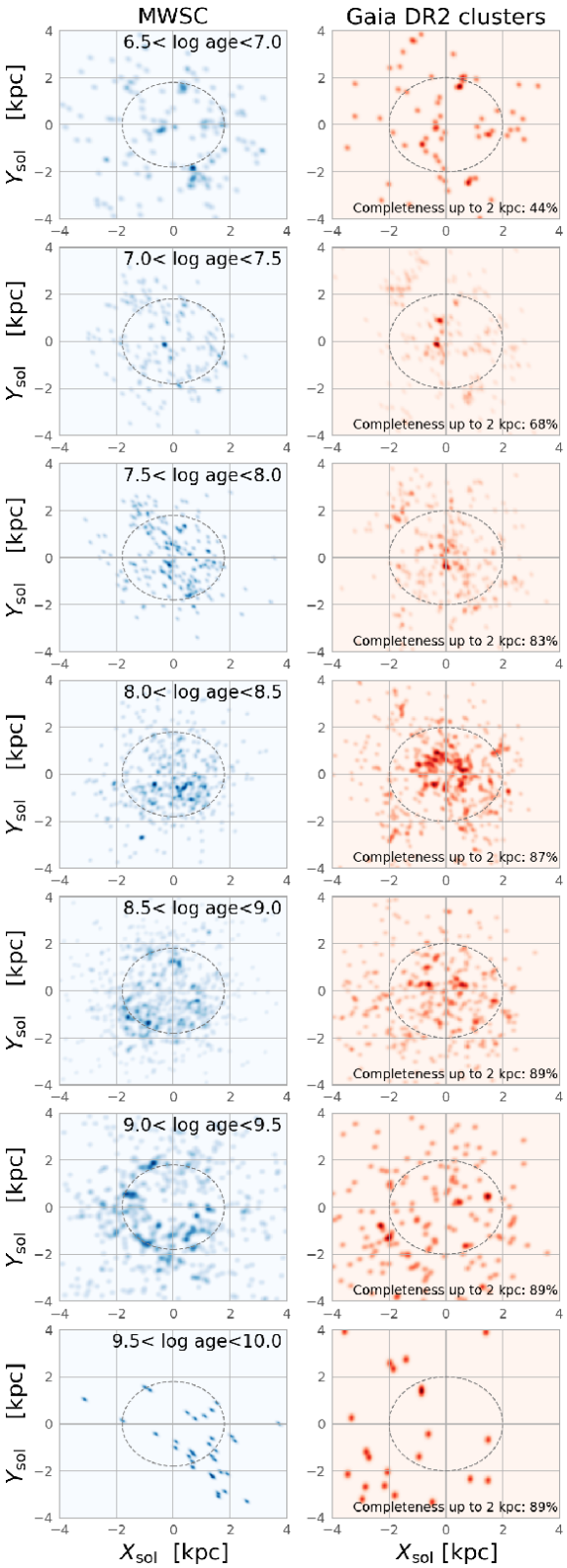

Fig. 3.11: Galactic distribution of the open clusters in Anders et al. (2019), sliced into logarithmic age bins. Left: pre-Gaia census using the MWSC catalogue (Kharchenko et al., 2013). Right: Post-Gaia DR2 census, using the catalogue of Cantat-Gaudin et al. (2020). Figure by Anders et al. (2020).

can give us a lower limit for the age of the Milky Way and the Universe (11.2 Gyr, Krauss & Chaboyer, 2003). As for open clusters, their ages can be estimated through the isochrone fitting of their whole sequence, putting constraints on the older tails of Galactic stars.

The solar twins as benchmarks for Galactic astronomy Solar-type stars are stars with atmospheric parameters, i.e. $T_{\rm eff}$ and log g, very similar to those of Sun ($T_{\rm eff,\odot}$ = 5771 K and log $g_\odot$ = 4.44 dex, Ayres et al., 2006). If they have also similar metallicity ($-0.1 <$ [Fe/H] < 0.1 dex), they are called solar twins (Meléndez et al., 2009, 2014b). Their well-known stellar parameters are extremely important for the calibration of fundamental observable quantities and stellar ages. Solar twins are used as calibrators of age-chemical properties relationships, because their ages can be measured with a higher accuracy than for other stars, typically with uncertainties of $\sim$ 0.5 Gyr (Bedell et al., 2014; Nissen, 2015; Spina et al., 2018b). Their stellar parameters are, indeed, usually obtained from high-quality spectra, differentially analysed with respect to the Sun. In this way, the impact of all unknown systematic errors due to model atmospheres can be characterised and subtracted. Therefore, small uncertainties on their $T_{\rm eff}$ and log g correspond to small uncertainties on their stellar age. Indeed, they can be employed as calibrators in age-chemical abundances relations.

4

CALIBRATING A RELATIONSHIP BETWEEN AGE AND THE [C/N] ABUNDANCE RATIO WITH OPEN CLUSTERS

In this Chapter, I discuss the relation between stellar age and [C/N], a chemical clock composed by elements whose surface abundances have been modified by stellar evolution. The changes in [C/N] are strongly dependent on the stellar mass, and thus in the stellar age. Starting from the ages determined with isochrone fitting for the open clusters observed by Gaia-ESO and APOGEE surveys, I calibrated a relationship between cluster age and the [C/N] in their evolved stars by selecting post-FDU stars and studying the occurrence of non-canonical mixing.

The results presented here are described in the published paper Casali et al. (2019) on the scientific journal *Astronomy & Astrophysics*, volume 629, page A62.

4.1. DATA SAMPLES

4.1.1. GAIA-ESO SAMPLE

The Gaia-ESO survey (Gilmore et al., 2012; Randich et al., 2013, hereafter GES), as mentioned in Chapter 2, is a high-resolution spectroscopic survey that observed about 10^5 stars whose spectra were collected with the two different observing modes of FLAMES spectrograph: GIRAFFE (R~20000) and UVES (R~47000).
The data were reduced as described in Sacco et al. (2014) and Gilmore et al. (in preparation) for UVES and GIRAFFE, respectively. The stellar atmospheric parameters of the stars considered in this work, UVES FGK stars (the only stars with the C and N abundances), were determined as described in Smiljanic et al. (2014). The calibration and homogenisation of stellar parameters and abundances obtained by the different working groups were performed as described by Pancino et al. (2017) and Hourihane et al. (in preparation), respectively. All data used here are included in the fourth and fifth internal GES data releases (IDR4 and IDR5). Because the C and N abundances of the stars in common to both releases were not re-derived in IDR5, we adopted the C and N values presented in IDR4 for these stars. Hereafter we do not specify the GES release because we used IDR5, but for stars in

common, we adopted the C and N abundances of IDR4, which are absent from IDR5. In particular, the method used to derive the abundances we discuss here is described in Tautvaišienė et al. (2015). Here, we briefly recall the main steps of the analysis. C and N abundances were derived from molecular lines of C_2 (Brooke et al., 2013) and CN, respectively (Sneden et al., 2014). In the analysis of the optical stellar spectra, the $^{12}C^{14}N$ molecular bands in the spectral range 6470−6490 Å, the C_2 Swan (1,0) band head at 5135 Å, the C_2 Swan (0,1) band head at 5635.5 Å were used. The selected C_2 bands do not suffer from non-local thermodynamical equilibrium (NLTE) deviations, and thus are better suited for abundance studies than [C I] lines. All molecular bands and atomic lines were analysed through spectral synthesis with the code BSYN (Tautvaišienė et al., 2015) and all synthetic spectra were calibrated to the solar spectrum of Kurucz (2005).

Open Clusters	R.A.[a] (J2000)	Dec.[a]	R_{GC} (kpc)	z (pc)	RV[b] (km s^{-1})	[Fe/H][a] (dex)	log(Age[yr])	Ref. Age and Distance
Berkeley 31	06:57:36	+08:16:00	15.16±0.40	+340±30	+56.99 ± 0.14	−0.27±0.06	$9.40^{+0.05}_{-0.05}$	Cignoni et al. (2011)
Berkeley 36	07:16:06	−13:06:00	11.30±0.20	−40±10	+62.70 ± 0.13	−0.16±0.10	$9.84^{+0.03}_{-0.03}$	Donati et al. (2012)
Berkeley 44	19:17:12	+19:33:00	6.91±0.12	+130±20	−8.71 ± 0.19	+0.27±0.06	$9.20^{+0.07}_{-0.09}$	Jacobson et al. (2016)
Berkeley 81	19:01:36	−00:31:00	5.49±0.10	−126±7	+48.14 ± 0.26	+0.22±0.07	$8.93^{+0.05}_{-0.05}$	Magrini et al. (2015)
M67	08:51:18	+11:48:00	9.05±0.20	+405±40	+34.7 ± 0.9[a]	−0.01±0.04	$9.63^{+0.05}_{-0.05}$	Salaris et al. (2004)
Melotte 71	07:37:30	−12:04:00	10.50±0.10	+210±20	+50.8 ± 1.3[a]	−0.09±0.03	$8.92^{+0.08}_{-0.11}$	Salaris et al. (2004)
NGC 2243	06:29:34	−31:17:00	10.40±0.20	+1200±100	+59.65 ± 0.05	−0.38±0.04	$9.60^{+0.11}_{-0.15}$	Bragaglia & Tosi (2006)
NGC 6005	15:55:48	−57:26:12	5.97±0.34	−140±30	−24.75 ± 0.35	+0.19±0.02	$9.08^{+0.10}_{-0.12}$	Piatti et al. (1998)
NGC 6067	16:13:11	−54:13:06	6.81±0.12	−55±17	−38.65 ± 0.28	+0.20±0.08	$8.00^{+0.18}_{-0.30}$	Alonso-Santiago et al. (2017)
NGC 6259	17:00:45	−44:39:18	7.03±0.01	−27±13	−32.98 ± 0.49	+0.21±0.04	$8.32^{+0.06}_{-0.07}$	Mermilliod et al. (2001)
NGC 6705	18:51:05	−06:16:12	6.33±0.16	−95±10	+35.67 ± 0.19	+0.16±0.04	$8.48^{+0.04}_{-0.05}$	Cantat-Gaudin et al. (2014)
NGC 6802	19:30:35	+20:15:42	6.96±0.07	+36±3	+13.44 ± 0.60	+0.10±0.02	$9.00^{+0.08}_{-0.10}$	Jacobson et al. (2016)
Rup 134	17:52:43	−29:33:00	4.60±0.10	−100±10	−40.78 ± 0.15	+0.26±0.06	$9.00^{+0.01}_{-0.01}$	Carraro et al. (2006)
Pismis 18	13:36:55	−62:05:36	6.85±0.17	+12±2	−27.94 ± 0.29	+0.22±0.04	$9.08^{+0.05}_{-0.06}$	Piatti et al. (1998)
Trumpler 23	16:00:50	−53:31:23	6.25±0.15	−18±2	−60.74 ± 0.38	+0.21±0.04	$8.90^{+0.05}_{-0.06}$	Jacobson et al. (2016)
NGC 4815	12:57:59	−64:57:36	6.94±0.04	−95±6	−29.53 ± 0.21	+0.11±0.01	$9.18^{+0.04}_{-0.04}$	Friel et al. (2014)
Trumpler 20	12:39:32	−60:37:36	6.86±0.01	+134±4	−39.82 ± 0.14	+0.15±0.07	$8.48^{+0.07}_{-0.08}$	Donati et al. (2014)

Table 4.1: Parameters of the open clusters in the GES sample. Ref: [a]Magrini et al. (2018). [b] RVs are determined with the GIRAFFE sample of high-probability cluster members.

The selected clusters are shown in Table 4.1, where we summarise their basic properties from the literature: coordinates, Galactocentric distances (R_{GC}), heights above the plane (z), mean radial velocity (RV) of cluster members, median metallicity [Fe/H], logarithmic ages, and the references for ages and distances.

We made a first quality check on the GES catalogue by excluding from our sample stars with highly uncertain stellar parameters (i.e. including only stars with $T_{\rm eff} > 0$, $eT_{\rm eff} < 500$, $\log g > -0.5$, and $e\log g < 0.5$) and with a signal-to-noise ratio S/N < 20. We selected giant stars in open clusters and in the Galactic field. We performed a membership analysis of stars in clusters with a Bayesian approach that took into account GES and *Gaia* information. Membership probabilities were estimated from the RVs (from GES) and proper motion velocities (from *Gaia*) of stars observed with GIRAFFE. A maximum likelihood method was used to determine the probability of cluster membership by fitting two quasi-Gaussian distributions to the velocity data. The basic supposition was that the set of stars that we observed as potential cluster members is draw from two populations. One distribution defines cluster members, and a second much broader distribution represents the background population. These two populations show different velocity distributions: the velocities of

the first are close to the average velocity of the cluster, and the second population shows a much wider range of velocities. The mean value and standard deviation of the background population were fixed for the final calculation of cluster membership. If substructure was evident in the velocity distributions, the cluster was simultaneously fitted with two independent populations and targets were assigned a membership probability for each population. Most clusters, especially the older ones, present a single population. More details on the membership estimation are reported in Jackson et al. (2020). For our analysis, we selected stars with a membership probability of at least 0.8, which means that the average probability is $P^{mean}_{memb.}$ for cluster members. This is listed in Table 4.4.

4.1.2. APOGEE SAMPLE

The APOGEE (see Chapter 2 and Zasowski et al., 2013; Majewski et al., 2017) is a large spectroscopic survey in the near-infrared (H band) that observed over 10^5 stars with high S/N. We here use the DR14 release[1], which is the second data release of the fourth phase of the Sloan Digital Sky Survey (SDSS-IV, York et al., 2000; Blanton et al., 2017). The DR14 release contains data for approximately 263,000 stars. In the same way as for the GES sample, we selected stars based on the quality of their measurements according to the following criteria: $T_{\rm eff} > 0$, $eT_{\rm eff} < 500$, $\log g > -0.5$, $e\log g < 0.5$, and S/N > 20.

To identify the open clusters in the APOGEE catalogue, we started our search by defining a master list of known open clusters. We used the Kharchenko et al. (2013) catalogue, where coordinates and angular radii of clusters are listed. For most of the cluster in our list, a cluster membership has recently been published (Donor et al., 2018). For these clusters, we therefore selected the member stars of Donor et al. (2018), but for the four clusters that were not available, we computed the membership by adopting a similar approach as in Donor et al. (2018).

We performed the membership selection by retaining all stars within a circle with a radius three times the reference radius and centred on the cluster coordinates. We selected as member stars those within $\pm 2\sigma$ from the mean metallicity and RV. The open clusters we selected are listed in Table 4.2, where we give the following parameters: coordinates, Galactocentric distances R_{GC}, heights from the Galactic plane z, mean RV, metallicities, and logarithmic ages.

The C and N abundances were computed within the pipeline ASPCAP (García Pérez et al., 2016), which compares the observed spectra to a grid of synthetic spectra to determine stellar parameters. A χ^2 minimisation determined the best-fit spectrum, and the corresponding stellar parameters were assigned to the observed star. The abundances of C and N were measured from molecular lines of CO and CN (García Pérez et al., 2016).

4.1.3. AGE SCALE OF OPEN CLUSTERS

Star clusters offer a unique opportunity with respect to field stars because they have well-determined ages through isochrone fitting because so many members are observed throughout the cluster sequence. This makes them powerful tools for calibrating the relations between stellar ages and chemical properties of stars.

[1] https://www.sdss.org/dr14/irspec/spectro_data/

Open Clusters	R.A.^{f} (J2000)	Dec.^{f} (J2000)	R_{GC} (kpc)	z (pc)	RV (km s^{-1})	[Fe/H]^b (dex)	log(Age[yr])	Ref. Age
Berkeley 17	05:20:37	+30:35:24	9.79	−114	-73.7 ± 0.8^a	-0.11 ± 0.03	$9.98^{+0.05}_{-0.05}$	Friel et al. (2005)
Berkeley 53	20:55:57	+51:03:36	8.66	216	7.5^b	$+0.00\pm0.02$	$9.09^{+0.02}_{-0.02}$	Maciejewski et al. (2009)
Berkeley 66	03:04:04	+58:44:24	14.07	22	-50.6 ± 0.2^c	-0.13 ± 0.02	$9.54^{+0.12}_{-0.12}$	Phelps & Janes (1996)
Berkeley 71	05:40:57	+32:15:58	11.25	51	-25.5 ± 6.0^d	-0.20 ± 0.03	$9.00^{+0.15}_{-0.15}$	Maciejewski & Niedzielski (2007)
FSR0494	00:25:41	+63:45:00	11.43	91	-63.3 ± 1.5^b	$+0.01\pm0.02$	$8.70^{+0.08}_{-0.10}$	This work
IC166	01:52:23	+61:51:54	11.68	−13	-40.5 ± 1.5^b	-0.06 ± 0.02	$9.00^{+0.08}_{-0.10}$	Schiappacasse-Ulloa et al. (2018)
King 5	03:14:46	+52:41:49	9.85	−164	-52.0 ± 12.0^e	-0.11 ± 0.02	$9.10^{+0.10}_{-0.10}$	Maciejewski & Niedzielski (2007)
King 7	03:59:07	+51:46:55	10.35	−47	-11.9 ± 2.0^b	-0.05 ± 0.02	$8.82^{+0.06}_{-0.07}$	Dias et al. (2002)
NGC 188	00:47:24	+85:15:18	9.13	761	-42.4 ± 0.1^l	0.14 ± 0.01	$9.87^{+0.04}_{-0.04}$	Fornal et al. (2007)
NGC 1193	03:05:53	+44:22:48	13.30	−1264	-82.0 ± 0.39^f	-0.22 ± 0.02^g	$9.70^{+0.10}_{-0.10}$	Kyeong et al. (2008)
NGC 1245	03:14:48	+47:15:11	10.60	−464	-29.7 ± 1.1^h	-0.06 ± 0.02	$8.95^{+0.05}_{-0.05}$	Subramaniam (2003)
NGC 1798	05:11:38	+47:41:42	13.05	443	-2.0 ± 10.0^i	-0.18 ± 0.02	$9.15^{+0.09}_{-0.09}$	Park & Lee (1999)
NGC 2158	06:07:26	+24:05:31	12.75	148	26.9 ± 1.9^h	-0.15 ± 0.02	$9.28^{+0.11}_{-0.11}$	Salaris et al. (2004)
NGC 2420	07:38:23	+21:34:01	10.61	967	73.6 ± 0.2^m	-0.12 ± 0.02	$9.47^{+0.17}_{-0.17}$	Pancino et al. (2010)
NGC 2682 (M67)	08:51:23	+11:48:54	8.63	470	33.6 ± 0.1^n	-0.05 ± 0.03	$9.63^{+0.05}_{-0.05}$	Salaris et al. (2004)
NGC 6705	18:50:59	-06:16:48	6.50	−84	35.1 ± 0.3^m	$+0.16\pm0.02$	$8.48^{+0.07}_{-0.07}$	Cantat-Gaudin et al. (2014)
NGC 6791	19:20:53	+37:46:48	7.80	932	-47.4 ± 0.1^o	$+0.42\pm0.05$	$9.90^{+0.02}_{-0.02}$	Wu et al. (2014)
NGC 6811	19:37:22	+46:23:42	7.86	255	6.7 ± 0.1^p	-0.01 ± 0.02	$9.00^{+0.07}_{-0.07}$	Janes et al. (2013)
NGC 6819	19:41:17	+40:11:42	7.69	348	2.3 ± 0.1^q	$+0.11\pm0.03$	$9.28^{+0.02}_{-0.02}$	Wu et al. (2014)
NGC 6866	20:03:57	+44:09:36	7.88	158	13.7 ± 0.1^m	$+0.07\pm0.07^r$	$8.85^{+0.10}_{-0.10}$	Janes et al. (2014)
NGC 7789	23:57:25	+56:43:48	8.91	−168	-54.7 ± 1.3^h	$+0.05\pm0.03$	$9.21^{+0.12}_{-0.12}$	Pancino et al. (2010)
Teutsch 51	05:53:50	+26:49:48	11.78	31	2.7^b	-0.28 ± 0.02	$8.90^{+0.10}_{-0.10}$	Dias et al. (2002)
Trumpler 5	06:36:29	+09:28:12	10.59	49	-49.7 ± 1.9^s	-0.40 ± 0.01^s	$9.45^{+0.04}_{-0.04}$	Kim et al. (2009)

Table 4.2: Open clusters in the APOGEE sample. Ref: [a]Friel et al. (2005), [b]Donor et al. (2018), [c]Villanova et al. (2005), [d]Zhang et al. (2015), [e]Friel et al. (2002), [f]Kharchenko et al. (2013), [g]Netopil et al. (2016), [h]Jacobson et al. (2011), [i]Carrera (2012), [l]Gao (2014), [m]Mermilliod et al. (2008), [n]Geller et al. (2015), [o]Tofflemire et al. (2014), [p]Molenda-Żakowicz et al. (2014), [q]Dias et al. (2002), [r]Frasca et al. (2016), [s]Donati et al. (2015).

A large sample of clusters is observed in the GES and APOGEE surveys, which cover sizable ranges in ages, distances, and metallicities. The GES IDR5 contains 38 Galactic open clusters, and in 15 of them, red giant stars have been observed, while there are 23 clusters in APOGEE with red giant stars (see Tables 4.1 and 4.2).

We adopted cluster ages from the recent literature. Because a reliable and homogeneous age determination of star clusters is important for our project, we verified the literature ages against a common set of isochrones for consistency.

We compared the log g-T_{eff} diagrams of member stars of GES and APOGEE clusters with the PISA isochrones (for details, see Dell'Omodarme et al., 2012; Tognelli et al., 2018). These correspond to the ages and metallicities in Tables 4.1 and 4.2.

For the open clusters in the GES sample, we also add stars that were observed with GIRAFFE, mainly in the main sequence, to better characterise the cluster sequence. The agreement between the literature ages and metallicities and the corresponding isochrones is remarkably good because most of them were recently redetermined by the Gaia-ESA consortium in a homogeneous way (see, e.g., Donati et al., 2014; Friel et al., 2014; Jacobson et al., 2016; Magrini et al., 2017; Overbeek et al., 2017; Tang et al., 2017; Randich et al., 2018). For the APOGEE sample, most of the clusters are in agreement with the PISA isochrones that were computed with the literature ages and metallicities. We only redetermined the age of FSR0494, for which the PISA isochrone for the age given by Kharchenko et al. (2013) was inconsistent with the present data. The new age is listed in Table 4.2. In the left panels of Fig. 4.3 and in Figs 4.16, 4.17, and 4.18 in the Appendix 4.A of this Chapter, we show the log g-T_{eff} diagrams of member stars of each GES cluster with the corresponding PISA isochrones. The colour-magnitude diagrams of NGC 4815, NGC 6705 and Trumpler 20 are

shown in Tautvaišienė et al. (2015). In Fig. 4.4 and in Figs 4.19, 4.20, 4.21, 4.22, and 4.23 (left panels) we present the log g-T_{eff} diagrams of APOGEE member stars and the PISA isochrones.

4.2. SELECTION CRITERIA

To build up a relationship between the cluster [C/N] abundance ratios and their ages, it is necessary to select member stars in the red giant branch (RGB) whose carbon and nitrogen surface abundances have been modified by passing through the FDU event. Moreover, it is important to exclude stars that have suffered extra-mixing effects.

4.2.1. SELECTION OF RED GIANT STARS BEYOND THE FDU

We derived a quantitative criterion to select among the member stars of our sample open clusters those that have passed the FDU. To identify the location in the log g-T_{eff} diagram at which the FDU occurs for clusters of different ages and metallicities, in particularly the surface gravity log g, we used the same set of isochrones as we employed to determine the cluster ages. We considered isochrones in the age and metallicity ranges of our clusters, that is, with [Fe/H] from −0.4 to +0.4 dex and with ages from 0.1 to 10 Gyr. For these isochrones, we obtained the surface abundances of C and N.

The surface gravity that corresponds to the FDU was identified by selecting a proper value where the [C/N] starts to decrease monotonically in the corresponding isochrone. During the FDU, the surface [C/N] abundance progressively decreases as surface convection reaches increasingly deeper regions inside the star. We tried two different approaches: (1) the point where [C/N] starts to decrease monotonically, or (2) the point where the derivative $d[C/N]/d\log g$ is highest. We tested these two criteria on clusters with ages larger than 2 Gyr and found that the difference in the location of the FDU in the log g plane is quite negligible for our purposes (about 0.1 dex).

On the other hand, the second method (the point where $d[C/N]/d\log g$ is highest) is not suitable for clusters with ages below 500 Myr/1 Gyr. The reason is that for these ages, the extension of the convective envelope and consequently the surface [C/N] abundance changes slowly with log g. This causes a significant difference between the $\log g$ at FDU that is estimated using the two methods.

Figure 4.1 shows as an example the variation of [C/N] versus $\log g$ for isochrones of 200 Myr and 2 Gyr (for solar metallicity, [Fe/H]=0 dex). For the 2 Gyr case the interval of $\log g$ where [C/N] decreases is $\Delta\log g \approx 0.3$-0.4 dex, while for young clusters the interval is larger, about 0.6-0.7 dex. The maximum of the derivative $d[C/N]/d\log g$ corresponds to about the median point of the interval (see circles in Fig. 4.1). Because the interval of $\log g$ during the giant branch in young clusters is large, the adoption of the maximum derivative underestimates $\log g$ at the FDU by about 0.3 dex with respect to the alternative criterion. For this reason, we decided to use the first approach, and accordingly identified the $\log g$ FDU as the point where [C/N] starts to decrease monotonically in all clusters we analysed (see triangles in Fig. 4.1).

For each cluster in the GES and APOGEE samples, the values of log g that correspond to the FDU are shown in Table 4.3. To estimate the uncertainties in log g at which the

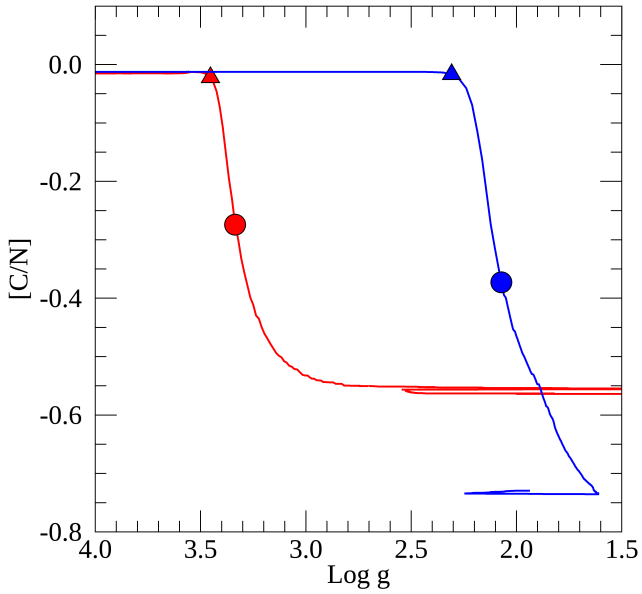

Fig. 4.1: [C/N] vs. log g of 200 Myr (red line) and 2 Gyr (blue line) [Fe/H]=0.0 dex PISA isochrones. The triangle represents the point where [C/N] starts to decrease monotonically, and the circle represents the point where the derivative $d[C/N]/d\log g$ is highest.

FDU occurs, we considered the effect of the uncertainties on the age and metallicity on the position of the FDU in the log g(FDU) versus age plane, as shown in Fig. 4.2. At younger ages, the uncertainty on the location of the FDU is mainly due to the uncertainties on the age. For the youngest clusters with ages < 1 Gyr, the uncertainty in the determination of log g of the FDU can be very large because the log g range in which the FDU occurs is wide (~1 dex in log g). Typical uncertainties of clusters with ages of about 1 Gyr range from 0.1 to 0.3 Gyr (see Tables 4.1 and 4.2), which implies an uncertainty in the determination of log g of the FDU of ~0.05 dex. For the oldest clusters, the main variation in the FDU position is related to the uncertainty in metallicity: from 2 to 9 Gyr, a variation of [Fe/H] of ±0.15 dex (a typical 2 or 3σ uncertainty on cluster [Fe/H]) implies a change in the FDU log g from 0.05 to 0.1 dex, respectively. To select stars that have passed the FDU, we took the uncertainties on the estimation of the theoretical position of the FDU and on the derived spectroscopic gravities into account. These uncertainties were added to FDU log g (shown in Table 4.3) in order to determine a lower limit in the selection of stars beyond the FDU.

4.2.2. C AND N VARIATIONS BEYOND THE FDU: THE EFFECT OF EXTRA MIXING

Selecting stars that have passed the FDU indeed defines a broad class of giant stars: lower RGB stars, i.e. stars just after the subgiant phase, at the beginning of the RGB; stars in the red clump (RC), and stars in the upper RGB. After the FDU, star evolve along the RGB, where additional mixing can occur, producing a further decrease of the C/N ratio (see e.g. Gratton et al., 2000; Martell et al., 2008). The non-canonical mixing or extramixing might be driven by rotation and by the thermohaline mechanisms (Lagarde et al., 2012).

Open Clusters	log g at FDU (dex)
GES clusters	
Berkeley 31	3.5
Berkeley 36	3.5
Berkeley 44	3.4
Berkeley 81	3.1
Melotte 71	3.1
NGC 2243	3.5
NGC 6005	3.3
NGC 6067	2.1
NGC 6259	2.4
NGC 6802	3.2
Rup134	3.2
Pismis 18	3.3
Trumpler 23	3.1
APOGEE clusters	
Berkeley 17	3.5
Berkeley 53	3.3
Berkeley 66	3.5
Berkeley 71	3.2
FSR0494	2.8
IC166	3.2
King 5	3.3
King 7	3.0
NGC 1193	3.5
NGC 1245	3.2
NGC 1798	3.3
NGC 188	3.6
NGC 2158	3.4
NGC 2420	3.5
NGC 6791	3.6
NGC 6811	3.2
NGC 6819	3.4
NGC 6866	3.1
Teutsch 51	3.1
Trumpler 5	3.4
NGC 7789	3.4
GES and APOGEE clusters	
M67	3.4
NGC 6705	2.6

Table 4.3: Surface gravity, log g, at FDU for the open clusters in the GES and APOGEE samples.

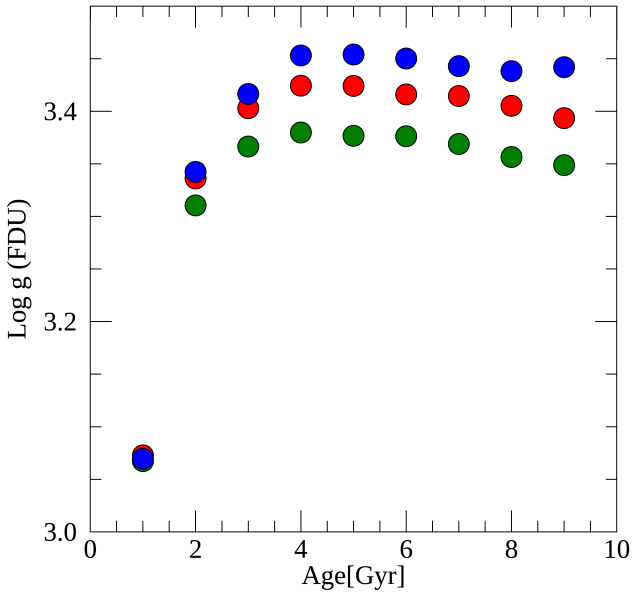

Fig. 4.2: Theoretical log g at the FDU as a function of age and metallicity. Three different colours indicate three different metallicities: [Fe/H]=0 (red), [Fe/H]=−0.15 (green), and [Fe/H]=+0.15 (blue).

The term "thermohaline" indicates an instability developed along the RGB at the bump[2] luminosity, when the gradient of molecular weight becomes negative ($\nabla\mu = d\ln\mu/d\ln P < 0$) in the external region of the H-burning shell surrounding the He-core. Therefore, the effects of the non-canonical mixing are mainly expected along the upper RGB, after the RGB bump phase. They are stronger at low metallicity and for low-mass stars (see the lower panel of Fig. 1 of Masseron & Gilmore, 2015; Shetrone et al., 2019). On the other hand, at solar metallicity and for massive stars, the effect is quite weak and almost negligible compared to the uncertainties of measured C/N (see, e.g. Shetrone et al., 2019). Masseron et al. (2017) confirmed the presence of the extra mixing in the upper part of the RGB for low-mass stars.

Observational evidence of extra-mixing that occurs during the RGB bump phase has been the detection of a further depletion of Li abundance along the RGB in globular clusters (e.g. Lind et al., 2009; Mucciarelli et al., 2011). During the bump, the thermohaline convection is expected to be more efficient and to rapidly transport surface Li into the internal hotter regions, where it is destroyed. The same mechanism can modify C and N abundances.

Open clusters usually do not reach very low metallicities and thus are not expected to show strong extra mixing. Nevertheless, the GES data allow us to determine cluster by cluster whether this extra mixing occurs by considering the Li abundance, A(Li)=log(Li/H)+12, and [C/N]. Then we can safely exclude the stars with strong extra mixing with lower [C/N], which would affect our age determination. In our sample, the lowest metallicities are those of Berkeley 31 ([Fe/H]=−0.27±0.06) and NGC 2243 ([Fe/H]=−0.38±0.04) in the GES sam-

[2] A temporary drop and rise of stellar luminosity due to the H burning shell, present in a RGB star, that reaches the chemical discontinuity created by the first dredge-up.

ple and of Trumpler 5 ([Fe/H]=−0.40±0.01) and Teutsch 51 ([Fe/H]=−0.28±0.03) in the APOGEE sample. As shown in Fig. 1 of Masseron & Gilmore (2015), [C/N] is expected to remain the same at solar metallicity from the lower RGB to RC phase, but is expected to be modified in the upper RGB, if at lower metallicity. Although from a theoretical point of view we do not expect strong extra-mixing effects in the metallicity range of open clusters, the Li abundance available in the GES sample can be used to determine correlations between Li, [C/N] abundances, and the evolutionary phase of member stars of the same clusters. We can thus identify possible extra-mixing processes in a metallicity range that has so far been poorly investigated in this respect.

In stars belonging to the same cluster, we expect to have a large dispersion of lithium abundance even before the RGB bump. This dispersion can be explained with several mechanisms: rotational mixing (Pinsonneault et al., 1992; Eggenberger et al., 2010), mass loss (Swenson & Faulkner, 1992), diffusion (Michaud, 1986), gravity waves (Montalbán & Schatzman, 2000; Talon & Charbonnel, 2005), and overshooting (Xiong & Deng, 2009). For instance, stars with a range of rotation velocities might have depleted Li at different rate. Rotation velocity is indeed responsible for the transport of chemical species and a higher rotation allows a deeper dredge-up (e.g. Balachandran, 1990; Lèbre et al., 2005), which modifies the Li content on the main sequence (e.g. the Li dip). However, the efficiency of this rotation-induced mixing can explain the spread of A(Li), but its effect is too weak to reproduce the drop of Li in some stars beyond the bump (see e.g. Mucciarelli et al., 2011). A non-canonical mixing is therefore necessary to explain Li depletion beyond the bump. Li depletion caused by thermohaline mixing is expected to be combined with a further decline of C and an enhancement of N, with a global decrease of [C/N] in lithium-depleted stars.

In Fig. 4.3 (in the Appendix 4.A of this Chapter we present all clusters in Figs 4.16, 4.17, and 4.18) we show two examples of clusters in the GES survey. In these figures we present the log g-$T_{\rm eff}$ diagrams (left panels), [C/N] versus A(Li) (central panels), and [C/N] abundance versus $T_{\rm eff}$ (right panels) of giant stars that have passed the FDU. We consider a star to be Li-depleted if A(Li)<0.4 dex or if its A(Li) is an upper limit. For most clusters, Li-depletion occurs in stars beyond the RGB bump (but not for all clusters, see e.g. M67). In many cases, Li-depletion is associated with a variation of [C/N] with respect to the bulk of stars with A(Li)>0.4 dex. In the rightmost panel, we also show [C/N] as a function of $T_{\rm eff}$. For our analysis, we conservatively removed stars with A(Li)<0.4 dex to maintain a sample of giant stars with homogeneous conditions and similar [C/N] abundances (with the exception of the stars of M67, for which we have only Li-depleted stars whose [C/N] is in good agreement with previous literature results, Bertelli Motta et al., 2017). However, we recall that the final A(Li) during the giant phase is strongly related to the initial Li abundance during the main sequence: a main-sequence star with a strong rotational velocity might deplete its surface Li abundance more than a star that rotates at a lower rate. For stars with low A(Li) but normal [C/N] with respect to the bulk of stars of the cluster (see, e.g. Pismis 18, NGC 6067), the origin of the Li under-abundance might be related to their condition during the main sequence. We also considered the location of stars in the log g-$T_{\rm eff}$ diagram and excluded stars beyond the RGB bump when their [C/N] differed by more than 1σ from the average [C/N] of the stars located before the bump.

In Fig. 4.4 (in Figs 4.19, 4.20, 4.21, 4.22, and 4.23 in the Appendix 4.A of this Chapter we present all clusters) we show the log g-$T_{\rm eff}$ diagram (left panel) and [C/N] abundance ver-

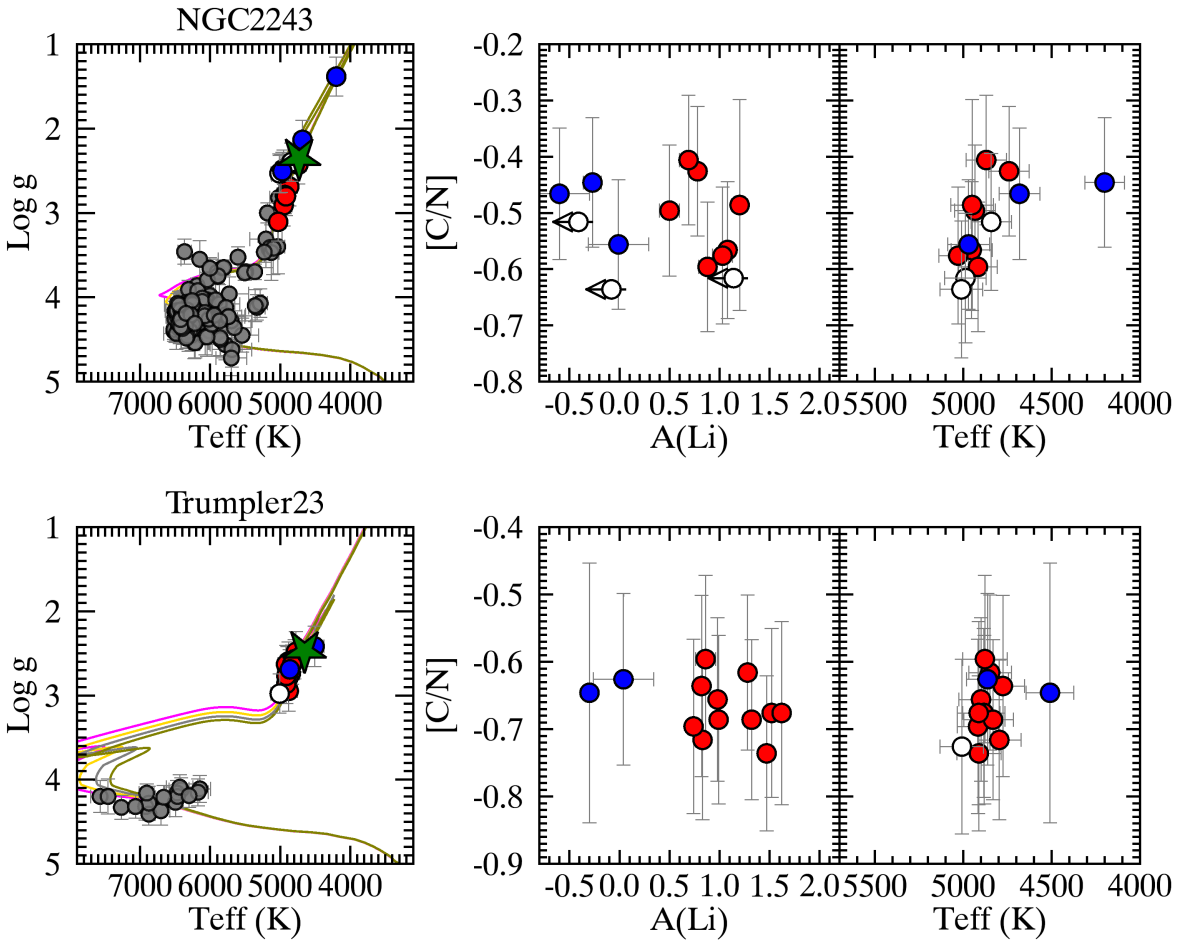

Fig. 4.3: GES clusters NGC 2243 and Trumpler 23: log g-$T_{\rm eff}$ diagrams with PISA isochrones 3.7, 4.0, 4.3, and 4.5 Gyr and 0.7, 0.8, 0.9, and 1.0 Gyr, respectively (left panels), and member stars beyond the FDU, A(Li) vs. [C/N] (central panel), and [C/N] abundance vs. $T_{\rm eff}$ (right panel). Stars with A(Li)>0.4 are shown with red circles, stars with A(Li)<0.4 with blue circles, stars with upper limit measurements of A(Li) are indicated with empty circles, and main sequence, subgiant stars or stars without C and N are shown with grey circles. The green star represents the position of the RGB bump.

sus $T_{\rm eff}$ (right panels) for giant stars belonging to two APOGEE clusters. For these clusters, we do not have information on Li abundance. We therefore used the information on the location on the log g-$T_{\rm eff}$ diagram and the variation of [C/N] to exclude stars for our final sample: we excluded stars beyond the RGB bump, but only if their [C/N] differed by more than 1σ from the average [C/N] of the stars located before the bump.

From stellar evolution theory, we would expect that clusters that have evolved stars beyond the FDU have lower [C/N] values if extra-mixing processes occur (see e.g. Lagarde et al., 2012). For some clusters we observe an opposite effect: at least one star that is more evolved along the isochrone has a higher [C/N] abundance (see e.g. NGC 6705 and NGC 6866) than the stars located at the clump. This unexpected result might be due to incorrect stellar parameters or abundances. These stars are not considered in the final average values. In addition, in many clusters (see e.g. NGC 2420, Trumpler 5, and NGC 6819) we removed several stars (blue circles) that are probably non-members based on their lo-

cation, which is quite far from the best-fit isochrone, and based on their discrepant [C/N]. They were not considered when we computed the final average value.

Globally, the effect of the extra mixing seems to be very limited in the metallicity range of open clusters: no clear and systematic correlation is found between the location of an RGB star in the log g-$T_{\rm eff}$ diagram and the [C/N] value. For some clusters this effect is appreciable, for instance NGC 6791, in which many stars above the bump have systematically lower [C/N] abundances, while in other clusters, for example NGC 6819, the stars above the bump show similar [C/N] as the clump stars. In addition, where a Li abundance is available, the correlation of Li depletion with lower [C/N] values is weak, as expected as a consequence of an extra-mixing episode. Only for the oldest clusters do we observe a [C/N] decrease for stars with A(Li)<0.4 dex caused by a more efficient dredge-up or thermohaline extra mixing (see e.g. Berkeley 31 and Berkeley 26). On the other hand, for younger clusters, A(Li)<0.4 dex is often coupled with higher values of [C/N] with respect to stars with A(Li)>0.4 dex (see e.g. NGC 6005, Rup 134, Pismis 18, and Trumpler 23). This can be related to the higher mass of their evolved stars in which thermohaline instability does not occur (Lagarde et al., 2019). Thus, the mechanisms of Li depletion can be uncorrelated to those that modify the C and N abundances. The latter can be related to rotation-induced mixing that has an effect on the internal chemical structure of main-sequence stars, observable during the RGB phase (see. e.g. Charbonnel & Lagarde, 2010). The anti-correlation in young clusters between A(Li) and [C/N] in Li-depleted stars cannot easily be explained by the current models and deserves further investigation. It might be associated with the Li abundance in the main sequence and is inherited during the following evolutionary phases.

4.3. AGE-[C/N] RELATIONSHIP USING OPEN CLUSTERS

In Table 4.4 we present the results of our analysis: the mean [C/N] abundance ratio of the member giant stars (with selection criteria described in the previous sections) and the number of stars for each cluster in the GES and APOGEE samples. The uncertainties in Table 4.4 are the formal errors on the weighted mean, and within brackets, we list the standard deviation σ. They take the uncertainties on C and N abundances into account. Using the solar values from Grevesse et al. (2007), we computed the average [C/N] ratio in each cluster in the GES sample. For APOGEE clusters the solar-scaled abundance ratios are already given in their database. Solar abundances in the APOGEE survey are adopted from Asplund (2005), which is consistent, for most elements, with those in Grevesse et al. (2007), including C and N.

For three clusters of the GES sample, Trumpler 20, NGC 6705, and NGC 4815, we used the literature [C/N] that is estimated only for post-FDU stars from Tautvaišienė et al. (2015) based on GES results (C and N abundances are not re-derived in the next data releases, therefore they are not present in GES IDR4 and IDR5, which we used in this Chapter).

Two clusters are in common between the two surveys, M67 and NGC 6705. They can also be used to cross-calibrate the [C/N] abundances in the two surveys, together with a few other stars in common that mainly are benchmark stars. In M67, there are three stars in common between GES and APOGEE with [C/N] abundances. The average post-FDU abundance in M67, using APOGEE DR14, is [C/N]=−0.57±0.01, while the GES results give [C/N]=−0.37±0.07. The C and N abundances of stars in M67 along the evolutionary

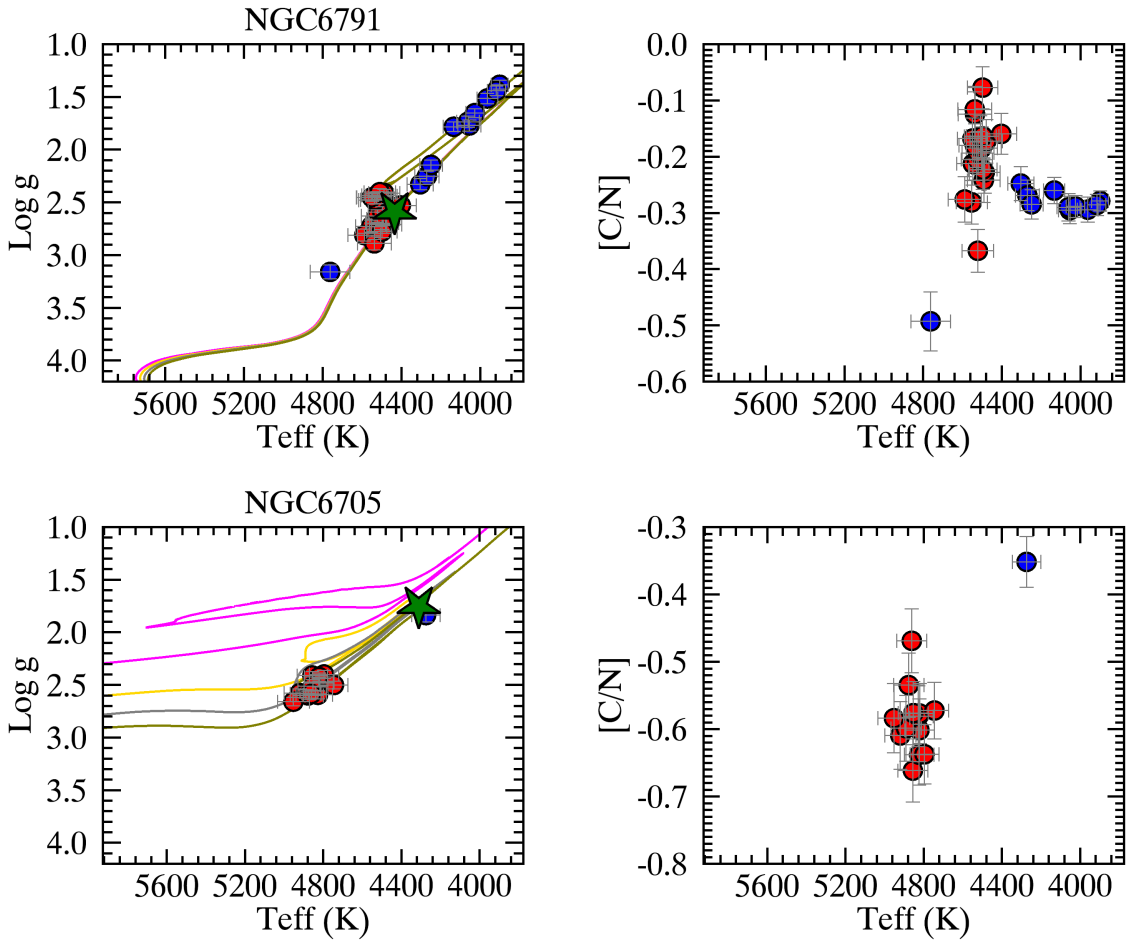

Fig. 4.4: APOGEE clusters NGC 6791 and NGC 6705: log g-$T_{\rm eff}$ diagrams with PISA isochrones 7.3, 7.6, 7.9, 8.2 Gyr for NGC 67091 and 0.1, 0.2, 0.3, 0.4 Gyr for NGC 6705 (left panels). [C/N] abundance vs. $T_{\rm eff}$ are shown in the right panels. Symbols and colours are the same as in Fig. 4.3.

sequence have been studied in detail by Bertelli Motta et al. (2017) using APOGEE DR12. Their post-FDU stars have an average [C/N]= −0.46±0.03, which is in good agreement with the expectation of theoretical models for stars with a mass and metallicity of the evolved stars of M67 (see Fig. 9 of Salaris et al., 2015). The results for M67 in APOGEE DR14 are slightly higher because of an offset in the [C/N] abundances from APOGEE DR12 to the latest APOGEE DR14 release. In Fig. 4.5 we compare [C/N] in three stars in common between APOGEE (DR12 and DR14) and GES. The [C/N] values of APOGEE DR14 are systematically lower than those in DR12. The values of GES and APOGEE DR12 are in better agreement (close to the one-to-one relationship). We note that Souto et al. (2019) have recently reanalysed 83 APOGEE DR14 spectra of stars in M67. The analysis performed in this paper is more accurate than the standard analysis (K. Cunha, S. Hasselquist, private communication). Five stars are in common between GES and the sample of Souto et al. (2019), two of them with C and N abundances. For these stars the agreement in [C/N] is within 0.01 dex. We therefore used the reanalysis of Souto et al. (2019) to compute the mean [C/N] of giant stars after the FDU in M67, which is [C/N]=−0.50±0.09. In the following analysis, we adopt for M67 an average between the GES and the results of Souto et al. (2019). The three stars of M67 in GES have A(Li)<0.4 dex, but their [C/N] is consistent with the other stars in APOGEE

Open Clusters	[C/N] (dex)	# member stars	$P^{mean}_{memb.}$
GES			
Berkeley 31	-0.32 ± 0.12	1	0.87
Berkeley 36	-0.30 ± 0.26	1	0.89
Berkeley 44	-0.38 ± 0.12	2	1.00
Berkeley 81	-0.64 ± 0.04 (0.07)	11	0.99
Melotte71	-0.65 ± 0.09	2	
NGC 2243	-0.51 ± 0.05 (0.08)	7	1.00
NGC 6005	-0.64 ± 0.04 (0.05)	9	0.97
NGC 4815[a]	-0.70 ± 0.11 (0.11)	5	
NGC 6067	-0.87 ± 0.04 (0.08)	9	0.99
NGC 6259	-0.84 ± 0.04 (0.04)	12	0.99
NGC 6802	-0.67 ± 0.04 (0.08)	7	1.00
Rup134	-0.63 ± 0.05 (0.06)	16	0.98
Pismis18	-0.74 ± 0.05 (0.03)	5	0.99
Trumpler23	-0.68 ± 0.04 (0.04)	9	1.00
Trumpler20[a]	-0.60 ± 0.12 (0.12)	42	
APOGEE			
Berkeley 17	-0.24 ± 0.02 (0.06)	7	
Berkeley 53	-0.52 ± 0.03 (0.05)	4	
Berkeley 66	-0.36 ± 0.03 (0.08)	4	
Berkeley 71	-0.66 ± 0.04 (0.18)	7	
FSR0494	-0.60 ± 0.04 (0.09)	5	
IC166	-0.69 ± 0.02 (0.20)	15	
King 5	-0.57 ± 0.03 (0.01)	5	
King 7	-0.53 ± 0.03 (0.04)	3	
NGC 1193	-0.44 ± 0.04 (0.09)	3	
NGC 1245	-0.64 ± 0.02 (0.11)	23	
NGC 1798	-0.44 ± 0.02 (0.06)	8	
NGC 188	-0.32 ± 0.01 (0.04)	10	
NGC 2158	-0.41 ± 0.02 (0.13)	18	
NGC 2420	-0.40 ± 0.02 (0.07)	11	
NGC 6791	-0.20 ± 0.01 (0.06)	19	
NGC 6811	-0.68 ± 0.03 (0.01)	4	
NGC 6819	-0.49 ± 0.01 (0.03)	14	
NGC 6866	-0.69 ± 0.03 (0.06)	6	
Teutsch 51	-0.58 ± 0.06 (0.04)	4	
Trumpler 5	-0.37 ± 0.02 (0.04)	9	
NGC 7789	-0.52 ± 0.01 (0.03)	17	
GES and APOGEE			
M67-GES	-0.37 ± 0.07 (0.06)	3	
M67-APOGEE DR14	-0.57 ± 0.01 (0.07)	23	
M67-APOGEE DR14[b]	-0.50 ± 0.09	21	
M67-adopted (DR14[b]-GES)	-0.43 ± 0.11	–	
NGC 6705-GES[a]	-0.69 ± 0.09	27	
NGC 6705-APOGEE DR14	-0.60 ± 0.01 (0.03)	12	
NGC 6705-adopted	-0.64 ± 0.09	–	

Table 4.4: Mean post-FDU [C/N] of the open clusters in the GES and APOGEE samples. The values were derived here, with the exception of *a*, which is taken from Tautvaišienė et al. (2015), and *b*, which we adopted from Souto et al. (2019). $P^{mean}_{memb.}$ is the membership probability.

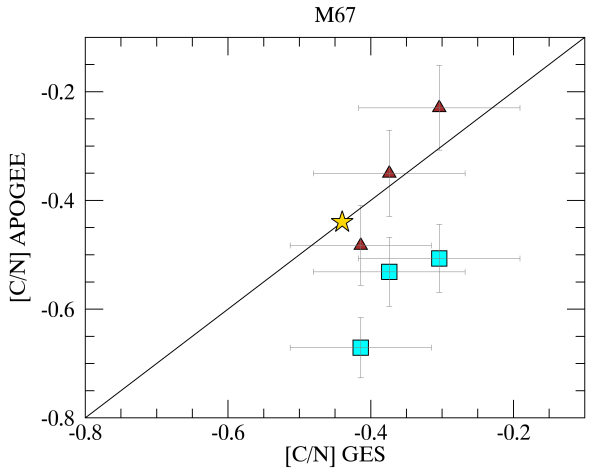

Fig. 4.5: Stars in common between GES and APOGEE (DR12 is shown by brown triangles and DR14 by cyan squares) in M67. The continuous line is the one-to-one relation. The yellow star shows the theoretical location of the FDU in the models of Salaris et al. (2015) for the age and metallicity of M67.

and with the theoretical model of Salaris et al. (2015). For these reasons we include them in the analysis.

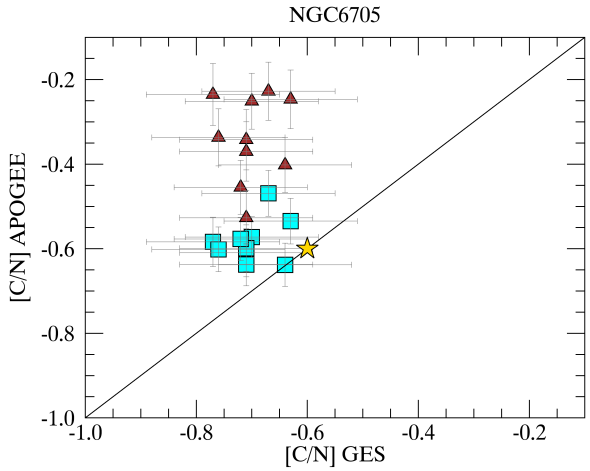

Fig. 4.6: Stars in common between GES and APOGEE (DR12 is shown by brown triangles and DR14 by cyan squares) in NGC 6705. The continuous line is the one-to-one relation. The yellow star shows the theoretical location of the FDU in the models of Salaris et al. (2015) for the age and metallicity of NGC 6705.

The other cluster in common between the two surveys is NGC 6705. In Fig. 4.6 we show the [C/N] abundances of NGC 6705 member stars in common between APOGEE (DR12 and DR14) and GES. As for M67, the [C/N] values of APOGEE DR14 are systematically lower than those in DR12. On the other hand, for this cluster the values of DR14 are in much better agreement with the GES results. In the following analysis, we adopt for NGC 6705 an average between the GES from Tautvaišienė et al. (2015) and the APOGEE DR14 results.

To identify possible systematic offsets or trends, we made a global cross-match between APOGEE DR12 and DR14 and GES. In Fig. 4.7 we show the [C/N] abundances of stars in common between GES and the two APOGEE releases. We note a general better agreement

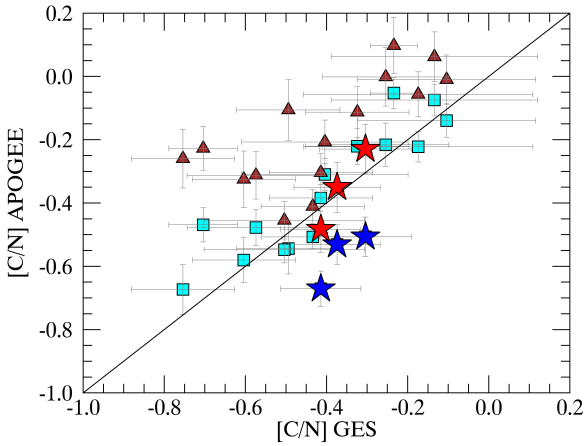

Fig. 4.7: Stars in common between GES and APOGEE (DR12 is shown by brown triangles and DR14 by cyan squares). The continuous line is the one-to-one relation. The red stars are the abundances in M67 for APOGEE DR12 and the blue stars show APOGEE DR14.

of APOGEE DR14 with GES, while the [C/N] abundances in APOGEE DR12 are usually offset of ~0.2 dex. In the plot of Fig. 4.7 we highlight the abundances of the three stars of M67. These stars are indeed outliers in APOGEE DR14, with a negative offset with respect to GES. For the other stars, there are no systematic offsets and the agreement between the two sets of results is good within the errors. This allows us to securely combine the GES and APOGEE DR14 samples of clusters (with the exception of the results of M67, for which we adopt the results of Souto et al., 2019).

In Fig. 4.8 we show the relationship between [C/N] in GES and APOGEE clusters and their logarithmic ages.

With the ages expressed in logarithmic form, the relationship is linear, with a Pearson coefficient of R=0.85, and it has the expression

$$\log[\mathrm{Age(yr)}] = 10.54(\pm0.06) + 2.61(\pm0.10)[\mathrm{C/N}]. \tag{4.1}$$

This relationship has an important implication because if we know the evolutionary stage of a giant star and we can measure its [C/N] abundance ratio, we can infer its age. However, some caveats need to be explicitly discussed here: *i)* the relationship in Eq.4.1 is empirical and it is built using open clusters whose metallicity range is $-0.4<$[Fe/H]$<+0.4$. Thus, its application outside this [Fe/H] range is not correct. *ii)* At low metallicity, the effect of non-canonical extra mixing in post-FDU stars increases and thus the measured [C/N] loses its dependence on stellar mass (and thus age). *iii)* Although the ages of giant stars are poorly constrained by isochrone fitting, and thus their age estimate through Eq. 4.1 is a step forwards, the uncertainties on [C/N] and ages are still high, as we discuss in the next paragraphs.

4.3.1. ERROR ESTIMATE

It is known that the measurements of stellar ages are usually affected by large uncertainties. However, accurate knowledge of stellar ages is a fundamental constraint for the scenarios of

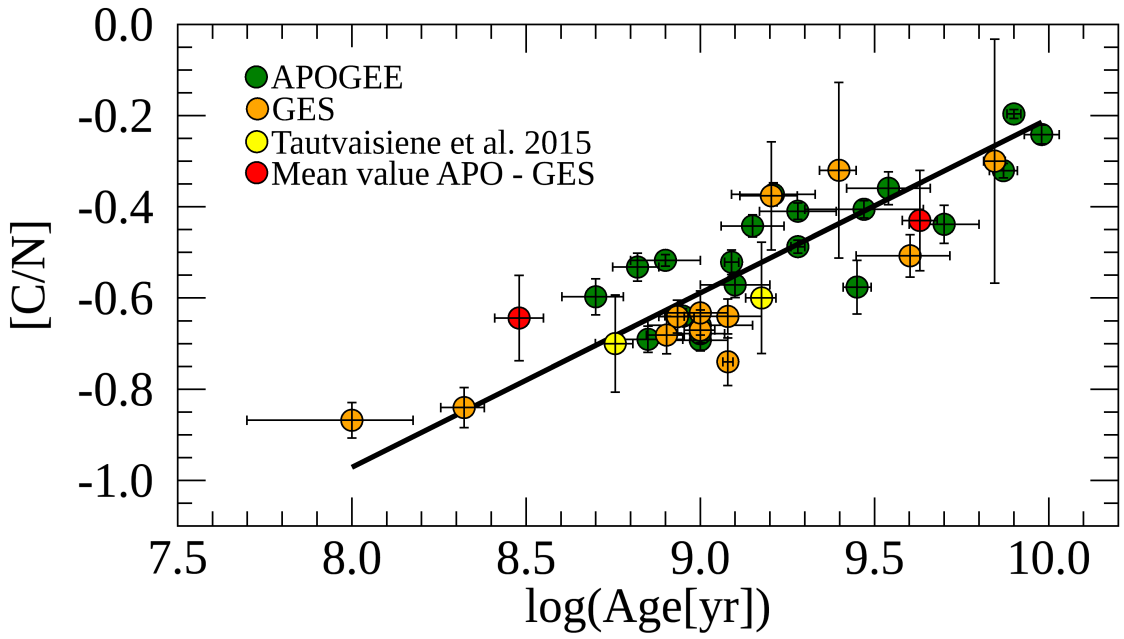

Fig. 4.8: Average [C/N] ratios of cluster member stars with log g cut as a function of log(Age[yr]) for the GES (orange circles) and the APOGEE (green circles) surveys. The yellow circles represent the GES literature results by Tautvaišienė et al. (2015). The red circles represent the mean value [C/N] for NGC 6705 and M67. The straight line is the linear weighted least-squares fit of the data.

the formation and evolution of the different components of our Galaxy. Asteroseismology data from CoRoT and Kepler have improved our knowledge of stellar ages, but they are limited to still small samples of stars. In this framework, chemical clocks such as [C/N], but also [Y/Mg] and [Y/Al] (Tucci Maia et al., 2016; Spina et al., 2016; Feltzing et al., 2017; Spina et al., 2018b; Delgado Mena et al., 2019), might be important auxiliary tools because they can be obtained for large numbers of stars. However, it is important to have a clear idea of the uncertainties related to the use of abundance ratios to derive the age of a star.

From the GES results, the typical uncertainties on the C and N abundances are 0.05 dex and 0.065 dex, respectively, with typical uncertainties on the abundance ratio [C/N] of ~0.10 dex. They affect the uncertainties on the logarithmic ages, giving a mean value of about ~0.26 dex on the logarithm of the age. These uncertainties translate into ~55-60% for the linear ages. For the APOGEE results, the typical uncertainties on the C and N abundances are ~0.04 dex for both elements, with a typical uncertainty on the abundance ratio [C/N] of ~0.06 dex. As for GES, this implies a mean uncertainty on the logarithm of the age of ~0.17 dex and of ~40-45% for the linear ages. Typical uncertainties are listed in Table 4.5.

However, another important part in the error budget is the uncertainty in the parameters of the fit of the linear relationship of Eq. 4.1. Combining both GES and APOGEE sample, we lower the uncertainties on the slope and on the intercept of the linear relationship. At the moment, the uncertainties on the parameters of the fit are of the order of ~0.06 and ~0.10 on the intercept and slope, respectively. We expect to have a more accurate fit of the relationship at GES completion, when about 80 open clusters in GES IDR6 will be available to GES consortium for publications. At the moment, the age estimate with [C/N] abun-

log(Age[yr])	e(log(Age[yr]))	e(Age)%
GES		
8.0-8.5	0.24	55%
8.5-9.0	0.26	60%
9.0-9.5	0.26	60%
9.5-10.0	0.26	60%
APOGEE		
8.0-8.5	0.19	45%
8.5-9.0	0.19	45%
9.0-9.5	0.17	40%
9.5-10.0	0.17	40%

Table 4.5: Typical uncertainties on logarithmic and linear age in different ranges of logarithmic age.

dance can be considered as an additional tool to give an independent estimate of the age of field stars, in particular for giant stars, for which it is not appropriate to determine the age through isochrone fitting because isochrones of different ages are only little different.

4.3.2. COMPARISON WITH PREVIOUS RESULTS

A relationship between logarithmic age and [C/N] has been provided for the APOGEE DR12 catalogue: Martig et al. (2016) presented an empirical relationship between [C/N] and stellar masses (and thus stellar ages) based on the asteroseismic mass estimates from the APOKASC survey (a spectroscopic follow-up by APOGEE DR12 of stars with asteroseismology data from the Kepler Asteroseismic Science Consortium, Borucki et al., 2010). To compare this with our results, we cross-matched the APOKASC catalogue of Martig et al. (2016) with APOGEE DR14 and found the mean offset between the DR12 and DR14 abundances. We applied the offset to the DR12 APOKASC abundances to have them on the same scale as our clusters.

In Fig. 4.9 we plot the ages from Martig et al. (2016) and [C/N] measurements from DR12 (scaled to DR14), together with the results of our sample of the open clusters and the relation of Eq.4.1. We note that the two samples have different slopes at older ages, where the effect of extra mixing might be higher. In the oldest regime (log(Age[yr])>9.5), the ages obtained by Martig et al. (2016) are ~ 0.2 dex younger than ours at fixed [C/N]. Mackereth et al. (2017) showed that Martig et al. (2016) underestimated the ages in the older regime by up to a factor of 2 when compared with those based on asteroseismological masses. Therefore, our relationship provide ages that agree better with those of Mackereth et al. (2017). For the youngest ages, at a given [C/N] our ages correspond to [C/N] values close to the APOGEE DR12 rescaled ages, although with a large dispersion. This is true in the region where the two samples overlap, even if the APOKASC sample does not populate the youngest-age regions, where many star clusters are located, reaching a lower limit of about log(Age[yr])~8.8. The combination of ages from asteroseismology with those from isochrone fitting in young open clusters deserves to be investigated and to be fully exploited to obtain a calibration of the [C/N]-Age relation in a wider age range.

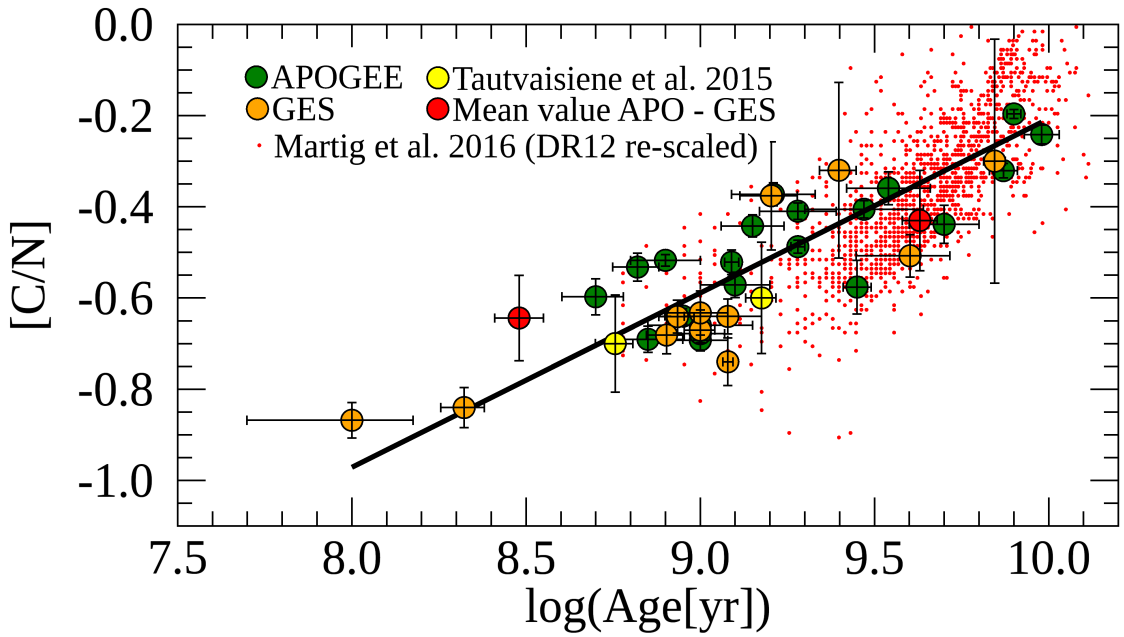

Fig. 4.9: Comparison between the field stars in APOKASC with [C/N] vs. age computed by Martig et al. (2016) (red dots) and those obtained here using open clusters in the APOGEE and GES surveys (symbols and colour codes are the same as in Fig. 4.8).

4.4. COMPARISON WITH THEORETICAL MODELS

Later phases of stellar evolution affect the abundances of C and N, and therefore the abundances of these elements do not trace the initial chemical composition of stars, but they are modified by stellar nucleosynthesis and by internal mixing. In this framework, it is of interest to compare our results with predictions of various theoretical models of stellar evolution, with the limits of such comparisons in mind, such as *i)* imperfect correspondence between the stellar models that are used for the isochrones that were adopted to derive the ages of open clusters and those adopted to predict surface [C/N] abundances, *ii)* possible offsets in [C/N] between models and observations, and *iii)* comparison of different types of stars in model and observations.

We compared our results with models in two different ways: a classical comparison with a set of standard stellar evolution models that have been computed for different metallicities (Salaris et al., 2015), and a more innovative approach that combines a stellar population synthesis model of the Galaxy with a complete grid of stellar evolution models (Lagarde et al., 2017).

In Fig. 4.10 we compare the observed [C/N] at the FDU versus age with theoretical predictions of Salaris et al. (2015). We recall that in our observations we selected giant stars beyond the FDU, and avoided stars after the RGB bump with measurable effects of extra mixing in their [C/N] abundances and/or that were Li-depleted. The models of Salaris et al. (2015) are computed with the BaSTI stellar library (Pietrinferni et al., 2004, 2006), and they include the effect of the overshooting. The theoretical curves give the [C/N] abundance after the FDU at a given stellar age. They are provided for different metallicities in the age

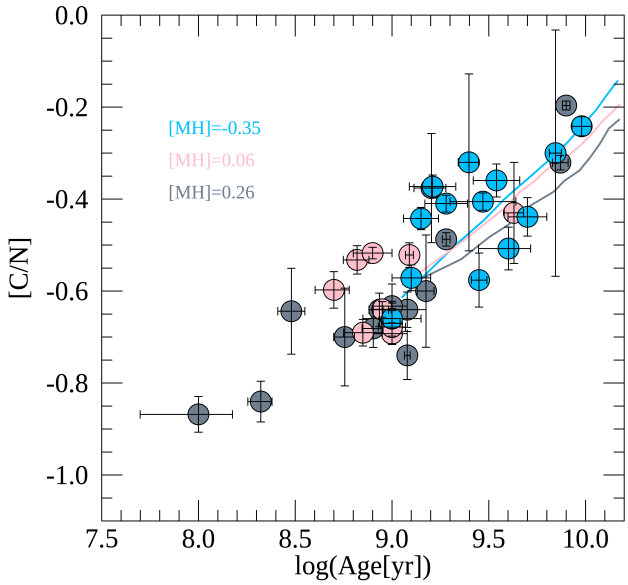

Fig. 4.10: Comparison of [C/N] and age between the theoretical models by Salaris et al. (2015) and the open clusters in GES and APOGEE surveys. The models are computed for different total metallicities [M/H]. Their colour codes are shown in the legend. The clusters are divided into three metallicity bins: [Fe/H]≤ -0.10 (light blue circles), $-0.1 \leq$ [Fe/H] $\leq +0.1$ (pink circles), and [Fe/H] $\geq +0.1$ (grey circles).

range 1-10 Gyr. We selected three curves that cover the metallicity range of our sample clusters.

The data of open clusters follow the general trend of the models, which confirms the predicted increase in [C/N] with age. In the age range where both observations and models are available, we have colour-coded them in the same way to facilitate the association of the observations with the corresponding curves. Model curve and observations agree in general within the uncertainties, but no trend with metallicity can be seen for the observations.

In Fig. 4.11 we compare our data with the results of the model of Lagarde et al. (2017) for three ranges of metallicities. The models of Lagarde et al. (2012) have been applied to an improved stellar population model of the Galaxy by Lagarde et al. (2017), providing global, chemical, and seismic properties of the thin-disc stellar population. The authors estimated the effect of the thermohaline mixing in thin-disc giants, which produce measurable effects on the [C/N] ratios of stars of different metallicities. They derived mean relations between [C/N] and age, which can be used to estimate ages for thin-disc RC giants as a function of their [Fe/H]. Because the open clusters are a thin-disc population and we mainly selected low RGB and RC stars in them, we can compare our results with the models of Lagarde et al. (2017). The data are in qualitative agreement with the model curves of Lagarde et al. (2017), which predict lower [C/N] values for the oldest stars. On the other hand, the open cluster data are in better agreement with the model curves of Salaris et al. (2015), whose models show an increasing [C/N] abundance with age that better follows the observed trend in the oldest clusters. Both models are computed for ages > 1 Gyr and for different metallicities (in the plot we show the models computed for the metallicity range of our sample of clusters).

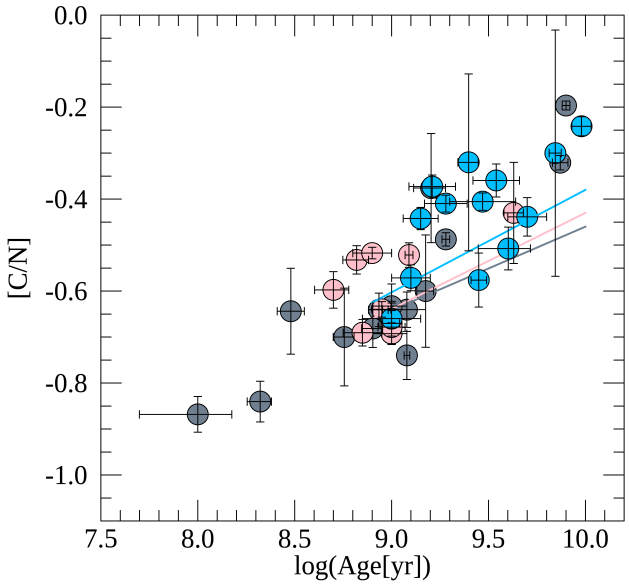

Fig. 4.11: Comparison between age and [C/N] of the thin-disc RC giant modelled by Lagarde et al. (2017) (continuous lines in light blue, pink, and grey) and the clusters in GES and APOGEE. The clusters and models are divided into three metallicity bins: [Fe/H]≤ −0.10 (light blue), −0.1 ≤ [Fe/H] ≤ +0.1 (pink), and [Fe/H] ≥ +0.1 (grey).

In the data, at a given age, we do not distinguish between trends of clusters with different metallicities. However, in the metallicity range spanned by the data, model predictions would differ by only ~0.1 dex considering the two metallicity extremes. This difference is comparable with typical [C/N] uncertainty.

4.5. APPLICATION TO FIELD STARS

As mentioned by Masseron & Gilmore (2015), passing from [C/N] measurements to assign masses and ages is tempting, but at the same time, it is risky because of several unknown or underestimated effects such as: the exact evolutionary stage of each of the observed stars, the metallicity dependence of C and N abundances after the FDU, and the effect of the extra mixing at different ages and metallicities (cf. Lagarde et al., 2017).

Keeping in mind these limits, we combined the sample of giant stars in the GES and APOGEE databases with C and N abundances aiming at identifying age trends in the disc populations. We selected giant stars have passed the FDU. To identify the maximum log g at which the FDU can appear, we considered our grid of isochrones (Pisa isochrones, see Dell'Omodarme et al., 2012) at different ages and metallicities. For each of them we derived the value of log g that corresponds to the point where [C/N] starts to decrease monotonically, that is, log g (FDU). For most of the field stars, which are usually older than the cluster stars, the mean value of the surface gravity at the FDU is log g ~3.4, with a slight dependence on metallicity (see Fig.4.2). We also excluded stars above the RGB bump (considering the most conservative case of stars of 2-3 Gyr, the age of the bulk of the stars in our sam-

ple, for which the RGB bump is located at log g ~2.4). Therefore, in the following analysis, we selected giant field stars with 2.4< log g <3.4. In addition, we used the line-of-sight distances derived by Bailer-Jones et al. (2018) with *Gaia* DR2. They used a distance prior that varies smoothly as a function of Galactic longitude and latitude according to a Galaxy model. We applied the relationship of Eq. 4.1 to giant field stars and took its limits of applicability into account: −0.4<[Fe/H]<+0.4 and 0.1 Gyr<age<10 Gyr, which is the range of metallicity and age of the clusters we studied here.
There are about 67,000 giant stars, of which ~ 270 belong to GES, in the our combined sample for which we can estimate the age. Based on the distance obtained with *Gaia*, we can locate them in the Galaxy. With our determination of stellar ages, we can investigate the age trends in the thin- and thick-disc populations.

In Fig. 4.12 we show [α/Fe] (computed with Ca, Si, and Mg in both surveys) versus [Fe/H] for the APOGEE and GES sample, colour-coded by their [C/N] abundance ratio. The dichotomy between the α-enhanced thick-disc stars and the lower [α/Fe] thin-disc stars is also evident in terms of their [C/N] (see Chapter 1 for more details on thin and thick discs). As has been observed by Masseron & Gilmore (2015) in their analysis of the APOGEE catalogue for DR12, we can see a clear gradient in [C/N], with the thin-disc stars having a lower [C/N]. At a given metallicity, [C/N] increases for higher [α/Fe] (see also Hasselquist et al., 2019). The gradient in [C/N] can then be translated into a gradient in ages, as shown in Fig. 4.13. In this plot there are two approximations: *i)* the relationship of Eq. 4.1 has been applied outside the range of metallicity −0.4<[Fe/H]<+0.4 and also to thick-disc stars, with different [α/Fe] and thus different initial [C/Fe]; *ii)* stars with derived age >10 Gyr are shown in red. Their ages are estimated by applying the relationship outside its range of applicability, and for this reason, they do not represent a correct age estimate and we can just say they are old. There is a clear division in age between thin- and thick-disc stars: the youngest stars are present in the thin disc, and their ages become greater with increasing α-element content. The thick-disc stars are in general older than the thin-disc stars. Most of them have only lower limit estimate of their ages, with age $\gtrsim$ 10 Gyr.

In Fig. 4.14 we present the histogram of the derived stellar ages in different bins of $|z|$ and R_{GC}, covering a radial region 3 < R_{GC} < 15 kpc and a vertical region $|z|$ < 2 kpc. We divided our sample into several radial and vertical regions, as was done by Hayden et al. (2015). In this plot and in the following Table 4.6 and Fig. 4.15, we apply the relationship of Eq. 4.1 in the metallicity range −0.4<[Fe/H]<+0.4 and do not include lower limit measurements. In Table 4.6 we show the median ages and σ in each bin. The bins close to the plane contain the youngest stars, but they also have a non-negligible tail of old stars. The stars located in the bins at intermediate height are older, and even more so, stars located at 1 kpc< $|z|$ <2 kpc. This is also appreciable from Table 4.6, which shows a systematically increasing age for stars that are located above the Galactic plane. In the bins that characterise the thin disc 0 kpc< $|z|$ <0.5 kpc, the youngest population is located in the inner bins, and the ages slightly increase towards the outskirts.

In Fig. 4.15 we show the [α/Fe] versus [Fe/H] plane divided into same bins as in Fig. 4.14. For lower z, the thin-disc population is prominent. It is characterised by a low-[α/Fe]. Conversely, for higher z, the population of thick-disc stars starts to increase. It is more prominent in the inner regions.

The bottom panels of Fig. 4.15 show the thin-disc population closer to the plane. In

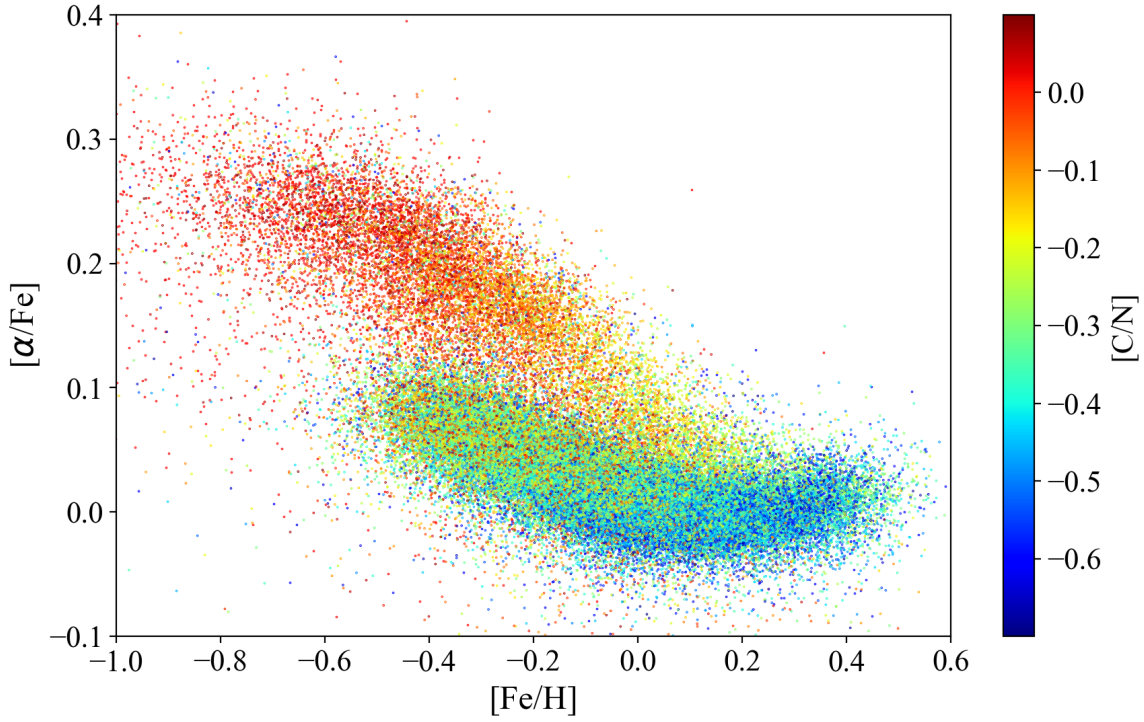

Fig. 4.12: [α/Fe] as a function of [Fe/H] for field stars in the APOGEE DR14 and GES samples. The stars are colour-coded by [C/N].

the 3 kpc <R_{GC}< 7 kpc ranges the populations is dominated by thin-disc metal-rich stars, where the stars with the highest metallicity are the youngest stars. The histograms of the age distribution in each bin in $|z|$ and R_{GC} in Fig. 4.14 and the respective medians and σ in Table 4.6 show that the population in 3 kpc <R_{GC}< 7 kpc at low z is mainly young. Therefore, the inner bin is dominated by young and metal-rich stars, with low [α/Fe]. In the outer regions 7 kpc <R_{GC}< 11 kpc, the thin disc includes a wider range of [Fe/H], from −0.4 to 0.4. Following our age estimate, the younger stars are located in the lower envelope of the distribution, at low [α/Fe]. There is a consistent number of old stars with both super- and sub-solar metallicity. In the outer regions at 11 kpc <R_{GC}< 15 kpc, the metal-rich stars start to disappear.

The central panels of Fig. 4.15 show the thin-disc population at intermediate height above the plane. In the innermost regions at 3 kpc<R_{GC}<7 kpc, the thin disc is poorly populated, unlike the region at 7 kpc<R_{GC}<11 kpc. This effect is due to the observational selection of the APOGEE survey, for which the observations are located in particular towards the outer regions at 7-11 kpc when compared with the inner regions at 3-7 kpc. The stars in these two panels do not reach the low [α/Fe] and the young ages of the corresponding panels at lower z. Their median ages are older than the medians at the same R_{GC}, but lower z (see Table 4.6). The outer regions contain fewer metal-rich stars, and they are younger on average, as their medians show when compared with those in the inner regions at intermediate z (see Table 4.6).

The top panels of Fig. 4.15 show the thin-disc population at a great height above the plane. Stars are almost absent from the innermost regions because of the sample selection

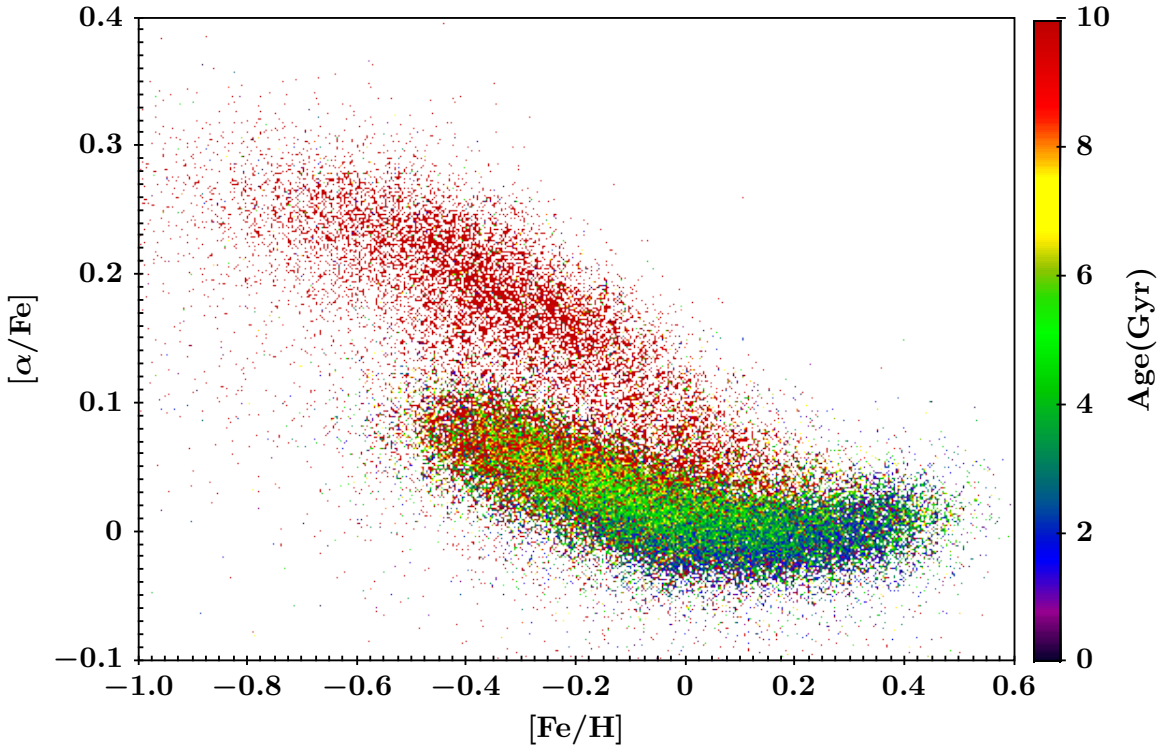

Fig. 4.13: [α/Fe] as a function of [Fe/H] for field stars in the APOGEE DR14 and GES samples. The stars are colour-coded by ages.

in the range of applicability of our relationship, based on which they would be older than 10 Gyr. From 7 to 11 kpc, there is a signature of thin-disc stars with a wide age range. Finally, in the outermost regions at 11-15 kpc only few young and intermediate-age thin disc stars are present.

4.6. SUMMARY AND CONCLUSIONS

This Chapter, based on the paper Casali et al. (2019), shows all results regarding to the study of the first family of chemical clocks listed in the Chapter 3: chemical abundance ratios related to the stellar evolution. The most representative of this category is the carbon-to-nitrogen ratio [C/N].

In particular, the [C/N] abundance ratio is a good age indicator for stars in the RGB evolutionary phase after the FDU. Using open clusters in the GES and APOGEE surveys, we calibrated the relationship between cluster age (from isochrone fitting of the whole cluster sequence) and [C/N] abundance ratio of stars that have passed the FDU. We selected RGB stars beyond the FDU to study the effects of extra-mixing processes in their [C/N] abundances. We compared the [C/N] measurements and ages of open clusters with the APOKASC sample by Martig et al. (2016) and the predictions of stellar evolutionary models by Salaris et al. (2015) and Lagarde et al. (2017). We found a good agreement. With the current accuracy of age and abundance measurements, however, we cannot confirm the variation in age-[C/N] relationship with metallicity in the [Fe/H] range that is traced by open clusters.

R_{GC} (kpc)	|z| (kpc)	Median age (Gyr)	σ
3 – 5	1 – 2	2.95	2.95
5 – 7	1 – 2	5.06	2.81
7 – 9	1 – 2	5.80	2.69
9 – 11	1 – 2	5.34	2.61
11 – 13	1 – 2	4.00	2.57
13 – 15	1 – 2	4.06	2.34
3 – 5	0.5 – 1	4.20	2.87
5 – 7	0.5 – 1	4.79	2.57
7 – 9	0.5 – 1	4.23	2.50
9 – 11	0.5 – 1	3.98	2.39
11 – 13	0.5 – 1	3.75	2.42
13 – 15	0.5 – 1	3.97	2.44
3 – 5	0 – 0.5	1.82	2.53
5 – 7	0 – 0.5	2.32	2.44
7 – 9	0 – 0.5	2.63	2.35
9 – 11	0 – 0.5	3.05	2.28
11 – 13	0 – 0.5	3.17	2.40
13 – 15	0 – 0.5	3.04	2.45

Table 4.6: Median and σ of the age for each bin in height on the plane z and Galactocentric distance R_{GC}.

We used our relationship to derive the ages of field stars in a combined GES and APOGEE sample. In the plane [α/Fe] versus [Fe/H], a clear dichotomy between the [C/N] abundances in the thin and thick disc was evident, as has previously been observed by Masseron & Gilmore (2015), and consequently stellar ages. We extrapolated our relation to estimate the ages for thin-disc stars and derived lower limit ages for the thick-disc stars. As expected, we find that stars belonging to the thin disc are on average younger than the stars in the thick disc. The typical age of the thin-disc stars decreases in the inner part of the disc at low z and towards the outskirts. The former indicates that the metal-rich stars in the inner disc represent the later phases of the Galactic evolution, while the latter is expected from an inside-out formation of the disc.

These immediate applications of the relationships between ages and [C/N] probe the power of chemical clocks to improve our knowledge of stellar ages. The next step will be to combine other chemical clocks, related to the Galactic evolution, for instance [Y/Mg], to give further constraints to the ages of stars in different evolutionary stages.

4.A. LOG g-T_{eff} DIAGRAMS

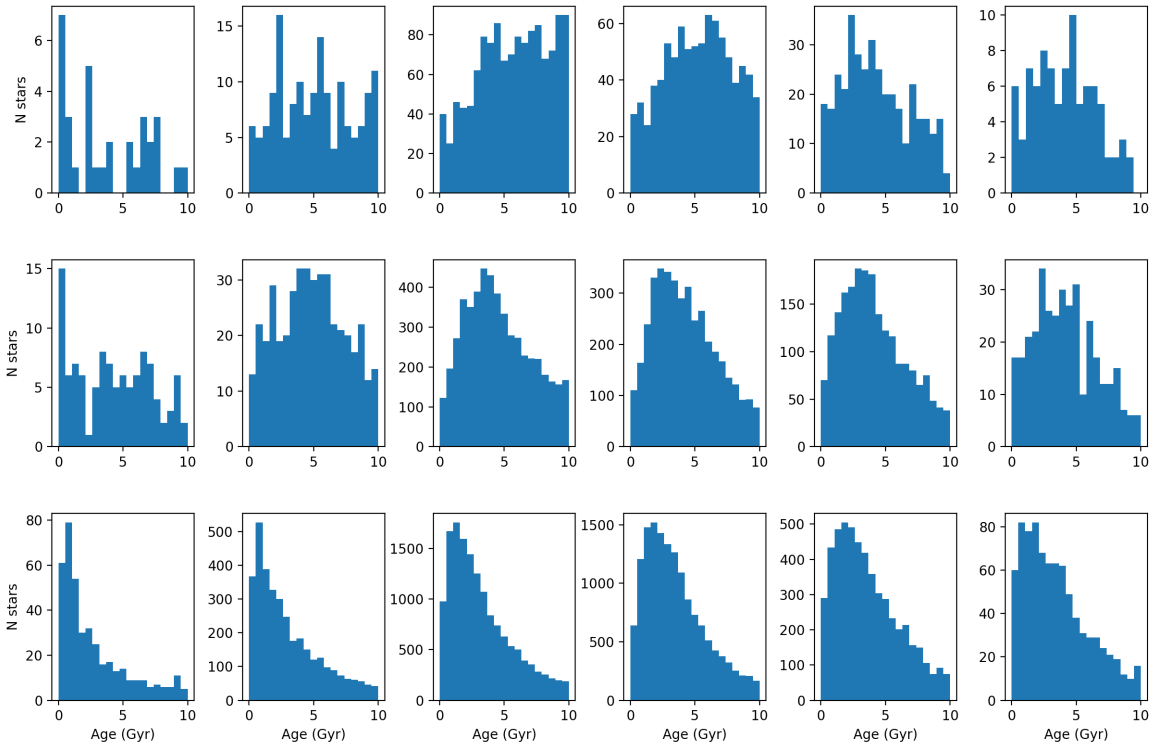

Fig. 4.14: Histograms of the age for each bin in height on the plane |z| and Galactocentric distance R_{GC}. Each panel corresponds to the respective panel in Fig. 4.15.

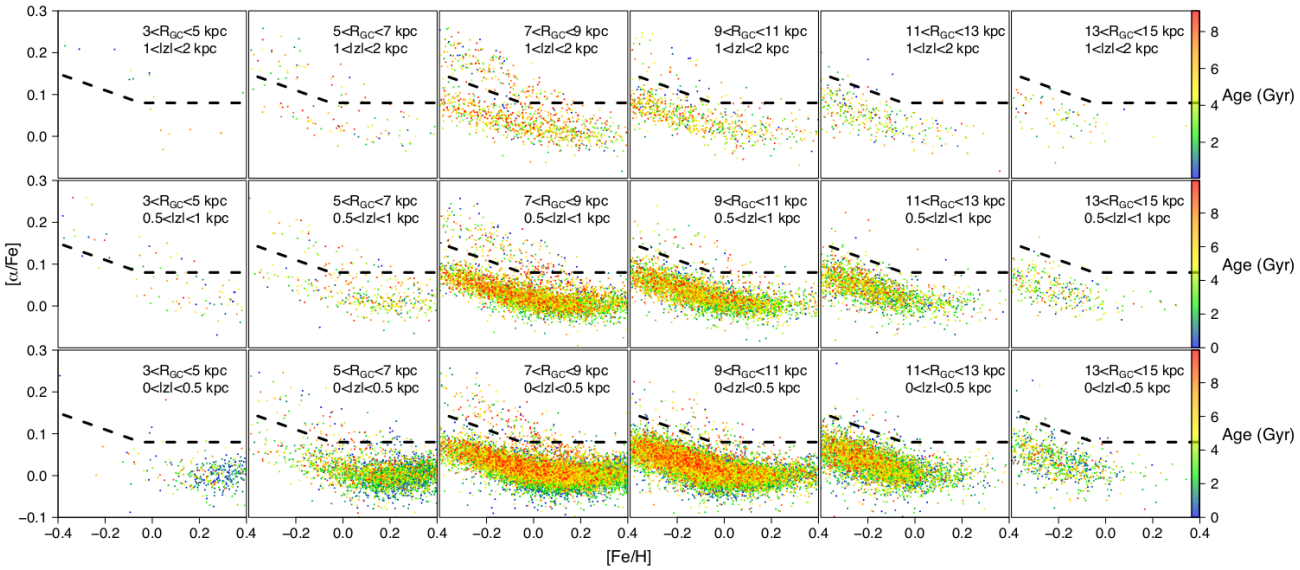

Fig. 4.15: [α/Fe] as a function of [Fe/H] for field stars in the APOGEE sample. The stars are colour-coded by ages. The dashed line shows the separation between thin- and thick-disc populations. Each plot contains stars selected by means of Galactocentric radius R_{GC} and height z, labelled in each figure.

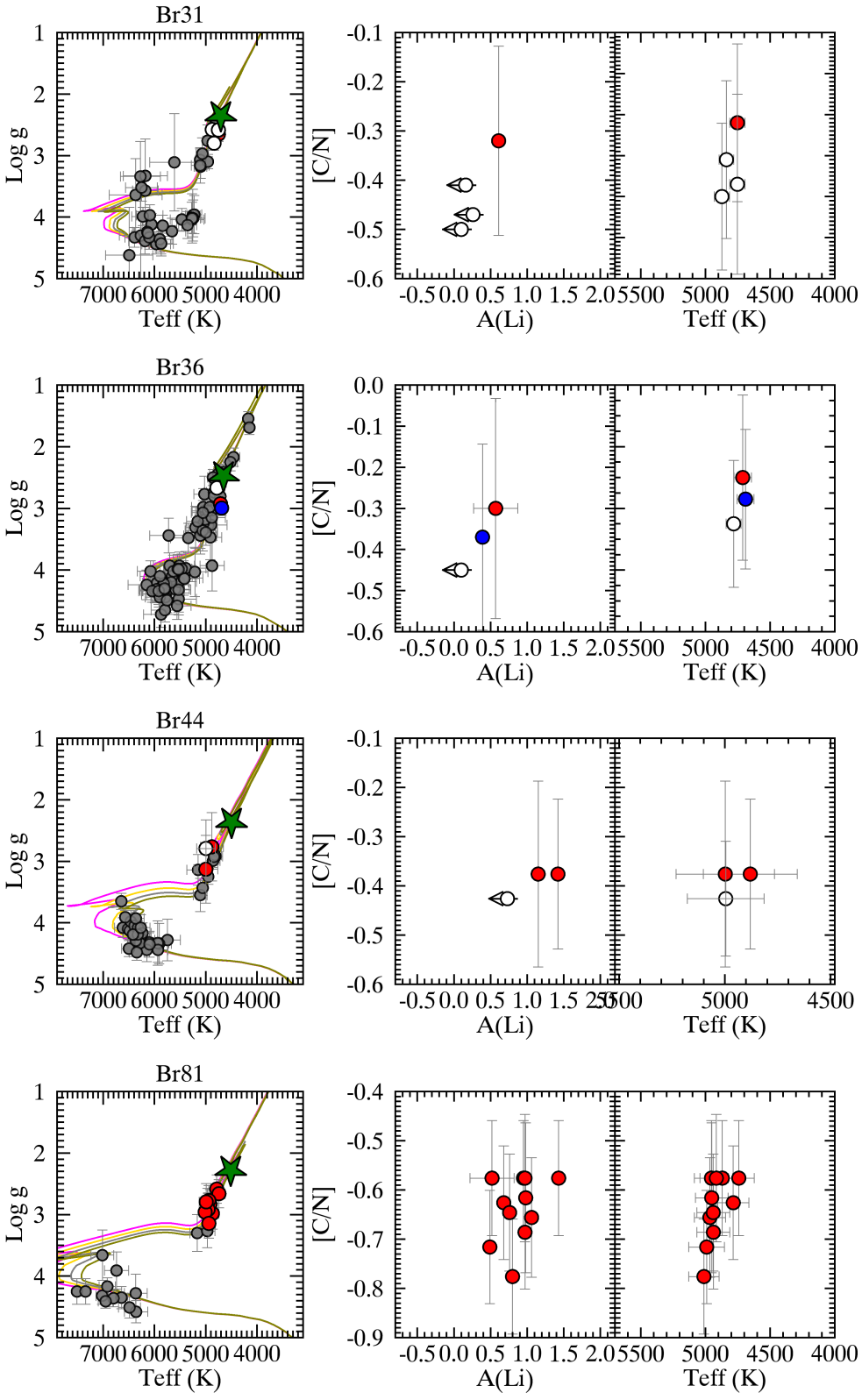

Fig. 4.16: log g-T_{eff} diagram with PISA isochrones (left panel) and member stars beyond the FDU, A(Li) vs. [C/N] (central panel), and [C/N] abundance vs. T_{eff} (right panel) of the GES clusters. Symbols and colours are the same as in Fig. 4.3. The isochrones are 2.1, 2.3, 2.5, and 2.7 Gyr, 6.0, 6.5, 7.0, and 7.5 Gyr, 1.1, 1.4, 1.7, and 2.0 Gyr, and 0.7, 0.8, 0.9, and 1.0 Gyr, respectively.

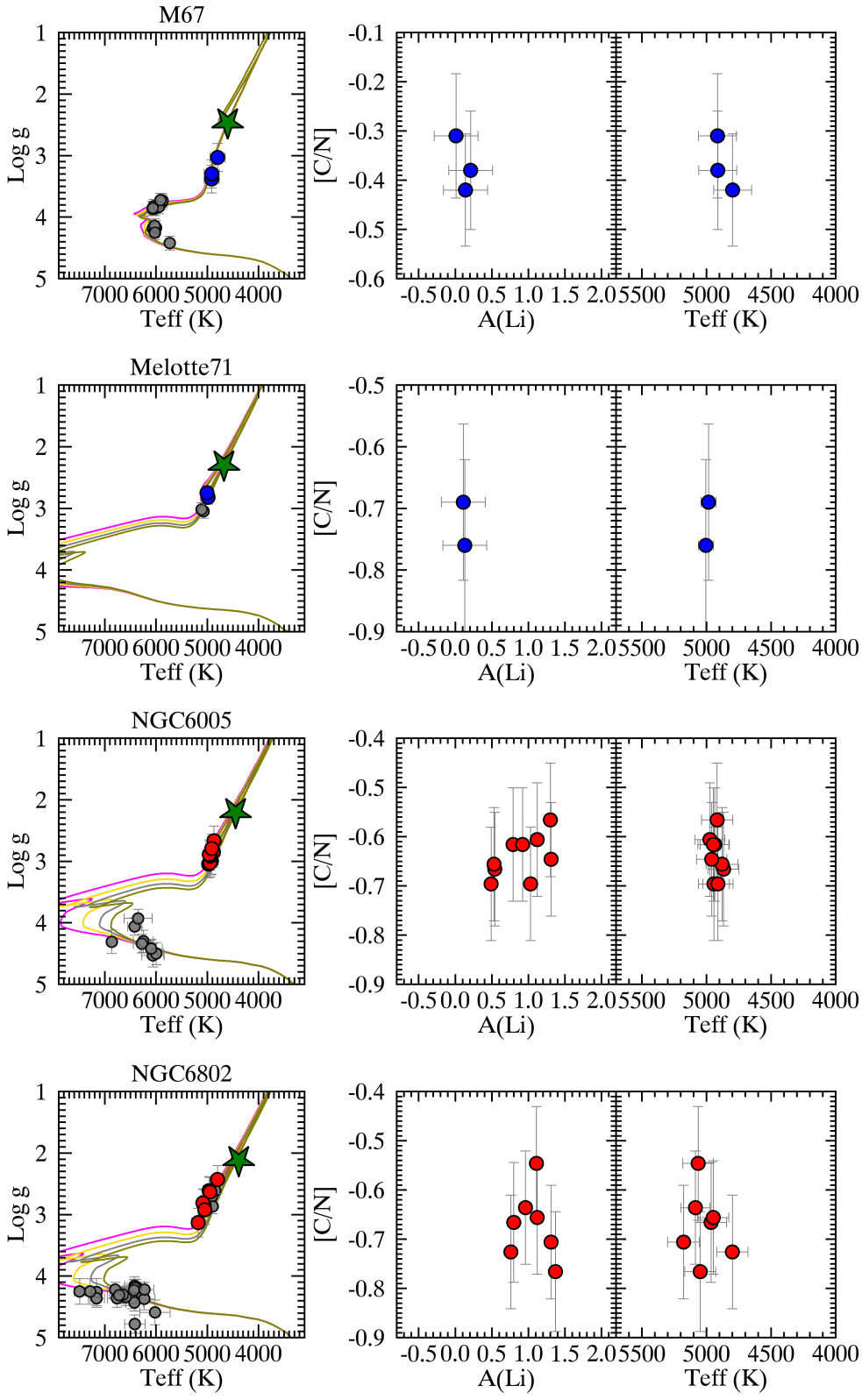

Fig. 4.17: log g-T_{eff} diagram with PISA isochrones (left panel) and member stars beyond the FDU, A(Li) vs. [C/N] (central panel), and [C/N] abundance vs. T_{eff} (right panel) of the GES clusters. Symbols and colours are the same as in Fig. 4.3. The isochrones are 3.7, 4.0, 4.3, and 4.5 Gyr, 0.7, 0.8, 0.9, and 1.0 Gyr, 0.8, 1.0, 1.2, and 1.4 Gyr, and 0.8, 1.0, 1.2, and 1.4 Gyr, respectively.

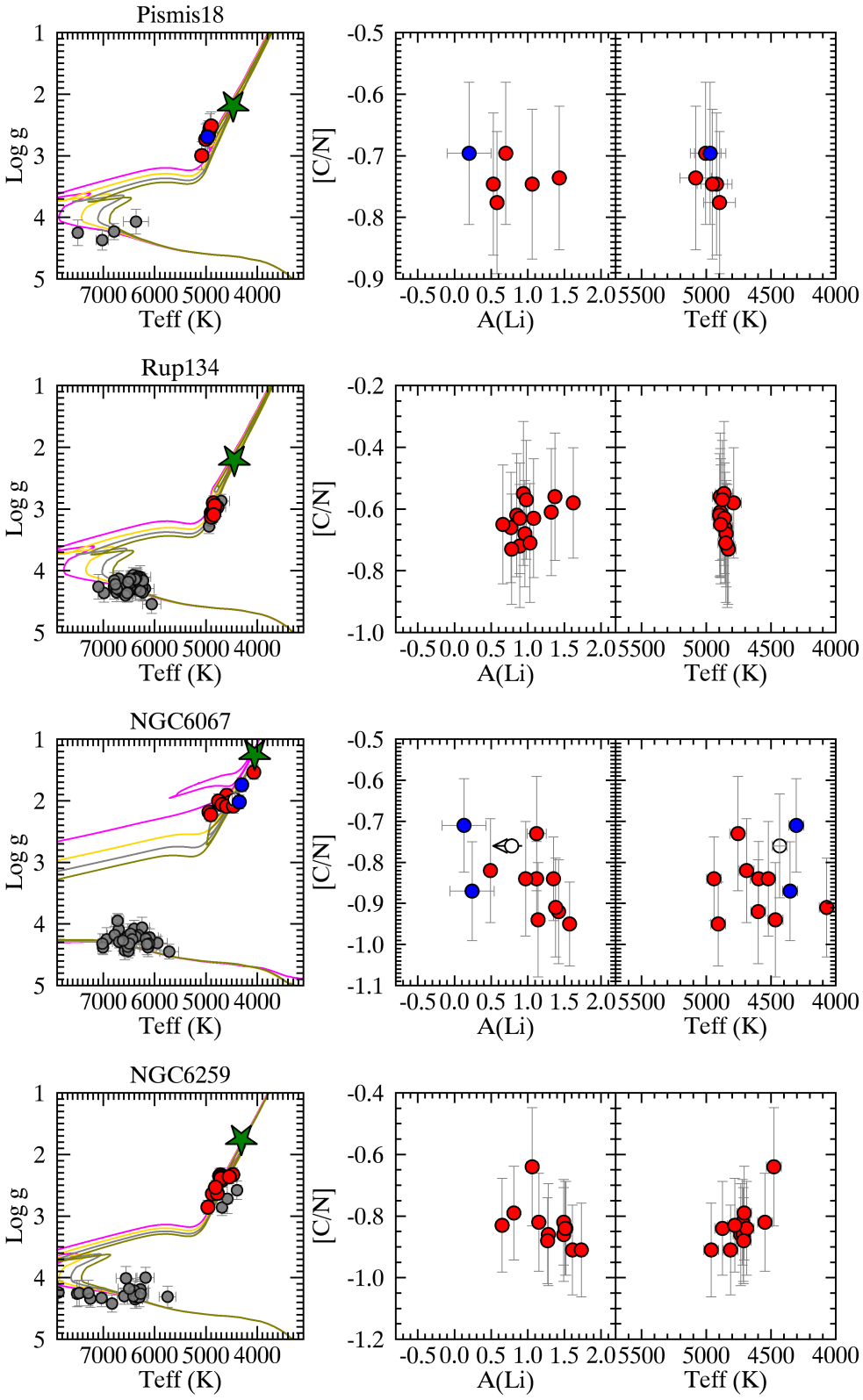

Fig. 4.18: log g-T_{eff} diagram with PISA isochrones (left panel) and member stars beyond the FDU, A(Li) vs. [C/N] (central panel), and [C/N] abundance vs. T_{eff} (right panel) of the GES clusters. Symbols and colours are the same as in Fig. 4.3. The isochrones are 0.8, 1.0, 1.2, and 1.4 Gyr for the first two clusters, and 0.05, 0.1, 0.2, and 0.3 Gyr, and 0.1, 0.2, 0.3, 0.4 Gyr.

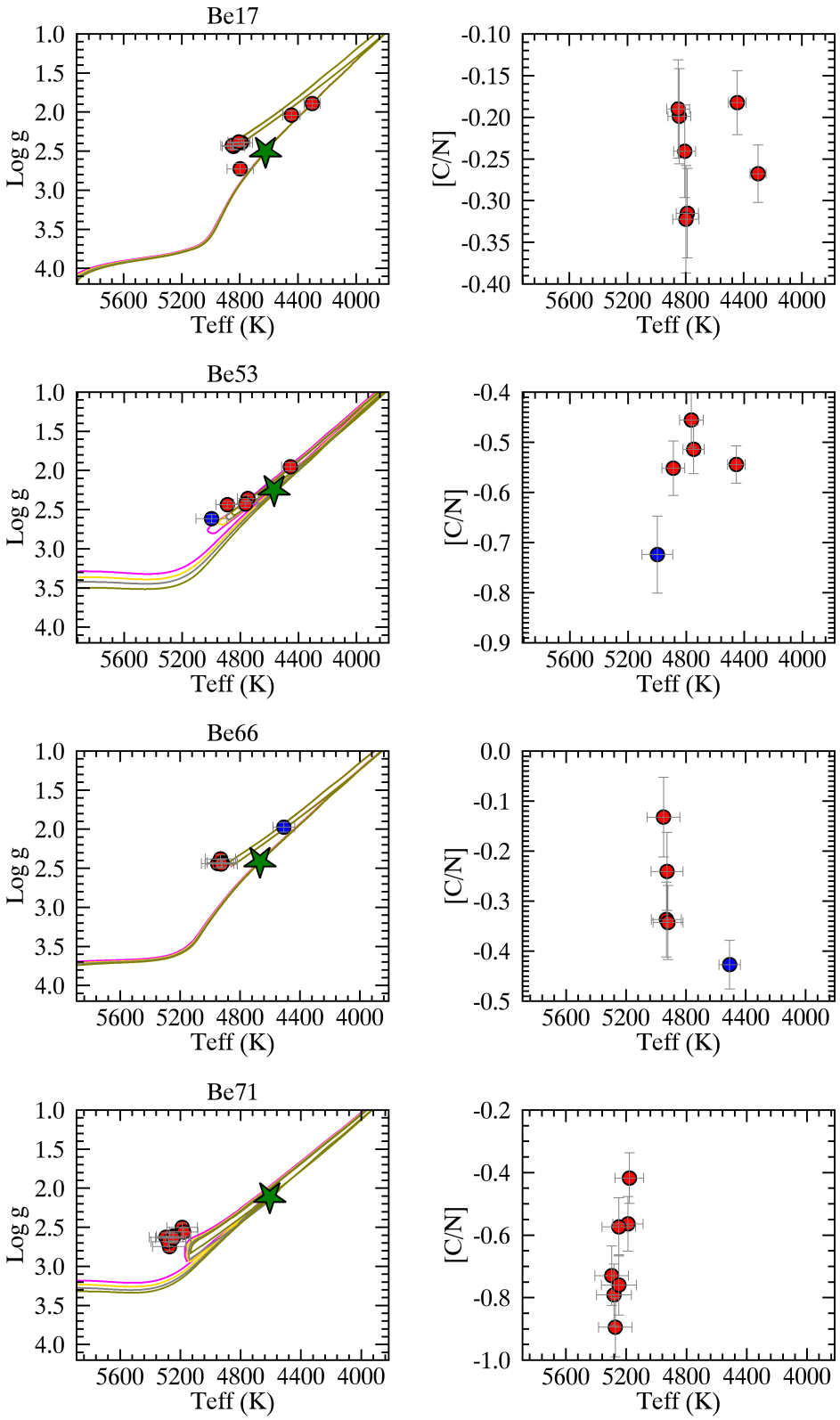

Fig. 4.19: log g-T_{eff} diagram with PISA isochrones (left panel) and [C/N] abundance vs. T_{eff} (right panel) of the APOGEE clusters. Symbols and colours are the same as in Fig. 4.4. The isochrones are 8.8, 9.1, 9.4, and 9.7 Gyr, 0.1, 1.2, 1.4, and 1.7 Gyr, 3.2, 3.4, 3.6, and 3.8 Gyr, and 0.8, 0.9, 1.0, and 1.1 Gyr, respectively.

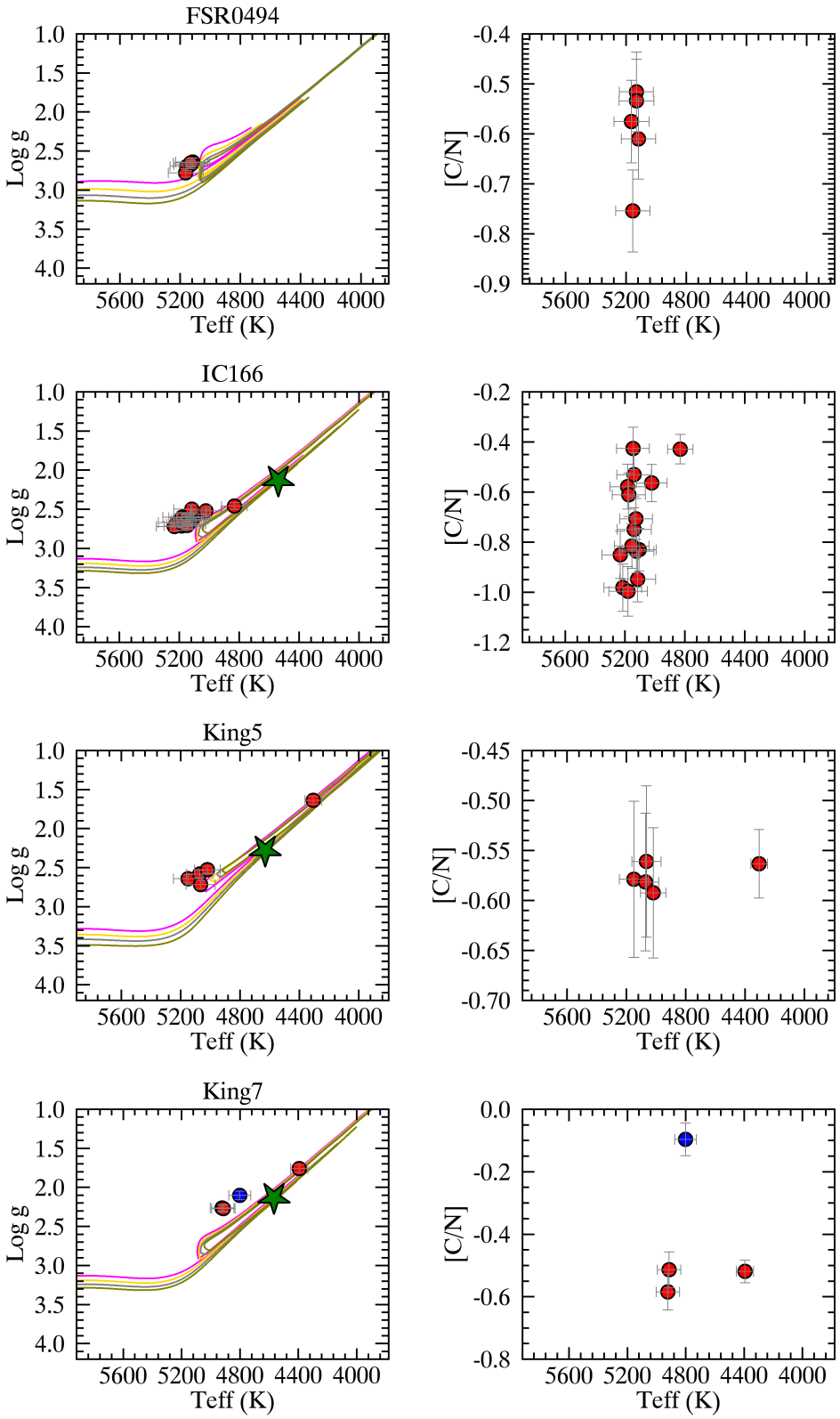

Fig. 4.20: log g-T_{eff} diagram with PISA isochrones (left panel) and [C/N] abundance vs. T_{eff} (right panel) of the APOGEE clusters. Symbols and colours are the same as in Fig. 4.4. The isochrones are 0.4, 0.5, 0.6, and 0.7 Gyr, 0.6, 0.8, 1.0, and 1.2 Gyr, 1.0, 1.2, 1.4, and 1.7 Gyr, and 0.4, 0.5, 0.6, and 0.7 Gyr, respectively.

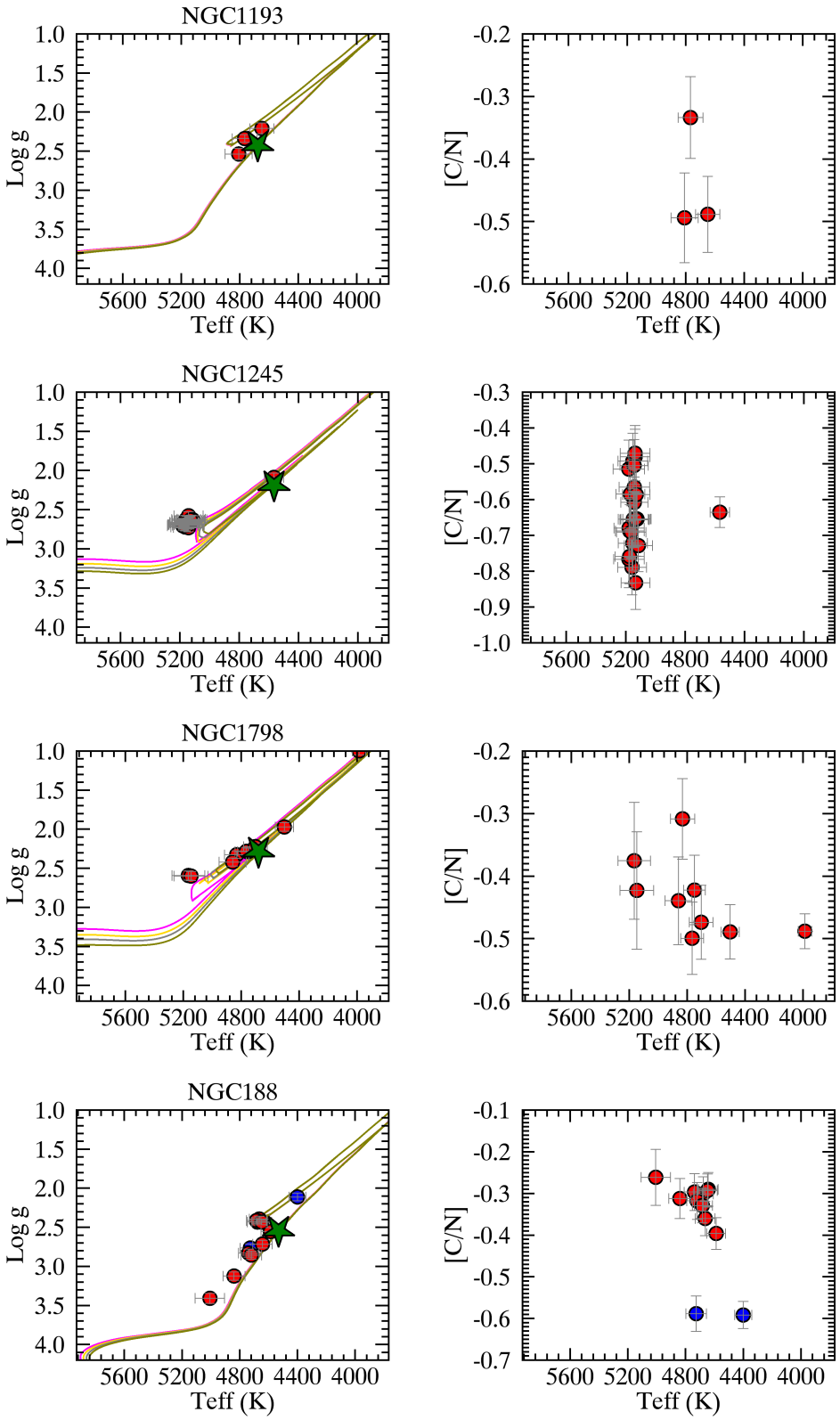

Fig. 4.21: log g-T_{eff} diagram with PISA isochrones (left panel) and [C/N] abundance vs. T_{eff} (right panel) of the APOGEE clusters. Symbols and colours are the same as in Fig. 4.4. The isochrones are 4.6, 4.8, 5.0, and 5.2 Gyr, 0.7, 0.8, 0.9, and 1.0 Gyr, 1.0, 1.2, 1.4, and 1.7 Gyr, and 7.3, 7.6, 7.9, and 8.2 Gyr, respectively.

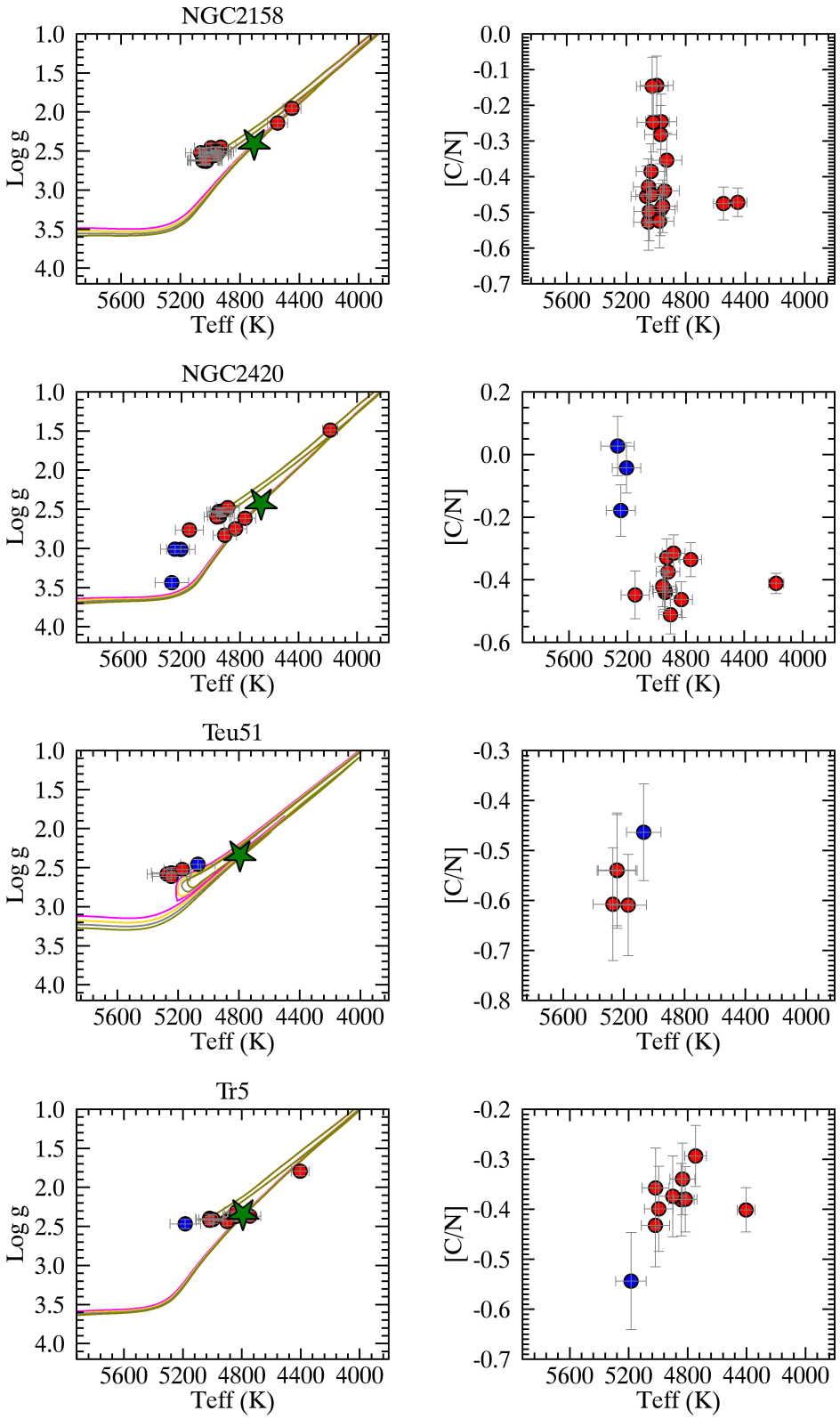

Fig. 4.22: log g-T_{eff} diagram with PISA isochrones (left panel) and [C/N] abundance vs. T_{eff} (right panel) of the APOGEE clusters. Symbols and colours are the same as in Fig. 4.4. The isochrones are 1.7, 1.9, 2.1, and 2.3 Gyr, 2.6, 2.8, 3.0, and 3.2 Gyr, 0.7, 0.8, 0.9, and 1.0 Gyr, and 2.6, 2.8, 3.0, and 3.2 Gyr, respectively.

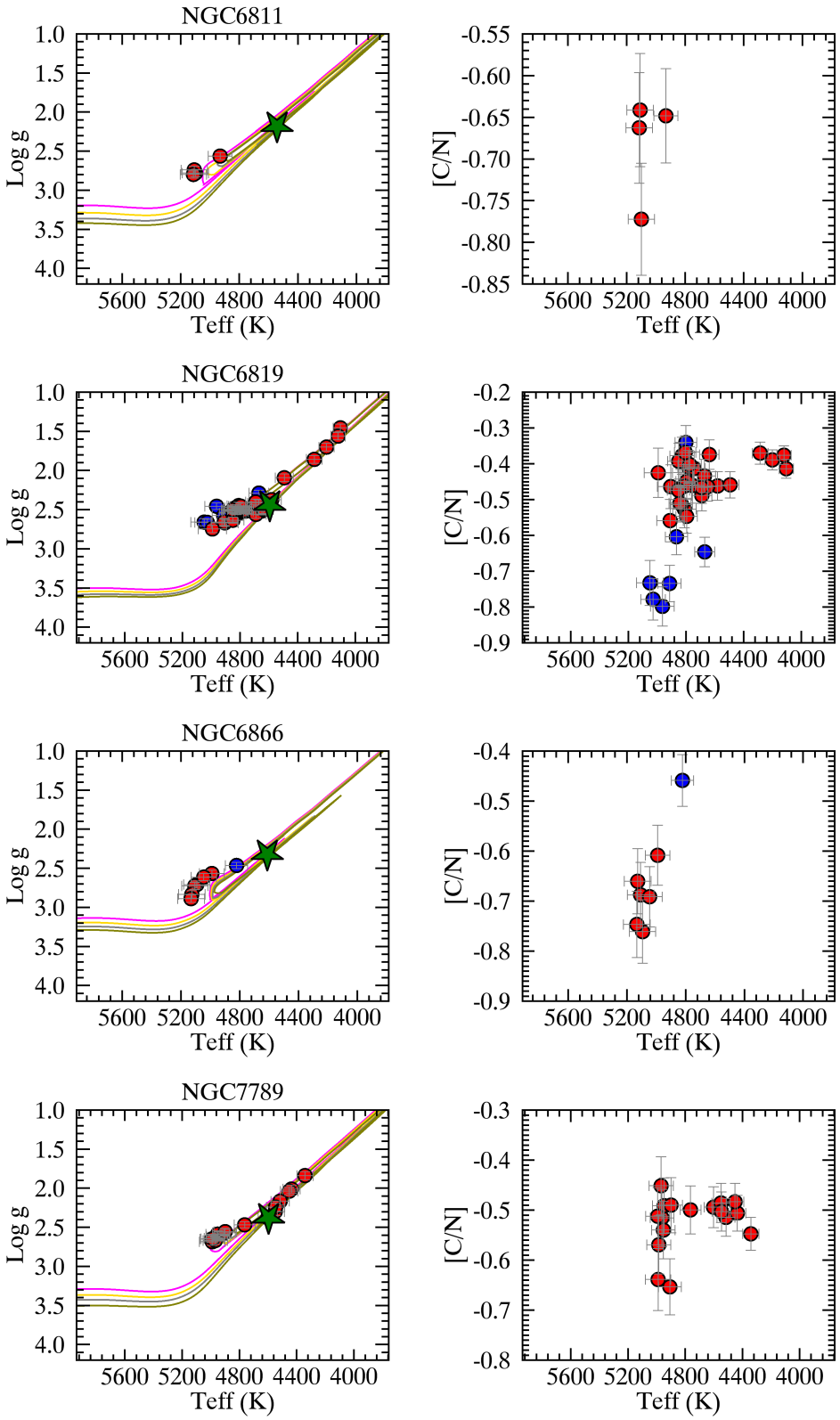

Fig. 4.23: log g-T_{eff} diagram with PISA isochrones (left panel) and [C/N] abundance vs. T_{eff} (right panel) of the APOGEE clusters. Symbols and colours are the same as in Fig. 4.4. The isochrones are 0.8, 1.0, 1.2, and 1.4 Gyr, 1.7, 1.9, 2.1, and 2.3 Gyr, 0.7, 0.8, 0.9, and 1.0 Gyr, and 1.0, 1.2, 1.4, and 1.7 Gyr, respectively.

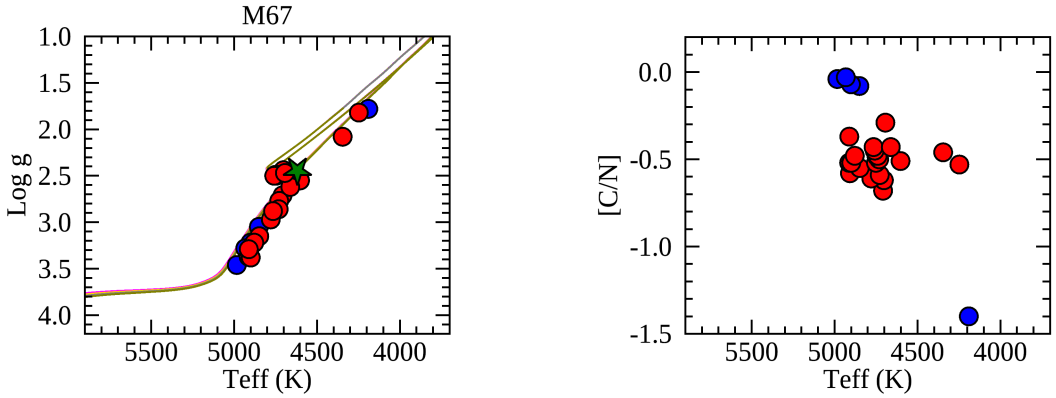

Fig. 4.24: log g-T_{eff} diagram with PISA isochrones (left panel) and [C/N] abundance vs. T_{eff} (right panel) of M67 by Souto et al. (2019). Symbols and colours are the same as in Fig. 4.4. The isochrones are 3.8, 4.0, 4.2, and 4.4 Gyr.

5

THE NON-UNIVERSALITY OF THE AGE-CHEMICAL CLOCKS-METALLICITY RELATIONS IN THE GALACTIC DISC

In this Chapter, I discuss relations between stellar ages and some abundance ratios based on pairs of elements, e.g. [Y/Mg], produced with different contributions of Type II (SNe II) and Type Ia (SNe Ia) supernovae or asymptotic giant branch (AGB) stars, and thus with different time scales. I have chosen the best combinations of elements that show the most marked growth with respect to age. The aim of the present work is to calibrate such relations between using a large sample of solar-type stars, studied through the differential spectral analysis of high-resolution spectra.

In this work, I investigate the variations of the relations among chemical clocks, stellar age and metallicity in the whole Galactic disc, studying the limits of their application.

The results presented in this Chapter are described in the published paper Casali et al. (2020b) on the scientific journal *Astronomy & Astrophysics*, volume 639, page A127.

5.1. SPECTRAL ANALYSIS

High-resolution stellar spectra are necessary to determine accurate stellar parameters and abundances, from which we can obtain both stellar ages and abundance ratios. However, standard spectroscopy can suffer from systematic errors, for instance in the model atmospheres and modelling of stellar spectra (Asplund, 2005), because of the usual assumptions that affect stars with different stellar parameters and metallicity in different ways, such as for example static and homogeneous one-dimensional models. To minimise the effects of systematic errors when studying solar-like stars, we can perform a differential analysis of those stars relative to the Sun (e.g. Meléndez et al., 2006; Meléndez & Ramírez, 2007). Their well-known stellar parameters are extremely important for the calibration of fundamental observable quantities and stellar ages.

Recent studies on solar twins have reached very high precision on stellar parameters and chemical abundances of the order of 0.01 dex in Fe and 0.5 Gyr in age (e.g. Meléndez et al., 2009, 2014a; Ramírez et al., 2009, 2014a,b; Liu et al., 2016; Spina et al., 2016, 2018b),

thanks to the differential analysis technique. This level of precision can be useful for revealing detailed trends in the abundance ratios and opens the door to a more accurate understanding of the Galactic chemical evolution, unveiling more details with respect to the large surveys.

In following subsections, we show the data sample and explain our differential spectral analysis based on equivalent width measurements, performed on high-resolution stellar spectra of solar-like stars.

All the details on stellar spectroscopy, differential analysis and tools used in this work are better explained in Appendix A.

5.1.1. DATA SAMPLE AND DATA REDUCTION

In our analysis we employ stellar spectra collected by the HARPS spectrograph (Mayor et al., 2003). The instrument is installed on the 3.6 m telescope at the La Silla Observatory (Chile) and delivers a resolving power, R, of 115,000 over a 383 - 690 nm wavelength range.

We obtain the reduced HARPS spectra from the ESO Archive. These are exposures of solar-like stars, with T_{eff} within ±200 K and log g within ±0.2 dex from the solar parameters. In addition, for the analysis we select only spectra with signal-to-noise ratios $S/N > 30$ px^{-1}, which have been acquired with a mean seeing of 0.98". This sample comprises 28,985 HARPS spectra of 560 stars. In Table 5.1, we list the dataset IDs, dates of observation, program IDs, seeing, exposure times, S/N and the object names of the single spectra employed in the analysis.

Name	Spectrum ID	Observation date	Program ID	Seeing	Exposure Time (s)	S/N
HD114853	HARPS.2017-03-12T04:22:10.194.fits	12/03/2017	198.C-0836(A)	0.70	900	271
HD114853	HARPS.2017-07-11T23:49:19.456.fits	11/07/2017	198.C-0836(A)	1.32	900	285
HD11505	HARPS.2011-09-27T06:37:22.718.fits	27/09/2011	183.C-0972(A)	0.96	900	279
HD11505	HARPS.2011-09-16T07:05:21.491.fits	16/09/2011	183.C-0972(A)	0.89	900	219
HD11505	HARPS.2007-10-14T04:10:42.910.fits	14/10/2007	072.C-0488(E)	0.93	900	281
HD115231	HARPS.2005-05-12T02:34:31.050.fits	12/05/2005	075.C-0332(A)	0.49	900	193
HD115231	HARPS.2005-05-13T02:40:27.841.fits	13/05/2005	075.C-0332(A)	0.99	900	171
...	...	...	...	...	...	...

Table 5.1: Information about the HARPS spectra of the sample of solar-like stars.The full version of this table is available online at the CDS.

All spectra are normalised using `IRAF`[1]'s `continuum` and are Doppler-shifted with `dopcor` using the stellar radial velocity value determined by the pipeline of the spectrograph. All the exposures of a single object are stacked into a single spectrum using a Python script that computes the medians of the pixels after having re-binned each spectrum to common wavelengths and applied a 3-σ clipping to the pixel values.

In addition to the solar-like stars, the sample includes a solar spectrum acquired with the HARPS spectrograph through observations of the asteroid Vesta to perform a differential analysis with respect to the Sun.

[1] http://ast.noao.edu/data/software

5.1.2. STELLAR PARAMETERS AND CHEMICAL ABUNDANCES

Equivalent widths[2] (EWs) of the atomic transitions of 25 elements (i.e. C, Na, Mg, Al, Si, S, Ca, Sc, Ti, V, Cr, Mn, Fe, Co, Ni, Cu, Zn, Sr, Y, Zr, Ba, Ce, Nd, Sm, and Eu) are measured with `Stellar diff`[3], described in Sect. A.7. We use the master list of atomic transitions of Meléndez et al. (2014a) that includes 98 lines of Fe I, 17 of Fe II, and 183 for the other elements, detectable in the HARPS spectral range (3780-6910 Å).

This code allows the user to interactively select one or more spectral windows for the continuum setting around each line of interest. Ideally, these windows coincide with regions devoid of other absorption lines. Once the continuum is set, we employ the same window settings to calculate continuum levels and fit the lines of interest with Gaussian profiles in every stacked spectrum. Therefore, the same assumption is taken in the choice of the local continuum around a single line of interest for all the spectra analysed here. This is expected to minimise the effects of an imperfect spectral normalisation or unresolved features in the continuum that can lead to larger errors in the differential abundances (Bedell et al., 2014).

After the EW measurements via `Stellar diff` for each spectra, we apply a line clipping, removing 19 lines of Fe I with uncertainties on EWs lying out of the 95% of their probability distribution for more than five stars. These are removed for all of stars from the master line list to calculate their atmospheric parameters ($T_{\rm eff}$, log g, [Fe/H], ξ). The EW measurements are processed by the *qoyllur-quipu* (q2) code[4] (Ramírez et al., 2014b, see also Sect. A.7) which determines the stellar parameters through a line-by-line differential analysis of the EWs of the iron lines relative to those measured in the solar spectrum. Specifically, the q2 code iteratively searches for the three equilibria (excitation, ionisation, and the trend between the iron abundances and the reduced EW log[EW/λ]). The iterations are executed with a series of steps starting from a set of initial parameters (i.e. the nominal solar parameters) and arriving at the final set of parameters that simultaneously fulfil the equilibria. We employ the Kurucz (ATLAS9) grid of model atmospheres (Castelli & Kurucz, 2004), the version of MOOG 2014 (Sneden, 1973), and we assume the following solar parameters as input to q2: $T_{\rm eff}$ = 5771 K, log g = 4.44 dex, [Fe/H] = 0.00 dex and ξ = 1.00 km s^{-1} (Ayres et al., 2006). The errors associated with the stellar parameters are evaluated by the code following the procedure described in Epstein et al. (2010) and Bensby et al. (2014). The typical precision for each parameter, which is the average of the distribution of the errors, is $\sigma(T_{\rm eff})$ = 10 K, σ(log g) = 0.03 dex, σ([Fe/H]) = 0.01 dex, and $\sigma(\xi)$ = 0.02 km s^{-1}.

This high precision is related to different factors: *(i)* the high S/N for a good continuum setting of each spectrum, with a typical value of 800 measured on the 65$^{\rm th}$ spectral order (we calculate the S/N for each combined spectrum as the sum in quadrature of the subexposures); *(ii)* the high spectral resolution of HARPS spectrograph (R~115,000) which allows blended lines to be resolved; *(iii)* the differential line-by-line spectroscopic analysis, which allows us to subtract the dependence on log gf and to reduce the systematic errors due to the atmospheric models, comparing stars very similar to the Sun; and *(iv)* the negligible contribution from telluric lines, since the spectra are the median of several exposures, where the typical number is 50.

[2] EW is the width of a rectangle having height equal to that of continuum emission and area equal to the area in the spectral line.

[3] `Stellar diff` is a Python code publicly available at `https://github.com/andycasey/stellardiff`.

[4] The q2 code is a free Python package, available online at `https://github.com/astroChasqui/q2`.

Once the stellar parameters and the relative uncertainties are determined for each star, q2 employs the appropriate atmospheric model for the calculation of the chemical abundances. All the elemental abundances are scaled relative to the values obtained for the Sun on a line-by-line basis. In addition, through the `blends` driver in the MOOG code and adopting the line list from the Kurucz database, q2 is able to take into account the hyperfine splitting effects in the abundance calculations of Y, Ba, and Eu (we assumed the HFS line list adopted by Meléndez et al., 2014a). Although this is correct in principle, it does leave the analysis open to some possible errors. Ideally, the lines should be fully modelled and the observed line shape compared with the modelled one (see e.g. Bensby et al., 2005; Feltzing et al., 2007). However, the analysis presented here is robust enough for our purposes, because we deal with stars that have very similar stellar parameters (T_{eff} and log g close to solar ones). This means that any systematic error should cancel to first order in the analysis. Finally, the q2 code determines the error budget associated with the abundances [X/H] by summing in quadrature the observational error due to the line-to-line scatter from the EW measurements (standard error), and the errors in the atmospheric parameters. When only one line is detected, as is the case for Sr and Eu, the observational error is estimated through the uncertainty on the EW measured by `Stellar diff`. The final stellar parameters and chemical abundances are listed in Tables 5.2 and 5.3, respectively.

id	RA (J2000)	DEC	T_{eff} (K)	logg (dex)	[Fe/H] (dex)	ξ (km s^{-1})	Age (Gyr)
HD220507	23:24:42.12	−52:42:06.76	5689±3	4.26±0.01	0.019±0.003	1.02±0.01	10.7±0.6
HD207700	21:54:45.20	−73:26:18.55	5671±3	4.28±0.01	0.052±0.003	1.00±0.01	10.3±0.5
HIP10303	02:12:46.64	−02:23:46.79	5710±3	4.39± 0.01	0.096±0.002	0.93±0.01	6.5±0.6
HD115231	13:15:36.97	+09:00:57.71	5683±5	4.35±0.01	−0.098±0.003	0.97±0.01	10.7±0.6
HIP65708	13:28:18.71	−00:50:24.70	5761±5	4.26±0.01	−0.047±0.004	1.12±0.01	9.9±0.5
HD184768	19:36:00.65	+00:05:28.27	5687±4	4.31±0.01	−0.055±0.003	1.02±0.01	11.0±0.5
HIP117367	23:47:52.41	+04:10:31.72	5866±3	4.36±0.01	0.024±0.003	1.14±0.01	5.6±0.5
...	...	...	...	...	...	...	...

Table 5.2: Atmospheric parameters and stellar ages determined for the sample of solar-like stars. The full version of this table is available online at the CDS.

5.1.3. STELLAR AGES

During their lives, stars evolve along a well-defined stellar evolutionary track in the Hertzsprung-Russell diagram that mainly depends on their stellar mass and metallicity. Therefore, if the stellar parameters are known with sufficient precision, it is possible to estimate the age by comparing the observed properties with the corresponding model. Following this approach, we estimate the stellar ages using the q2 code, which also computes a probability distribution function for age for each star of our sample. It makes use of a grid of isochrones to perform an isochrone fitting comparing the stellar parameters with the grid results and taking into account the uncertainties on the stellar parameters. The q2 code uses the difference between the observed parameters and the corresponding values in the model grid as weight to calculate the probability distribution; it performs a maximum-likelihood calculation to determine the most probable age (i.e. the peak of the probabil-

id	[CI/H]	[NaI/H]	[MgI/H]	[AlI/H]	[SiI/H]	[SI/H]	[CaI/H]	[ScI/H]	[ScII/H]
HD220507	0.145±0.021	0.062±0.007	0.161±0.015	0.175±0.007	0.085±0.002	0.084±0.015	0.070±0.004	0.092±0.023	0.126±0.011
HD207700	0.171±0.012	0.094±0.008	0.169±0.014	0.208±0.010	0.115±0.003	0.120±0.006	0.099±0.004	0.129±0.027	0.157±0.01
HIP10303	0.087±0.007	0.106±0.002	0.093±0.009	0.123±0.006	0.101±0.001	0.075±0.032	0.099±0.004	0.098±0.015	0.121±0.008
HD115231	−0.038±0.011	−0.143±0.003	0.044±0.038	0.02±0.017	−0.047±0.003	−0.061±0.007	−0.019±0.005	−0.012±0.031	−0.011±0.006
HIP65708	0.077±0.019	−0.026±0.021	0.053±0.007	0.074±0.003	0.003±0.003	−0.008±0.012	−0.003±0.006	0.013±0.017	0.043±0.013
HD184768	0.098±0.155	−0.007±0.002	0.074±0.013	0.13±0.002	0.031±0.002	0.040±0.019	0.005±0.005	0.049±0.027	0.091±0.005
HIP117367	0.003±0.082	0.076±0.012	0.040±0.006	0.052±0.005	0.047±0.002	0.031±0.013	0.021±0.004	0.033±0.007	0.056±0.006
...	...	...	...	...	...	...	...	...	...

[TiI/H]	[TiII/H]	[VI/H]	[CrI/H]	[CrII/H]	[MnI/H]	[FeI/H]	[FeII/H]	[CoI/H]	[NiI/H]
0.124±0.005	0.127±0.006	0.089±0.006	0.032±0.006	0.025±0.009	−0.005±0.009	0.019±0.003	0.016 ±0.005	0.084±0.004	0.030±0.003
0.160±0.005	0.148±0.007	0.137±0.007	0.070±0.006	0.057±0.010	0.066±0.006	0.052±0.003	0.050 ±0.005	0.145±0.003	0.076±0.003
0.112±0.004	0.108±0.006	0.121±0.006	0.110±0.005	0.108±0.007	0.159±0.008	0.096±0.003	0.100 ±0.005	0.119±0.004	0.113±0.004
0.025±0.006	0.003±0.007	−0.035±0.006	−0.087±0.006	−0.101±0.006	−0.207±0.010	−0.097±0.004	−0.101±0.007	−0.084±0.009	−0.123±0.004
0.048±0.006	0.057±0.007	0.003±0.006	−0.051±0.006	−0.042±0.005	−0.140±0.007	−0.047±0.005	−0.047±0.006	−0.020±0.007	−0.058±0.004
0.076±0.005	0.066±0.006	0.042±0.009	−0.050±0.005	−0.05±0.008	−0.101±0.009	−0.055±0.004	−0.055±0.006	0.043±0.004	−0.029±0.004
0.030±0.005	0.039±0.005	0.029±0.005	0.020±0.004	0.031±0.007	0.013±0.006	0.025±0.003	0.021 ±0.005	0.042±0.007	0.035±0.003
...	...	...	...	...	...	...	...	...	...

[CuI/H]	[ZnI/H]	[SrI/H]	[YII/H]	[ZrII/H]	[BaII/H]	[CeII/H]	[NdII/H]	[SmII/H]	[EuII/H]
0.103±0.036	0.138±0.022	−0.013±0.007	−0.036±0.01	−0.044±0.02	−0.028±0.005	0.041±0.017		0.065±0.011	0.103±0.007
0.145±0.034	0.180±0.024	0.001±0.006	−0.014±0.007	−0.038±0.023	0.002±0.008	0.074±0.016	0.064±0.010	0.065±0.008	0.126±0.007
0.128±0.008	0.097±0.010	0.158±0.006	0.135±0.007	0.103±0.023	0.077±0.013	0.083±0.025	0.111±0.010		0.081±0.008
−0.116±0.010	−0.083±0.004	−0.097±0.007	−0.102±0.017	−0.066±0.008	−0.076±0.012	0.039±0.014	0.100±0.008	0.159±0.007	0.17±0.008
−0.027±0.020	0.027±0.009	−0.101±0.008	−0.095±0.007	−0.091±0.009	−0.072±0.014	0.016±0.016	0.059±0.007	0.097±0.008	0.057±0.008
0.024±0.025	0.081±0.022	−0.068±0.006	−0.114±0.007	−0.119±0.005	−0.107±0.005	−0.009±0.014		0.004±0.012	0.041±0.008
0.043±0.021	0.037±0.008	0.007±0.005	0.004±0.008	−0.015±0.005	−0.012±0.006	0.014±0.017	0.043±0.010	0.002±0.010	0.026±0.008
...	...	...	...	...	...	...	...	...	...

Table 5.3: Chemical abundances for the sample of solar-like stars. The full version of this table is available online at the CDS.

ity distribution). The q2 code also calculates the 68% and 95% confidence intervals, and the mean and standard deviation of these values. We adopt the grid of isochrones computed with the Yale-Potsdam Stellar Isochrones (YaPSI) models (Spada et al., 2017). We take into account the α-enhancement effects on the model atmospheres, using the relation $[M/H] = [Fe/H] + \log(0.638 \cdot 10^{[\alpha/Fe]} + 0.362)$ (Salaris et al., 1993), where we employ magnesium as a proxy for the α-abundances.
Typical uncertainties on our age determinations (i.e. the average of the half widths of the 68% confidence intervals) are 0.9 Gyr. The ages of the solar-like stars can be found in Table 5.2.

5.1.4. A CHECK ON THE SPECTROSCOPIC LOG G

In Fig. 5.1, we present a comparison between the log g values derived through our spectroscopic analysis and those from *Gaia* photometry and parallaxes. Photometric gravities were obtained using the following equation

$$\log(g) = \log(M/M_{\odot}) + 0.4 \times M_{\rm bol} + 4 \times \log(T_{\rm eff}) - 12.505 \quad (5.1)$$

where $M/M_{\odot}$ is the stellar mass (in solar mass units) computed through a maximum-likelihood calculation performed by q2 as described in the previous section, $M_{\rm bol}$ is the bolometric magnitude obtained from the luminosity published in the *Gaia* DR2 catalogue (Lindegren et al., 2018) using the relation $M_{\rm bol} = 4.75 - 2.5 \times \log(L/L_{\odot})$, and $T_{\rm eff}$ is the spectroscopic effective temperature (we tested the use of the *Gaia* photometric $T_{\rm eff}$ and the variations in log g are negligible). In Fig. 5.1, we plot solar-like stars with relative errors on their parallaxes lower than 10% and with uncertainties on their stellar parameters within 90% of their distributions. Photometric surface gravities derived via stellar distances agree fairly well with the spectroscopic gravities suggesting that 3D non local thermodynamic equilibrium (non-LTE) effects on the Fe I and Fe II abundances have only a small effect on the

derived spectroscopic gravities. The median of the difference between the two log g is ~0.02 dex, which is smaller than the scatter due to their uncertainties of the order of ~0.03 dex. Figure 5.1 shows that the consistency level of the two sets of gravities depends on stellar metallicity. Namely, metal-rich stars have spectroscopic gravities that are slightly smaller than the photometric values, while those obtained for the metal-poor stars are higher. The slight discrepancy between the two gravities could be imputed to a number of factors, including systematic effects in the differential analysis of stars with metallicities that are different from that of the Sun, the dependence of the grid of isochrones on stellar metallicity, or other assumptions on the photometric log g calculation.

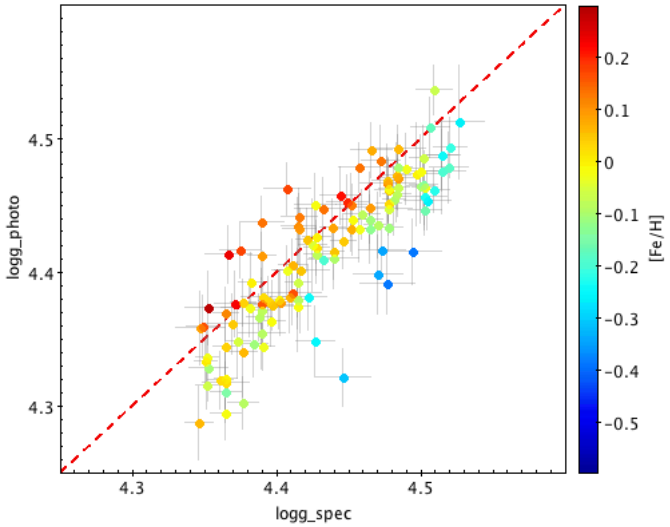

Fig. 5.1: Comparison between photometric and spectroscopic log g, where the stars are colour-coded by metallicity.

5.1.5. ORBITAL PARAMETERS

All stars in our sample are observed by the *Gaia* satellite, and they are available in the DR2 database. We use the `GalPy`[5] package of Python, in which the model `MWpotential2014` for the gravitational potential of the Milky Way is assumed (Bovy, 2015). Through the Python package `AstroPy` and the astrometric information by *Gaia* DR2, we convert the celestial coordinates (RA and DEC form Table 5.2) into the Galactocentric radius (R_{GC}) and height above the Galactic plane (z), assuming a solar Galactocentric distance R_0 = 8 kpc and a height above the Plane z_0 = 0.025 kpc (Jurić et al., 2008). A circular velocity at the solar Galactocentric distance equal to V_c= 220 km s^{-1} and the Sun's motion with respect to the local standard of rest [$U_\odot$,$V_\odot$,$W_\odot$] = [11.1, 12.24, 7.25] km s^{-1} (Schönrich et al., 2010) are used to calculate the Galactic space velocity (U,V,W) of each star. As results of the orbit computation, we obtain, among several parameters, the eccentricity of the orbit e, the perigalacticon and apogalacticon[6] radii, and the guiding radius R_g, that is $R_{GC}\upsilon_\phi/V_c$, where υ_ϕ is the Galactocentric tangential velocity of the star.

[5] Code available at http://github.com/jobovy/galpy

[6] Perigalacticon and apogalacticon: the points in the orbit of a star at which it is closest and farthest to the Galactic centre.

In Fig. 5.2 we present two different panels showing the distribution of guiding radius R_g and eccentricity e. Approximately 95% of the stars in our sample have R_g between 6 and 9 kpc (top panel) and orbits with $e < 0.3$ (bottom panel). Only two stars have a guiding radius of ~4 – 4.5 kpc and very eccentric orbits ($e \sim 0.6$), implying their birth place is located far from the solar neighbourhood. If we assume that the R_g is a good proxy of the Galactocentric distance where the stars were formed, then we can conclude that the stars in our sample were born within a restricted range of Galactocentric distances compared to the typical variation of the [X/Fe] ratios with R_g predicted by models (e.g. Magrini et al., 2009, 2017). However, it is possible that a fraction of the stars in our sample have not preserved their kinematical properties due to interaction with spiral arms or giant molecular clouds losing all information on their origin, and therefore we cannot exclude the presence of other migrators in our sample.

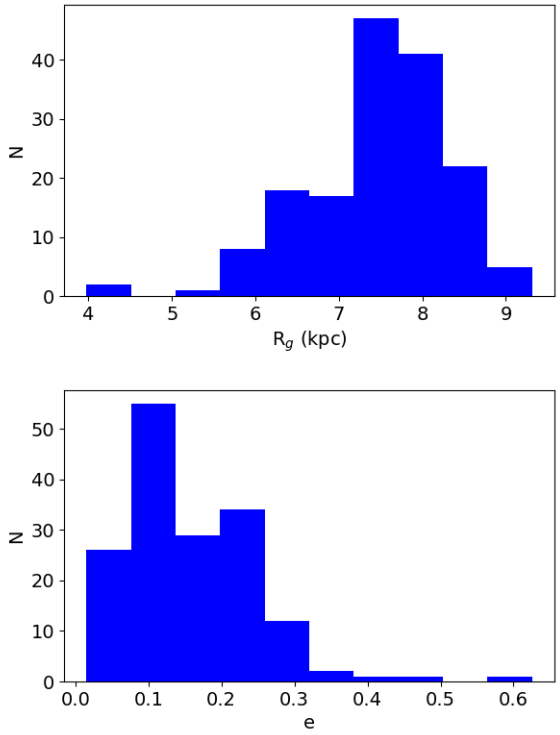

Fig. 5.2: Distribution of the guiding radius R_g (top panel) and a distribution of the eccentricity e (bottom panel) for our sample of solar-like stars.

5.2. [X/FE] VERSUS AGE RELATIONS

In this section, we briefly reiterate the main sites of production of the chemical elements and how they affect the [X/Fe]–age relation, as already mentioned in Chapter 3.

In Fig. 5.3, we show abundance ratios versus age trends for 24 elements and/or ions over iron in the metallicity range −0.1 to +0.1 dex. We select stars in $T_\odot \pm 200$ K and $\log g_\odot \pm 0.2$ dex, removing those with larger uncertainties on the atmospheric parameters, that is larger than 95% of their distributions. The stars are plotted with different symbols and

colours: the red diamonds are thick-disc stars, whereas the thin-disc stars are shown with blue circles. We select the thick-disc stars through the [α/Fe] versus [Fe/H] plane with [α/Fe]=([Ca/Fe]+[Si/Fe]+[Ti/Fe]+[Mg/Fe])/4 (excluding S because of its large scatter). The separation in chemical properties is also related to the age separation between the two populations, which is located at a look-back time of ~8 Gyr (Haywood et al., 2013; Nissen, 2015; Bensby et al., 2014). The different slopes for the relations of these elements versus age outline a different contribution of the main stellar nucleosynthesis processes, such as for instance, those related to the ejecta of SNe II, SNe Ia, and AGB stars. As we can see from Fig. 5.3, the relations of [α/Fe] (with α elements of our sample Mg, Si, S, Ca, Ti) versus age have positive slopes, in agreement with their production over a shorter timescale with respect to iron. SNe II indeed eject mainly α-elements and elements up to the iron peak, including Fe, into the interstellar medium (ISM) within short timescales (<10^{-2} Gyr); while SNe Ia produce mainly Fe and iron-peak elements (e.g. Cr, Mn, Co, Ni), with a minor amount of α-elements and over longer timescales (~1 Gyr; Matteucci, 2014; Spina et al., 2016). Indeed, at the beginning of the Galactic formation, the metal content of the most metal-poor stars was produced by SNe II. At later times, SNe Ia started to explode, contributing to a metal mixture with a smaller [α/Fe] ratio with respect to the oldest stars and creating the typical positive slope for [α/Fe] versus age trends. Therefore, the iron peak elements (V, Cr, Mn, Co, Ni, Cu, Zn) over iron show slightly positive or negligible slopes with age. This is consistent, within the errors, with a null slope that reflects similar mechanisms of production of all iron-peak elements and Fe. Finally, neutron capture elements are produced in the ejecta of AGB stars (mainly s-elements) or during mergers of neutron stars or a neutron star and a black hole (mainly r-elements). Indeed, almost pure s-process elements (e.g. Sm, Sr, Zr, Y) over iron have a negative slope due to their delayed production from successive captures of neutrons by iron-peak elements in low-mass AGB stars with respect to the early contribution of SNe Ia and SNe II that produce iron. The elements with a lower contribution from the s-process and a high contribution from the r-process, such as Eu (see Fig. 6 in Spina et al., 2018b), have flatter [X/Fe]–age distributions than the almost pure s-process elements. This means that the production of s-process elements has been more efficient within the last gigayear.

5.3. CHEMICAL CLOCKS

Abundance ratios of pairs of elements produced over different timescales (e.g. [Y/Mg] or [Y/Al) can be used as valuable indicators of stellar age. Their [X/Fe] ratios show opposite behaviours with respect to stellar age (see e.g. [Mg/Fe] and [Y/Fe] in Fig. 5.3, decreasing and increasing, respectively, with stellar age). Therefore, their ratio, for example [Y/Mg], shows a steep increasing trend with stellar age. However, as pointed out by Feltzing et al. (2017) and Delgado Mena et al. (2019), their relations might have a secondary dependence on metallicity. Moreover, Titarenko et al. (2019) found the existence of different relations between ages and [Y/Mg] for a sample of stars belonging to the thin and thick discs.

The most studied chemical clocks in the literature are [Y/Mg] and [Y/Al] (Tucci Maia et al., 2016; Nissen, 2015; Nissen et al., 2017; Slumstrup et al., 2017; Spina et al., 2016, 2018b). However, some recent studies have extended the list of chemical clocks to other ratios and found interesting results (Delgado Mena et al., 2019; Jofré et al., 2020).

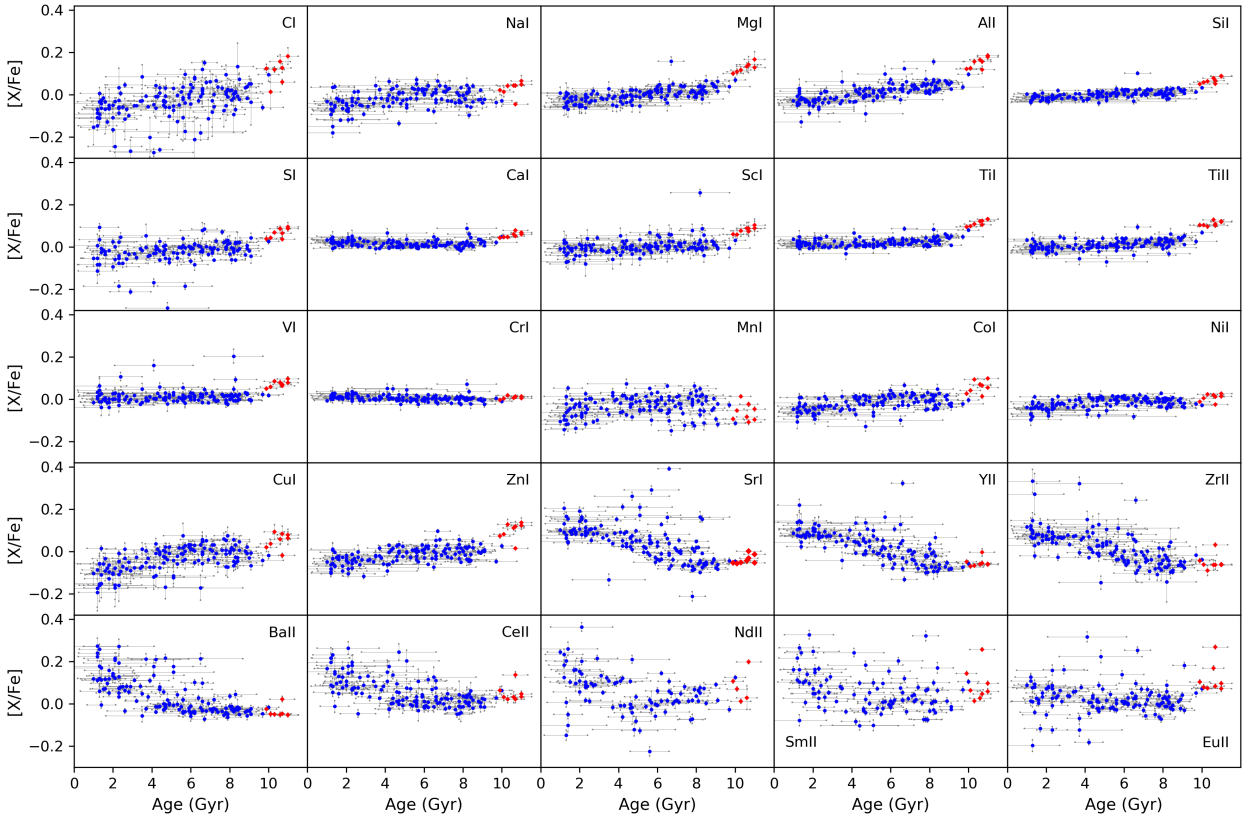

Fig. 5.3: [X/Fe] ratio as a function of stellar age. The blue dots represent the thin disc stars, while the red diamonds are the thick disc populations. The stars are within the metallicity range of $-0.1 <$ [Fe/H] $< +0.1$ dex.

5.3.1. SIMPLE LINEAR REGRESSION

In Fig. 5.4, we show the effect of metallicity in our sample stars, where two chemical clocks ([Y/Mg] and [Y/Al]) are plotted as a function of stellar age. The points are colour-coded by metallicity and the linear fits in four different metallicity bins ([Fe/H] < -0.3, $-0.3 <$ [Fe/H] < -0.1, $-0.1 <$ [Fe/H] $< +0.1$, and [Fe/H] $> +0.1$) are shown. The slopes of these fits depend on the metal content: the more metal-rich sample has a flatter slope, while the more metal-poor samples have steeper slopes.

In Table 5.4, we show the parameters of orthogonal distance regression fits for [Y/Mg] and [Y/Al]. In the first three metallicity bins for both abundance ratios, the difference in slopes is within 1-σ, not showing a strong variation with metallicity in the subsolar and solar ranges. On the other hand, in the more metal-rich bin, the slope is definitively flatter. The slopes obtained in the solar metallicity bin ($-0.1 <$ [Fe/H] $< +0.1$) are in good agreement with previous literature results (Delgado Mena et al., 2019; Spina et al., 2018b) for the same metallicity range. The differences in the slopes and intercepts obtained in the high-metallicity bin are statistically significant (see the Pearson correlation coefficient in Table 5.4). This indicates that the metallicity is an important additional parameter that cannot be neglected in the use of abundance ratios to derive stellar ages.

Following the work of Delgado Mena et al. (2019), we analyse the correlation coefficients between abundance ratios and stellar age for other ratios in addition to [Y/Al] and

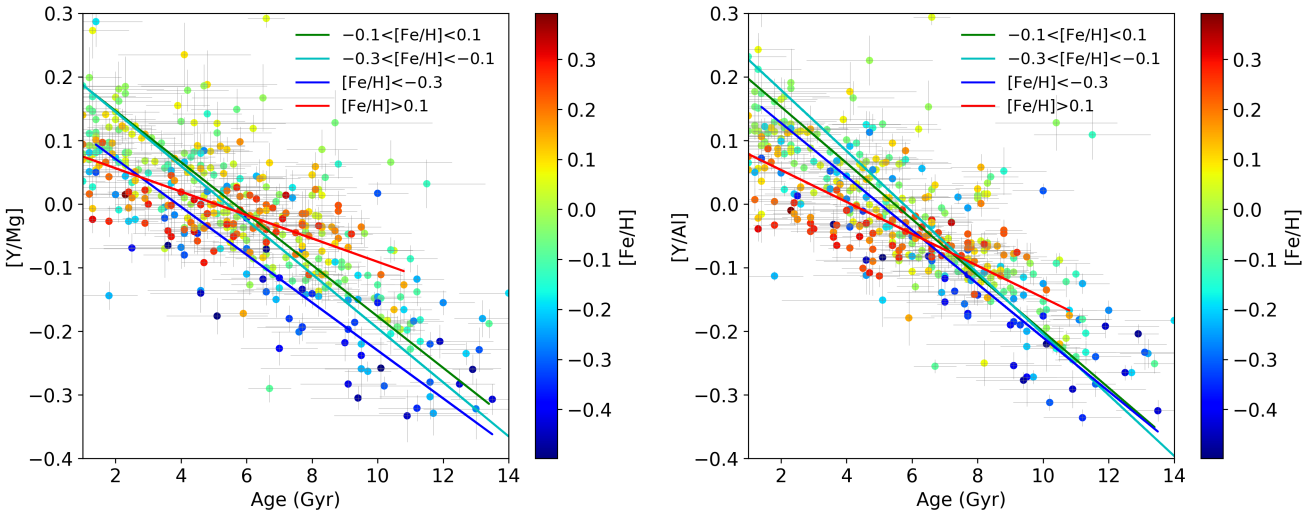

Fig. 5.4: [Y/Mg] and [Y/Al] as a function of age. The dots are colour-coded by [Fe/H]. The lines correspond to the linear functions described in Table 5.4 in four different bins of metallicity: [Fe/H]<−0.3 (blue), −0.3<[Fe/H]<−0.1 (turquoise), −0.1<[Fe/H]<+0.1 (green), and [Fe/H]>+0.1 (red).

[A/B]	metallicity bin	slope	intercept	Pearson coefficient
[Y/Mg]	[Fe/H] < −0.3	−0.038 ± 0.005	0.146 ± 0.050	−0.76
[Y/Mg]	−0.3 < [Fe/H] < −0.1	−0.042 ± 0.004	0.223 ± 0.029	−0.63
[Y/Mg]	−0.1 < [Fe/H] < +0.1	−0.040 ± 0.002	0.228 ± 0.015	−0.74
[Y/Mg]	[Fe/H] > +0.1	−0.018 ± 0.002	0.093 ± 0.010	−0.59
[Y/Al]	[Fe/H] < −0.3	−0.042 ± 0.005	0.212 ± 0.035	−0.83
[Y/Al]	−0.3 < [Fe/H] < −0.1	−0.048 ± 0.004	0.275 ± 0.031	−0.64
[Y/Al]	−0.1 < [Fe/H] < +0.1	−0.044 ± 0.002	0.241 ± 0.015	−0.79
[Y/Al]	[Fe/H] > +0.1	−0.025 ± 0.002	0.104 ± 0.012	−0.64

Table 5.4: Slopes and intercepts of the four linear fits shown in Fig. 5.4.

[Y/Mg]. We consider ratios between s-process (negative slope of [X/Fe] vs. age) and α-elements (positive slope) or iron-peak elements (flat/slightly positive slope). We evaluate the correlation between chemical clocks and stellar age using the Pearson coefficient. In Table 5.5, we show the abundances ratios with the highest Pearson correlation coefficient for the chemical abundance ratios studied in this work.

5.3.2. MULTIVARIATE LINEAR REGRESSION

As shown in Fig. 5.4, the metallicity represents a third important variable to take into account when we search for the relations between abundance ratios and stellar age. Our sample, which is composed of stars similar to the Sun, is indeed a good way to test the metallicity dependence in a range from −0.7 to +0.4 dex, disentangling the effect of the other parameters.

In our analysis, we consider age (measured from the isochrone fitting via maximum-likelihood calculation) and metallicity (via spectroscopic analysis) as independent vari-

[A/B]	Pearson coefficient
[Y/Mg]	−0.87
[Y/Al]	−0.88
[Y/Ca]	−0.87
[Y/Si]	−0.86
[Y/TiI]	−0.87
[Y/TiII]	−0.86
[Y/Sc]	−0.84
[Y/V]	−0.84
[Y/Co]	−0.80
[Sr/Mg]	−0.84
[Sr/Al]	−0.87
[Sr/TiI]	−0.83
[Sr/TiII]	−0.81

Table 5.5: Pearson coefficients of [A/B] abundance ratios vs. stellar age.

ables, while the abundance ratios are the dependent variables. We derive the relations in the form [A/B]=f(X), where X represents the independent variables, in this case age and [Fe/H], while [A/B] is a generic abundance ratio used as a chemical clock. For each relation, we produce the adjusted R^2 (adj-R^2) parameter, a goodness-of-fit measurement for multivariate linear regression models, taking into account the number of independent variables. We perform the fitting, selecting the *best* sample of solar-like stars: ±100 K and ±0.1 dex from the T_{eff} and the log g of the Sun, respectively. Stars with uncertainties on stellar parameters and chemical abundances larger than 95% of their distributions or with uncertainties on age $\gtrsim$ 50% and stars with an upper limit in age are excluded. These upper limits are due to their probability age distributions, which are truncated before they reach the maximum. This truncation due to the border of the YAPSI isochrone grid excludes solar-like stars younger than 1 Gyr. In addition, we identify and exclude stars that are anomalously rich in at least four s-elements in comparison to the bulk of thin disc stars. These are easily identifiable because they lie outside 3-σ from a linear fit of data in Fig. 5.3: namely CWW097, HIP64150, HD140538, HD28701, HD49983, HD6434, and HD89124. We also exclude a few stars belonging to the halo ($v_{tot} > 200$ km s^{-1}).

The parameters of the multivariate linear regressions are shown in Table 5.6: the constant c±Δc, the coefficient of [Fe/H] $x_1 \pm \Delta x_1$, and the coefficient of [A/B] $x_2 \pm \Delta x_2$. The regressions with the lower adj-R^2 are those involving abundance ratios between s-process and iron-peak elements. These ratios have flatter trends with stellar age. In the following analysis, we consider only the relations with adj$-R^2$>0.70.

Finally, we invert the relations [A/B] = f(Age, [Fe/H]) to have relations in the form Age = f([A/B], [Fe/H]), referred to as "stellar dating relations" hereafter. The new coefficients are shown in Table 5.6, labelled as c′, x'_1, and x'_2, the constant and coefficients of [Fe/H] and [A/B], respectively.

First, we validate the multivariate regressions by comparing the ages derived with them and the input values, that is, ages obtained with the isochrone fitting through the maximum-likelihood calculation. The agreement is good and there are no trends.

We then compare our results to those of Delgado Mena et al. (2019) in which a similar

[A/B]	c	x_1	x_2	Δc	Δx_1	Δx_2	adj$-R^2$	c'	x'_1	x'_2
[Y/Mg]	0.161	0.155	−0.031	0.009	0.028	0.002	0.80	5.245	5.057	−32.546
[Y/Al]	0.172	0.028	−0.035	0.009	0.029	0.002	0.78	4.954	0.796	−28.877
[Y/TiII]	0.132	0.146	−0.026	0.008	0.026	0.002	0.78	5.026	5.591	−38.219
[Y/TiI]	0.116	0.185	−0.025	0.008	0.024	0.001	0.81	4.597	7.326	−39.514
[Y/Ca]	0.099	0.142	−0.020	0.007	0.020	0.001	0.79	5.000	7.143	−50.462
[Y/Sc]	0.137	0.052	−0.026	0.009	0.029	0.002	0.67	5.304	2.017	−38.649
[Y/Si]	0.135	0.076	−0.025	0.008	0.025	0.001	0.75	5.311	3.003	−39.325
[Y/V]	0.116	−0.020	−0.024	0.008	0.026	0.002	0.66	4.869	−0.852	−41.921
[Y/Co]	0.163	−0.061	−0.029	0.009	0.029	0.002	0.67	5.699	−2.146	−35.018
[Sr/Mg]	0.184	0.218	−0.030	0.010	0.032	0.002	0.77	6.129	7.276	−33.401
[Sr/Al]	0.194	0.089	−0.034	0.010	0.031	0.002	0.77	5.737	2.631	−29.532
[Sr/TiI]	0.139	0.248	−0.025	0.009	0.028	0.002	0.78	5.655	10.103	−40.753
[Sr/TiII]	0.154	0.209	−0.025	0.010	0.031	0.002	0.74	6.052	8.203	−39.268
[Y/Zn]	0.170	−0.075	−0.029	0.009	0.028	0.002	0.68	5.853	−2.595	−34.370
[Sr/Zn]	0.194	−0.006	−0.029	0.010	0.032	0.002	0.65	6.819	−0.220	−35.072
[Sr/Si]	0.159	0.139	−0.025	0.010	0.031	0.002	0.70	6.341	5.553	−39.994
[Zn/Fe]	−0.065	0.061	0.012	0.006	0.019	0.001	0.42	5.481	−5.180	84.381

Table 5.6: Multivariate linear regression parameters. Coefficients c, x_1, and x_2 of the relations $[A/B] = c + x_1 \cdot [Fe/H] + x_2 \cdot Age$, where [Fe/H] and age are the independent variables. Δc, Δx_1, and Δx_2 are the uncertainties on the coefficients. c', x'_1, and x'_2 are the coefficients of the inverted stellar dating relation $Age = c' + x'_1 \cdot [Fe/H] + x'_2 \cdot [A/B]$. Finally, adj$-R^2$ is the adjusted R^2 parameter.

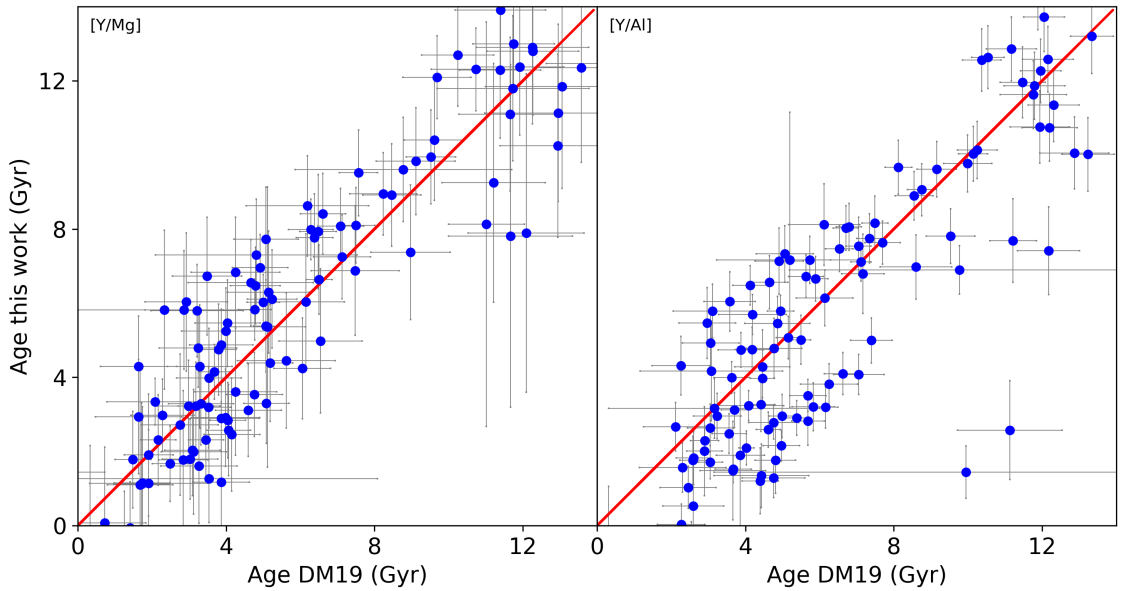

Fig. 5.5: Comparison of the ages derived by Delgado Mena et al. (2019) and those inferred in the present work with both of our relations: [Y/Mg] and [Y/Al] vs. Age. The circles are the ages of the stars in common between the two works. The red lines are the one-to-one relations.

approach was used to estimate dating relations between abundance ratios, metallicity, and age. The main differences between our work and that of Delgado Mena et al. (2019) are as follows: *(i)* the selection of the calibration sample, which is composed of 1111 FGK stars, includes stars with a large variety of stellar parameters and not only solar-like stars, as in ours; *(ii)* Delgado Mena et al. (2019) do not perform a differential analysis; and *(iii)* they use a grid of isochrones based on PARSEC stellar evolutionary models, together with *Gaia* DR2 parallaxes, to determine the stellar ages. To validate our stellar dating relations, we apply both relations to the sample of solar-like stars in common between the present work and Delgado Mena et al. (2019). Despite the differences in the two approaches, the agreement between the ages inferred with our relations and those of Delgado Mena et al. (2019) is good (see Fig. 5.5, where the red lines are the one-to-one relations). There are no major trends between the two sets of ages.

5.4. COMPARISON WITH OPEN CLUSTERS

A meaningful validation of our relations is a comparison with star clusters, which are important benchmarks for stellar age. In this section, we compare the age from the literature for 19 open clusters available in the GES iDR5 with the corresponding ages derived using our stellar dating relations.

5.4.1. THE OPEN CLUSTER SAMPLE IN THE GES IDR5

We use the open clusters (OCs) available in GES iDR5, taking into account the membership described in Jackson et al. (2020) and in the previous Chapter. These clusters are already listed in the Table 4.1, however in this work we add two clusters, excluded in the previous Chapter because devoid of giants with [C/N]: NGC 2420 and NGC 6633.

We recall the complete list of OCs in Table 5.7, where we summarise their basic properties from the literature: coordinates, Galactocentric distances (R_{GC}), heights above the plane (z), median metallicity [Fe/H], ages, and the references for ages and distances. We use homogeneous data sets for age from the GES papers.

5.4.2. AGE RE-DETERMINATION WITH CHEMICAL CLOCKS

To compare the two data sets, we compute the median abundance ratios of giant and subgiant star members in each cluster. In addition, since the abundances in GES are in the 12 + log(X/H) form, we need to define our abundance reference to obtain abundances on the solar scale – in order to have the abundances in the [X/H] scale to compare with the solar-like stars. Table 5.8 shows three different sets of abundances: the solar abundances from iDR5 computed from archive solar spectra, the solar abundances by Grevesse et al. (2007), and the median abundances of giant stars in M67. The cluster M67 is known to have the same composition as the Sun (e.g. Randich et al., 2006; Pasquini et al., 2008; Önehag et al., 2014; Liu et al., 2016) and can therefore be used to confirm the abundance reference. The GES solar and M67 abundances are in agreement with the reference solar abundances from Grevesse et al. (2007). The average abundances for the three member giant stars in M67 from the iDR5 recommended values are given together with their standard deviations and the typical errors on each measurement (in parenthesis; see third column of Table 5.8).

Cluster	RA[(a)] (J2000)	DEC[(a)]	R_{GC} (kpc)	z (pc)	[Fe/H][(a)] (dex)	Age (Gyr)	Ref. Age & Distance
NGC 6067	16:13:11	−54:13:06	6.81±0.12	−55±17	0.2 ± 0.08	0.1 ± 0.05	Alonso-Santiago et al. (2017)
NGC 6259	17:00:45	−44:39:18	7.03±0.01	−27±13	0.21 ± 0.04	0.21 ± 0.03	Mermilliod et al. (2001)
NGC 6705	18:51:05	−06:16:12	6.33±0.16	−95±10	0.16 ± 0.04	0.3 ± 0.05	Cantat-Gaudin et al. (2014)
NGC 6633	18:27:15	+06 30 30	7.71		−0.01 ± 0.11	0.52 ± 0.1	Randich et al. (2018)
NGC 4815	12:57:59	−64:57:36	6.94±0.04	−95±6	0.11 ± 0.01	0.57 ± 0.07	Friel et al. (2014)
NGC 6005	15:55:48	−57:26:12	5.97±0.34	−140±30	0.19 ± 0.02	0.7 ± 0.05	Hatzidimitriou et al. (2019)
Trumpler 23	16:00:50	−53:31:23	6.25±0.15	−18±2	0.21 ± 0.04	0.8 ± 0.1	Jacobson et al. (2016)
Melotte 71	07:37:30	−12:04:00	10.50±0.10	+210±20	−0.09 ± 0.03	0.83 ± 0.18	Salaris et al. (2004)
Berkeley 81	19:01:36	−00:31:00	5.49±0.10	−126±7	0.22 ± 0.07	0.86 ± 0.1	Magrini et al. (2015)
NGC 6802	19:30:35	+20:15:42	6.96±0.07	+36±3	0.1 ± 0.02	1.0 ± 0.1	Jacobson et al. (2016)
Rup 134	17:52:43	−29:33:00	4.60±0.10	−100±10	0.26 ± 0.06	1.0 ± 0.2	Carraro et al. (2006)
Pismis 18	13:36:55	−62:05:36	6.85±0.17	+12±2	0.22 ± 0.04	1.2 ± 0.04	Piatti et al. (1998)
Trumpler 20	12:39:32	−60:37:36	6.86±0.01	+134±4	0.15 ± 0.07	1.5 ± 0.15	Donati et al. (2014)
Berkeley 44	19:17:12	+19:33:00	6.91±0.12	+130±20	0.27 ± 0.06	1.6 ± 0.3	Jacobson et al. (2016)
NGC 2420	07:38:23	+21:34:24	10.76		−0.13 ± 0.04	2.2 ± 0.3	Salaris et al. (2004); Sharma et al. (2006)
Berkeley 31	06:57:36	+08:16:00	15.16±0.40	+340±30	−0.27 ± 0.06	2.5 ± 0.3	Cignoni et al. (2011)
NGC 2243	06:29:34	−31:17:00	10.40±0.20	+1200±100	−0.38 ± 0.04	4.0 ± 1.2	Bragaglia & Tosi (2006)
M67	08:51:18	+11:48:00	9.05±0.20	+405±40	−0.01 ± 0.04	4.3 ± 0.5	Salaris et al. (2004)
Berkeley 36	07:16:06	−13:06:00	11.30±0.20	−40±10	−0.16 ± 0.1	7.0 ± 0.5	Donati et al. (2012)

Table 5.7: Parameters of the open clusters in the GES sample. Ref: [(a)]Magrini et al. (2018).

In the following, we normalise our abundances to the M67 abundances, as done in other GES consortium papers, such as Magrini et al. (2017, 2018) since most of the cluster member stars are giants. The median abundance ratios scaled to M67 are shown in Table 5.9 where the uncertainties are the scatter errors on the median ($1.235 \cdot \sigma / \sqrt{N}$).

Element	Sun (iDR5)	Sun (Grevesse et al., 2007)	M67 giants (iDR5)
Mg I	7.51±0.07	7.53±0.09	7.51±0.02(±0.05)
Al I	6.34±0.04	6.37±0.06	6.41±0.01(±0.04)
Si I	7.48±0.06	7.51±0.04	7.55±0.01(±0.06)
Ca I	6.31±0.12	6.31±0.04	6.44±0.01(±0.10)
Ti I	4.90±0.08	4.90±0.06	4.90±0.01(±0.09)
Ti II	4.99±0.07	–	5.01±0.01(±0.10)
Y II	2.19±0.12	2.21±0.02	2.15±0.01(±0.09)

Table 5.8: Abundance references.

A large number of open clusters in our sample have ages younger than 1 Gyr, while our relations are derived from a sample of stars whose ages (from isochrone fitting) cannot be extended below 1 Gyr. We need to verify the possibility of extrapolating our relations towards the youngest regimes using solar-like stars with younger ages derived from independent methods. We adopt the literature ages for five solar-like stars analysed with our differential analysis. Their ages cannot be computed with our maximum-likelihood isochrone fitting since they are located close to the border of the YAPSI isochrone grid. Their ages are derived from the age of stellar associations to which they belong or they are calculated through gyrochronologic measurements: HD1835 (600 Myr, in Hyades, Rosén et al., 2016), HIP42333, HIP22263 (0.3±0.1 Gyr, 0.5±0.1 Gyr, Aguilera-Gómez et al., 2018), HIP19781 (in Hyades, Leão et al., 2019), HD209779 (55 Myr, in IC2391, Montes et al., 2001). In Fig. 5.6 we show the location of the five young solar-like stars with our sample of solar-like stars. These

Cluster	# stars	[Y/Mg] (dex)	[Y/Al] (dex)	[Y/TiI] (dex)	[Y/TiII] (dex)	[Y/Ca] (dex)	[Y/Si] (dex)
Berkeley 31	5 (G)	−0.01±0.03	0.02±0.03	0.01±0.04	−0.07±0.04	0.06±0.04	0.03±0.04
Berkeley 36	5 (G)	−0.05±0.06	−0.07±0.06	0.00±0.07	−0.04±0.07	0.13±0.06	−0.02±0.06
Berkeley 44	7 (G)	0.14±0.07	0.19±0.07	0.13±0.08	−0.04±0.14	0.26±0.07	0.18±0.07
Berkeley 81	13 (G)	0.09±0.03	0.07±0.03	0.13±0.05	0.17±0.05	0.19±0.04	0.08±0.04
M67	3 (G)	0.00±0.01	0.00±0.01	0.00±0.01	0.00±0.01	0.00±0.01	0.00±0.01
Melotte 71	4 (G)	0.07±0.01	0.15±0.01	0.13±0.02	0.09±0.01	0.03±0.01	0.09±0.03
NGC 2243	17 (16 G, 1 SG)	−0.04±0.03	0.00±0.03	0.00±0.05	−0.04±0.04	−0.02±0.09	−0.01±0.03
NGC 2420	28 (24 G, 4 SG)	0.07±0.03	0.13±0.03	0.08±0.03	0.04±0.03	0.07±0.03	0.08±0.03
NGC 4815	6 (G)	0.11±0.09	0.16±0.08	0.19±0.10	0.10±0.08	0.12±0.09	0.08±0.07
NGC 6005	9 (G)	−0.01±0.02	0.02±0.02	0.03±0.03	0.02±0.02	0.05±0.02	−0.05±0.02
NGC 6067	12 (G)	0.08±0.04	0.03±0.05	0.06±0.05	0.13±0.04	0.05±0.07	0.02±0.04
NGC 6259	12 (G)	−0.05±0.02	−0.05±0.02	0.00±0.04	0.07±0.03	0.04±0.02	−0.08±0.02
NGC 6633	3 (G)	0.08±0.02	0.18±0.02	0.19±0.02	0.11±0.01	0.09±0.01	0.07±0.01
NGC 6705	28 (G)	−0.03±0.03	−0.10±0.03	0.05±0.04	0.08±0.04	0.02±0.04	−0.09±0.03
NGC 6802	10 (G)	0.17±0.02	0.14±0.02	0.23±0.03	0.10±0.02	0.24±0.02	0.13±0.02
Rup 134	16 (G)	−0.08±0.02	−0.08±0.02	−0.03±0.02	−0.04±0.02	0.04±0.02	−0.14±0.02
Pismis 18	6 (G)	0.05±0.04	0.10±0.04	0.13±0.04	0.06±0.04	0.12±0.04	0.00±0.04
Trumpler 20	34 (G)	0.12±0.02	0.16±0.02	0.17±0.02	0.08±0.02	0.15±0.02	0.04±0.02
Trumpler 23	10 (G)	−0.05±0.04	−0.02±0.04	0.05±0.06	0.01±0.04	0.11±0.05	−0.10±0.04

Table 5.9: Abundance ratios of open clusters in the GES sample. G: giants, SG: sub-giants.

follow the same trend as the solar-like stars with ages > 1 Gyr, demonstrating the continuity between the two samples and allowing us to extrapolate our relations up to 0.05 Gyr, the age of the youngest solar-like star in the sample.

In Fig. 5.7, we show the abundance ratios of the solar-like stars versus age, together with those of OCs in the metallicity bin of −0.4<[Fe/H]<+0.3 (range of cluster metallicity). The two populations follow similar trends. However, some of the youngest open clusters are located outside the distribution of the solar-like stars.

In particular, this different behaviour is highlighted in Fig. 5.8, where we compare their literature ages with the age obtained from our relations in Table 5.6. We use the general formula $\mathrm{Age} = c' + x'_1 \cdot [\mathrm{Fe/H}] + x'_2 \cdot [\mathrm{A/B}]$, where [Fe/H] and [A/B] of OCs are known. There is a group of clusters for which the agreement with most of the chemical clocks is good. Most of these clusters are located at R_{GC} >7 kpc, except for the outermost cluster, Berkeley 31. The cluster lies at R_{GC} ∼15 kpc and its age derived with the stellar dating relations is slightly higher than the literature values (except for [Y/Ca]). On the other hand, the ages derived for the innermost OCs at $R_{GC} < 7$ kpc are higher than their literature age values or are negative in a few cases (not reliable ages). We recall that our stellar dating relations already take into account the dependence on [Fe/H].

To understand our failure to reproduce the ages of clusters located far from the solar neighbourhood, we vary the form of the multivariate linear regressions shown in the Sect. 5.3.2, adding a term containing $x_3 \cdot [\mathrm{Fe/H}] \cdot \mathrm{Age}$. This term takes into account the dependence of age on the metallicity. The addition of this term is not sufficient to reconcile the ages derived from the chemical clocks with the literature ages for the inner disc open clusters. Indeed, in Fig. 5.9 we present the residuals of the regression for [Y/Mg] as a function of [Fe/H]. There is a similar scatter on the residuals both for solar-like stars (the density contour) and open clusters (marked with the star symbol), colour-coded by their Galacto-

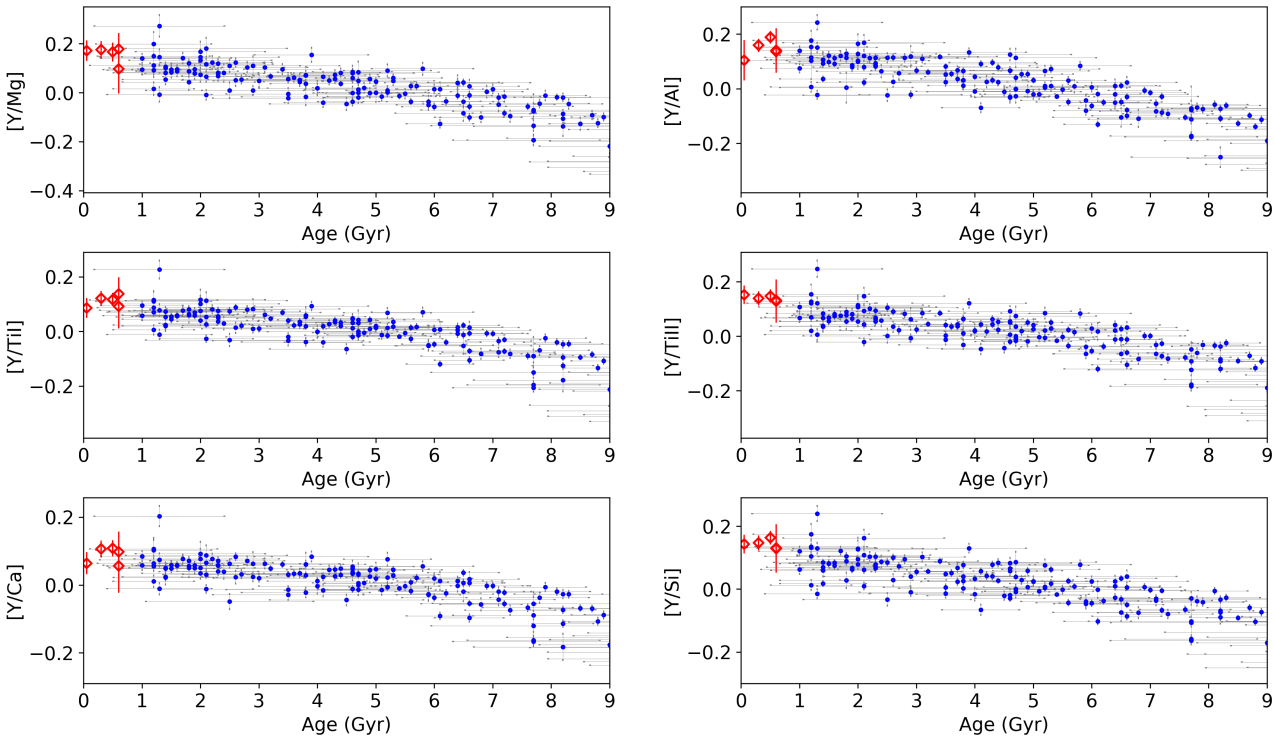

Fig. 5.6: Abundance ratio vs. stellar age. The blue dots are our sample of solar-like stars and the red diamonds represent the five solar-like stars with ages from the literature and abundances from our analysis.

centric distance. However, OCs with $R_{GC} < 7$ kpc have larger age residuals than the other clusters or solar-like stars, as mentioned above.

Moreover, we calculate the Y abundances using the photometric log g computed in Sect. 5.1.4 in order to verify its effect on our results since the yttrium abundances derived from Y II lines are sensitive to gravity. The median difference between spectroscopic gravities and the photometric ones is +0.02 dex in the solar metallicity regime (−0.1<[Fe/H]<0.1) and −0.015 dex in the super-solar regime ([Fe/H]>0.1). These differences produce a median difference in [Y/H] of +0.01 dex and −0.01 dex in the two respective regimes, a negligible effect for our purpose. We calculate the chemical ages applying the multivariate linear regression as explained in Sect. 5.3.2 with the Y abundances deduced by photometric log g, finding no significant variation with respect to the chemical ages obtained using the spectroscopic log g. In the following section, we discuss some hypotheses capable of explaining this discrepancy.

5.5. THE NON-UNIVERSALITY OF THE RELATIONS BETWEEN AGES AND ABUNDANCE RATIOS INVOLVING S-PROCESS ELEMENTS

The aim of the present study, together with other previous works (e.g. Feltzing et al., 2017; Spina et al., 2018b; Delgado Mena et al., 2019, among many others), is to find stellar dating relations between ages and some abundance ratios that are applicable to the whole Galaxy,

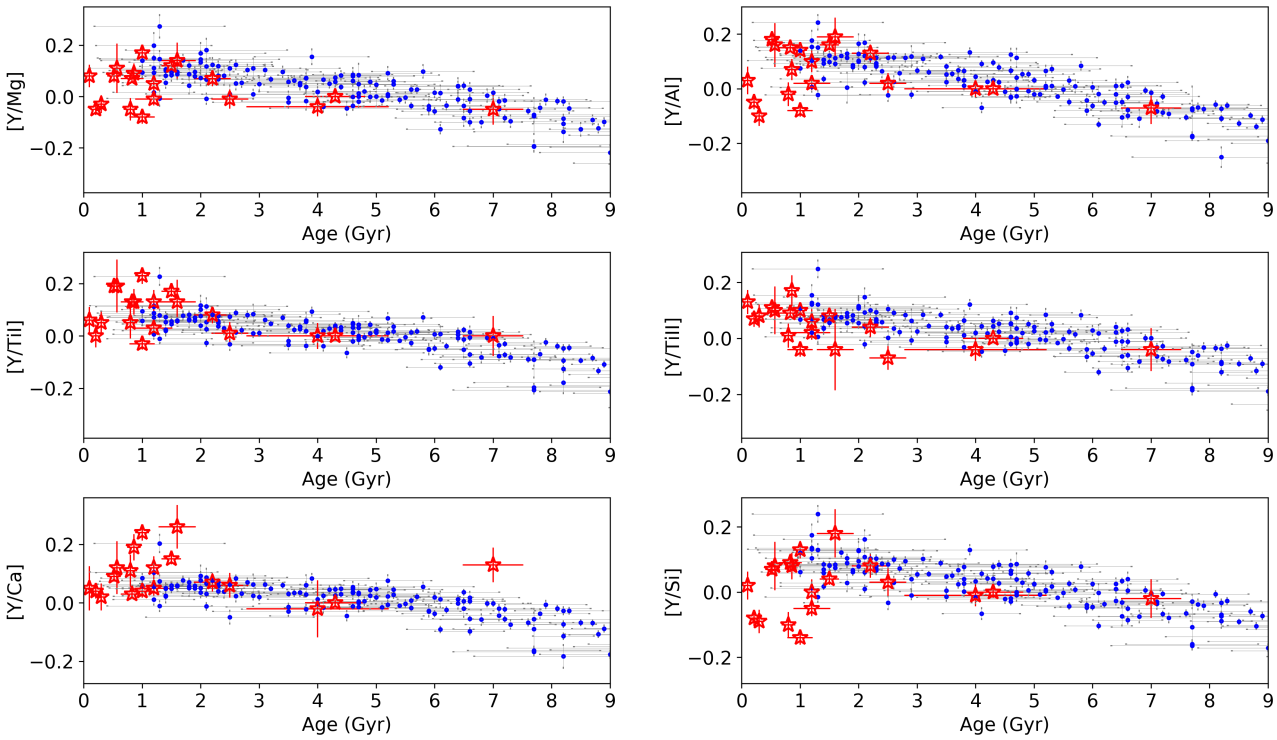

Fig. 5.7: Abundance ratio vs. stellar age. The blue dots show the values of our solar-like stars and the red stars represent the mean values for the open clusters in the GES sample.

or at least to vast portions of it. The opening questions in Feltzing et al. (2017) focus on the possible universality of the correlation between for example [Y/Mg] and age found in a sample of the solar-like stars, and, if it holds, also for larger ranges of [Fe/H], or for stars much further than the solar neighbourhood or in different Galactic populations, such as those in the thick disc.

As we mention in Chapter 1 and Sect. 5.2, s-processes occur in low- and intermediate-mass AGB stars (see, e.g. Busso et al., 2001; Karakas & Lugaro, 2016), with timescales ranging from less than a gigayear to several gigayears for the higher and lower mass AGB stars, respectively. On the other hand, α elements (in different percentages) are produced by core-collapse supernovae during the final stages of the evolution of massive stars on shorter timescales. Combining the enrichment timescales of the s-process and α-elements, younger stars are indeed expected to have higher [s/α] ratios than older stars. However, the level of [s/α] reached in different parts of the Galaxy at the same epoch is not expected to be the same. Enlarging the sample of stars or star clusters outside the solar neighbourhood means that we have to deal with the complexity of the Galactic chemical evolution. This includes radial variation of the star formation history (SFH) in the disc driven by an exponentially declining infall rate and a decreasing star formation efficiency towards the outer regions (see, e.g. Magrini et al., 2009, and in general, multi-zone chemical evolution models). Consequently, different radial regions of the disc experience different SFHs, which produce different distributions in age and metallicity of the stellar populations. At each Galactocentric distance, the abundance of unevolved stars, which inherited heavy nuclei from the contributions of previous generations of stars, is thus affected by the past SFH. Last but not least, there is a strong metallicity dependence of the stellar yields. The metallicity dependence of

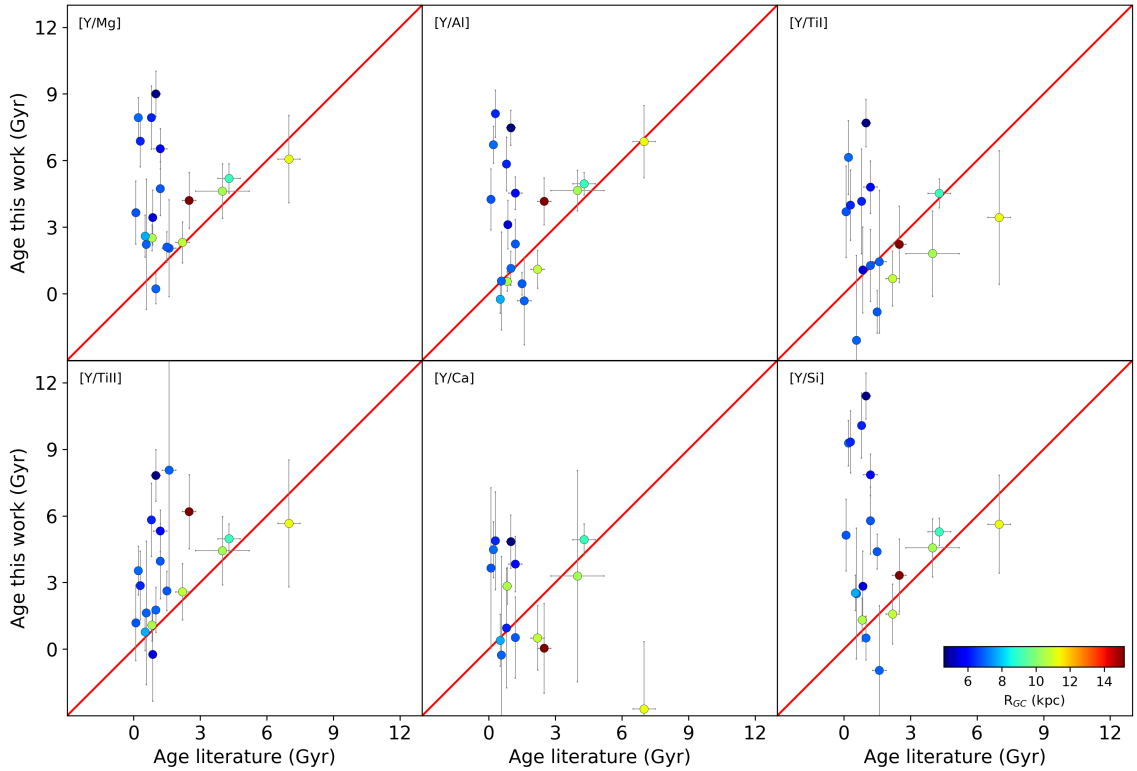

Fig. 5.8: Comparison between the ages from the literature and the ages inferred in the present work for the open clusters. The symbols are colour-coded by their Galactocentric distances. We note that we only show positive upper limit ages in this plot.

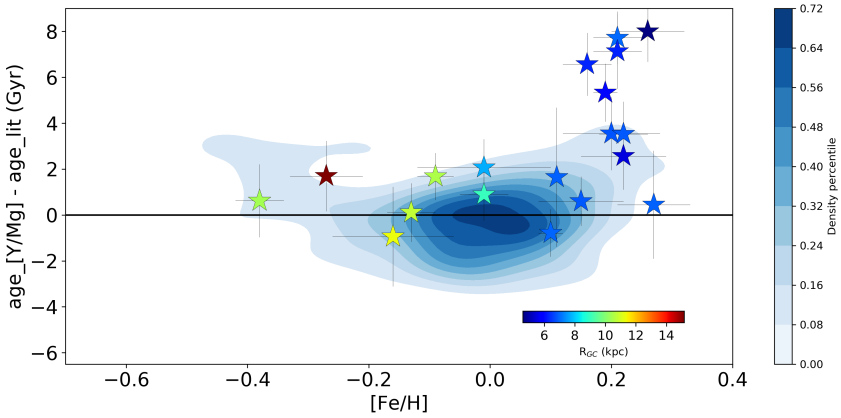

Fig. 5.9: Residuals between the chemical-clock ages from [Y/Mg] and the literature ages as a function of [Fe/H]. The contours represent the density of the sample of solar-like stars, while the stars represent the open clusters, colour-coded by R_{GC}.

the stellar yield is particularly important for neutron-capture elements produced through the s-process. Indeed, being secondary elements, the production of the s-process elements strongly depends on the quantity of seeds (iron) present in the star. However, at high metallicity the number of iron seeds is much larger than the number of neutrons. Consequently, in the super-solar metallicity regime, a less effective production of neutron-capture ele-

ments with respect to iron is predicted (Busso et al., 2001; Karakas & Lugaro, 2016). In addition, at high metallicity there might be a lower number of thermal pulses during the AGB phase, with a consequent lower final yield of s-process elements (see, e.g. Goriely & Siess, 2018). Moreover, the production of Mg also depends on metallicity, in particular at high [Fe/H] where stellar rotation during the latest phases of the evolution of massive stars increases the yield of Mg (Romano et al., 2010; Magrini et al., 2017). The interplay between the stellar yield and the metallicity of progenitors produces a different evolution at different Galactocentric distances.

The combination of these dependencies points toward a relation between [Y/Mg], or in general [s/α], and age that changes with Galactocentric distance. Following the suggestions of Feltzing et al. (2017), we first study the stellar dating relations from chemical clocks for a sample of the solar-like stars in the solar neighbourhood, considering a large metallicity range to investigate their metallicity dependence. This was discussed in Sect. 5.3.

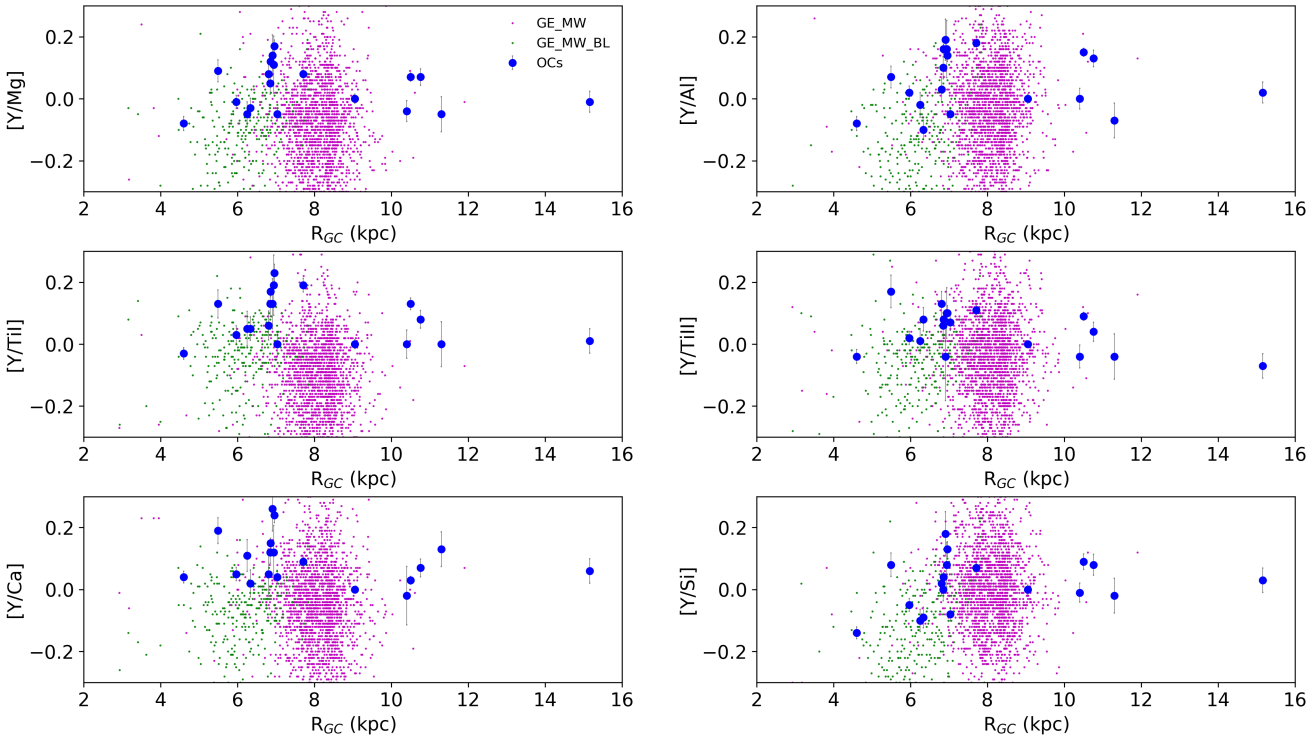

Fig. 5.10: Chemical clocks, including yttrium, as a function of Galactocentric distance. The filled circles represent the open clusters, while the small dots represent field stars in the solar neighbourhood (magenta) and in the inner regions of the disc (green).

Here, we present the analysis of stars located far away from the solar neighbourhood using a sample of open clusters observed by the Gaia-ESO with a precise determination of age and distance. The sample gives us important indications on the variation of the [s/α] in different parts of the Galaxy. In Fig. 5.10, we present different abundance ratios in OCs, including yttrium, as a function of Galactocentric distance R$_{GC}$. The ratio [s/α] decreases with decreasing Galactocentric radii for R$_{GC}$ < 6 kpc, exhibits a maximum around the solar radius (except for [Y/Ca]) and then shows a slight decrease with increasing distance for R$_{GC}$ > 9 kpc. Moreover, along the OC data, we also plot the Gaia-ESO samples of inner disc stars (labeled with GE_MW_BL in the GES survey) and those from the solar neighbourhood

(GE_MW). We calculate their Galactocentric distances from coordinates RA, DEC, and parallaxes of *Gaia* DR2 as explained in Sect. 5.1.5. Field stars show a behaviour that is similar to that of the OCs, with a lower [Y/Mg] for the inner Milky Way populations (i.e. for $R_{GC} < 8$ kpc). It is interesting to notice that in the inner disc, the bulk of field stars, usually older than stars in clusters, show an even lower [s/α] than the open cluster stars.

5.5.1. THE OVERPRODUCTION OF S-PROCESS ELEMENTS AT HIGH [FE/H]

As shown in the previous sections, stars with the same age but located in different regions of the Galaxy have different composition. Thus, the stellar dating relations between abundance ratios and stellar ages based on a sample of stars located in limited volumes of the Galaxy cannot be easily translated into general stellar dating relations valid for the whole disc. The driving reason for this is that the SFH strongly effects the abundances of the s-process elements and the yields of low- and intermediate-mass stars depend non-monotonically on the metallicity (Feltzing et al., 2017). This effect was already noticed by Magrini et al. (2018, see their Fig. 11), where [Y/Ba] versus age was plotted in different bins of metallicity and Galactocentric distance. The innermost bin, dominated by metal rich stars, shows a different behaviour with respect to the bins located around the solar location.

We include the literature s-process yields (see, e.g. Busso et al., 2001; Maiorca et al., 2012; Cristallo et al., 2011; Karakas & Lugaro, 2016) in our Galactic Chemical Evolution (GCE) model (Magrini et al., 2009). In Fig. 5.11, we show, as an example, the results of the chemical evolution of Magrini et al. (2009) in which we have adopted the yields of Maiorca et al. (2012). The three curves give the relations between stellar age and [Y/Mg] at three different Galactocentric distances (inner disc, solar neighbourhood, and outer disc). The GCE models at R_{GC} of 9 kpc and 16 kpc show a similar trend and reproduce the pattern of OCs and solar-like stars very well. The agreement is completely lost at R_{GC}=6 kpc, where the faster enrichment of the inner disc for GCE produces a higher [Y/Mg], which is not observed in the open clusters.

Similar results are obtained adopting the yields from the FRUITY database (Domínguez et al., 2011; Cristallo et al., 2011), and from the Monash group (Lugaro et al., 2012; Fishlock et al., 2014; Karakas & Lattanzio, 2014; Shingles et al., 2015; Karakas & Lugaro, 2016; Karakas et al., 2018) in the GCE. As shown in Fig. 5.12, in which the yields of yttrium Y are shown in different bins of metallicity Z for different stellar masses (1.3, 1.5, 2, 2.5, 3, 4, 5 $M_{\odot}$), we can see that in the first two sets of yields the production of s-process elements increases at high metallicity. This produces an increasing abundance of s-process elements in the inner disc, which is not observed in the abundances of the open cluster sample. The yields by Maiorca et al. (2012) have a flatter trend with the metallicity, which is not able to reproduce the behavior of open clusters with R_{GC}<7 kpc. A similar result is shown in Griffith et al. (2019), where the median trends of Y, Ba, and La exhibit peaks near solar [Mg/H] and plateaus at low metallicity, and a decreasing trend at high [Mg/H]. These latter authors explain their finding as the result of a metallicity dependence on AGB yields, but they do not consider the different SFH of each radial region of the Galaxy.

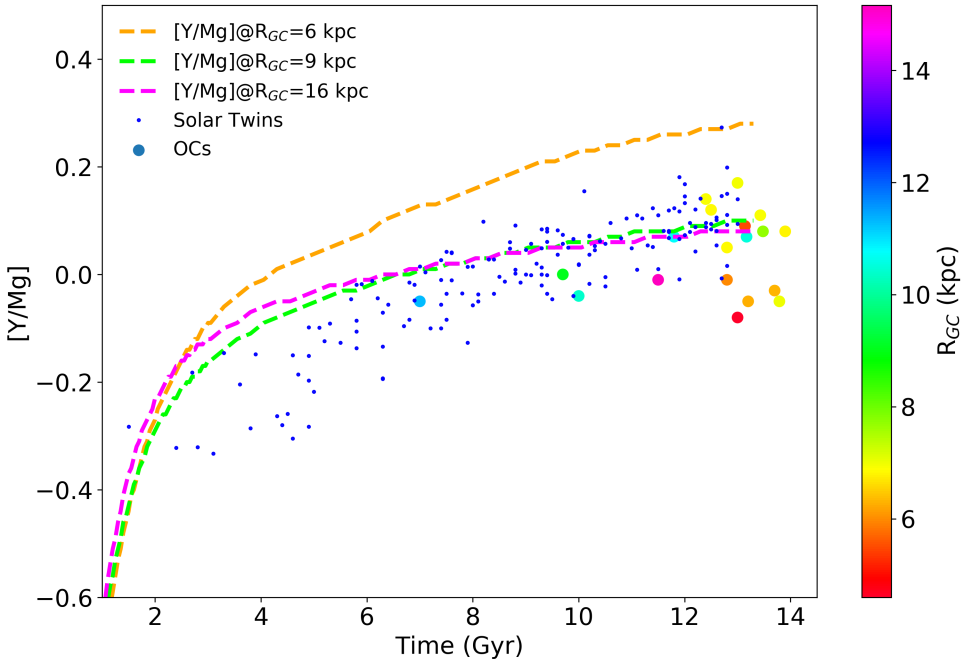

Fig. 5.11: [Y/Mg] vs. time of Galactic evolution. The lines represent the chemical evolution models computed to different Galactocentric distances. The small blue dots are the solar-like stars, while the filled circles, colour-coded by R_{GC}, are the open clusters.

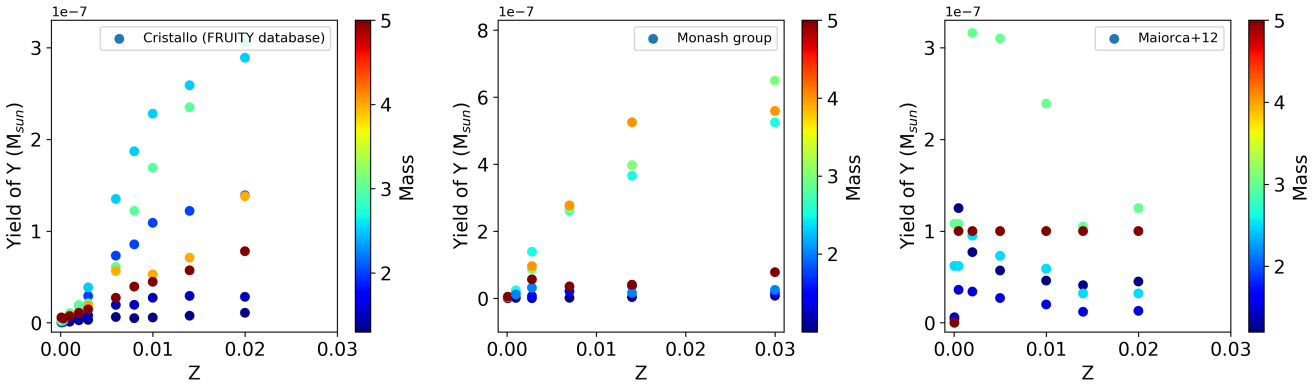

Fig. 5.12: Comparison of yields of Y from the FRUITY database, the Monash group, and Maiorca et al. (2012) as a function of metallicity Z. The circles are colour-coded by stellar mass.

5.5.2. A SUGGESTION FOR THE NEED FOR NEW S-PROCESS YIELDS AT HIGH METALLICITY

We investigate which set of *empirical* yields is necessary to reproduce the observed lower trends, i.e. [Y/Mg] or [Y/Al] versus age, in the inner disc than in the solar neighbourhood. The s-process element yields depend on the metallicity in two different ways; that is, they depend *(i)* on the number of iron nuclei as seeds for the neutron captures, and *(ii)* on the flux of neutrons. The former decreases with decreasing metallicity, while the latter increases because the main neutron source – ^{13}C – is a primary process. ^{13}C is produced

by mixing protons into the He-shell present in low-mass AGB stars, where they are captured by the abundant ^{12}C, which itself is produced during the 3α process (also a primary process). This means that the amount of ^{13}C does not depend on the metallicity. The neutron flux depends (approximately) on ^{13}C/^{56}Fe, which increases with decreasing metallicity. This means there are more neutrons per seed in low-metallicity AGB stars and less in high-metallicity AGB stars (see Busso et al., 2001; Karakas & Lugaro, 2016). Consequently, we should expect less s-process elements to be produced at high metallicity.

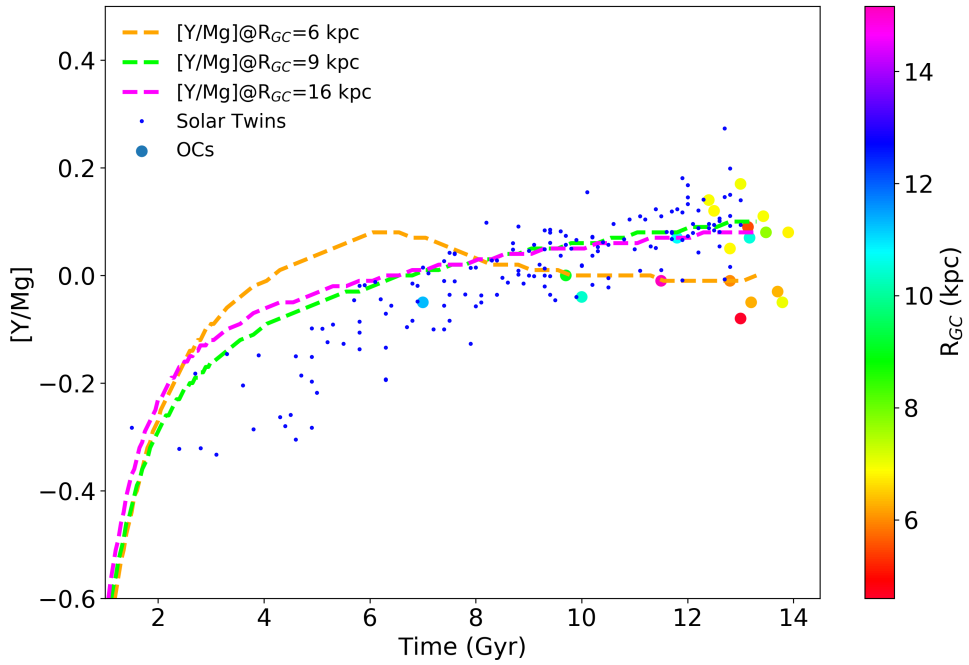

Fig. 5.13: [Y/Mg] vs. time of Galactic evolution. The lines represent the chemical evolution models computed to different Galactocentric distances where the stellar yields are suppressed. Symbols as in Fig. 5.11.

We tested a set of yields to investigate their behaviour at high metallicity. Yields for subsolar metallicities were left unchanged from their Maiorca et al. (2012) values, while we depressed the yields at super-solar metallicity by a factor of ten. In Fig. 5.13, we show the time evolution of [Y/Mg] in three radial regions of our Galaxy adopting our *empirical* yields for Y. The curves at 9 and 16 kpc are the same as those shown in Fig. 5.11 computed with the original yields of Maiorca et al. (2012), while the curve at R_{GC} = 6 kpc is affected by the depressed yields at high metallicity. If the Y production in those regions was indeed less efficient with respect to the production of Mg, we would therefore have a lower [Y/Mg]. Clearly, this is simply an empirical suggestion that needs a full new computation of stellar yields for low- and intermediate-mass AGB stars. However, there are also other possibilities, such as for instance the adoption of yields for Mg and Y that take into account the stellar rotation in massive stars; these yields are higher at high metallicity because of a more efficient rotation. The rotating massive stars produce the s-process elements preferentially at the first peak (Sr, Y and Zr) during the hydrostatic phase, and then expel the elements at collapse, suggesting that the production of Y and Mg might be coupled. The

combined production of Y and Mg might produce a global flattening in the trend of [Y/Mg] versus age at high-metallicity. An exhaustive discussion of the origin of the change of slope of the relation between [Y/Mg] and age is outside the scope of the present paper. However, it is clear that a revision of the s-process yields at high metallicity is necessary to explain the current data.

5.6. APPLICATION TO FIELD STARS

We conclude that the stellar dating relations from chemical clocks derived through a multivariate linear regression in Sect. 5.3.2 are not valid throughout the whole Galaxy, but can only be applied in the solar neighbourhood. A natural application of our stellar dating relations is to the high-resolution sample of solar neighbourhood stars observed with UVES by the Gaia-ESO (see Stonkutė et al., 2016, for the definition of the target selection). The selection of stars in a limited volume close to the Sun allows us to use the relations built from our solar-like stars located in a similar region.

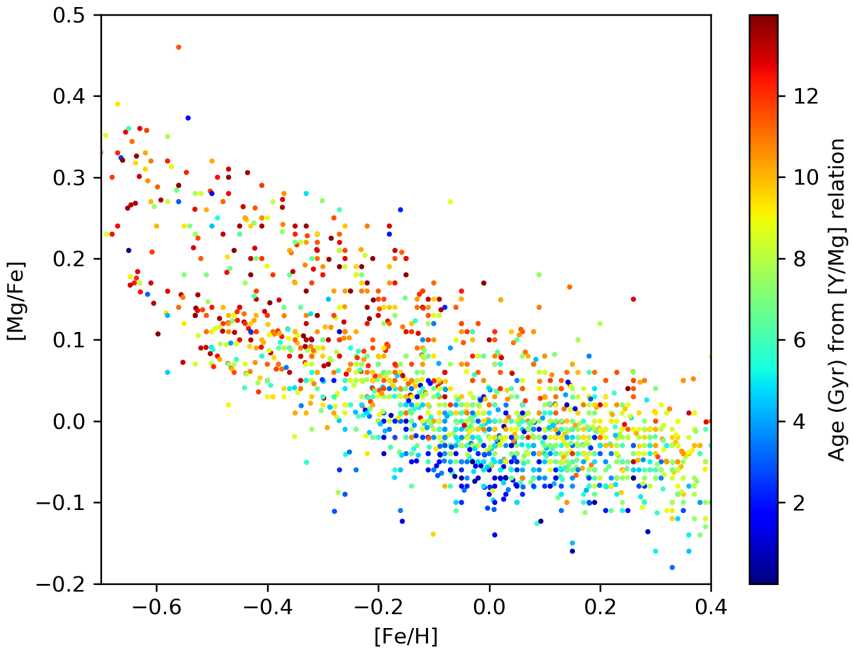

Fig. 5.14: [Mg/Fe] vs. [Fe/H] of solar neighbourhood stars present in the Gaia-ESO. The stars are colour-coded according to their age computed with the stellar dating relation [Y/Mg]–[Fe/H]–age.

We select stars present in the Gaia-ESO survey with the `GES_TYPE` "GE_MW", that is stars belonging to the solar neighbourhood. This sample is mainly composed of stars in the evolutionary phases around the turn-off. For each of them, we derived their age using the stellar dating relation $\text{Age} = 5.245 + 5.057 \cdot [\text{Fe/H}] - 32.546 \cdot [\text{Y/Mg}]$, where [Fe/H] and [Y/Mg] are known from the GES survey. Figure 5.14 shows [Mg/Fe] versus [Fe/H] for this sample in the range of metallicity of our solar-like stars, $-0.7 \leq [\text{Fe/H}] \leq 0.4$, where each field star is colour-coded by its age. There is a clear dichotomy between thin- and thick-disc stars and

an evident gradient in age along the thin disc, as already shown by Titarenko et al. (2019), who traced the differences between the two discs with [Y/Mg]. The oldest stars are present in high-α thick disc, while the youngest stars are located in the thin disc. The average age of thin-disc stars increases with decreasing [Fe/H] and increasing [Mg/Fe]. We obtained a similar result as shown in Fig. 4.13 in the Chapter 4, where we plotted giant field stars in the [α/Fe] vs. [Fe/H] plane colour-coded by age calculated using the [C/N] chemical clock.

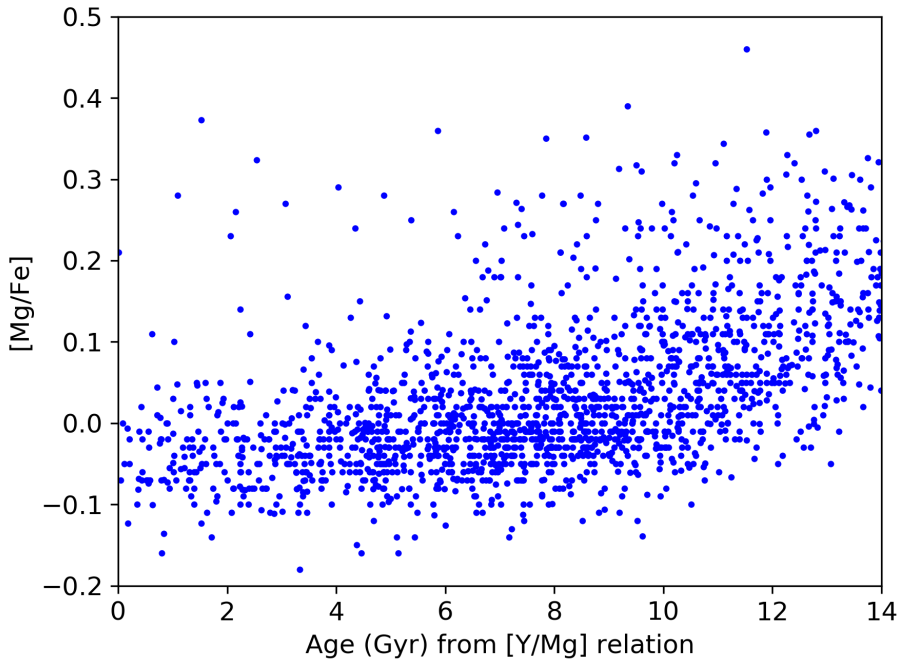

Fig. 5.15: [Mg/Fe] vs. age of solar neighbourhood stars present in the Gaia-ESO deduced from the stellar dating relation [Y/Mg]–[Fe/H]–age.

This dichotomy is also clear if we plot [Mg/Fe] as a function of the age inferred in this work using the dating relation [Y/Mg]–[Fe/H]–age. In Fig. 5.15, we can see how stars up to 8 Gyr show a similar content of [Mg/Fe] around the solar value, while beyond 8 Gyr their [Mg/Fe] ratios begin to increase with increasing age (Bensby et al., 2014). This difference in [Mg/Fe] clearly represents the dichotomy between thin and thick disc, where stars with an approximately solar [Mg/Fe] value belonging to the thin disc are younger than [Mg/Fe]-rich stars lying in the thick disc. In particular, the slope changes about 8 Gyr ago, during the epoch where the thin disc started to form (Bensby et al., 2014; Helmi et al., 2018).

5.7. SUMMARY AND CONCLUSIONS

This Chapter, based on the paper (Casali et al., 2020b), shows our results on the second family of chemical clocks listed in the Chapter 3.

In detail, we present the differential line-by-line analysis of high-quality HARPS spectra of a sample of solar-like stars (with parameters close to the solar ones for T_{eff} and log g), with metallicity [Fe/H] spanning from −0.7 to +0.4 dex. We obtain precise estimates of their

atmospheric parameters (T_{eff}, log g, [Fe/H] and ξ) and abundances of 25 elements and/or ions (24 abundance ratios over iron). We derive their ages through isochrone fitting.

We investigate the relations between [X/Fe] and stellar age, confirming strong correlations between [X/Fe] and stellar age for the s-process (negative slope) and α-elements (positive slope), while for the iron-peak elements the relations are nearly flat.

We select the best abundance ratios (higher correlation coefficients), which are usually the ratios involving an s-element and an α-element. We perform a multivariate linear regression for 17 different ratios taking into account the metallicity dependence. We compare our results with the literature, finding good agreement.

To check the validity of our relations outside the solar neighbourhood, we apply them to the sample of open clusters in the Gaia-ESO survey located at a wide range of Galactocentric distances 4 kpc<R_{GC}<16 kpc. The literature ages obtained from isochrone fitting of the full cluster sequence of clusters located at R_{GC}>7 kpc are in good agreement, on average, with the ages derived from our stellar dating relations. On the other hand, the ages derived for the innermost OCs at R_{GC}<7 kpc are much older than the literature ones. This different behaviour points towards different [s/α]–[Fe/H]–age relations depending on the location in the disc. In principle, we might expect that, combining the enrichment timescales of the s-process and α-elements, younger stars should have higher [s/α] ratios than older ones. However, this does not happen everywhere in the disc in the same way: [s/α] for the youngest and most metal-rich stars in the inner regions is lower than that of stars in the solar neighbourhood with similar ages. This discrepancy might be related to two different aspects: *(i)* the different SFHs, with a consequently different distribution in age and metallicity of the stellar populations in each region, and *(ii)* the strong and non-monotonic metallicity dependence of the s-process stellar yields. The latter is related to the secondary nature of the s-process elements, whose yields depend on the number of iron seeds and on the flux of neutrons.

The s-process yields present in the literature (Maiorca et al., 2012; Karakas & Lugaro, 2016; Cristallo et al., 2011) are not able to reproduce the Y abundances of stars and star clusters in the inner disc. We investigate the use of a set of empirical yields introduced in our GCE model for the Milky Way (Magrini et al., 2009) to reproduce the observed trends, namely a lower [s/α] in the inner disc than in the solar neighbourhood. To reproduce the inner disc clusters, a reduced production of yttrium by a factor of ten at high metallicity is required. Another possibility could be to include stellar rotations in massive stars, which might affect both s-process and Mg abundances at high metallicity.

Finally, we apply our [Y/Mg]–[Fe/H]–age relation to the field stars observed with UVES in the Gaia-ESO survey, specifically those located in the solar neighbourhood, in order to derive their ages. The ages derived with our relation confirm the dichotomy in age between the thin and thick disc, as shown in the [Mg/Fe] versus [Fe/H] plane, similar to what was found in the previous Chapter and in Casali et al. (2019). This immediate application confirms the potential power of chemical clocks to improve our knowledge of stellar ages.

With the present work, we confirm the existence of several relations between abundance ratios and stellar ages. These relations have a secondary dependence on metallicity, which can be taken into account. These relations, built from a sample of stars located in the solar neighbourhood, cannot be applied to star clusters located in regions of the Galaxy with different SFH, in particular in the inner disc. The [Y/Mg]–[Fe/H]-age relation, and

similar relations involving s-process elements and α- elements, are not universal. Their form depends on the location in the Galaxy. The reasons for this may be found in the differences in the SFHs (peaks of the age and metallicity distribution function) and in the non-monotonic dependence of the s-process yields on metallicity. A better understanding of the s-process in the supersolar-metallicity regime in low- and intermediate-mass AGB stars is indeed also necessary to clarify the use of abundance ratios as chemical clocks.
This failure of the employment of the chemical clocks to determine the stellar ages does not concern the age indicator [C/N] (Casali et al., 2019). In fact, [C/N] is related to stellar evolution, and only to a minor extent to global Galactic evolution.

6

STELLAR POPULATION ASTROPHYSICS (SPA) WITH TNG

In this Chapter, I present the results on my contribution in the Large observing programme, called Stellar Population Astrophysics (SPA) at the Telescopio Nazionale Galileo (TNG) in Canary Islands. The aim of this project is a full characterisation of the chemistry of nearby clusters and, together with other large spectroscopic surveys, will provide the framework for a comprehensive chemo-dynamical modelling of the disk formation and evolution.

The results presented in this Chapter are described in the paper Casali et al. (2020a) published in the scientific journal *Astronomy & Astrophysics*, volume 643, page A12.

6.1. INTRODUCTION

This project is focused on star clusters, the most versatile astronomical objects. Within our Galaxy, they play a key role in the study of both stellar and Galactic evolution, as we can see in the Chapter 1: they allow us to study the formation and evolution of stars (e.g. Krause et al., 2020; Krumholz & McKee, 2020), the dynamics of stellar systems (e.g. Sacco et al., 2017b; Kuhn et al., 2019; Piatti et al., 2019), and they provide robust constraints on the formation timescales and the chemical and dynamical history of the Milky Way (e.g. Friel et al., 2002; Bragaglia & Tosi, 2006; Magrini et al., 2009; Reddy et al., 2016; Jacobson et al., 2016; Spina et al., 2017; Casamiquela et al., 2019; Zhong et al., 2020; Donor et al., 2020; Chen & Zhao, 2020).

A large number of star clusters are included among the targets of the large spectroscopic surveys. In particular, the latest internal release of Gaia-ESO survey provides data for 81 open clusters, in most cases with more than 100 member stars; APOGEE DR16 presently has spectra for 128 open clusters (Donor et al., 2020), but generally with only a few stars per cluster; WEAVE, which will begin soon, will target about 300 open clusters. The observations of large spectroscopic surveys, together with *Gaia* data, have improved our understanding of Galactic chemical evolution (e.g. Magrini et al., 2017, 2018; Donor et al., 2020), the Milky Way structure (e.g. Meingast et al., 2019; Cantat-Gaudin et al., 2020; Castro-Ginard et al., 2020; Anders et al., 2020) and the cluster formation and disruption processes (e.g. Sacco et al., 2017a; Bravi et al., 2018; Piatti et al., 2019). In addition, *Gaia* has enabled

the discovery and characterisation of a large number of clusters in the solar neighbourhood and beyond (Cantat-Gaudin et al., 2018a,b, 2020; Sim et al., 2019; Liu & Pang, 2019; Castro-Ginard et al., 2018, 2020), and at the same time has allowed some candidate clusters to be discarded (see e.g. Kos et al., 2018; Cantat-Gaudin & Anders, 2020, for discussion), and several extended structures to be identified, such as strings and filaments, which are often connected to known clusters (e.g. Kounkel & Covey, 2019), streams (e.g. Meingast et al., 2019), extended halos (e.g in M67 by Carrera et al., 2019), and tidal tails (e.g. in Praesepe by Röser & Schilbach, 2019). *Gaia* data, in combination with spectral information on kinematics (from radial velocities) and abundances, are driving a revolution in the study of open clusters and, in general, of the whole Milky Way.

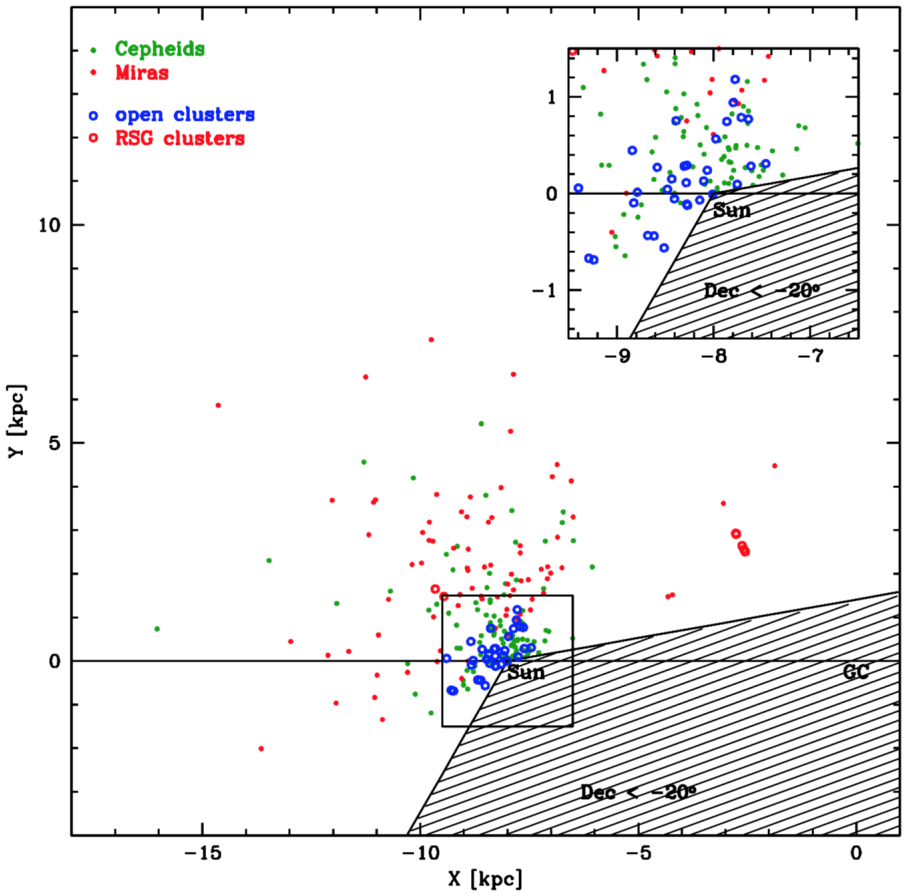

Fig. 6.1: Location of the proposed targets in the Galactic plane. The shaded area indicates the disc region not accessible from the TNG. The sample is composed by 105 Cepheids (green dots) and 82 Mira (red dots) variables, 8 young RSG clusters (red circles) and 32 OCs (blue circles).

In this framework, the aims of the Stellar Population Astrophysics (SPA) project, an ongoing Large Programme running on the 3.6 m Telescopio Nazionale Galileo (TNG) at the Roque de los Muchachos Observatory (La Palma, Spain), are to contribute to our understanding of the star formation and chemical enrichment history of our Galaxy by providing high-resolution spectra of a sample of stars in the Solar neighbourhood. The SPA project is obtaining high-resolution spectra of 532 stars, covering a wide range of ages and properties (see Origlia et al., 2019, for a general description), such as Cepheids and stars in both

young and old open clusters of spectral type from A to K (see Fig. 6.1 to see their location in the Galactic disc). In particular, the sample is formed by 80 young ($t < 300$ Myr) Classical Cepheids, 82 intermediate age (from several hundreds of Myrs to several Gyrs) Miras, and 25 old ($t > 10$ Gyr) type II Cepheids, in the Galactocentric range of 4–17 kpc; 75 red supergiants hosted in six young ($t \sim 10$ Myr) clusters/associations; 170 bright main sequence stars of AFGK spectral types and 70 more evolved stars hosted in 32 open clusters, within 1.5 kpc from the Sun and with age ranging from a few tens Myrs to a few Gyrs. These stars are observed in the optical and near-infrared (NIR) bands at high spectral resolution using GIARPS, a combination of HARPS-N and GIANO-B echelle spectrographs. The combination of HARPS-N and GIANO-B, covering the full optical and NIR range out to the K band, can allow our community to provide the first, comprehensive age-resolved chemical map of the Solar neighborhood and the thin disc over almost its entire extension, as seen from the Northern hemisphere at a spectral resolution $R > 50,000$. The aim of SPA is to obtain a large variety of elemental abundances in order to seek possible global trends, such as for example [X/Fe]–age relations. Chemical characterisation combined with the kinematic counterpart from *Gaia* and other surveys will provide a framework for a comprehensive chemo-dynamical modelling of disc formation and evolution in the Solar vicinity. The present study is part of a series of papers dedicated to the results of the SPA project. So far, the series includes a paper on the red supergiants in Alicante 7 and Alicante 10 (Origlia et al., 2019), and studies of the young open clusters ASCC 123 (Frasca et al., 2019) and Praesepe (D'Orazi et al., 2020). Part of our goal is to gain kinematic and chemical information on open clusters that have never been studied before or for which very little spectroscopic data is available. This is the case of the four clusters presented here, Collinder 350, Gulliver 51, NGC 7044, and Ruprecht 171. One of them, Gulliver 51, is a new cluster discovered using *Gaia* DR2 data (Cantat-Gaudin et al., 2018a), while only one star was observed spectroscopically in Collinder 350, and NGC 7044 has only been studied with low-resolution spectra.

6.2. THE CLUSTER SAMPLE

The SPA project is observing a large sample of nearby star clusters, allowing complete characterisation of the open clusters located in the Solar neighbourhood. Most of these clusters are located within 1.5-2 kpc of the Sun in order to match the zone where *Gaia* data reach their highest precision. We need to obtain, in a reasonable amount of time, sufficiently high S/N to permit precise abundance determination from spectra at the very high resolution of GIARPS. This means that our magnitude limit is about $G = 12 - 12.5$ mag. The targets are main sequence stars in the closer and younger clusters and giant stars in the older ones. In general, we try to target stars on the red clump, because they are suitable for precise analysis and constitute a homogeneous sample with many other previous projects (e.g. Bragaglia, 2008; Casamiquela et al., 2019, for the BOCCE and OCCASO projects, respectively). In a few cases, for interesting clusters that are more distant and/or extincted, only stars on the brighter part of the red giant branch can be observed.

In the present work, we discuss the analysis of four open clusters that are deemed important to characterise the nearby regions of our Galaxy because of their location and age, but for which very little spectroscopic data are available. Their ages range between 0.3 and

3 Gyr and they are located from ~300 pc to about 3300 pc from the Sun at different Galactocentric distances and altitudes above the Galactic plane.

Collinder 350 was listed for the first time in the catalogue of Collinder (1931), but the first study of its properties was presented by Kharchenko et al. (2005). The cluster was also studied using *Gaia* DR1/TGAS data by Cantat-Gaudin et al. (2018b) and Yen et al. (2018, who derived an age of 1 Gyr). Pakhomov et al. (2009) obtained high-resolution spectroscopy of one star, indicated as HD161587 (our Cr350_1), and derived a metallicity of [Fe/H]= $+0.11 \pm 0.06$ dex together with the abundances of many species. Blanco-Cuaresma et al. (2015) and Blanco-Cuaresma & Fraix-Burnet (2018), also from one single star (at resolution R=80 000, with the NARVAL spectrograph), derived a lower value for the metallicity, [Fe/H]= -0.10 ± 0.01 (or 0, depending on normalisation) and 0.03 dex, respectively. On the other hand, there are no high-resolution spectroscopic observations of the other three clusters.

NGC 7044 has been studied using photometry several times in the past (see Kaluzny, 1989; Aparicio et al., 1993; Sagar & Griffiths, 1998), with a general consensus on its age of around 1.5 Gyr, and a high reddening. An estimate of the metallicity and radial velocity of ten member stars in NGC 7044 is provided by Warren & Cole (2009) using low-resolution spectroscopy and the IR Ca II triplet (CaT) technique. These authors derived a mean metallicity [Fe/H]= -0.16 ± 0.09 dex and a mean radial velocity RV= -50.56 ± 2.18 km s^{-1}.

Even less information is available for Ruprecht 171: after the classification by Ruprecht (1966), the cluster was studied by Tadross (2003) who derived an age 3.2 Gyr, a reddening $E(B-V) = 0.12$ mag, and a distance $d = 1140$ pc using the isochrone fitting of the NIR JHK_s photometric data.

Finally, Gulliver 51 was only recently discovered by Cantat-Gaudin et al. (2018a), who reported the serendipitous discovery of 60 candidate clusters based on *Gaia* DR2 data, which were named 'Gulliver'. They were identified as groups of stars with coherent proper motions and parallaxes, and a more concentrated distribution on the sky than the field population. An age of 0.8 Gyr, reddening $E(B-V) = 0.375$ mag, and a distance of 1330 pc were attributed to Gulliver 51 by Monteiro & Dias (2019) based on automated isochrone fitting to *Gaia* DR2 colour-magnitude diagrams (CMDs).

For the first three clusters, distance, reddening, age, and proper motions are reported in the catalogue of Kharchenko et al. (2013). All have updated values by Cantat-Gaudin et al. (2018a, 2020) using *Gaia* DR2 data. Table 6.1 gives the coordinates, proper motions (μ_α, μ_δ), parallax, distance (d), Galactocentric distance ($R_{\rm GC}$), altitudes above the Galactic plane (z), extinction (A_V), and age of the clusters by Cantat-Gaudin et al. (2020). Figure 6.2 shows the CMDs of the four clusters, in which the stars observed by the SPA project are highlighted.

This is the first work dedicated exclusively to these four clusters. In this work we provide, for the first time (except for Collinder 350, for which high-resolution spectroscopy of a single star is available), results based on high-resolution spectroscopy for a number of candidate members in each cluster. Our aim is to perform a full characterisation in terms of atmospheric parameters and chemical abundances.

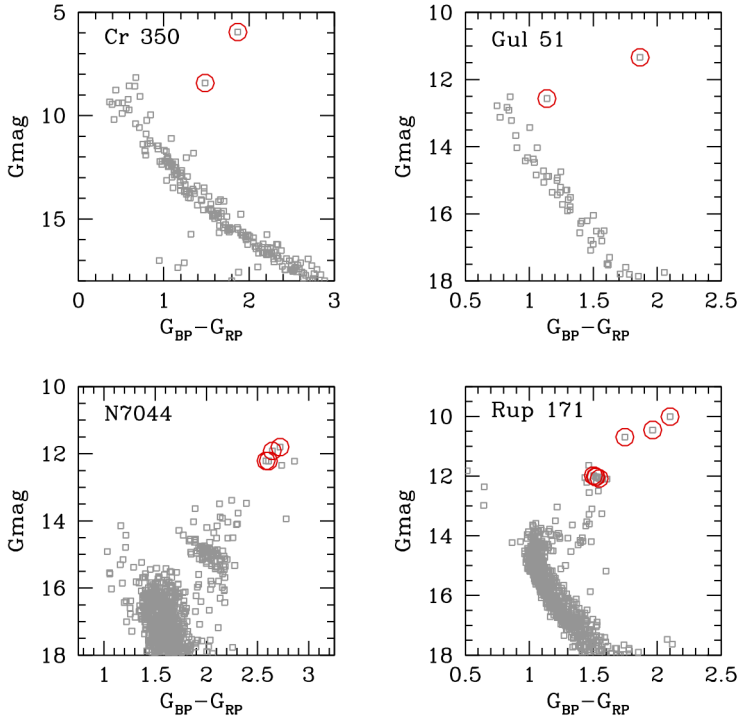

Fig. 6.2: Colour-magnitude diagrams with *Gaia* DR2 photometric data (G_{mag} vs. $G_{BP}-G_{RP}$) of the four clusters. The red circles indicate the member stars observed by SPA project.

Cluster	R.A. (J2000)	Dec.	μ_α (mas yr^{-1})	μ_δ (mas yr^{-1})	parallax (mas)	log(Age) (yr)	A_V (mag)	d (pc)	R_{GC} (kpc)	z (pc)
Collinder 350	17:48:14.26	+01:20:25.42	-4.965 ± 0.387	-0.019 ± 0.243	2.708 ± 0.129	8.77	0.52	371	8.02	94
Gulliver 51	02:01:20.40	+63:48:03.60	-4.892 ± 0.097	-0.149 ± 0.079	0.647 ± 0.026	8.56	1.42	1536	9.41	52
NGC 7044	21:13:08.16	+42:29:38.40	-4.978 ± 0.142	-5.526 ± 0.151	0.273 ± 0.078	9.22	1.78	3252	8.73	−235
Ruprecht 171	18:32:02.88	−16:03:43.20	$+7.677 \pm 0.187$	$+1.091 \pm 0.165$	0.620 ± 0.066	9.44	0.68	1522	9.41	52

Table 6.1: Parameters of the open clusters sample from Cantat-Gaudin et al. (2020).

6.3. OBSERVATIONS AND DATA SAMPLE

We select high-probability member stars among the red giant branch (RGB) and red clump (RC) stars. The membership probability was taken from Cantat-Gaudin et al. (2018a) who used *Gaia* DR2 proper motions and parallaxes. The observations of these four clusters were conducted from 18 to 22 August 2018 and from 10 to 15 August 2019 with GIARPS using both the optical echelle spectrograph HARPS-N (R ~ 115 000, spectral range = 0.39 – 0.68 μm, Cosentino et al., 2014) and the NIR spectrograph GIANO-B (R ~ 50 000, spectral range = 0.97 – 2.45 μm, Oliva et al., 2006). The spectra were acquired with total exposure times ranging from 600 to 7200 seconds depending on the star brightness, in order to reach an S/N per pixel at red wavelengths of $S/N > 30$. Exposure times longer than 1800 seconds were usually split into two or three sub-exposures to reduce the contamination of cosmic rays and to avoid saturation. The stars analysed in the present work are shown in Table 6.2 with their coordinates, *Gaia* magnitudes, parallax, radial velocity (RV), exposure time, and S/N. The RV was measured by cross-correlating the target spectrum with a template, which was chosen as the synthetic BT-Settl spectrum (Allard et al., 2011) with $T_{\rm eff}$ and $\log g$ closer

to the target. Very broad lines, such as Na I D_2 and Balmer lines, as well as strong telluric features were excluded from the cross-correlation function CCF analysis. For this task we used ad hoc software developed by us in the IDL environment. The CCF peak was fitted with a Gaussian to evaluate its centroid and full width at half maximum (FWHM). The RV error was estimated by the fitting procedure accounting for the CCF noise far from the peak. Here we only make use of HARPS-N spectra, which are better suited for our analysis methods (see following Sect. 6.5). GIANO spectra will be presented in a forthcoming paper.

Gaia DR2 ID	ID	R.A. (J2000)	Dec.	G (mag)	$BP-RP$ (mag)	RV (km s^{-1})	Exposure Time (s)	S/N	parallax (mas)
4372743213795720704	Cr350_1	266.603650	+1.044348	5.96	1.87	−14.57	600	172	2.910±0.061
4372572888274176768	Cr350_2	267.182595	+1.164203	8.42	1.48	−14.73	1800	158	2.770±0.074
517925575042048384	Gul51_1	30.326628	+63.79737	11.34	1.86	−57.36	7200	68	0.725±0.025
517953750028538240	Gul51_2	30.213987	+63.96327	12.57	1.14	–	7200	34	0.645±0.030
1969807040026523008	NGC7044_1	318.321873	+42.48457	11.80	2.72	−49.88	7200	46	0.336±0.034
1969807276235623552	NGC7044_2	318.330484	+42.50797	11.92	2.64	−49.15	7200	36	0.216±0.035
1969806073644788992	NGC7044_3	318.397775	+42.46081	12.21	2.58	−49.45	7200	34	0.280±0.032
1969800576086654592	NGC7044_4	318.256943	+42.40348	12.22	2.61	−49.44	7200	31	0.333±0.035
4103073693495483904	Rup171_1	277.989813	−15.98095	10.01	2.10	5.55	3600	53	0.746±0.061
4102882309792631552	Rup171_2	278.022116	−16.13376	10.45	1.96	5.32	7200	66	0.638±0.046
4103072765721906816	Rup171_3	278.033168	−16.00760	10.69	1.75	6.84	7200	85	0.667±0.054
4103101073850814208	Rup171_4	278.054888	−15.87125	12.02	1.52	5.46	7200	53	0.626±0.044
4102884023383492096	Rup171_5	278.030396	−16.10391	12.03	1.52	6.03	7200	45	0.677±0.044
4103073418617487104	Rup171_6	278.013899	−15.99949	12.03	1.52	5.81	7200	38	0.629±0.043
4103072933225072512	Rup171_8	277.945748	−16.03430	12.06	1.53	6.28	7200	36	0.639±0.043

Table 6.2: Observed candidate member stars for the four clusters.

6.4. PHOTOMETRIC PARAMETERS

In Table 6.3, we present the photometric parameters $T_{\rm eff,Gaia}$ and log $g_{\rm Gaia}$ obtained from *Gaia* DR2 photometry and parallaxes, and the parameters obtained from the comparison with the best-fit isochrone ($T_{\rm eff,iso}$ and log $g_{\rm iso}$), projecting the *Gaia* colours and magnitudes on a set of PARSEC isochrones (Bressan et al., 2012). Our aim is to use these parameters as an input to estimate the spectroscopic ones. The photometric gravities from *Gaia* photometry are obtained using the same equation employed in the Chapter 5:

$$\log(g_{\rm Gaia}) = \log(M/M_{\odot}) + 0.4 \cdot M_{bol} + 4 \cdot \log(T_{\rm eff,Gaia}) - 12.505, \tag{6.1}$$

where $M/M_{\odot}$ is the stellar mass (in solar mass units) obtained as the mass at the main sequence turn off (MSTO) of the isochrones at their literature cluster age; and M_{bol} ($M_{bol} = -2.5 \cdot \log(L/L_{\odot}) + 4.75$) is the bolometric magnitude computed from the luminosity present in the *Gaia* DR2 catalogue (Li et al., 2018) and corrected considering the average distance for each cluster. In parenthesis in Table 6.3, we give the log g with M_{bol} computed with the luminosity corrected considering the individual distances derived by Bailer-Jones et al. (2018) and the mean extinction values of the clusters reported in Table 6.1; $T_{\rm eff,Gaia}$ is the photometric effective temperature from *Gaia* obtained with the calibration of giant stars by Mucciarelli & Bellazzini (2020) for the *Gaia* colour $BP-BR$. In first approximation, we consider solar metallicities for our clusters. As a test, we also re-compute the photometric effective temperatures using average metallicities from spectroscopic analysis, finding a negligible correction. For the coolest stars of the sample (all stars of NGC 7044 and Rup171_1),

as their $BP-RP$ colours fall outside the calibration range of Mucciarelli & Bellazzini (2020), we adopt the effective temperature of *Gaia* DR2 as $T_{\rm eff,\,Gaia}$, for which we are aware of the inadequacy, especially at those very low temperatures and for cluster members (see Andrae et al., 2018; Gaia Collaboration et al., 2018b). For clusters affected by high extinction and in crowded regions, the photometric parameters are indeed unreliable because of the spatial variations of the reddening, which is usually assumed to be constant, and because of the more difficult extraction of the fluxes of the individual stars. The photometric gravities of the four observed stars of NGC 7044, the most distant and extincted cluster of our sample, range from 0.8 to 1.34 dex (obtained with the individual distances), which is unexpected, because they have very similar colours and magnitudes (see Fig. 6.2). Their parallaxes have percentage errors larger than 10%, and they differ by more than 3σ from the mean cluster parallax. In addition, the individual extinctions available in *Gaia* DR2 (albeit suffering from the same limitation as *Gaia* DR2 $T_{\rm eff}$) vary from star to star, and are not available for all the cluster members. Therefore, the photometric parameters of the observed stars in NGC 7044 have to be considered as just a starting point for the following spectroscopic analysis. In a similar way, the two stars observed in Gul 51 both have high extinction in *Gaia* DR2, which varies from star to star ($A_G \sim 1$ mag for Gul 51_1 and more than 2.5 mag for Gul 51_2). We adopt the average cluster extinction as in Cantat-Gaudin et al. (2020), however differential extinction can significantly affect photometric stellar parameters, with strong effects on the photometric $T_{\rm eff}$ and $\log\, g$. In Ruprecht 171, we observed seven stars, four of them with very similar colours and magnitudes. This cluster is closer and less affected by extinction. The photometric parameters of the four hottest stars (Rup171_4-5-6-8) are indeed very similar. Finally, Collinder 350 is close and not significantly affected by extinction.

Regarding the stellar parameters $T_{\rm eff,iso}$ and $\log\, g_{\rm iso}$, we select the best isochrone for each cluster, starting from the cluster parameters of Cantat-Gaudin et al. (2020) and fine-tuning them with our grid of isochrones. The presence of high differential reddening produces, in some cases, differences between the two methods for estimating the photometric stellar parameters and confirms that they can only be used as priors for our spectroscopic analysis.

6.5. SPECTRAL ANALYSIS

We follow two different approaches to analyse our sample stars. The first one is a spectral analysis using the EWs with FAMA (Magrini et al., 2013a), while the second one is a spectral fitting with ROTFIT (Frasca et al., 2006, 2019).

Stellar spectroscopy and the DOOp and FAMA tools used in this Chapter are presented in more details in Appendix A.

6.5.1. EQUIVALENT WIDTH ANALYSIS WITH FAMA

We perform a spectral analysis based on the EWs to determine the atmospheric parameters and abundances of our sample stars. We measure the EWs of the spectral absorption lines with the DAOSPEC (Stetson & Pancino, 2008) tool in the form of DOOp (DAOSPEC Output Optimiser pipeline, an automatic wrapper; Cantat-Gaudin et al., 2014, see Sect. A.7). We use the master list of atomic transitions that was prepared for the analysis of the stellar

ID	$T_{\rm eff,Gaia}$ (K)	log $g_{\rm Gaia}$ (dex)	$T_{\rm eff,iso}$ (K)	log $g_{\rm iso}$ (dex)
Cr350_1	4030	1.24 (1.30)	4100	1.35
Cr350_2	4620	2.51 (2.54)	4880	2.71
Gul51_1	4453	1.90 (2.02)	4630	2.26
Gul51_2	6122*	2.93 (2.92)	6610	3.11
NGC7044_1	3825**	0.89 (1.04)	3850	0.98
NGC7044_2	3898**	0.98 (0.82)	3900	1.06
NGC7044_3	3929**	1.13 (1.14)	4000	1.23
NGC7044_4	4021**	1.20 (1.34)	4000	1.23
Rup171_1	3863**	1.25 (1.39)	3930	1.25
Rup171_2	3940	1.52 (1.53)	4090	1.54
Rup171_3	4220	1.68 (1.72)	4300	1.76
Rup171_4	4600	2.42 (2.41)	4750	2.52
Rup171_5	4600	2.43 (2.48)	4750	2.52
Rup171_6	4600	2.44 (2.43)	4750	2.52
Rup171_8	4600	2.38 (2.39)	4750	2.52

Table 6.3: Photometric stellar parameters from *Gaia* DR2 and PARSEC isochrones. (*) $T_{\rm eff}$ from the calibration of dwarf stars in Mucciarelli & Bellazzini (2020); (**) $T_{\rm eff}$ from *Gaia* DR2.

spectra for the Gaia-ESO survey (Heiter et al., 2015b). This line list includes quality flags, such as 'Y' (yes), 'N' (no), and 'U' (undetermined). These flags are assigned on the basis of the quality of the line profiles (at the spectral resolution of about 47000) and the accuracy of the log gf derived from the comparison of synthetic spectra with a spectrum of the Sun and Arcturus. If the profile of a given line is unblended in both the Sun and Arcturus and its log gf value is well determined, the flag will be 'Y/Y', and 'N/N' otherwise. In our analysis, we consider all lines, except those with 'N' for the log gf values. At high-spectral resolution, the line profile might differ from the Gaussian profile, especially for the strongest lines. However, this effect is usually negligible at least for EWs < 100−120 mÅ, which corresponds to the range we consider for the analysis, as discussed in Spina et al. (2020), who tested the effect of the use of a Voigt profiles in the measurement of the EWs of strong lines for HARPS spectra. The two measurements, that is those made with a Gaussian and those with a Voigt profile, are consistent, and the uncertainty due to the choice of the profile is negligible with respect to the uncertainty related to continuum placement.

We determine the atmospheric parameters with MOOG in the automatic form, FAMA (Fast Automatic MOOG Analysis, Magrini et al., 2013a, see Sect. A.7). FAMA uses MOOG in its 2014 version (Sneden et al., 2012) and MARCS model atmospheres (Gustafsson et al., 2008) to determine stellar parameters and to calculate abundances. It iteratively searches for the three equilibria: the ionisation equilibrium, excitation equilibrium, and minimisation of the trend between the reduced EW log(EW/λ) and the iron abundance. To avoid saturated and overly weak lines, in our analysis we only consider lines with 20 mÅ < EW < 120 mÅ for iron, and 5mÅ < EW < 120 mÅ for other elements.

Finally, FAMA computes the elemental abundances of Li, C, Na, Mg, Al, Si, Ca, Sc, Ti (I and II), V, Cr, Fe (I and II), Co, Ni, Y, Zr (I and II), La, Ce, and Eu.

In Table 6.4 we present the results of our spectral analysis in which the four stellar parameters ($T_{\rm eff}$, log g, [Fe/H], and ξ) are varied up to convergence. The errors in parenthesis for [Fe/H] are the errors on the abundances generated by the uncertainties in the determination of the atmospheric parameters (see Magrini et al., 2013a, for the errors estimate performed by FAMA). One of the stars of Gulliver 51 (Gul51_2) is a fast rotator, and therefore it cannot be analysed with FAMA; we compute its $v \sin i$ using ROTFIT and list this in Table 6.5. The results are presented in the left panel of Fig. 6.3.

ID	$T_{\rm eff}$ (K)	log g (dex)	[Fe/H] (dex)	ξ (km/s)
Cr350_1	4100±100	1.35±0.23	−0.24±0.02(±0.10)	1.76±0.10
Cr350_2	5170±110	2.85±0.27	−0.03±0.06(±0.10)	1.58±0.09
Gul51_1	4730±90	2.45±0.26	−0.08±0.04(±0.09)	1.52±0.08
NGC7044_1	3980±90	0.95±0.20	−0.42±0.02(±0.14)	1.93±0.09
NGC7044_2	3950±70	1.06±0.20	−0.36±0.02(±0.14)	1.91±0.11
NGC7044_3	4000±100	1.23±0.21	−0.36±0.03(±0.14)	1.73±0.13
NGC7044_4	4010±90	1.23±0.20	−0.35±0.02(±0.14)	1.82±0.10
Rup171_1	3950±90	1.18±0.21	−0.38±0.04(±0.14)	1.66±0.12
Rup171_2	4100±70	1.54±0.20	−0.20±0.03(±0.13)	1.57±0.08
Rup171_3	4300±80	1.76±0.22	−0.16±0.04(±0.10)	1.59±0.10
Rup171_4	4860±80	2.82±0.19	0.06±0.04(±0.10)	1.37±0.09
Rup171_5	4850±110	2.71±0.28	0.01±0.05(±0.10)	1.46±0.08
Rup171_6	4880±150	2.91±0.20	0.08±0.01(±0.10)	1.34±0.14
Rup171_8	4800±90	2.79±0.24	0.08±0.05(±0.09)	1.34±0.08

Table 6.4: Stellar parameters obtained with FAMA.

From the left panel of Fig. 6.3, we notice a trend between metallicity and $T_{\rm eff}$. In particular, the coolest (lowest log g) stars of our sample reach the lowest metallicities. For clusters with member stars spanning wide ranges in $T_{\rm eff}$ and log g (Ruprecht 171 and Collinder 350), the trends are particularly evident: three stars of Ruprecht 171 (Rup171_1, Rup171_2, Rup171_3) and one of Collinder 350 (Cr350_1) with $T_{\rm eff} < 4300$ K and log g between 1 and 1.8 dex have much lower metallicity than the other members of the same clusters. For clusters in which only cool giants are observed, such as NGC 7044, their [Fe/H] is lower than the literature value −0.16 dex (Warren & Cole, 2009). Moreover, given the location of the clusters close to the Sun and their age younger than 3 Gyr, we expect a metal content near to the solar one (within ±0.10, considering a slope of −0.07 dex kpc^{-1} for the radial metallicity gradient, see, e.g. Zhong et al., 2020, and references therein). This is indeed true for the hottest stars of our sample. For instance, the metallicity of Cr350_2 is [Fe/H]=-0.03 ± 0.06 in agreement within the errors with the literature value (+0.03 dex, Blanco-Cuaresma & Fraix-Burnet, 2018), and the mean metallicity of Rup171_4, Rup171_5, Rup171_6, Rup171_8, all RC stars, is slightly super-solar (mean value [Fe/H]= $+0.06 \pm 0.03$ dex).

The trends with $T_{\rm eff}$ and log g are thus general considering our sample clusters as a whole: stars located in the upper RGB, the coolest ones, are more metal-poor than stars located in RC. This topic is not new, since it has already been addressed in the analysis of

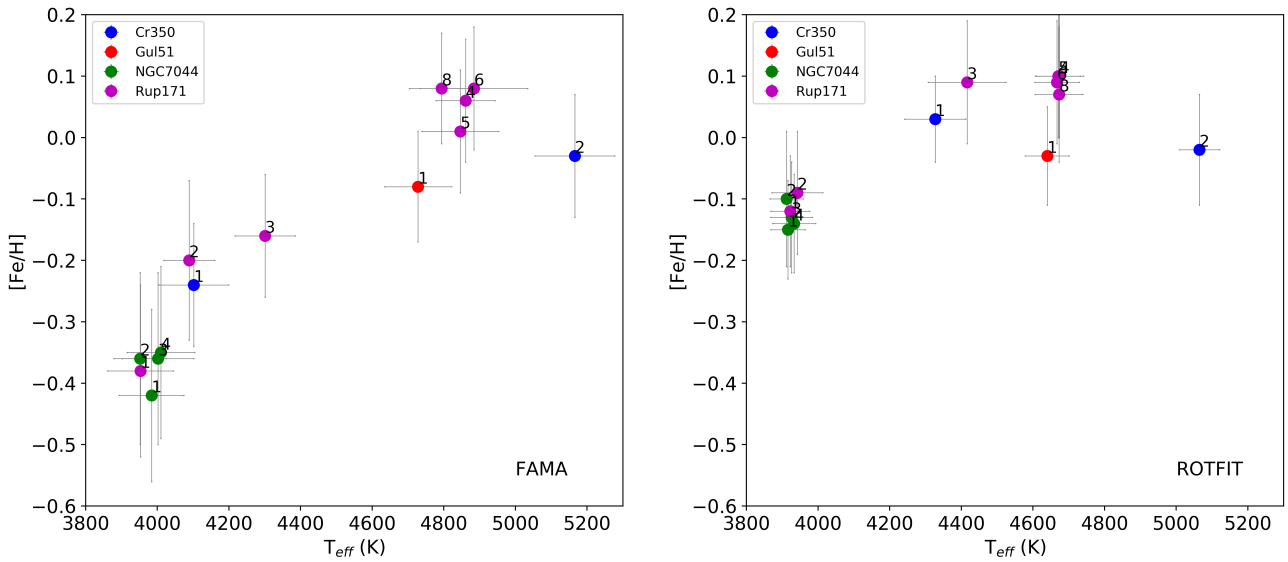

Fig. 6.3: [Fe/H] vs. $T_{\rm eff}$ for the results obtained with FAMA (left panel) and ROTFIT (right panel). The labels indicate the ID of each star member.

cool stars on the upper RGB (see, e.g. Worley et al., 2010; Worley & Cottrell, 2010) and is discussed in more detail in Sect. 6.6.

6.5.2. SPECTRAL ANALYSIS WITH ROTFIT

We also analyse our sample stars with the code ROTFIT (Frasca et al., 2006, 2019). ROTFIT uses a grid of template spectra and performs a χ^2 minimisation of the difference between the template and target spectrum in selected spectral regions. The grid of templates is composed of high-resolution spectra of stars with known parameters present in the ELODIE archive[1]. In order to use this grid, we need to degrade our HARPS-N spectra to the resolution of ELODIE (R = 42 000) and to resample them on the ELODIE spectral points ($\Delta\lambda = 0.05$Å).

The templates are aligned in wavelength with the analysed target spectrum through a cross-correlation function. They are broadened by convolution with a rotational profile of increasing $v \sin i$ to minimise the χ^2. For each analysed spectral region, the weighted average of the parameters obtained for the ten best templates is taken. In particular, we analyse 28 spectral chunks, each of 100 Å in width, in the wavelength range 4000–6800 Å. The final parameters ($T_{\rm eff}$, log g and the iron abundance [Fe/H]) are the average of the results of the individual spectral region, weighted according to the χ^2.

The atmospheric parameters, spectral type, and $v \sin i$ obtained with ROTFIT are presented in Table 6.5. With ROTFIT, we can also provide the atmospheric parameters of Gul51_2, the fast rotator that cannot be analysed with FAMA. It is a hot star and its $T_{\rm eff}$ and log g, derived by ROTFIT, are in agreement with the values of the TESS catalogue (Stassun et al., 2018): log $g = 4.12 \pm 1.54$ dex and $T_{\rm eff} = 7621$ K. The metallicity of this star is in agreement, within the errors, with the [Fe/H] of the other member star, Gul51_1. However, a very large error is associated with this value because of the lower S/N and its fast-rotator nature,

[1] http://atlas.obs-hp.fr/elodie/

and therefore we do not consider it in the computation of the mean value of metallicity of Gul 51.

The right panel of Fig. 6.3 shows the metallicity [Fe/H] as a function of $T_{\rm eff}$ for the ROTFIT results. The analysis with ROTFIT yields a smaller difference in [Fe/H] between cool and warm stars of the same cluster. However, there are some residual differences between the cooler stars (ID 1, 2) and the hotter ones in Ruprecht 171. Finally, as shown by Table 6.5 and Fig. 6.3, the metallicity obtained for NGC 7044 is in agreement with the CaT value.

ID	$T_{\rm eff}$ (K)	log g (dex)	[Fe/H] (dex)	Sp.Type	$v \sin i$ (km s^{-1})
Cr350_1	4330±90	1.28±0.24	0.03 ± 0.07	K3II	1.3±1.6
Cr350_2	5070±60	2.99±0.19	−0.02 ± 0.09	G8III	6.7±1.0
Gul51_1	4640±60	2.66±0.12	−0.03 ± 0.08	K0III	2.3±1.3
Gul51_2	7520± 298	4.06±0.23	−0.16 ± 0.13	A9IV	251.6±27.2
NGC7044_1	3920±50	1.53±0.16	−0.15 ± 0.08	K5III	2.0±1.8
NGC7044_2	3910±50	1.51±0.16	−0.10 ± 0.11	K5III	1.8±1.8
NGC7044_3	3930±60	1.50±0.19	−0.13 ± 0.09	K5III	1.7±1.7
NGC7044_4	3930±60	1.50±0.17	−0.14 ± 0.08	K5III	2.0±1.8
Rup171_1	3920±50	1.56±0.13	−0.12 ± 0.09	K5III	2.0±1.6
Rup171_2	3940±70	1.56±0.14	−0.09 ± 0.10	K3.5IIIb	1.6±1.6
Rup171_3	4420±110	2.13±0.43	0.09 ± 0.10	K2III	1.4±1.5
Rup171_4	4670±70	2.67±0.12	0.10 ± 0.10	K1.5III	0.7±0.9
Rup171_5	4670±60	2.66±0.13	0.10 ± 0.10	K1.5III	0.8±1.1
Rup171_6	4670±60	2.64±0.14	0.09 ± 0.10	K0III	1.0±1.2
Rup171_8	4670±60	2.64±0.14	0.07 ± 0.11	K1.5III	0.7±0.9

Table 6.5: Stellar parameters derived with ROTFIT.

6.6. THE COOL GIANT STARS

In this section, we investigate the causes of the low metallicities measured with the EWs in the cool giants. In principle, stars in open clusters should present a homogeneous chemical composition (see, e.g. Bovy et al., 2016), at least within some range, typically of few ~0.01 dex (cf. Liu et al., 2016; Spina et al., 2018a, for examples of the possible presence of some degree of inhomogeneity in open clusters). However, stars belonging to the same open cluster, but in different evolutionary stages, might display more notable differences in their chemical patterns. These differences can be due to physical phenomena, such as atomic diffusion and mixing (e.g. Lagarde et al., 2019; Casali et al., 2019; Bertelli Motta et al., 2017; Semenova et al., 2020), or to analysis effects, such as non-local thermodynamic equilibrium (NLTE) effects or correlations between atmospheric parameters and abundances (see, e.g. Blanco-Cuaresma et al., 2015, for a review). In addition, the analysis of cool giant stars can be affected by several complications, such as the presence of a forest of molecular lines, possible asymmetric shapes of the lines due to mass loss, deviations from hydrostatic equilibrium, the presence of giant convective cells, and the deviations from LTE (see, e.g.

Asplund, 2005; Bergemann & Nordlander, 2014). Here we discuss some aspects of the cool giant analysis, including the choice of the stellar parameters, the correction for NLTE, the selection of the line list, the adoption of the atmosphere models, and the continuum placement.

6.6.1. THE ROLE OF STELLAR PARAMETERS

We investigate the effect of adopting stellar parameters from *Gaia*, which are calculated based on their photometry, rather than the spectroscopic ones with FAMA which are based on the EW analysis. If there is indeed a deviation from the hydrostatic equilibrium, the gravity derived from the ionisation balance might be incorrect, and thus produce incorrect abundances. The simultaneous determination of the stellar parameters from spectroscopy can produce, for instance, a degeneration among those parameters, producing a correlation between log g and [Fe/H] (cf. Blanco-Cuaresma et al., 2014). Therefore, the use of temperature and log g independent of spectroscopy might solve this eventual degeneracy. First of all, we fix the gravity to the values of Table 6.3 using both the gravities from *Gaia* and from the comparison with isochrones, and let $T_{\rm eff}$, ξ, and [Fe/H] vary up to convergence. We then keep the photometric log g and $T_{\rm eff}$ constant, while ξ and [Fe/H] are varied up to convergence. Even with these choices, the global trends of [Fe/H] versus $T_{\rm eff}$, with cool and low-gravity stars having a lower metal content than the other member stars, are still present with the EW method (e.g. a discrepancy in metallicity of ~ 0.3 and ~ 0.2 dex, respectively, between the coolest and hottest star of Ruprecht 171).

6.6.2. THE NLTE EFFECTS

FAMA uses MOOG to compute abundances in the LTE approximation. The photospheres of cool giants, with their low surface gravities and thus low densities, might depart from LTE, being translucent over large radial extensions. Thus, the radiative rates can dominate the collisional rates for many atomic transitions (cf. Short & Hauschildt, 2003). This effect is usually in place in low-gravity giant stars, but it is stronger for metal-poor stars. The departure from LTE could be due to the high excitation levels of Fe I, which do not thermally couple to the ground state of Fe II. Another aspect of the departure could be the treatment of poorly known inelastic collisions with hydrogen atoms (Mashonkina et al., 2011). There are indeed several studies showing that NLTE effects in the ionisation balance of Fe I/Fe II are larger for giant metal-poor stars (e.g. Bergemann et al., 2012; Mashonkina et al., 2011; Collet et al., 2005, and references therein) than for their counterparts at higher metallicity. Since iron lines are used to derive stellar parameters, we aim to estimate the effect of NLTE in the spectra of our giant stars, even if their metallicity is not so low that we expect a strong departure from LTE.

We estimate the NLTE abundance corrections for each Fe line using the calculator by the MPIA NLTE group[2] (Bergemann et al., 2012). The NLTE abundance corrections are computed as $\Delta\mathrm{Fe} = \log\mathrm{A(Fe)}_{\rm NLTE} - \log\mathrm{A(Fe)}_{\rm LTE}$, which is the difference between the NLTE and LTE abundances. These corrections on the considered Fe lines are of the order 0.001 – 0.02 dex. They are negligible as expected for solar metallicity giants (Bergemann et al., 2012), even at the very low surface gravities of the coolest stars of our sample. Thus, these

[2] http://nlte.mpia.de/gui-siuAC_secE.php

corrections alone cannot justify the discrepancy in metallicity among members of the same cluster, and they do not affect the determination of the spectroscopic stellar parameters from the EW analysis.

6.6.3. THE LINE LIST

The spectra of cool stars, with $T_{\rm eff} < 5000$ K, are characterised by strong line crowding and consequent blending. However, HARPS-N has high spectral resolution, R=115 000, which makes the problem of the blending less dominant. As pointed out by Tsantaki et al. (2013), the identification of unblended EWs of photospheric lines and the continuum placement are difficult tasks in cool stars. This might lead to incorrect measurement of the EWs with consequent errors in the derived stellar parameters. Following the work of Tsantaki et al. (2013), we adopt their line list designed for the analysis of cool stars. However, we reiterate that the line list of Tsantaki et al. (2013) is designed for cool solar-type stars. In cool giant stars, the effect of crowding and continuum placement can be even more severe.

To understand whether or not the difference in metallicity is due to the Gaia-ESO line list (used to obtain the results in Table 6.4), we perform the EW spectral analysis using the line list by Tsantaki et al. (2013). The atmospheric parameters achieved by both line lists are consistent within the errors. Moreover, there are still differences between the [Fe/H] in stars in distinct evolutionary stages within the same cluster.

6.6.4. THE MODEL ATMOSPHERES

Finally, we test the influence of the choice of model atmospheres on the determination of stellar parameters and abundances. To perform our test, we recompute the stellar parameters using the Kurucz models (Castelli & Kurucz, 2003) instead of the MARCS spherical models. The differences are negligible for all parameters. However, as discussed by Short & Hauschildt (2003), for giants of spectral types G to M, the failure in reproducing the relation between $T_{\rm eff}$ and the colours in the blue and violet regions of the spectrum, such as $B-V$, is typical of most model atmospheres. Bessell et al. (1998) indicated the incomplete or erroneous opacity in the blue-violet region as the origin of that discrepancy. Since this problem affects different types of model atmospheres, the change of model does not help to solve the discrepancy.

6.6.5. SUGGESTIONS ON [FE/H] DETERMINATION IN COOL STARS

The problem of obtaining overly low metallicity in cool stars has been known for a long time, but a clear solution is still missing. An example of this effect in open clusters is the star at the tip of the RGB of the cluster Collinder 261. This star is cooler than the other studied members, and its measured metal content is lower than the other stars (Carretta et al., 2005; Friel et al., 2003).

There is not a single explanation to clarify the differences in metallicities in stars of the same cluster belonging to different evolutionary phases, in particular the upper RGB. For the cluster with a larger number of observed member stars, Ruprecht 171, we severely underestimate [Fe/H] with the EW method (maximum differences > 0.4 dex) in stars cooler than ~ 4300 K and with log $g < 1.8$ dex. This effect is smaller with parameters and metallicities derived through ROTFIT. In this case, the maximum differences in [Fe/H] between

the coolest and hottest stars are of the order of ~0.2 dex. For NGC 7044, we are limited by the observations of four member stars, all around the RGB tip, and therefore we cannot compare the cool stars with the warm ones. From them, it is difficult to evaluate whether or not their [Fe/H] values are underestimated. However, the [Fe/H] measured with ROTFIT is higher by about 0.2 dex with respect to [Fe/H] determined with the EWs. In addition, the former metallicity is in better agreement with the literature value (albeit based on the CaT method, which is not free from large uncertainties and biases). We analyse two member stars of Collinder 350. For the hottest one, spectral fitting and EW methods are in agreement, while for the coolest one the EW method tends to underestimate its [Fe/H], as in the other cool giants.

The combination of several aspects makes the determination of metallicity from the EW analysis in the cool giants ($T_{\rm eff} < 4300$ K, log $g < 1.8$ dex) unreliable, as shown in Fig. 6.4, where we present the difference in [Fe/H] between FAMA and ROTFIT as a function of $T_{\rm eff}$, colour-coded by log g. From our analysis described in the previous sections, we consider the principal causes to be as follows: the erroneous opacity in model atmospheres of cool G to M giant stars (see, e.g Bessell et al., 1998; Short & Hauschildt, 2003), and the large number of lines in the spectrum, both atomic ones and molecular bands for cool and metal rich stars, which makes it difficult to define the continuum near to the lines of interest and thus to measure reliable EWs. Regarding the continuum placement, we recall that DAOSPEC adopts a global and not local continuum and this aspect can only increase the difficulty in the continuum setting for cool giants. A clear example of this problem is seen in Fig. 6.5, where two normalised spectra are compared: the spectrum of the cool star Cr350_1 (top panel) and the spectrum of the warm star Cr350_2 (bottom panel). The continuum computed by DAOSPEC for Cr350_1 produces a normalised spectrum slightly above 1, in which the EWs are underestimated, in contrast to Cr350_2. As explained in Cantat-Gaudin et al. (2014), the continuum defined by DAOSPEC, on which the EW fit is based, is not the true continuum of the spectrum (i.e. the continuous star emission after all the lines are excluded), but an effective continuum, which is the true continuum depressed by a statistical estimate of the contaminating lines (the unresolved or undetected ones, producing a sort of line blanketing). The use of the effective continuum improves the measurement of unblended lines, as demonstrated in Cantat-Gaudin et al. (2014), but it is sometimes perceived as being too low, especially in spectra dominated by line crowding (i.e. in particular high-metallicity giant stars) or with decreasing S/N of the spectra. The case of Cr350_1 is a typical example of our limits in measuring the EWs of metal-rich giant stars, for which we likely underestimate the EWs and, consequently, we derive a lower [Fe/H] than in warmer stars. Moreover, it is known also from other works that the analysis based on EW measurements tends to underestimate the [Fe/H] of cool giant stars, as shown by the EW analyses of benchmark stars performed by different groups (Jofré et al., 2014; Heiter et al., 2015a). Consequently, for the spectra of stars cooler than 4300 K, ROTFIT, which is less prone to continuum setting and blending effects, produces more solid determinations of the stellar parameters than the EW analysis.

In what follows, we consider the results from the EW analysis only for stars hotter than 4300 K, namely one star in Collinder 350 and in Gulliver 51, and four stars in Ruprecht 171. In Table 6.6, we compare the mean metallicities of our cluster sample from ROTFIT (all sample) and from FAMA (only stars with $T_{\rm eff} > 4300$ K). The number of stars used to compute the average [Fe/H] is reported in parentheses. The two determinations of the mean

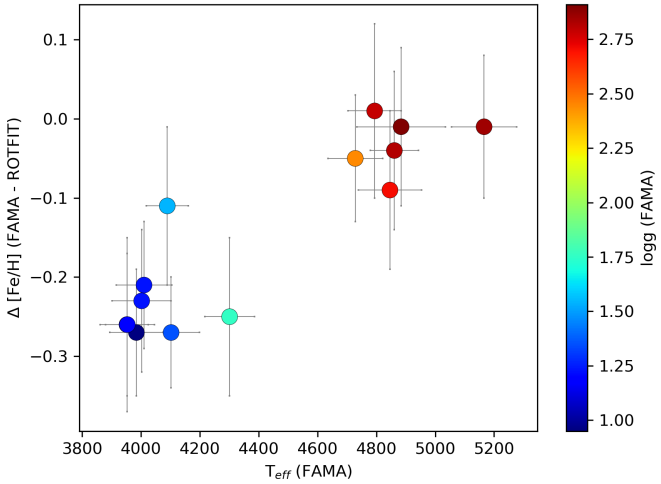

Fig. 6.4: Difference in [Fe/H] between FAMA and ROTFIT as a function of $T_{\rm eff}$, colour-coded by log g.

cluster metallicity are in good agreement within the uncertainties (1-σ standard deviation).

Cluster	[Fe/H] ROTFIT (all)	[Fe/H] FAMA (warm)
Collinder 350	0.00±0.08 (2)	−0.03±0.08 (1)
Gulliver 51	−0.03±0.08 (1)	−0.08±0.04 (1)
NGC 7044	−0.13±0.02 (4)	–
Ruprecht 171	0.03±0.09 (7)	0.06±0.03 (4)

Table 6.6: Mean metallicities of our sample open clusters.

6.7. CHEMICAL ABUNDANCES

Elemental abundances are computed with FAMA using the routines ABFIND and BLENDS of MOOG. The latter is used for elements that present hyperfine splitting in their lines. To compute the Solar-scaled abundances and abundance ratios [X/H] and [X/Fe], we define our Solar scale measuring the element abundances on a solar spectrum. For this task we use a spectrum of Ceres collected by the twin HARPS spectrograph at the 3.6 m ESO telescope. The Solar abundances are listed in Table 6.7, in which we show our Solar abundances and the photospheric Solar abundances from Grevesse et al. (2007). For the elements that cannot be measured in the Ceres spectrum, we use the values from Grevesse et al. (2007).

We cannot produce abundances for NGC 7044 and for the cool stars of Ruprecht 171 and Collinder 350 with the stellar parameters derived via EW analysis. In Table 6.8 we list the elemental abundances for each warm member star ($T_{\rm eff}$ > 4300 K), where the errors are the standard deviations on the mean of the abundances of each line for the given elements. When only one line is detected per element, the error is estimated propagating the uncertainty on its EW. The uncertainties reported in Table 6.8 do not take into account the

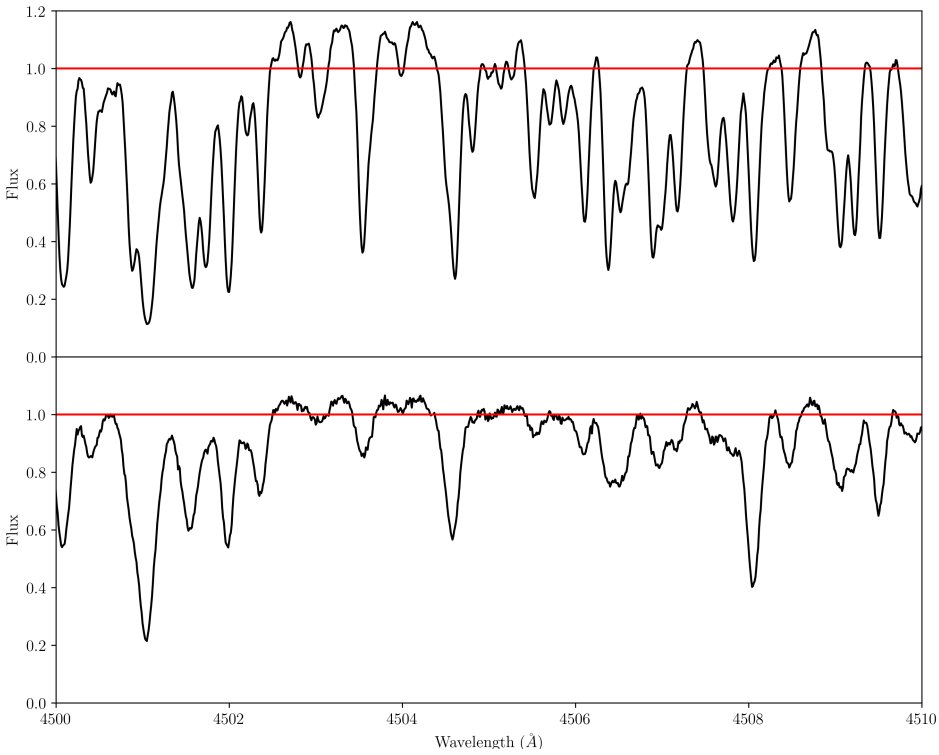

Fig. 6.5: Portion of the spectra, normalised with DAOSPEC, of the cool star Cr350_1 (top panel) and the warm star Cr305_2 (bottom panel) with the continuum (red line).

impact of the uncertainties on the stellar parameters, and are therefore lower limits in the total error budget. Typical errors due to stellar parameters are estimated for [Fe/H]. They are reported in Table 6.4 and range from 0.01 to 0.06 dex.

In Table 6.9, we report the mean abundance ratios for each cluster. The errors for Ruprecht 171 are the standard deviations of the mean, as we have four warm stars for these clusters; whereas, for Gulliver 51 and Collinder 350 we can use only one star, and therefore the uncertainties are the errors on each individual measurement.

6.7.1. COMPARISON WITH THE LITERATURE

Collinder 350 is the only cluster of our sample that has previous determinations of chemical abundances from high-resolution spectral analysis. The previous works on this cluster presenting high-resolution spectroscopy are Pakhomov et al. (2009), Blanco-Cuaresma et al. (2015), and Blanco-Cuaresma & Fraix-Burnet (2018). The first work analysed a spectrum of the star Cr350_1 collected with the red branch spectrograph ($R \sim 50\,000$) at the 2.16 m Telescope at the Xinglong Observatory in China. Pakhomov et al. (2009) found a metallicity of [Fe/H]=+0.11 ± 0.06 dex. Blanco-Cuaresma et al. (2015) and Blanco-Cuaresma & Fraix-Burnet (2018) analysed an archival NARVAL spectrum of a giant star ($R \sim 80\,000$), obtaining slightly different values of [Fe/H]=−0.10 ± 0.01 (or [Fe/H]=0.0 with different normalisation) and 0.03 dex, respectively. Table 6.10 shows the abundance ratios for Cr350_1 by Pakhomov et al. (2009) and for a giant star in Collinder 350, for which the coordinates are not available in the papers (Blanco-Cuaresma et al., 2015; Blanco-Cuaresma & Fraix-Burnet, 2018), compared with our results of Cr350_2. We exclude from the comparison the elements that are

Element	Sun (Ceres)	Sun (G07)
Li I	–	1.05 ± 0.10
C I	–	8.39 ± 0.05
Na I	6.22 ± 0.04	6.17 ± 0.04
Mg I	7.63 ± 0.02	7.53 ± 0.09
Al I	6.41 ± 0.02	6.37 ± 0.06
Si I	7.45 ± 0.04	7.51 ± 0.04
Ca I	6.29 ± 0.05	6.31 ± 0.04
Sc II	3.17 ± 0.03	3.17 ± 0.10
Ti I	4.87 ± 0.05	4.90 ± 0.06
Ti II	4.99 ± 0.07	–
V I	3.92 ± 0.07	4.00 ± 0.02
Cr I	5.62 ± 0.03	5.64 ± 0.10
Fe I	7.45 ± 0.09	7.45 ± 0.05
Fe II	7.47 ± 0.09	–
Co I	4.89 ± 0.08	4.92 ± 0.08
Ni I	6.23 ± 0.08	6.23 ± 0.04
Y II	2.11 ± 0.09	2.21 ± 0.02
Zr I	–	2.58 ± 0.02
Zr II	2.42 ± 0.06	–
La II	1.13 ± 0.36	1.13 ± 0.05
Ce II	–	1.70 ± 0.10
Eu II	–	0.52 ± 0.06

Table 6.7: Solar chemical abundances. G07: Grevesse et al. (2007).

Star	A(Li I)	n(Li I)	A(C I)	n(C I)	A(Na I)	n(Na I)	A(Mg I)	n(Mg I)	...
Cr350_2	1.41 ± 0.03	1	7.88 ± 0.07	2	6.43 ± 0.02	2	7.64 ± 0.12	2	
Gul51_1	1.05 ± 0.07	2	7.92 ± 0.06	1	6.26 ± 0.07	4	7.62 ± 0.01	2	
Rup171_4	–	–	7.98 ± 0.03	2	6.41 ± 0.07	4	7.73 ± 0.02	3	
Rup171_5	–	–	7.81 ± 0.08	1	6.43 ± 0.06	4	7.71 ± 0.01	2	
Rup171_6	–	–	7.99 ± 0.06	2	6.42 ± 0.03	4	7.67 ± 0.02	2	
Rup171_8	0.39 ± 0.06	1	7.92 ± 0.02	2	6.42 ± 0.06	4	7.70 ± 0.01	2	

Table 6.8: Elemental abundances of each star with $T_{eff} > 4300$ K, in the form 12 + log(X/H). n(X) represents the number of lines for each element. The full version of this table is available online at the CDS.

modified by stellar mixing, such as C and Na, because we do not compare the same star. Also, without taking into account the possible differences in solar reference abundances adopted in the studies mentioned above, Fig. 6.6 shows that most of our abundance ratios are in agreement within the errors between our work and those papers. The only exception is [La/Fe], for which we find a lower value.

Ratio	Cr 350	Gul 51	Rup 171
odd-elements			
[Na/Fe]	0.25 ± 0.10	0.12 ± 0.12	0.14 ± 0.03
[Al/Fe]	-0.01 ± 0.10	0.00 ± 0.09	0.02 ± 0.03
α-elements			
[Mg/Fe]	0.05 ± 0.15	0.07 ± 0.09	0.02 ± 0.04
[Si/Fe]	0.03 ± 0.12	0.07 ± 0.10	0.03 ± 0.02
[Ca/Fe]	-0.01 ± 0.12	-0.02 ± 0.10	-0.01 ± 0.02
[Sc/Fe]	0.00 ± 0.13	0.06 ± 0.11	0.09 ± 0.02
[Ti/Fe]**	0.00 ± 0.14	-0.01 ± 0.13	0.02 ± 0.03
iron-peak elements			
[V/Fe]	0.00 ± 0.15	0.04 ± 0.14	0.10 ± 0.03
[Cr/Fe]	0.02 ± 0.13	-0.01 ± 0.11	-0.01 ± 0.02
[Co/Fe]	-0.02 ± 0.14	-0.02 ± 0.14	0.10 ± 0.02
[Ni/Fe]	-0.06 ± 0.13	-0.05 ± 0.12	0.03 ± 0.02
neutron-capture elements			
[Y/Fe]	0.04 ± 0.16	0.08 ± 0.12	0.01 ± 0.03
[Zr/Fe]*,**	0.13 ± 0.14	0.21 ± 0.12	0.09 ± 0.04
[La/Fe]	-0.13 ± 0.13	-0.07 ± 0.12	-0.22 ± 0.03
[Ce/Fe]*	-0.04 ± 0.14	0.04 ± 0.14	-0.04 ± 0.03
[Eu/Fe]*	-0.03 ± 0.12	0.08 ± 0.29	-0.02 ± 0.06

Table 6.9: Mean abundance ratios for the clusters. Abundance ratios on our Solar scale, with the exception of (*), which are calculated using the solar value from Grevesse et al. (2007). (**) indicates the average value between [Ti I/Fe] and [Ti II/Fe], and [Zr I/Fe] and [Zr II/Fe].

6.8. RESULTS

Open clusters are among the best tracers of the radial metallicity distribution in the Galactic disc. Recent works within the Gaia-ESO and APOGEE surveys (e.g. Magrini et al., 2018; Donor et al., 2020) have investigated the shape of the radial metallicity gradient using relatively large numbers of homogeneously analysed clusters. We therefore have the opportunity to compare our sample clusters with the combined APOGEE DR16 (listed by Donor et al., 2020, 128 clusters), and old and young Gaia-ESO iDR5 open clusters samples listed by Magrini et al. (2018, 22 clusters) and Baratella et al. (2020, 6 clusters), respectively. Regarding the APOGEE data, we consider only open clusters with at least three member stars and with a high-quality flag, and therefore we reduce their number to 38 clusters. The result is shown in Fig. 6.7. The metallicity of our cluster sample is obtained as an average between the two values shown in Table 6.6. The metallicities of our four clusters, as well as ASCC 123 and Praesepe located around the Solar position, agree very well with the results of Gaia-ESO and APOGEE, and confirm an intrinsic dispersion of [Fe/H] at each Galactocentric radius. The innermost cluster, Ruprecht 171, shows instead a slightly lower metallicity than the other clusters located at similar Galactocentric distances. However, considering only the hottest member stars of Ruprecht 171 analysed through ROTFIT (ID from 3 to 8), we obtain [Fe/H]~0.09 dex, which is in better agreement with the global radial metallicity gradient, as shown in Fig. 6.7.

Ratio	BC18	BC15	P09	This work
[Fe/H]	0.03	-0.10 ± 0.01	0.11 ± 0.06	0.04 ± 0.11
[Mg/Fe]	-0.07	0.08 ± 0.03	0.05 ± 0.07	0.05 ± 0.15
[Al/Fe]	-0.08	–	0.06 ± 0.10	-0.01 ± 0.10
[Si/Fe]	-0.07	0.10 ± 0.06	0.07 ± 0.12	0.03 ± 0.12
[Ca/Fe]	0.04	0.06 ± 0.11	0.05 ± 0.13	-0.10 ± 0.12
[Sc/Fe]	0.00	–	$-0.03 \pm 0.06^*$	0.00 ± 0.13
[Ti/Fe]	-0.02	0.02 ± 0.11	-0.12 ± 0.10	-0.02 ± 0.16
[V/Fe]	-0.09	0.08 ± 0.07	-0.03 ± 0.08	0.00 ± 0.15
[Cr/Fe]	-0.02	0.05 ± 0.14	0.04 ± 0.08	0.02 ± 0.13
[Co/Fe]	-0.11	-0.01 ± 0.06	-0.06 ± 0.09	-0.02 ± 0.14
[Ni/Fe]	-0.10	-0.06 ± 0.11	-0.15 ± 0.08	-0.06 ± 0.13
[Y/Fe]	0.18	0.09 ± 0.17	0.05 ± 0.07	0.04 ± 0.16
[Zr/Fe]	0.13	–	$0.07 \pm 0.06^*$	0.13 ± 0.14
[La/Fe]	0.21	–	0.25 ± 0.11	-0.13 ± 0.13
[Ce/Fe]	0.15	–	0.10 ± 0.08	-0.04 ± 0.14
[Eu/Fe]	0.02	–	0.02 ± 0.13	-0.03 ± 0.12

Table 6.10: Abundances for Collinder 350. BC18: Blanco-Cuaresma & Fraix-Burnet (2018); BC15: Blanco-Cuaresma et al. (2015); P09: Pakhomov et al. (2009). Errors with * are lower limits.

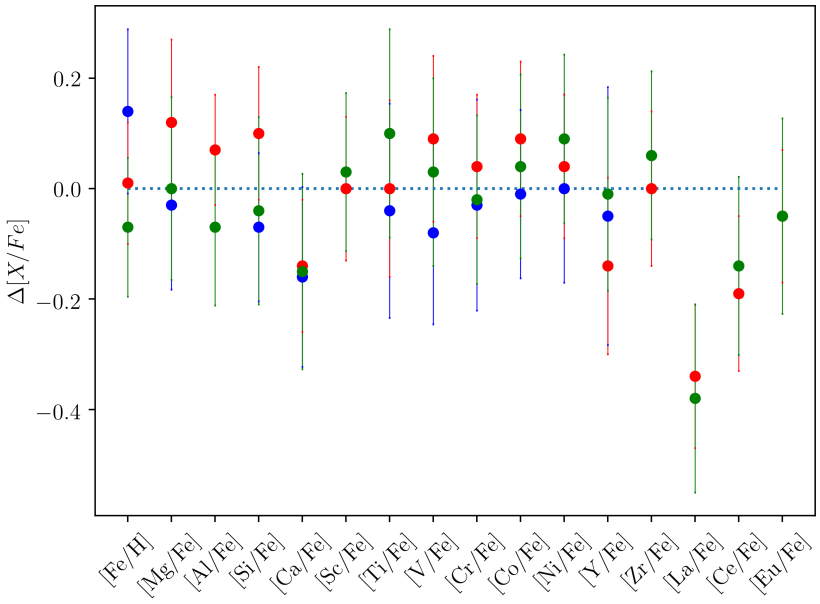

Fig. 6.6: Difference between our abundance ratios and the values from the literature: in green the comparison with Pakhomov et al. (2009), in blue the comparison with Blanco-Cuaresma et al. (2015), and in red the comparison with Blanco-Cuaresma & Fraix-Burnet (2018). In the last case, the error bars take into account only the errors on the abundance ratios computed in this work, and therefore they are lower limits.

6.8.1. [X/Fe] VERSUS [Fe/H]

In Fig. 6.8, we present [X/Fe] versus [Fe/H] for the element in common among our analysis, the APOGEE results in Donor et al. (2020), and the Gaia-ESO results in Magrini et al. (2017,

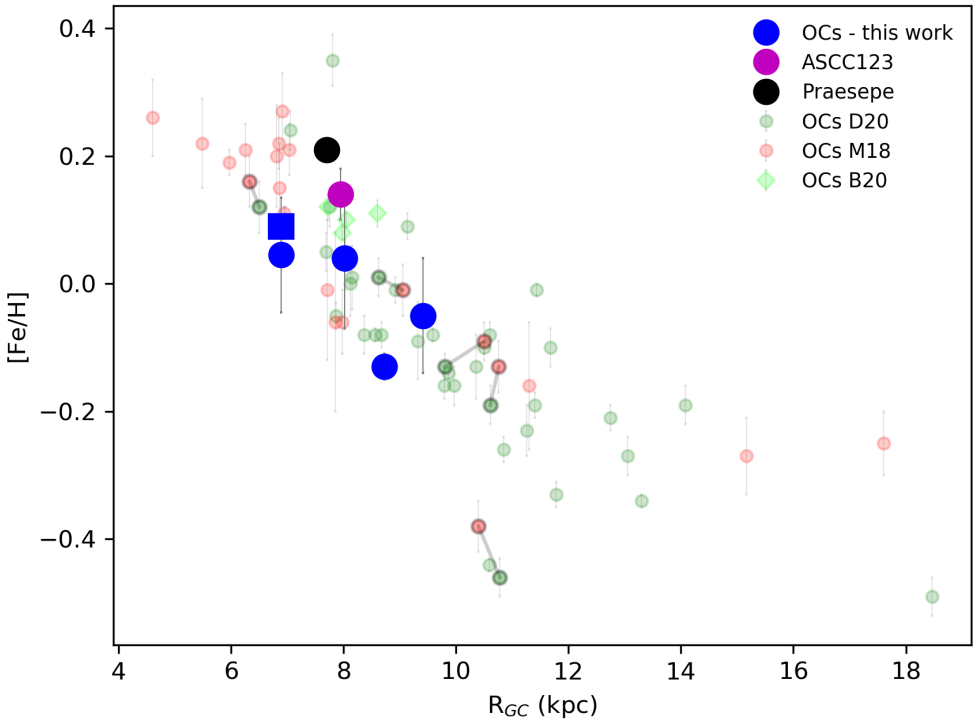

Fig. 6.7: Radial metallicity gradient: in red the results of Gaia-ESO iDR5 from Magrini et al. (2018), in green the results of APOGEE DR16 (clusters with at least three member stars and high-quality flag), and in blue our SPA clusters. The blue square is the mean [Fe/H] of Ruprecht 171 obtained with only the hottest stars analysed by ROTFIT (ID from 3 to 8). The clusters in common between APOGEE and Gaia-ESO are linked by a black line. The magenta and black circles are the SPA clusters ASCC 123 and Praesepe studied by Frasca et al. (2019) and D'Orazi et al. (2020), respectively. The light green diamonds are the young Gaia-ESO open clusters by Baratella et al. (2020).

for Ca, Sc, V, Cr), Magrini et al. (2018, for Zr, La, Ce, Eu), and Casali et al. (2020b, for Mg, Al, Si, Ti, Y; see Table 5.9). We also add the abundance ratios for two young SPA clusters: Praesepe from D'Orazi et al. (2020), and ASCC 123 from Frasca et al. (2019) – ASCC 123 abundances scaled using the solar reference of Grevesse et al. (2007). For the latter, we exclude the abundance ratios displayed as overabundant or under-abundant with respect to the field stars of Gaia-ESO DR4 in Frasca et al. (2019) .

Our clusters follow the main trends of the APOGEE and Gaia-ESO clusters: open clusters are a thin disc population, and they do not reach very low metallicities: their [Fe/H] is in the range [−0.5,+0.4]. The α elements (Mg, Ca, Si, Ti) all show an enhancement in [X/Fe] towards lower [Fe/H]. Their production is essentially due to core collapse supernovae (see, e.g. Woosley & Weaver, 1995). ASCC 123 is overabundant in [Ca/Fe] and under-abundant in [Si/Fe] with respect to other clusters. Aluminium and sodium are quite scattered, which is an effect of the internal mixing that causes some sodium overabundance at the surface of red giants more massive than ~1.5-2.0 $M_{\odot}$. A similar effect, even if not predicted by stellar evolution models, is observed for Al (cf. Smiljanic et al., 2016). The iron-peak elements (Sc, V, Cr, Co, Ni) follow an almost flat trend, with different degrees of scattering due to the difficulty in measuring some elements, such as for example V and Co. Finally, we compare

five neutron capture elements, four of them predominantly produced by the slow (s) process (Y, Zr, La, Ce) and one by the rapid (r) process, Eu. As in previous Chapter and Casali et al. (2020b), [Y/Fe] shows a peak at solar metallicity, and decreases at sub- and super-solar metallicities. [Zr/Fe] tends to increase towards lower metallicities, a signature of an important production in massive stars at early epochs. For [La/Fe] and [Ce/Fe], the general trend is similar to that of Zr, with an increasing trend at low [Fe/H]. The abundance ratios [La/Fe] of our clusters has an offset with respect to the Gaia-ESO sample. It might be due to the different solar scale for La used in Magrini et al. (2018): 1.00 dex (based on the giant stars of M67) against 1.13 dex, determined in our solar spectrum. Finally, Eu is an almost pure r-process element produced on shorter timescales and with a behaviour similar to the α-elements. This behaviour is confirmed by the combination of our sample with the literature one. In general, the abundance ratios of the SPA clusters follow the main trends.

6.8.2. [X/FE] VERSUS R_{GC}

In Fig. 6.9, we show the same abundance ratios as in Fig. 6.8, plotted as a function of Galactocentric distance, R_{GC}. As in Fig. 6.8, our open clusters follow the main trends. For the α-elements, we have a slight enhancement increasing towards the Galactic outskirts. This enhancement is an indication of the inside-out formation of the disc, in which inner regions formed at high star formation rates, thus being quickly enriched by products of SNe Ia with a consequent lower [α/Fe]. The gradients of the iron-peak elements (V, Cr, Co, Ni) are flat, with different levels of scatter, indicating the expected similarity with the [Fe/H] gradient. The [Sc/Fe] gradient resembles the [α/Fe] gradient, indicating a contribution from core-collapse supernovae in its nucleosynthesis. The [Y/Fe] gradient shows a peak at solar Galactocentric distance, and a decreasing trend towards the inner disc, as already discussed in previous Chapter and Casali et al. (2020b). Even the innermost SPA open clusters do not manifest any high [Y/Fe], but follow the trend of the literature, confirming a less efficient production of Y in the inner disc and at high metallicity. This behaviour is in common with the other neutron-capture elements with a predominance from s-process. The elements La and Ce share the same behaviour in the inner disc, while they are more enhanced in the outskirts as a consequence of their partial production also in massive stars. Finally [Eu/Fe] versus R_{GC} shows an increase in the outer disc, which is characteristic of a double mechanism of production of this element (Van der Swaelmen et al. in prep.).

6.8.3. [α/FE] VERSUS [FE/H]

In Fig. 6.10, we present [α/Fe] versus [Fe/H] (where [α/Fe] is the sum of [Mg/Fe], [Ca/Fe], [Si/Fe] and [Ti/Fe] divided by four) for our cluster sample as well as for ASCC 123 and Praesepe, together with the Gaia-ESO and APOGEE clusters, and the field stars from Gaia-ESO DR4. The cluster population is colour coded by age using 790 Myr for Praesepe (Brandt & Huang, 2015; D'Orazi et al., 2020), the mean value of the range of 100–250 Myr suggested in Frasca et al. (2019) for ASCC 123, and age determinations from Table 6.1 for our SPA clusters, from Magrini et al. (2017) for Gaia-ESO and from Donor et al. (2020) for APOGEE. While the field population is well separated in the two components of thin and thick discs, open clusters are essentially a thin-disc population: most clusters are located in the low-α thin disc with ages lower than 5 Gyr and the SPA clusters are in agreement with the thin-disc field stars within their errors. There are a few exceptions: the three clusters with high

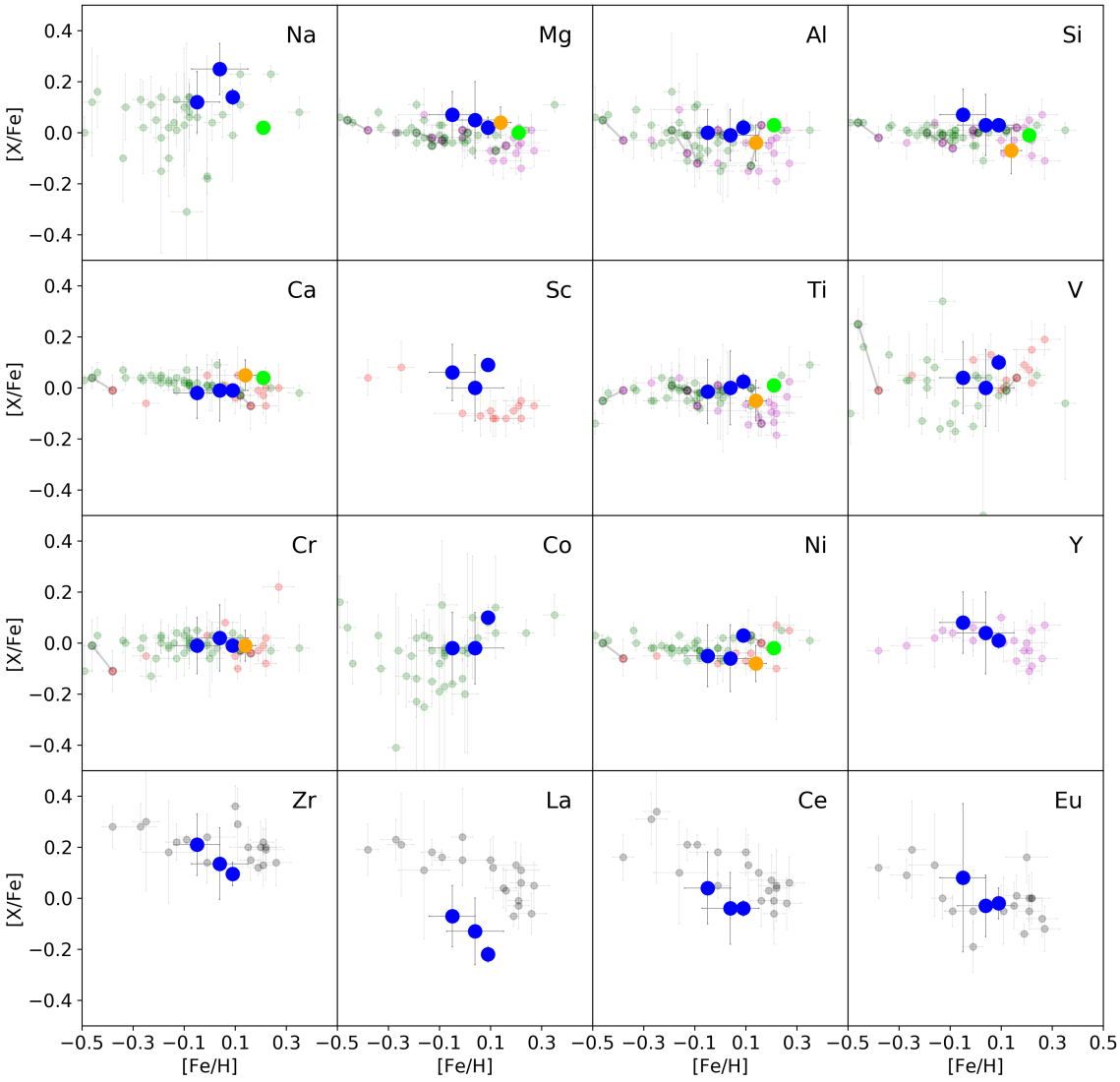

Fig. 6.8: Abundance ratios vs. [Fe/H]: blue indicates our SPA clusters with [Fe/H] as an average between the two values shown in Table 6.6; light green indicates Praesepe; and orange indicates ASCC 123. The transparent colours indicate the following: green circles are APOGEE DR16 open clusters listed in Donor et al. (2020); red circles are the open clusters of Gaia-ESO DR4 with the [X/Fe] ratios calculated in Magrini et al. (2017); magenta circles are the open clusters of Gaia-ESO iDR5 with the [X/Fe] ratios calculated in Casali et al. (2020b), not present in Magrini et al. (2017); and finally, black circles are the open clusters of Gaia-ESO iDR5 with the [X/Fe] ratios calculated in Magrini et al. (2018), not present in Magrini et al. (2017) and Casali et al. (2020b). The open clusters in common between APOGEE and Gaia-ESO are linked by a black line.

[Fe/H] are also slightly enhanced in [α/Fe]. As discussed for NGC 6705 in Magrini et al. (2014, 2015) and Casamiquela et al. (2018), they might be part of a young metal-rich and α-enhanced population similar to the ones found in the disc (see, e.g. Chiappini et al., 2015), and very recently also in the bulge (Thorsbro et al., 2020). Also in this case, the SPA open clusters follow the main trend of the thin-disc population.

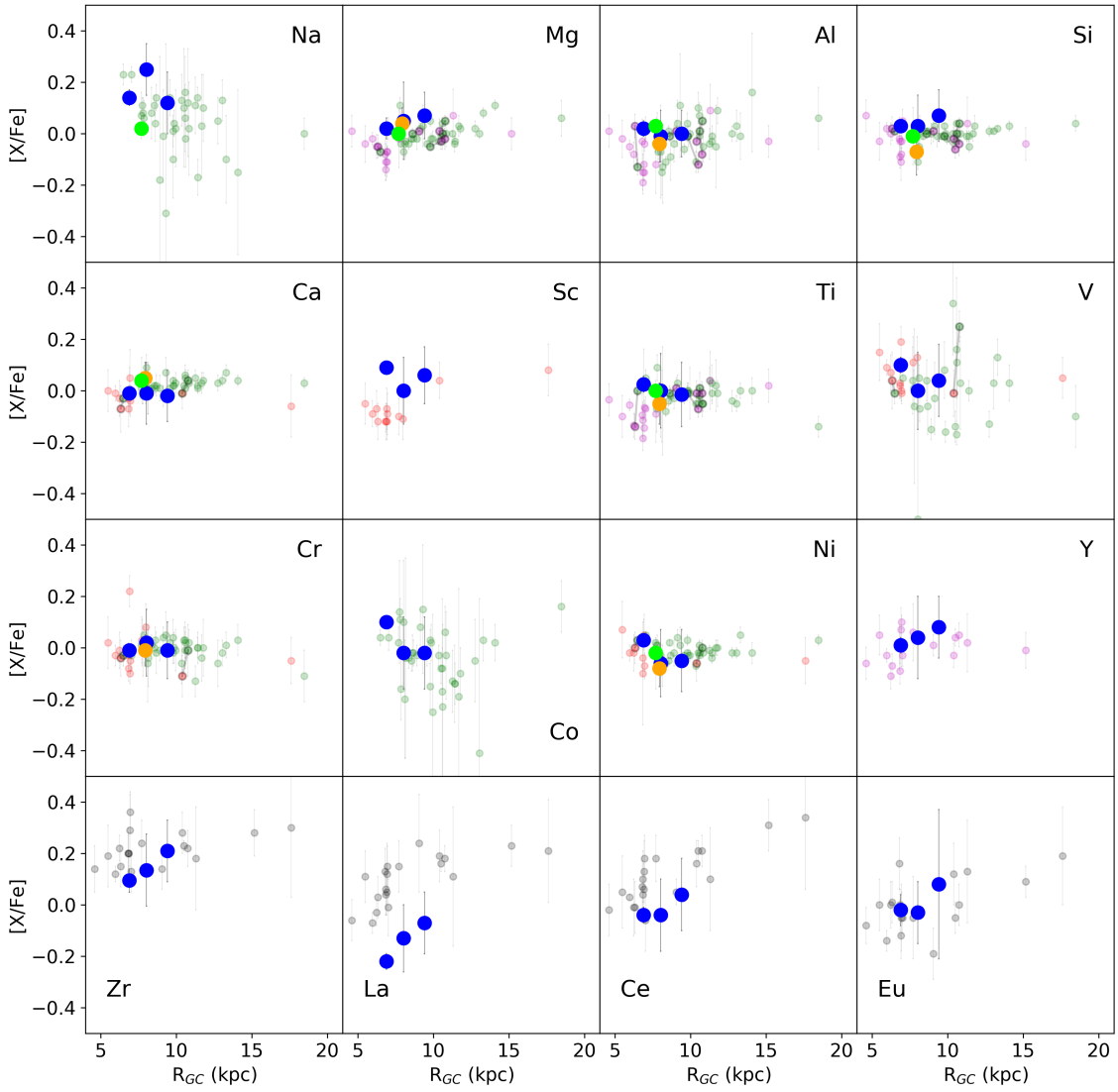

Fig. 6.9: Abundance ratios vs. Galactocentric distance R_{GC}. Symbols as in Fig. 6.8.

6.8.4. CARBON AND LITHIUM

We measure C and Li in some stars of our sample. Carbon is measured from the atomic lines (the adopted C I at 5052.144 Å and 5380.325 Å are not affected by strong NLTE; see e.g. Franchini et al., 2020), while lithium is measured from the EWs of the resonance doublet at 6708 Å, which is unblended at the high-spectral resolution of HARPS-N. The photospheric abundances of these elements are affected by stellar evolution during the RGB phase because of the first dredge up (FDU). During the FDU, as we saw in the Chapters 3 and 4, the stellar convective envelope penetrates into the inner regions and brings previously processed materials to the surface, enriching the external layers in N and He, and diluting the Li and C abundances (see Lagarde et al., 2012; Masseron & Gilmore, 2015; Salaris et al., 2015; Casali et al., 2019, for more details). After the FDU, the star evolves along the RGB where extra mixing such as that caused by the thermohaline mechanism likely dominates the abundance change of these elements (Lagarde et al., 2012). These effects are mainly

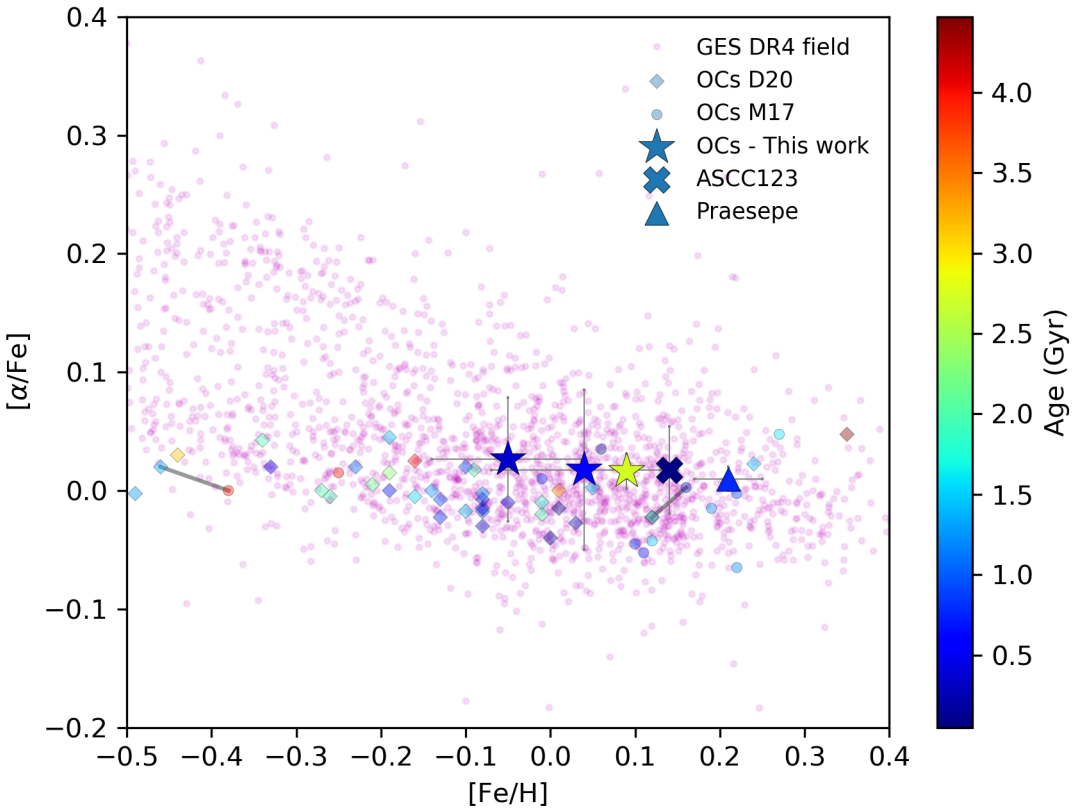

Fig. 6.10: [α/Fe] vs. [Fe/H] for the open clusters, colour-coded by stellar age. The SPA clusters of this work are marked with a star symbol, while the cross and the triangle are the SPA clusters ASCC 123 and Praesepe, respectively; the transparent circles are the Gaia-ESO clusters with the abundances from Magrini et al. (2017) and the transparent diamonds are the APOGEE clusters with the abundances from Donor et al. (2020). The magenta dots (not colour-coded by age) in transparency are the field stars of the Gaia-ESO survey (public release, available at ESO archive). Finally, clusters in common between APOGEE and Gaia-ESO are linked by a black line.

expected along the upper RGB, after the RGB bump phase. The incidence of thermohaline mixing dominates at low metallicity and for low-mass stars, while it is weaker in the Solar metallicity regime. Observational evidence of such extra-mixing processes are the very low lithium abundance after the RGB bump and the variation of the isotopic ratio $^{12}C/^{13}C$ (e.g. Lind et al., 2009; Mucciarelli et al., 2011; Lagarde et al., 2019).

In Fig. 6.11, we show C/H and Li/H for the stars of Collinder 350, Gulliver 51, and Ruprecht 171 as a function of their log g. The curves are the models of Lagarde et al. (2012) for three different masses (1.5, 2, 3 $M_\odot$, which encompass the range of turn-off masses for our clusters) for the standard (solid lines, s-models) and rotation-induced mixing models (dashed lines, r-models). The value C/H decreases with decreasing log g for the stars in Ruprecht 171, following the theoretical models of Lagarde et al. (2012) (see left panel of Fig. 6.11). Rup171_5 is located out of the locus of the theoretical models, however its C/H determination exhibits the largest uncertainties. The right panel shows the evolution of Li versus log g. The stars of Ruprecht 171, the oldest cluster of our sample, with a MSTO mass

of ~1.5 $M_\odot$, are in better agreement with models with rotation-induced mixing, while the stars in Collinder 350 and Gulliver 51, the youngest clusters of our sample, with the highest MSTO masses (~3 $M_\odot$), are in agreement with the predictions of the standard models, as expected for more massive stars at Solar metallicity.

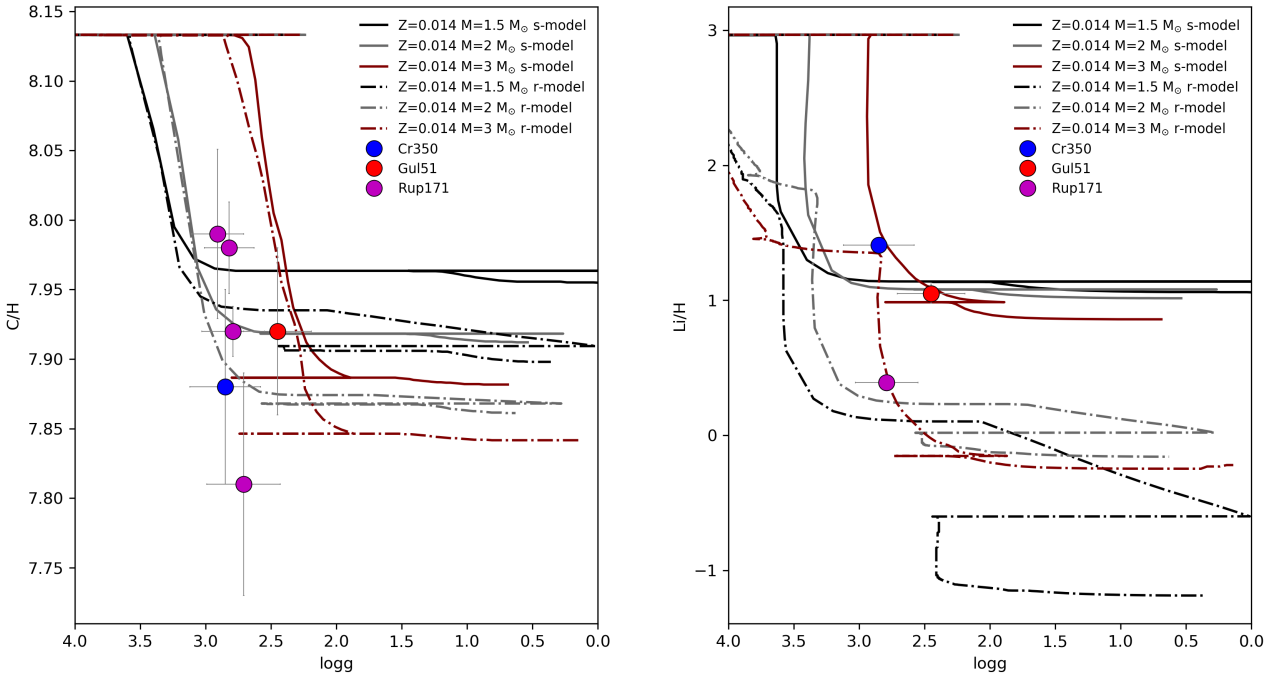

Fig. 6.11: C/H and Li/H versus log g. The circles are the stars of our sample and the curves are the theoretical models by Lagarde et al. (2012). Continuous lines are the standard models with masses of 1.5-2-3 $M_\odot$, and dashed lines are the models with rotation-induced extra-mixing for the same masses.

6.9. SUMMARY AND CONCLUSIONS

The SPA survey is extremely useful to characterise the Solar neighbourhood, in particular the nearby clusters, providing a wide variety of elements thanks to the high spectral resolution and large spectral coverage. In the framework of SPA, we present the analysis of four poorly studied clusters: Collinder 350, Gulliver 51, NGC 7044, and Ruprecht 171. We analyse the high-resolution HARPS-N spectra taken at the TNG for, respectively, two, one, four, and seven candidate member stars. These stars belong to the RGB or RC of the cluster evolutionary sequence. We perform, for the first time for these clusters (except for Collinder 350), a spectral analysis based on the EW measurements and spectral fitting to chemically characterise these clusters. With the EW analysis, we find a correlation between stellar parameters and metallicity for stars belonging to the same cluster, but in different evolutionary phases. In particular, the coolest stars (T_{eff} < 4300 K and log g < 1.8 dex) appear more metal-poor than the hottest ones of the same cluster. We investigate several possibilities that might explain this phenomenon, such as the influence of photometric parameters, NLTE effects, and the use of different line lists and model atmospheres. We conclude that the continuum placement is extremely challenging for these stars, and might lead to the derivation of incorrect metallicities. This is combined with the known inaccu-

racy of model atmospheres to reproduce some features of cool giants (Bessell et al., 1998). On the other hand, ROTFIT provides results which do not strongly depend on the evolutionary phase. For this reason we adopt them for the coolest stars of our sample. We derive chemical abundances for several elements for the stars with $T_{eff} > 4300$ K. We investigate the Galactic radial metallicity gradient comparing our SPA clusters with those of Gaia-ESO iDR5 (Magrini et al., 2018) and APOGEE DR16 (Donor et al., 2020). Collinder 350, Gulliver 51, NGC7044, and Ruprecht 171 closely follow the global radial metallicity gradient. We also present [X/Fe] versus [Fe/H] for elements in common with the SPA, APOGEE, and Gaia-ESO samples. The SPA open clusters follow the trends shown by the other clusters. For instance, the α-elements (Mg, Ca, Si, Ti) show an enhancement in [X/Fe] towards lower metallicity; the iron-peak elements (Sc, V, Cr, Co, Ni) follow an almost flat trend; and the s-process elements and Eu follow the general behaviour relatively well. We show the [X/Fe] ratios as a function of the Galactocentric distance and the SPA clusters follow the main trends. α-elements increase slightly towards the Galactic outskirts, implying an inside-out formation of the disc.

We also derive the abundances of C and Li, which are compared with the models of Lagarde et al. (2012). Models with rotation-induced mixing are necessary to explain the Li abundances for the stars in the older cluster, Ruprecht 171. No Li-rich stars are detected in our sample.

7

CONCLUSIONS

The aim of this Thesis is to present some aspects of Galactic Archaeology, a branch of Astrophysics that studies the structure and evolution of the Milky Way by measuring stellar ages and chemical compositions of its stellar populations. Stellar age is an important ingredient to trace the Galactic history and to investigate the Galactic structure in the previous epochs. Unfortunately, stellar age is one of the most elusive among the stellar properties. In fact, we are able to determine it with a good precision only in a few cases. The most common method to date stars is the so-called isochrone fitting, a comparison of stellar magnitudes and colours (or surface gravities and effective temperatures) with those predicted by stellar evolutionary models. This technique is more effective to date stars belonging to stellar clusters, which are composed by coeval and chemically homogeneous stars. However, it becomes less effective if we want to determine the age of individual stars, in particular in regions suffering degeneracy between isochrones of different ages and metallicity, such as red giant branch (RGB). The main focus of this Thesis is to investigate additional methods to infer stellar ages with respect to the most commonly used isochrone fitting. These methods are related the dependence of some abundance ratio to stellar age, as [C/N], [Y/Mg], [Y/Al] etc, the so-called chemical clocks. These ratios, calibrated on stars with well-known ages (such as open clusters or solar-like stars), allow us to derive ages of large sample of stars through empirical relationships. To use them, it is necessary a detailed knowledge of the elemental abundances of stars through the stellar spectroscopy. To investigate these abundance ratios and their dependence on stellar age, I used the data from two large spectroscopic surveys, the APOGEE and the Gaia-ESO surveys, together with ESO Archival spectra and my own observations.

The Thesis consists of three published projects that I led: Casali et al. (2019), A&A, Vol. 629, page A62; Casali et al. (2020b), A&A, Vol. 639, page A127; and Casali et al. (2020a), A&A, Vol. 643, page A12. Their results can be summarised as follows:

- **Calibrating a relationship between age and the [C/N] abundance ratio with open clusters.** This project uses the [C/N] ratio in red giant branch phase (RGB) to infer their ages. The value of [C/N] in RGB stars is strictly linked to the first dredge up (FDU), i.e. the penetration of the convective envelope towards the inner regions. During the FDU, previously processed materials are brought up to the surface (C and N), producing a variation in the chemical composition of the stellar surface. Since the amounts of C and N brought to the surface depend on stellar mass, and since,

in a given evolutionary phase, the age is related to the mass, [C/N] can be used as an age proxy for giant stars. To measure ages of large number of stars using [C/N], it is necessary to find an empirical relation starting from accurate calibrators with well-determined abundances and age. We used the open clusters in APOGEE and Gaia-ESO surveys to calibrate such relation. For each cluster, we selected star members that passed the first dredge up, but did not still pass the RGB bump, where an additional mixing, called *extra-mixing*, occurs. After this selection, we found an empirical relation between the average [C/N] ratios of RGB belonging to open clusters and their stellar ages. We applied it to a huge sample ($\sim 67,000$) of giant field stars present in APOGEE and Gaia-ESO surveys. We found a clear separation in age between thin- and thick-disc field stars: the youngest stars are present in the thin disc, and their ages become larger with increasing α-element content and with decreasing metallicity. Finally, we compared the [C/N] measurements and ages of open clusters with predictions of stellar evolutionary models and field stars in APOKASC sample, finding a good agreement.

- **The non-universality of the age-chemical-clocks-metallicity relations in the Galactic disc.** This project is based on the stellar dating using chemical clocks, such as [Y/Mg], [Y/Al], etc. These abundance ratios are composed by pair of elements produced with different contributions from supernovae Type II (α-elements such as Mg), Type Ia (iron-peak elements such as Co) or asymptotic giant branch stars (s-process elements such as Y), and thus released in the interstellar medium with different time scales. In particular the chemical clocks studied in this project are in the form [s-element/α-element], the ratios showing the strongest dependence on stellar ages. In this project, we analysed 560 spectra collected with HARPS spectrograph ($R \sim 115,000$) of solar-like stars through an accurate spectral analysis that minimises the systematic errors due to the model atmospheres, reducing the uncertainties on the stellar parameters and chemical abundances. This method is based on the differential line-by-line spectral analysis, with respect to the Solar spectrum. Through this spectral analysis, we studied the so-far largest available sample of solar-like stars. We obtained empirical relations between age, metallicity and chemical clocks [s/α] through a multivariate linear regression. An important point we discussed in this project is the spatial variation of the shape of the relations between [s/α] and stellar age. This variation is due to the evolution in the Milky Way disc that proceeded at distinct rates at different Galactocentric distances. We found that some widely used relationships are indeed non-universal in the disc. Their shape depends on the location in the Galaxy. As a consequence, the relations derived in the Solar neighbourhood cannot be applied, for instance, to star clusters located in the inner Galaxy, where the star formation history was different. This results has also important consequences for the nucleosynthesis of the s-process elements, such as Y. To reproduce the abundances in the inner disc clusters, a lower production of yttrium is required at high metallicity. Finally, we applied the [Y/Mg]-[Fe/H]-age relation to the solar neighbourhood field stars in the Gaia-ESO survey in order to derive their ages. The ages derived with the stellar-dating relation confirm the dichotomy in age between the thin and thick disc.

- **Stellar population astrophysics (SPA) with the TNG. The old open clusters: Collinder**

350, Gulliver 51, NGC 7044, Ruprecht 171. This project shows my personal contribution to an on-going large observing programme, called Stellar Population Astrophysics (SPA). SPA is carried out with the 3.6 m Telescopio Nazionale Galileo (TNG) at the Roque de los Muchachos Observatory (La Palma, Spain). The project aims to contribute to our understanding of the star formation and chemical enrichment history of our Galaxy, providing high-resolution spectra of a sample of stars in the Solar neighborhood. In this framework, we observed and analysed the high-resolution ($R \sim 115,000$) HARPS-N spectra of some member stars of four open clusters: Collinder 350, Gulliver 51, NGC7044, Ruprecht 171. These open clusters allow us to characterise the nearby regions of our Galaxy due their location (300 - 3300 pc from the Sun) and age (0.3-3 Gyr), so far little-studied from a spectroscopic point of view. We performed a spectral analysis based on the EW measurements and spectral fitting to characterise the chemical composition of several stars in each cluster. We found, for stars belonging to the same cluster, a correlation between stellar parameters and metallicity: the coolest stars ($T_{\rm eff} < 4300$ K and $\log\ g < 1.8$ dex) appear more metal-poor than the hottest ones. We investigated several possible aspects that can influence the analysis of the coolest giant stars, concluding that a combination of continuum placement and inaccurate model atmospheres might affect the final metallicity. Discarding those stars, we derived abundances for several elements. In particular, we investigated the Galactic radial metallicity gradient by comparing the SPA clusters with those of Gaia-ESO iDR5 and APOGEE DR16: Collinder 350, Gulliver 51, NGC7044 and Ruprecht 17, together with other star clusters analysed in previous SPA papers (ASCC 123 and Praesepe) follow well the global radial metallicity gradient. Also the abundances of the other elements, belonging to different nucleosynthesis channels, are in agreement with the Galactic trends. Finally, thanks to the wide spectral coverage of the SPA spectra, we derived abundances of some light elements, as C and Li, which are modified in giant stars by stellar evolution. The comparison between the observations and theoretical models confirms the necessity of some extra-mixing process, as the rotation-induced mixing.

A

STELLAR SPECTROSCOPY

The determination of the chemical composition of stellar photospheres plays a key role to our understanding of both stellar physics and the Galactic chemical evolution. The elemental abundances in the atmospheres of stars are derived through stellar spectroscopy, thanks to the measurements of absorption features.

In this Appendix, I present the background of the spectral analysis based on the equivalent width measurement. I give an historical overview and preliminary concepts on the stellar spectroscopy. I present the fundamental bases to understand the physics behind the spectroscopy. Then, I show the tools that I used for the spectral analysis and some recent methods, including differential analysis.

A.1. HISTORICAL OVERVIEW

A first step towards the understanding of stellar atmosphere date back to the first half of the 20th century, and it is related to the progress in atomic and molecular physics. The first observations of the solar spectrum were done by Joseph Fraunhofer. He observed many dark lines in the luminous solar spectrum, the strongest ones named Fraunhofer lines and labeled with a simple alphabetic system (see Fig. A.1). In the same years, G. Kirchhoff and R. Bunsen identified in the emission-line spectra produced in laboratory the same lines present in the absorption in stellar spectra. It was the fist step for the determination of the chemical composition of stars.

In 1922, Annie J. Cannon founded the basis of the modern spectral classifications, a system of ten spectral types – O, B, A, F, G, K, M, R, N, S – to catalogue stars. The classification was at the beginning related only to observable characteristics of the spectra, and, only later, it was connected to the physical properties of stars, such as their stellar temperatures (an example of this classification is shown in Fig. A.2). Few years later, Cecilia Payne-Gaposchkin analysed a library of stellar spectra and she was able to accurately relate the spectral classes of stars to their actual temperatures by applying the ionization theory developed by M. Saha. She showed that the great variation in stellar absorption lines was due to differing amounts of ionization at different temperatures, not to different amounts of elements. Her thesis concluded that hydrogen was the overwhelming constituent of stars, and it was the most abundant element in the Universe.

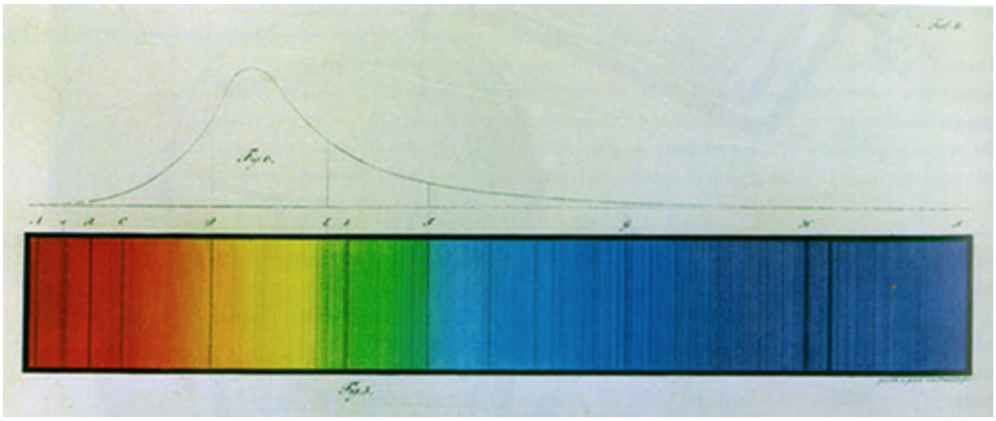

Fig. A.1: The spectrum of the Sun observed in 1814 by Fraunhofer. The letters indicate the positions of selected reference lines.

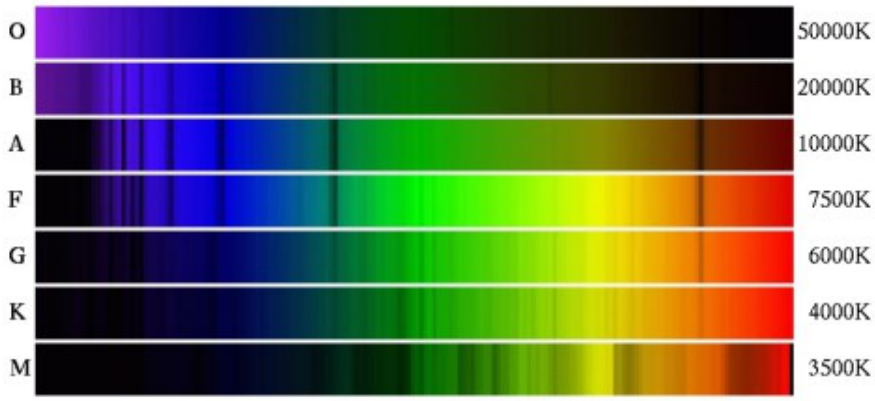

Fig. A.2: Spectral classification by A. J. Cannon.

A.2. PRELIMINARY CONCEPTS

In astrophysics, the term *metals* includes all elements heavier than helium He in the periodic table. It is common to denote the mass fractions of metals with Z, the so-called *metallicity*, while X and Y are used to indicate the mass fractions of hydrogen H and helium He, respectively. These three parameters are related through a relation: $X+Y+Z=1$. In the Sun, the metallicity is Z=0.0134 (Asplund et al., 2009).

Through the measurements of absorption lines in stellar atmosphere, it is possible to measure the chemical content of each single elements. In this case, we talk about *chemical abundances*, that is

$$\log\epsilon(\mathrm{X}) = \log(\mathrm{n_X}/\mathrm{n_H}) + 12$$

where $\mathrm{n_X}$ and $\mathrm{n_H}$ are the numbers of element X and hydrogen atoms per unit volume and $\log\epsilon(\mathrm{H}) \equiv 12$. In stellar spectroscopy, the abundances are scaled to the solar values, using the notation:

$$[\mathrm{X/H}] = \log(\mathrm{n_X}/\mathrm{n_H})_\star - \log(\mathrm{n_X}/\mathrm{n_H})_\odot$$

Usually, Z, transformed in abundances by number [M/H] (M is total abundance of metals), is approximated with [Fe/H], i.e., the iron abundance. The choice of iron as metallicity indicator derives from the prominence of its lines in the most common stars, the cool FGK stars.

A.3. STATISTICAL MECHANICS

The light that we receive from a star comes from its photosphere. A flux of photons, produced in the stellar interior, goes across the atmospheric layers and interacts with the atoms present there. The effective temperature, surface gravity, and chemical composition of a star can be determined through the characteristic features of its stellar spectrum. To properly interpret the observed spectra, we need to describe how light travels through the gas in the stellar atmosphere. Our tool to interpret the stellar spectra is statistical mechanics, which studies the statistical properties of a system composed of many particles. For example, a gas is composed by a large number of particles, having a well-defined distribution of velocity and energy. On the one hand, the distribution of velocities can be described with the **Maxwell-Boltzmann distribution**, which gives the fraction of particles in a given velocity range in the conditions of thermodynamical equilibrium (see Fig. A.3). The number of gas particles per unit volume having speeds between v and $v + dv$ is given by

$$n_v dv = n\left(\frac{m}{2\pi kT}\right)^{3/2} e^{\frac{-mv^2}{2kT}} 4\pi v^2 dv \tag{A.1}$$

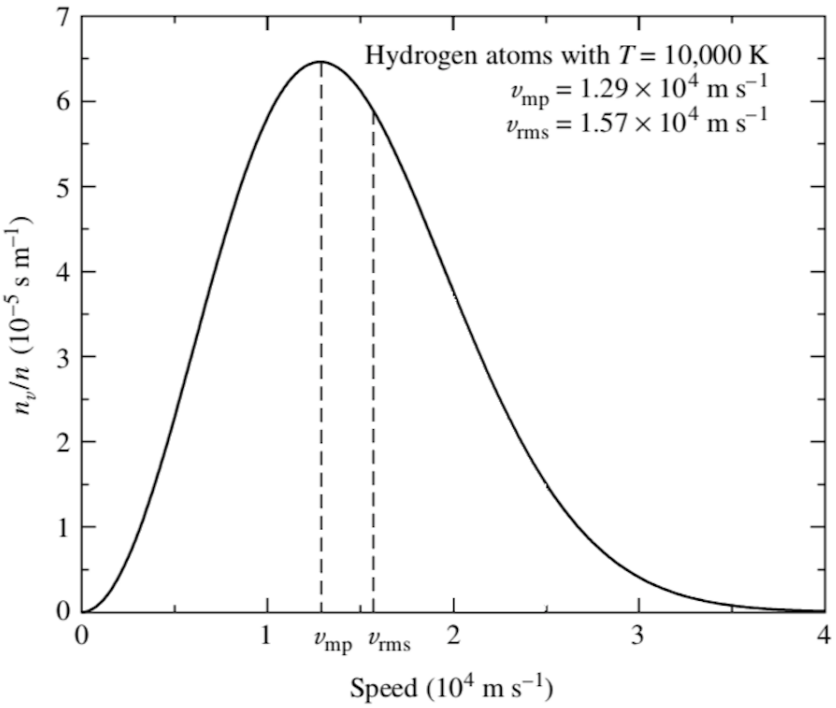

Fig. A.3: Maxwell-Boltzmann distribution function for hydrogen atoms at a temperature of 10,000 K. v_{mp} is the most probable speed, while v_{mp} is the root-mean-square speed (Carroll & Ostlie, 1996).

where n is the number of particles per unit volume, m is a particle mass, k is Boltzmann's constant, and T is the temperature of the gas. The exponent is formed by two terms: the kinetic energy $mv^2/2$, and the thermal energy kT. The distribution peaks when these

two energies are equal, at

$$v_{\mathrm{mp}} = \sqrt{\frac{2kT}{m}} \tag{A.2}$$

On the other hand, the distribution of the electrons in the energy levels (i.e. the orbitals) in each atom is described by the **Boltzmann equation**. The atoms of a gas lose and gain energy during collisions, and consequently how their orbitals are populated depends on the global condition of the gas. Given the number of atoms N_a with energy E_a and the number of atoms N_b with energy E_b, the Boltzmann equation gives

$$\frac{N_b}{N_a} = \frac{g_b e^{-E_b/kT}}{g_a e^{-E_a/kT}} = \frac{g_b}{g_a} e^{-(E_b - E_a)/kT} \tag{A.3}$$

where g is the statistical weight, i.e. the number of different quantum states with a given energy E. From this equation, we can deduce: if $E_b - E_a > 0$ and $T \to 0$, the thermal energy is not enough to move an atom to an energy higher level; if $E_b - E_a > 0$ and $T \to \infty$, all energy levels can be reached, without leaving under-populated the lower energy level. The Boltzmann equation shows that the ratio between the number of atoms of a given element in a given state of ionization in two specific energy levels (E_a and E_b), as a function of the system temperature.

If there is sufficient energy to remove an electron, an atom can be ionized, moving from the stage i to $i+1$. The relative number of atoms in different stages of ionization is given by the **Saha equation**.

However, to compute the ratio between the number of atom in the i and $i+1$ stages, we need to consider their initial configurations, which are not necessarily the ground state. If an atom or an ion is not, indeed, in the ground state, an average over the orbital energies needs to be considered to allow the possible partitioning of the atom's electrons among its orbitals. This average is computed taking into account the partition function Z, which is the weighted sum of the number of configurations in which the atom can arrange its electrons. The most energetic configurations are the less likely ones, as seen from the Boltzmann equation.

$$Z = \sum_{j=1}^{\infty} g_j e^{-(E_j - E_1)/kT} \tag{A.4}$$

where E_1 is the ground state, E_j is the excited state and g_j is the degeneracy.

If we identify the initial and final stages of ionization of an atom, i and $i+1$, and their corresponding partition functions Z_i and Z_{i+1}, the ratio between the number of atoms in the stage $i+1$ to the number of atoms in the stage i is given by Saha equation:

$$\frac{N_{i+1}}{N_i} = \frac{2Z_{i+1}}{n_e Z_i} \left(\frac{2\pi m_e kT}{h^2} \right)^{3/2} e^{-\chi_i/kT} \tag{A.5}$$

where n_e is the electron number density, 2 is related to the spin values of the free electron, the term in bracket is related to the free electron and χ_i is the ionization energy. We can express n_e as a function of electron pressure using the law of ideal gas $P_e = n_e kT$

$$\frac{N_{i+1}}{N_i} = \frac{2kTZ_{i+1}}{P_e Z_i} \left(\frac{2\pi m_e kT}{h^2} \right)^{3/2} e^{-\chi_i/kT} \tag{A.6}$$

The electron pressure term in this equation explains why stellar spectra are sensitive to the pressure, and consequently to the surface gravity, since stars are, usually, in hydrostatic equilibrium. P_e drives the equilibrium towards neutral state when it is high and towards the ionized state when it is low. This means that the electron pressure in a stellar atmosphere changes the line strengths. Moreover, the line strengths varies with spectral type and temperature, as shown in Fig. A.4.

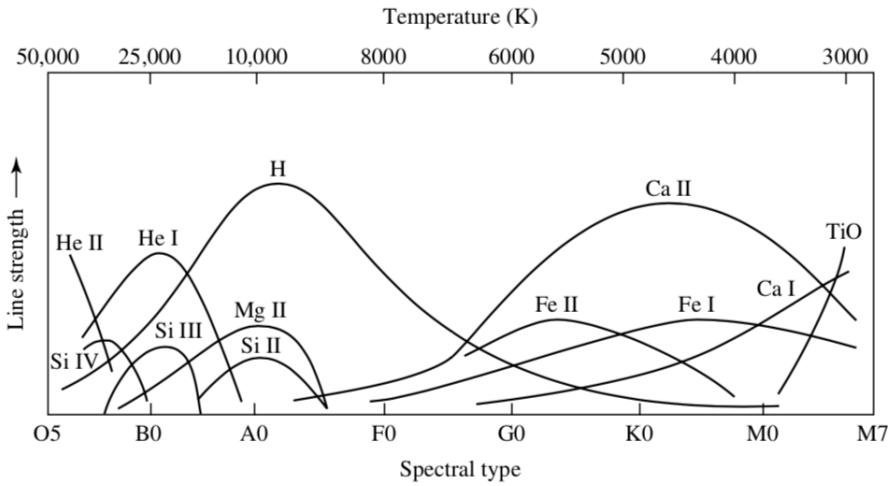

Fig. A.4: The dependence of spectral line strengths on temperature (Carroll & Ostlie, 1996).

In the next sections, I show how the Boltzmann and Saha equations can be used to characterise the conditions of stellar atmospheres.

A.4. STELLAR ATMOSPHERES

In this section, I describe how the light coming from the stellar interior crosses the gas in the atmosphere and how absorption lines are formed.

As a first approximation, a stellar spectrum can be considered as a blackbody spectrum, described by the Planck function B_λ. However, there are important differences: stellar spectra are characterised by large numbers of absorption lines, which decrease the intensity with respect to the blackbody emission, producing the so-called line blanketing (see Fig. A.5).

Since stars are not actually blackbodies, the definition of a single temperature to characterise the stellar spectrum is not possible. In fact, there are many different measurements of the temperature within a star, or better in a given location within a star: the effective temperature, obtained from the Stefan-Boltzmann law; the excitation temperature, defined by the Boltzmann equation; the kinetic temperature from the Maxwell-Boltzmann distribution; and the ionization temperature, defined by the Saha equation.

If we consider a gas confined in an ideal box, we can define a single temperature. In this case, the above defined temperatures converge to the same value. In the ideal box, the confined gas and the blackbody radiation reach an equilibrium with a single well-defined temperature and they are said to be in a steady state condition. In this case, there is not any

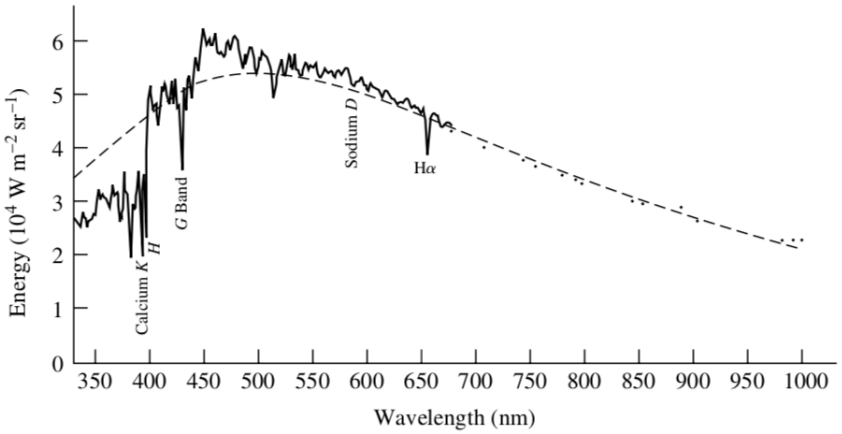

Fig. A.5: The spectrum of the Sun (solid line) over-plotted on the curve of an ideal blackbody (dashed line) having the Sun's effective temperature (Carroll & Ostlie, 1996).

flow of energy through the box and every process has the same rate of the opposite process. This condition is called *thermodynamic equilibrium*.

However, a star is not in perfect thermodynamic equilibrium, because there is a net outward flow of energy through the star, the temperature varies along the stellar radius, and there are collisions between particles and interactions with the radiation. In any case, the idealized case of a single temperature can still be employed if the distance over which the temperature significantly changes is larger than the distance traveled by the particles and photons between collisions. Indeed, the particles and photons are confined to a limited volume of constant temperature. In this case, we can talk about the **local thermodynamic equilibrium (LTE)**.

Consider a ray of light with a wavelength between λ and $\lambda + d\lambda$ passing through a surface of area dA at an angle θ, measured from the direction perpendicular to the surface, into a cone of solid angle $d\Omega$. The **specific intensity** I_ν is defined as (see also Fig. A.6):

$$I_\nu = \frac{\partial I}{\partial \lambda} = \frac{E_\lambda d\lambda}{d\lambda dt dA \cos\theta d\Omega} \tag{A.7}$$

Now, we consider a beam of parallel light rays travelling through a gas. Any process that removes photons from a beam of light is called absorption. In particular, the processes considered in the absorption term are: scattering of photons, true absorption of photons by atomic electrons, molecular energy-level transitions in cool gases. We can define the change in the intensity dI_λ of a ray of wavelength λ that crosses a gas as

$$dI_\lambda = -k_\lambda \rho I_\lambda ds \tag{A.8}$$

where ds is the travelled distance, ρ is the density of the gas and k_λ is called **absorption coefficient** or **opacity**, that is the cross section for absorbing photons of wavelength λ per unit mass and has units of $m^2 kg^{-1}$.

There are four primary sources of opacity that remove photons from a beam. They are:

- bound-bound transitions (excitations and de-excitations) that occur when a bound electron in an atom makes a transition from an orbital to another one;

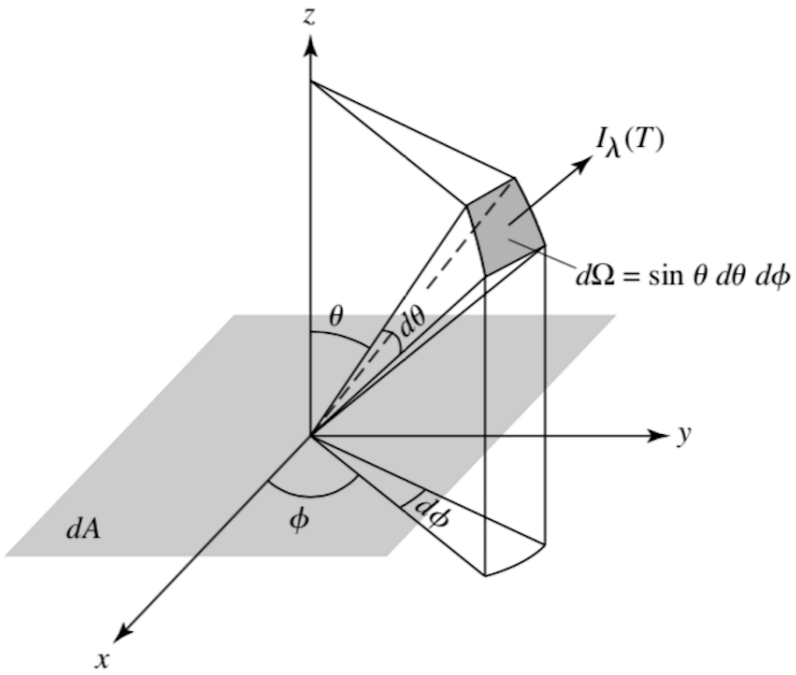

Fig. A.6: Specific intensity I_ν (Carroll & Ostlie, 1996).

- bound-free transitions (photo-ionizations) that occur when an incident photon has enough energy to ionize an atom;
- free-free transitions (scattering) that occur when a free electron close to an ion absorbs a photon, increasing the speed of the electron;
- electron scattering (Thomson scattering), when a photon is scattered by a free electron.

For scattered photons, the characteristic distance ℓ is the mean free path of the photons.

$$\ell = \frac{1}{n\sigma_\lambda} = \frac{1}{\rho k_\lambda} \tag{A.9}$$

From this equation, we can define the optical depth as

$$d\tau_\lambda = -k_\lambda \rho ds \tag{A.10}$$

where s is the distance measured along the path traveled by the photon. In particular, the difference in optical depth between two positions (initial position $s = 0$ and final position s) is

$$\Delta\tau_\lambda = \tau_{\lambda,f} - \tau_{\lambda,0} = -\int_0^s k_\lambda \rho ds < 0 \tag{A.11}$$

This equation means that the light is travelling through material with decreasing optical depth. Typically, the outermost layer of the stellar atmosphere can be considered with $\tau_\lambda = 0$ for all wavelengths; while the layer at $\tau_\lambda \sim 1$ is the deepest layer to which we can see and a photon can escape from that level of the stellar atmosphere. If $\tau_\lambda \gg 1$, the gas is said to be optically thick; if $\tau_\lambda \ll 1$, the gas is called optically thin. Since τ_λ depends on the

wavelength, a gas can be optically thin at a given λ and optically thick at another λ. For definition, the average level in the atmosphere from which photons escape is $\tau_\lambda = 2/3$. The optical depth might be considered as the number of mean free paths of a photon from the initial position to the stellar surface.

In an equilibrium state, there is not any change in total energy contained within a layer of the stellar interior or atmosphere. For this reason, absorption and emission have to be balanced. The term emission considers the processes that add photons to the light beam, such as scattering of photons or true emission of photons by electrons during atomic transitions. The main sources of emission are the same ones that produce the absorption: bound-bound, free-bound and free-free emission, and electron scattering.

The equation describing this mechanism is the **radiative transfer equation**, defined as (see also Fig. A.7):

$$\frac{1}{\rho}\frac{dI_\nu}{ds} = -k_\nu I_\nu + \epsilon_\nu \tag{A.12}$$

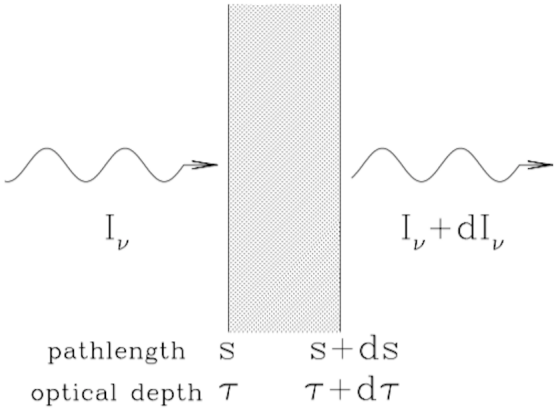

Fig. A.7: Radiative transfer (Draine, 2011).

This equation says how the energy is transported in the stellar interior, considering a beam of parallel light rays travelling through gas. The k_ν is the absorption coefficient (function of the composition, density, and temperature of the gas), while ϵ_ν is the emission coefficient and indicates how the energy is emitted in a volume dV.

Moreover, the ratio between the emission and absorption coefficients gives us the **source function**, which is of vital importance to solve the radiative transfer equation. It determines how rapidly the intensity of a light beam changes and describes the tendency of the photon population in the beam to look like the local source of photons in the surrounding gas. The source function is defined as:

$$S_\nu = \frac{\epsilon_\nu}{k_\nu} \tag{A.13}$$

and if we replace ϵ_ν / k_ν by S_ν in the transfer equation, we obtain:

$$-\frac{1}{\rho\, k_\nu}\frac{dI_\nu}{ds} = I_\nu - S_\nu \rightarrow \frac{dI_\nu}{d\tau_\nu} = I_\nu - S_\nu \tag{A.14}$$

According to the radiative transfer equation, if the intensity of the light does not vary ($dI_\nu/ds = 0$), then $I_\nu = S_\nu$. To solve it, we have to consider some approximations, and thus

the following considerations will be valid only when and where these approximations are applicable.

In the special case of blackbody radiation, in thermodynamic equilibrium, the source function is equal to the Planck function, $S_\nu = B_\nu$. Since a star cannot be in global thermodynamic equilibrium, we need to take into account two approximations: local thermodynamic equilibrium and plane parallel atmosphere. The first approximation is valid when the photon mean free path is smaller than the temperature scale height. Therefore, the photons are confined to a limited volume, a region of nearly constant temperature. For the second approximation, instead, we consider the stellar atmospheres physically thin with respect to the size of the star, and thus the gradients in temperature and specific intensity, which are much greater in the radial direction than in the transverse directions, are limited in thin atmospheres.

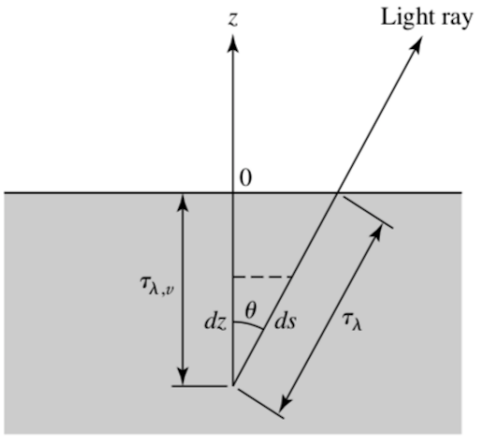

Fig. A.8: Plane parallel approximation (Carroll & Ostlie, 1996).

Using the notation in Fig. A.8, we can define the vertical optical depth, $\tau_{\lambda,\nu}$ as

$$\tau_{\lambda,\nu}(z) = \int_z^0 \rho k_\lambda dz \tag{A.15}$$

However, a ray that travels upward at an angle θ from the same initial position z has an optical depth measured along $ds = dz/\cos\theta$:

$$\tau_\lambda = \frac{\tau_{\lambda,\nu}}{\cos\theta} = \frac{\tau_{\lambda,\nu}}{\mu} \tag{A.16}$$

where μ is the directional cosine. In the plane parallel approximation, the vertical optical depth is a true vertical coordinate, analogous to z, and does not depend on the direction of travel of the light ray. For this reason, it can be used as a position coordinate in the transfer equation. Replacing τ_λ by $\tau_{\lambda,\nu}$ in Eq. A.14, we obtain the *plane parallel equation*:

$$\mu\frac{dI_\lambda}{d\tau_{\lambda,\nu}} = I_\lambda - S_\lambda \tag{A.17}$$

A.5. DETERMINATION OF STELLAR PARAMETERS AND CHEMICAL ABUNDANCES

The usual way to measure the strength of an absorption line is through its **equivalent width** (hereafter EW or W), which is the width of a rectangle having height equal to that of continuum emission and area equal to the area in the spectral line (see Fig. A.9). It is a measurement of the strength of spectral features and it is usually measured in mÅ. It is defined as:

$$EW = \int \frac{F_c - F_\lambda}{F_c} d\lambda \tag{A.18}$$

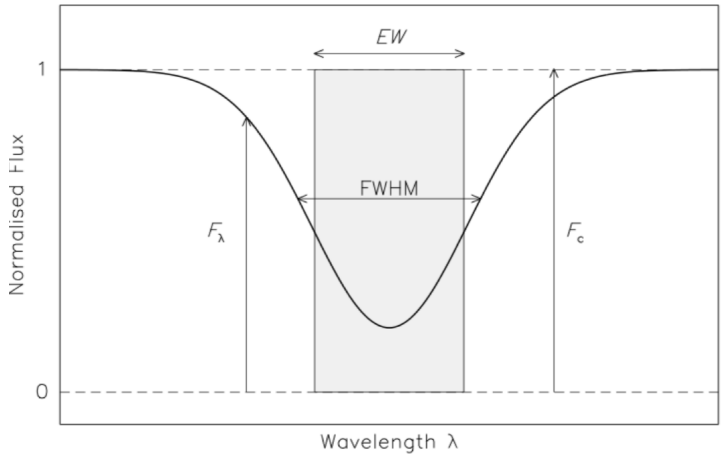

Fig. A.9: The profile of a typical spectral line (Carroll & Ostlie, 1996).

where F_c is the flux of the continuum and F_λ is the flux at the wavelength λ.

The opacity of the stellar material is greatest at the central wavelength and decreases moving into the wings. This means that the formation of the line centre is occurred at higher and cooler regions of the stellar atmosphere with respect to the wings of the same line, formed in deeper and hotter layers, until they merge with the continuum at $\tau_\nu = 2/3$. Therefore, the continuous spectrum is emitted in the deepest layers of the atmosphere, while the part of the light absorbed by atoms is removed from the beam in the higher atmosphere, forming the absorption line. If the number of the absorbers increases more and more, the line becomes deeper until the saturation.

A.5.1. LINE BROADENING

There are three main processes can be responsible for the broadening of spectral lines. Each mechanism has its own line shape.

- **Natural broadening.** Due to the uncertainty principle of Heisenberg, an electron in an excited states occupies its orbital for a short time, thus the energy cannot be precise: $\Delta E \approx \hbar/\Delta t$ where for a photon $E = hc/\lambda$. Then, the uncertainty in the photon wavelength is:

$$\Delta\lambda \approx \frac{\lambda^2}{2\pi c}\left(\frac{1}{\Delta t_i} + \frac{1}{\Delta t_f}\right) \tag{A.19}$$

where Δt_i and Δt_f are the lifetime of the electron in its initial and final state, respectively.

- **Doppler broadening.** In thermal equilibrium, the velocities of atoms follow the Maxwell-Boltzmann distribution with the most probable velocity $v_{mp} = \sqrt{2kT/m}$. The wavelengths are Doppler-shifted according to $\Delta\lambda/\lambda = \pm|v_r|/c$. Therefore, the width of a spectral line due to Doppler broadening is:

$$\Delta\lambda \approx \frac{2\lambda^2}{c}\sqrt{\frac{2kT}{m}} \tag{A.20}$$

- **Pressure broadening.** The atomic orbitals can be perturbed by collisions with a neutral atom or an ion. The general shape of the line is like that found for natural broadening, that is a Lorentz profile.

  An approximate calculation of the broadening can be done estimating the time between collisions:

$$\Delta t \approx \frac{\ell}{v} = \frac{1}{n\sigma\sqrt{2kT/m}} \tag{A.21}$$

  where ℓ is the mean free path, n is the number density and σ is the collision cross section. Thus, the width of the spectral line due to pressure broadening is:

$$\Delta\lambda = \frac{2\lambda}{c}\frac{1}{\pi\Delta t} \approx \frac{2\lambda}{c}\frac{n\sigma}{\pi}\sqrt{\frac{2kT}{m}} \tag{A.22}$$

The combination of Lorentz and Doppler profiles give a total profile called Voigt profile, where the Doppler broadening dominates near the center and the Lorentz broadening dominates on the wings of the line.

A.5.2. CALCULATION OF SPECTRAL LINES

The usual method to compute from an absorption line the abundance, N_a (the number of absorbing atoms per unit area), assumes that the photosphere of a star acts as a blackbody and the atoms above the photosphere remove the photons from the continuum to form the absorption lines in the spectrum. However, to use the strength of a line to infer the number of absorbers, we need to know the physical conditions of the stellar atmosphere, such as its temperature, density and composition, in which the line formed. The temperature and density determine, indeed, the Doppler and pressure broadening and they define the conditions of the Boltzmann and Saha equations, and thus how the atomic levels are populated.

In addition, to calculate the abundance, N_a, from a given atomic transition, we need to know the quantum-mechanical information of the involved energy levels. The probabilities of an electron to make a transition from the same initial orbital to another one are given by the so-called **f-values** or **oscillator strengths** for that orbital. The oscillator strength is the effective number of electrons per atom participating in a transition and is calculated numerically or measured in the laboratory. Thus, combining the atomic information of

an absorption line and a model atmosphere, with a radiative transfer code and with the measurement of the EWs from observed spectra, allows us to derive chemical abundances.

Another way to relate the equivalent width of an absorption line with the number of atoms producing the line is the **curve of growth**. Indeed, the equivalent width, W, of the line increases with the number of absorbers N_a. A curve of growth is a logarithmic graph, as shown in Fig A.10. When the density of the atoms is small (weak line), $W \propto N_a$ and the curve of growth is linear. When the density become higher, the center of the line becomes optically thick until it saturates (see Fig A.11), while the wings of the line are still optically thin and continue to deepen. In this case, the curve of growth changes the slope as $W \propto \sqrt{\ln N_a}$. If the number of absorbers still continues to increase, the width of the lines broadens due to the pressure broadening and the equivalent width grows more rapidly as $W \propto \sqrt{N_a}$.

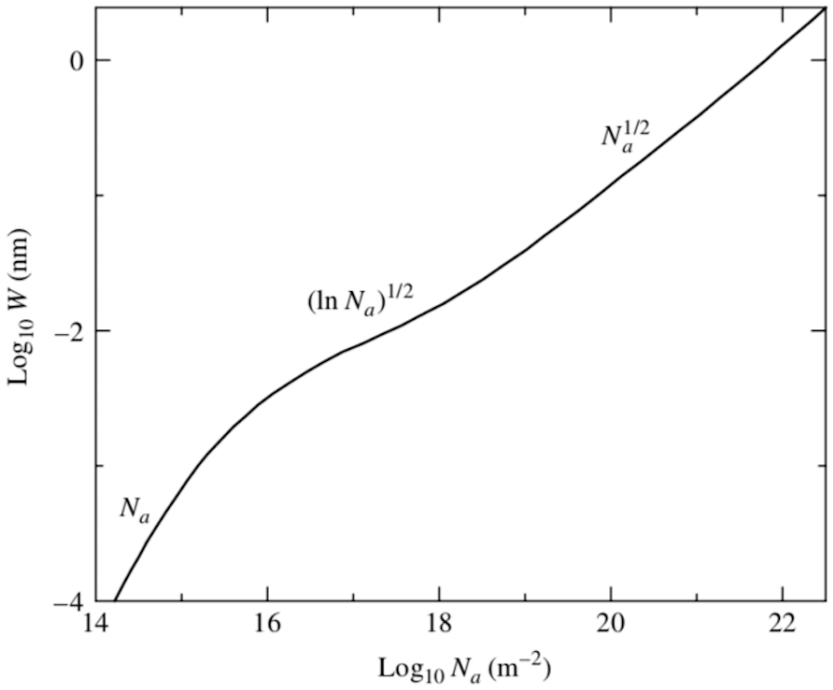

Fig. A.10: Curve of growth for the K line of Ca II. W is the equivalent width and N_a is the number of absorbers. Figure by Carroll & Ostlie (1996).

Therefore, using the curve of growth and a measured equivalent width, we can obtain the number of absorbing atoms. The number of absorbers can be obtained from the comparison between the equivalent widths of different absorption lines produced by the same atom/ion in the same state and a theoretical curve of growth.

Determination of effective temperature from spectroscopy To compute the effective temperature T_{eff} of a star from its spectrum, we require that the abundance of a given element (usually iron) is independent of the excitation potential of the individual lines. This is so because, all the lines of a given element should give the same abundance for the same star. The effective temperature is thus directly obtained from the Boltzmann equation: we

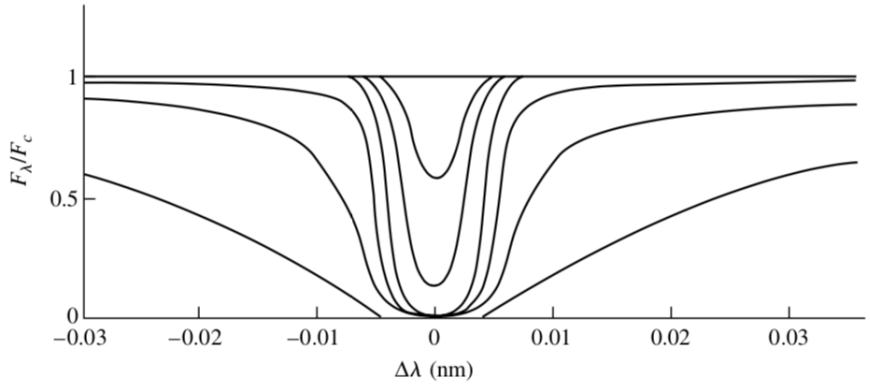

Fig. A.11: Equivalent width of the K line of Ca II with increasing number of absorbers until the saturation. Figure by Carroll & Ostlie (1996).

iteratively vary the $T_{\rm eff}$ in the model atmosphere as long as we reach the equilibrium between excitation potential and elemental abundance for all lines of this element (see top panel of Fig. A.12).

Determination of surface gravity from spectroscopy The surface gravity of a star of mass $M_\star$ and radius $R_\star$ is defined as $g = GM_\star/R_\star^2$, where G is the gravitational constant. The surface gravity of a star can be derived using the Saha equation.

For a given star and a given element, the abundance determined from the neutral state and the abundance obtained from the ionized state have to be equal. Indeed, the surface gravity is determined equalling the abundance of neutral and ionized iron, Fe I and Fe II (see bottom panel of Fig. A.12).

In hydrostatic equilibrium, the gravity is related to the electron pressure P_e: from the Saha equation, $N_{\rm Fe\,I}/N_{\rm Fe\,II} \propto 1/P_e$. Assuming that the star is in ionization equilibrium, we can estimate the electron pressure and thus the surface gravity. In the model atmosphere, we iteratively vary the surface gravity as long as we reach the equilibrium between the derived abundances of neutral and ionized species of the same element.

Determination of microturbulence The microturbulence ξ describes the photospheric turbulent motions on distances smaller than the mean free path of the photons. These motions broaden the spectral lines, and astronomers use the microturbunce as a free parameter introduced to remove the discrepancy between the empirical and theoretical curves of growth on their flat part (that is when $W \propto \sqrt{\ln N_a}$). It is necessary to compensate for the missing broadening. Usually, ξ is added in quadrature to the thermal Doppler line broadening. To derive the value of ξ, we iteratively vary in the model atmosphere the input ξ as long as we remove the trends between the abundance of iron and the logarithm of the reduced equivalent widths, EW/λ (see middle panel of Fig. A.12).

Determination of elemental abundance Knowing the effective temperature $T_{\rm eff}$ and surface gravity $\log g$, we can use the equivalent widths of different elements/ions to derive the abundances. In the following equation, we show the dependence of the abundances on the

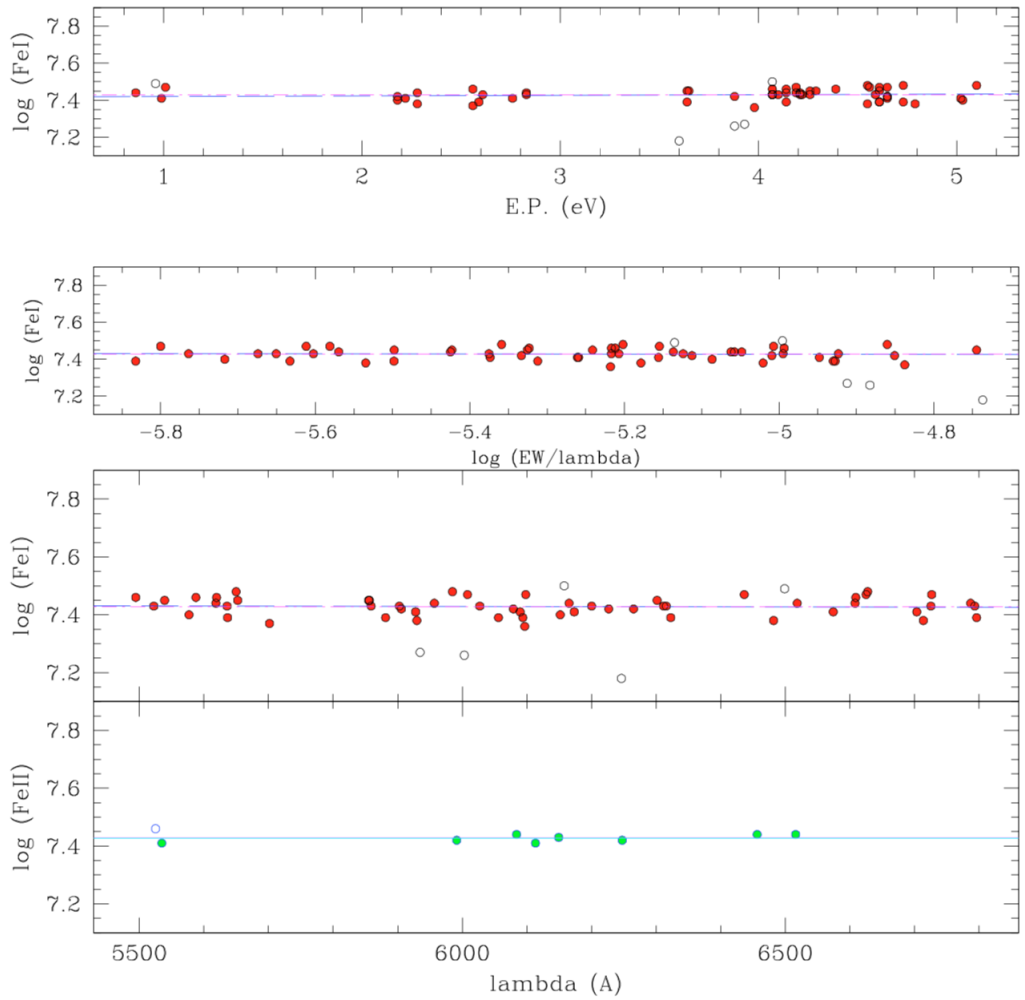

Fig. A.12: An example of the three equilibria to get $T_{\rm eff}$, log g and ξ from a solar spectrum. In the top panel, the excitation equilibrium is shown, used for the temperature determination. In the middle one the microturbulence equilibrium is displayed. In the bottom panel, the dependence of neutral (Fe I) and ionized (Fe II) iron abundances on the wavelength is shown, used for gravity determination (Magrini et al., 2013b).

stellar and atomic parameters, in the weak line regime.

$$\log\left(\frac{W_\lambda}{\lambda}\right) = \log\left(\frac{\pi e^2 N_i/N}{m_e c^2 U(T)} N_H\right) + \log A + \log(g_n f\,\lambda) - \frac{5040}{T}\chi - \log(k_\nu) \tag{A.23}$$

where W_λ is the equivalent width, while the first term on the right of equal is a constant for a given star, the second is the abundance, the third is the transition probability with g_n, the statistical weight of an atomic energy level, and f, the oscillator strength, the fourth contains the effective temperature and excitation potential, and the fifth is the absorption coefficient.

For weak lines, the equivalent width varies in a linear way with abundances. However, the abundance depends on the gf-value and varies with the inverse of the temperature. Moreover, the strength of lines of ionized elements depends on the pressure (thus surface gravity) and so on their curve of growth.

A good determination of the effective temperature $T_{\rm eff}$ and surface gravity log g is thus

necessary to correctly measure abundances. Once derived $T_{\rm eff}$ and log g, from the equivalent widths of absorption lines we can derive the abundances using their theoretical curve of growth (in which we have fixed $T_{\rm eff}$ and log g), or through radiative transfer code (see, e.g., MOOG or ATLAS, Sneden et al., 2014; Kurucz, 2005).

A.5.3. STELLAR ATMOSPHERE MODELS

In the spectral analysis, all of the ingredients presented in this Appendix, e.g. Saha and Boltzmann equations, thermodynamic equilibrium, radiative transfer, are combined with libraries of opacities to calculate temperature, pressure, and density at different depth from the surface in the stellar atmospheres. These models allow us to know the conditions inside the stellar atmospheres. In particular, they give us information about electronic pressure, temperature and the optical depth for photons at $\lambda = 5000$Å for ~ 50 layers of a stellar atmosphere. The characteristics of the stellar atmospheres are tabulated in several sets of model stellar atmospheres, where MARCS[1], Kurucz[2], ATLAS[3] are the most widely used. These model are built under some assumptions: local thermodynamic equilibrium, plane

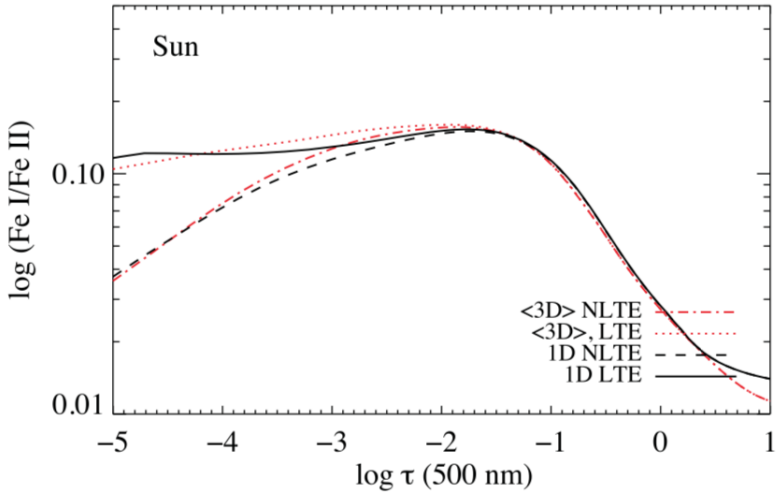

Fig. A.13: Total number densities of Fe I/Fe II for the Sun as a function of log τ. The different curves show the differences among 1D, 3D, LTE and NLTE models (Bergemann et al., 2012).

parallel and homogeneity of stellar atmospheres (1D-models). However, in real conditions, the atmospheres are not homogeneous, but they can have, e.g., stellar spots, granulations, non-radial pulsations, winds etc. Models taking into account these inhomogeneities are called 3D-models (Nordlund et al., 2009; Nordlund, 1982; Asplund, 2005). Moreover, in particular conditions, when the rate of photons absorption are larger than the rate of collisions, the LTE is no more a good approximation. In this case, we can talk about non-LTE conditions. It takes place in low gravities of high temperatures, especially for metal poor stars (Asplund, 2005; Bergemann et al., 2012; Bergemann & Nordlander, 2014). A comparison among 3D-1D and LTE-NLTE models is shown in Fig. A.13.

[1] http://marcs.astro.uu.se/
[2] http://kurucz.harvard.edu/grids.html
[3] http://www.stsci.edu/hst/observatory/crds/castelli_kurucz_atlas.html

A.6. DIFFERENTIAL SPECTROSCOPY

Standard spectroscopy suffers from systematic errors, as e.g., in modeling of stellar spectra and atmospheres, uncertainties in atomic data and in the damping approximations (Asplund, 2005), but also from the continuum setting and blended lines. A possible method to minimise the effects of systematic errors is to perform a differential analysis, line-by-line, of equivalent widths of solar-type stars relative to Sun (e.g. Meléndez et al., 2006; Meléndez & Ramírez, 2007; Meléndez et al., 2009). Namely, subtracting the equations A.23 for a solar-type star and for the Sun, we can remove the first term on the right of equal and $\log(g_n f \lambda)$ because they are the same for a solar-type star and the Sun. From the subtraction we obtain:

$$\log\left(\frac{W_{\lambda,\star}}{W_{\lambda,\odot}}\right) = \log A_\star - \log A_\odot - 5040\,\chi\left(\frac{1}{T_\star} - \frac{1}{T_\odot}\right) - \log\left(\frac{k_{\nu,\star}}{k_{\nu,\odot}}\right) \tag{A.24}$$

where the two last terms on the right of the equal are small for two similar stars. By analysing solar-type stars in a strictly differential way with respect to the Sun, the impact of most systematic errors can be characterised and subtracted. This approach leaves the error in the EW measurements (continuum setting and blended lines) as the unique major source of uncertainty.

A possible way to reduce the uncertainties due to the continuum setting and blended lines is to use high-resolution and high signal-to-noise ratio spectra, typically $R > 60,000$ and $S/N > 200$.

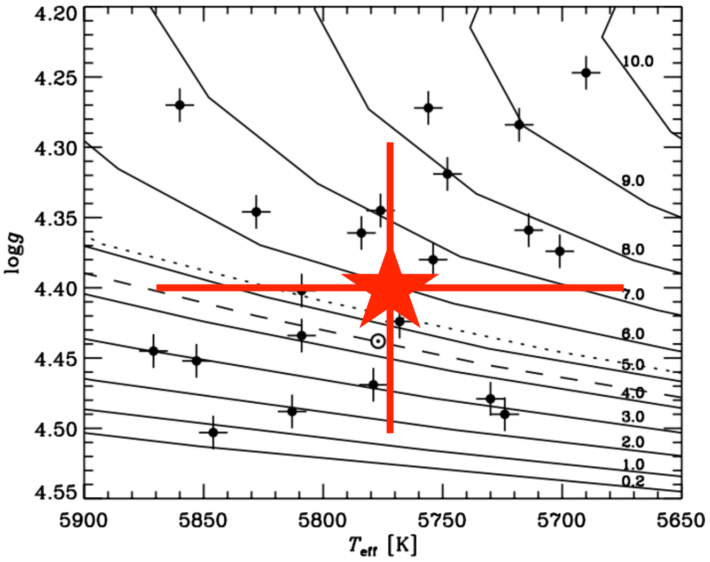

Fig. A.14: $T_{\rm eff}$ - log g diagram of solar type stars (black dots) compared with the typical uncertainties of a star analysed with standard spectroscopy (red symbol). The lines are Yonsei-Yale isochrones, theoretical models corrisponding to different ages. The solid ones are referred to [Fe/H] = 0.0 and [α/Fe] = 0.0, the dashed line to [Fe/H] = −0.05 and the dotted one to [α/Fe] = +0.1. The position of the Sun with an age of 4.55 Gyr is marked with a circle (Nissen, 2015).

Recent studies have reached a very high precision on stellar parameters and chemical abundances of the order of 0.01 dex (e.g. Meléndez et al., 2009, 2014a; Ramírez et al., 2009, 2014a,b) against 0.05-0.10 dex of standard spectroscopy. This high precision is shown in

Fig. A.14, where the solar type stars analysed in a differential way have uncertainties on $T_{\rm eff}$ and log g lower than typical uncertainties from standard spectroscopy (red star symbol). This level of accuracy can reveal detailed trends between star properties, as stellar age, and their abundances ratios, otherwise hidden.

A.7. TOOLS FOR THE SPECTRAL ANALYSIS WITH EQUIVALENT WIDTH

The spectral analysis described in the previous sections can be performed with different tools. In the following section, I present the tools that I used in my projects.

A.7.1. TOOLS FOR THE MEASUREMENT OF THE EWS

In the spectral analysis, described in Chapters 5 and 6, I used two tools to measure the EWs in spectra: DOOp and `Stellar Diff` .

DOOP

DOOp (DAOSPEC Output Optimiser pipeline, Cantat-Gaudin et al., 2014) is an automatic wrapper that uses BASH[4], IRAF[5] and DAOSPEC scripts in an iterative way, with a minimum of human intervention. It processes automatically each spectrum with DAOSPEC (Stetson & Pancino, 2008), a code that finds the absorption lines in stellar spectra, sets the continuum, and measures the full width half maximum (FWHM) that best fits the lines. DAOSPEC employs a fixed FWHM to facilitate the deblending of the lines, and estimates the continuum with Legendre polynomials after removing all fitted lines from the spectrum. Moreover, DAOSPEC uses an effective continuum, which is the true continuum depressed by a statistical estimate of the contaminating lines.

The outputs of DAOSPEC are two files containing the normalized and residual spectra and a list of the wavelengths, EWs of all the fitted features and a quality parameter. This quality parameter compares the local residuals around each line with the average residuals of the whole spectrum. The list also contains in the header the estimated radial velocity (RV) of the star, the FWHM used to fit the lines, the number of spectral lines, and a quality parameter defined as the root-mean-square value of the pixel-by-pixel flux residuals remaining in the spectrum after subtraction of all the fitted lines.

The goal of DOOp is to optimise the quality parameters of DAOSPEC in order to get the best measurements of EWs. The DAOSPEC parameters on which DOOp works are: short and long wavelength limit (SH, LO), minimum and maximum radial velocity (MI, MA), residual core flux (RE) and FWHM (FW). In details, SH and LO limit the wavelength range where DAOSPEC measures EW; MI and MA limit the radial velocity range where DAOSPEC estimates the RV; RE is the residual flux at the core of the deepest line in the spectrum; finally, FW sets the estimate of the resolution of the spectrum in units of pixel.

DOOp reads two input files: an "OPT file" necessary to set the basic options of the algorithm, an "input file" containing the list of spectra and six parameters for each of them:

[4] BASH is a Unix shell, a free software in common with all the operating systems based on UNIX and Linux.
[5] `http://ast.noao.edu/data/software`

OR (order of the polynomial for continuum fitting), FW, FI (=1 if this FWHM must be kept fixed, =0 if it must be optimised), RE and RV (radial velocity).

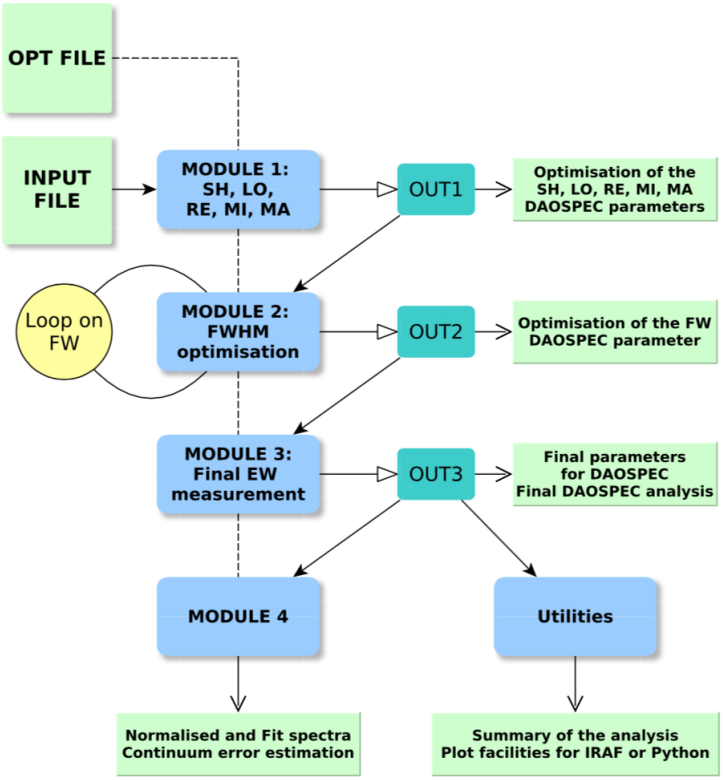

Fig. A.15: The work flow of the DOOp pipeline (Cantat-Gaudin et al., 2014).

After these two files are set, DOOp is ready to work. The analysis is performed by four modules and a task called "Utilities" (see Fig. A.15):

- Module 1 provides the parameters SH, LO, RE, MI, MA and a first estimete of EWs;
- Module 2 provides the best FWHM parameter for DAOSPEC in a iterative way as long as it reaches the convergence;
- Module 3 determines the FWHM that will be used for the final EW measurements;
- Module 4 performs two different tasks: one provides the fit and normalised spectra in FITS format; the other one provides EW measurements obtained by over- and underestimating the continuum level. The results of the second task can be used to quantify the error in the EW measurement due to the placement of the continuum;
- "Utilities" performs standard operations on the output files obtained by Module 3. Thanks to it, the user can easily visualise and compare the spectra and their corresponding fit.

STELLAR DIFF

`Stellar Diff`[6] is a Python code optimal for the differential spectroscopy of solar-like stars. It allows the user to measure the EW of a line, selecting one or more spectral windows for the continuum setting devoid of absorption features around each line of interest. These windows are identified using the solar spectrum and later they are applied for all studied spectra. An example is shown in Fig. A.16, where the line of interest is Fe I at 5247 Å, the pink bands are the windows inserted by user and the blue line is the fit for the local continuum and the line of interest.

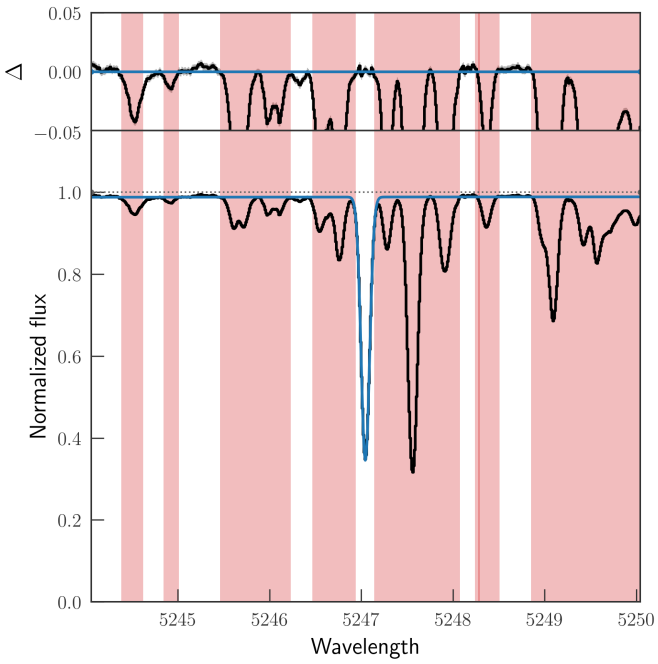

Fig. A.16: An example of the windows setting and the fitting of the continuum and the line-of-interest of Fe I at 5247 Å. The Δ is the residual of the fitting.

After identifying the windows for the solar spectrum, `Stellar Diff` employs the same window settings to calculate continuum levels and fit the lines of interest with Gaussian profiles for each spectrum. The adoption of same windows set found for the solar spectrum is necessary to minimise the effects of an imperfect spectral normalization or unresolved features in the continuum that can lead to larger errors in the differential abundances. Furthermore, `Stellar Diff` is able to identify points affected by hot-pixels or cosmic rays and remove them from the calculation of the continuum. The code delivers the EW of each line of interest along with its uncertainty.

A.7.2. TOOLS FOR THE DETERMINATION OF THE STELLAR PARAMETERS AND ABUNDANCES

Once the EWs are measured, other tools are necessary to determine the atmospheric parameters ($T_{\rm eff}$, log g, [Fe/H], ξ) and chemical abundances for each analysed spectrum. In my projects, I used FAMA and q2.

[6] `https://github.com/andycasey/stellardiff`

FAMA

FAMA (Fast Automatic Moog Analysis Magrini et al., 2013b) is a Perl code based on the ABFIND and BLENDS modules of the Fortran code MOOG (Sneden, 1973; Sneden et al., 2012). MOOG uses a model photosphere together with a list of atomic or molecular transitions to generate an emergent spectrum by solving the equation of radiative transfer. FAMA determines the stellar parameters, running MOOG in an iterative way to search for the equilibrium condition (excitation, ionization, and the trend between log n(Fe I) and EW), described in Sect A.5.2. In the iterative strategy of FAMA, $T_{\rm eff}$, log g, and ξ are adjusted step-by-step, changing the three parameters since the equilibria are reached. At each step a new model atmosphere is computed, the abundances are recalculated running MOOG and the equilibrium conditions are verified.

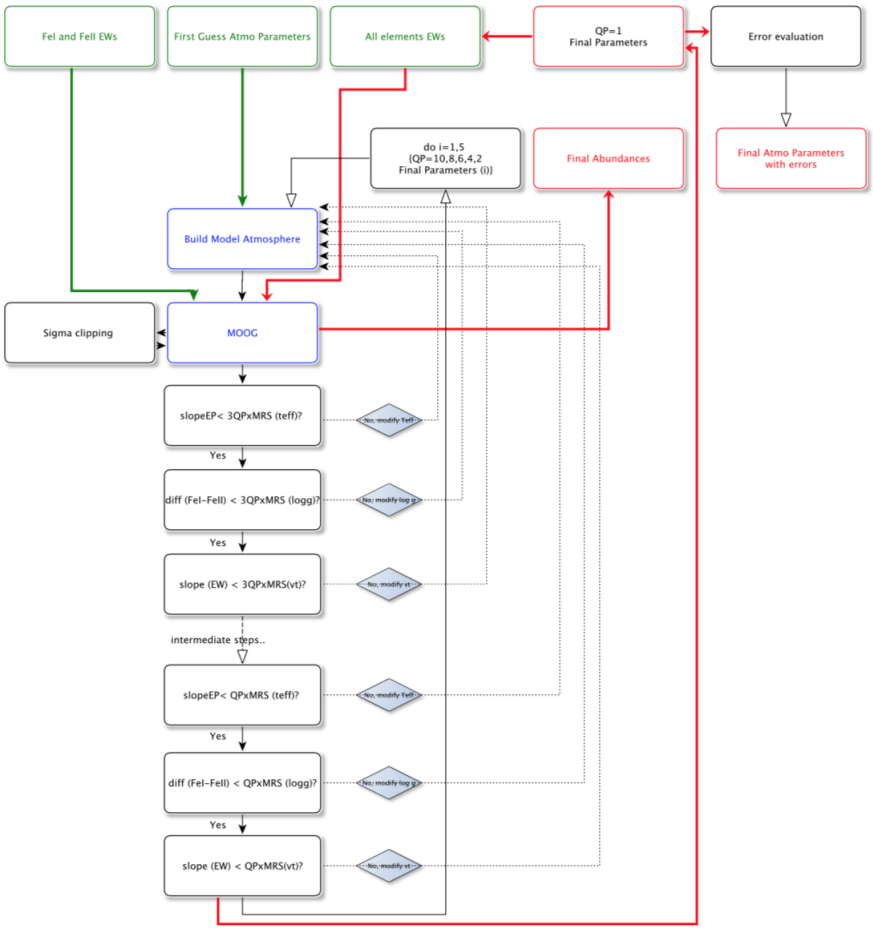

Fig. A.17: Work flow of FAMA code (Magrini et al., 2013b).

FAMA needs three files as input (see the work flow in Fig A.17): one containing EWs of Fe I and Fe II, a second one containing EWs of all elements, and a file with the input atmospheric parameters, built interpolating different atmospheric models. The first model atmosphere and the file with the EWs of iron are given to FAMA, which uses the driver ABFIND of MOOG to compute the abundances of Fe I and Fe II. The stellar parameters are varied by FAMA to reach the equilibrium conditions using the computed iron abundances. Finally, FAMA repeats the convergence path several times in order to ensure that the final

solution is independent from the initial parameters.

At the end of the last step, the final set of obtained stellar parameters, which satisfies the equilibrium conditions, is used to compute the elemental abundances. Finally, the errors associated with the stellar parameters and abundances are evaluated by FAMA following the procedure described in Magrini et al. (2013b).

Q2

q2[7] (*qoyllur-quipu2*, Ramírez et al., 2014a) is a Python code that processes the EW measurements of stars. It automatically estimates the atmospheric parameters and chemical abundances by performing a line-by-line differential analysis with respect to a reference spectrum. It is mostly used to analyse solar-like stars with respect to the Sun. This package employes MOOG (in its SILENT mode) using the excitation/ionization equilibria described in Sect. A.5.2.

Starting from the parameters of the reference star and from the file with all EWs (computed by `Stellar Diff`) for each spectrum, q2 finds the values that minimise the slopes of the differential iron abundance versus excitation potential and reduced EW as well as match the average Fe I and Fe II abundances in an iterative way. In each iteration, q2 changes the parameters in order to approach spectroscopic equilibrium. It is possible to set the initial steps for the changes to be applied to those parameters (usually 20 K, 0.1 dex, 0.1 dex for $T_{\rm eff}$, log g and ξ, respectively). It is also possible to set a maximum number of iterations (usually 150) in case q2 is not able to converge. After the parameters converge within the initial steps, they are divided by 2 and a new iteration block begins. The errors associated with the stellar parameters are evaluated by the code following the procedure described in Epstein et al. (2010) and Bensby et al. (2014). It takes into account the dependence between the parameters in the fulfilment of the three equilibrium conditions.

After finishing all iterations for each spectrum, q2 creates a file containing atmospheric parameters and their errors for each star. This file, together with the previous input file containing the EWs measurements, is given to q2 for a second run to obtain the elemental abundances. q2 is able to figure out when hyperfine structure (HFS) is needed and it creates MOOG linelists in the proper format (it uses the BLENDS driver instead of ABFIND in these situations). To calculate differential abundances, it is necessary to indicate the reference object, the Sun, and the model atmosphere. Finally, the errors for the abundances measurement are computed from the line-to-line scatter, quantified by the standard error, added in quadrature with the abundance errors that result from the propagation of errors in the stellar parameters. The output file from this second run of q2 contains both the absolute and relative abundances measured, their 1-σ line-to-line scatter, the error calculation including the propagation of errors from the stellar parameters and the number of line for given element. Moreover, q2 also allows us to calculate other fundamental stellar parameters such as mass and age using isochrones.

[7] The q2 code is a free Python package, available at `https://github.com/astroChasqui/q2`

A.8. OTHER TYPES OF SPECTRAL ANALYSES

Because of the large data sets from spectroscopic surveys, automated analysis techniques and classification algorithms are required to obtain robust estimates of the stellar parameters and abundances.

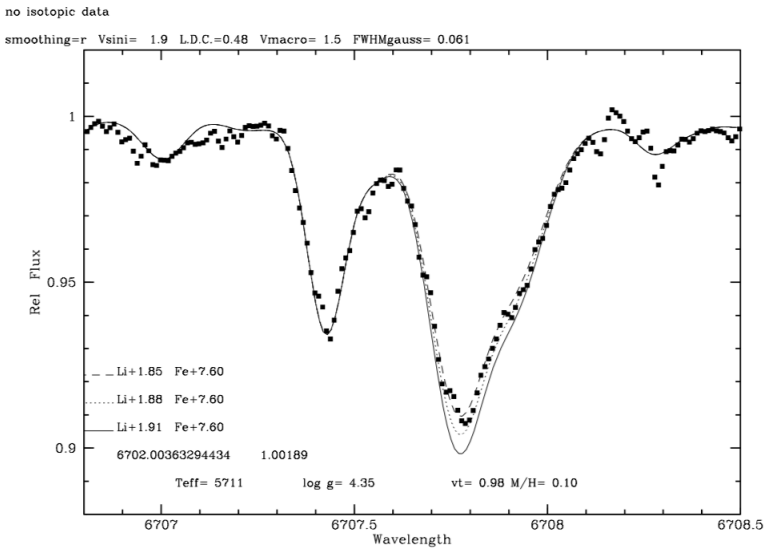

Fig. A.18: An example of spectral synthesis where the squares represent the observed spectrum, while the three lines the spectral models with different abundances of lithium (Delgado Mena et al., 2014).

Spectral synthesis consists in determining the atmospheric parameters, comparing the observed spectrum and a grid of synthetic spectra, finding the best match via χ^2 minimisation (see an example in Fig. A.18). Synthetic spectra grids need to span the parameter space of the observed stars (Kordopatis et al., 2011). Spectral synthesis can have a "line-fitting" or "full-spectrum-fitting" approach, i.e., by fitting isolated absorption lines one-by-one (e.g., MyGIsFOS, Sbordone et al., 2014; Stellar Parameters Determination Software, SPADES, Posbic et al., 2012), or by fitting full spectral ranges (e.g., the MATrix Inversion for Spectral SynthEsis, MATISSE, Recio-Blanco et al., 2006; FERRE, Allende-Prieto & Apogee Team, 2015). Spectroscopy Made Easy (SME, Valenti & Piskunov, 1996) distinguishes itself from the other codes since it synthesizes on-the-fly single absorption lines or parts of the spectrum to be matched with the observed ones.

Recent methods use the **data-driven approach** (see e.g. *The cannon*, a transfer machine-learning method developed for APOGEE, Ness et al., 2015). This approach relies on a subset of reference stars with well-determined atmospheric parameters. It consists in two steps: the first one is to create from the reference subset a model that describes a probability density function for the flux at every pixel in the spectrum as a function of the atmospheric parameters and chemical abundances; the second step is to assume that this model works for all the other objects of the sample.

Recently, **deep learning** using artificial neural networks (ANNs) is getting increasing attention from astronomers (Leung & Bovy, 2019; Fabbro et al., 2020). This method is interesting because, given a training set of data analysed with more traditional means, the deep learning can process high-resolution spectra in a very fast way. The deep learning is a subset of machine learning and uses multilayer ANNs connected to each other. It applies

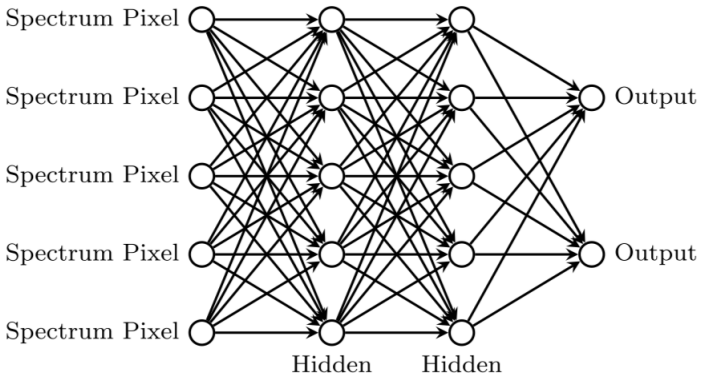

Fig. A.19: An artificial neural network (Leung & Bovy, 2019).

weights to each input value to compute an output (see Fig. A.19). The ANNs were originally inspired by biological systems such as human brains, which consist of numerous neurons interconnected by synapses. The deep learning takes data uncertainties in the training data into account and estimates uncertainty in predictions made with the ANNs.

BIBLIOGRAPHY

Aguilera-Gómez, C., Ramírez, I., & Chanamé, J. 2018, A&A, 614, A55

Allard, F., Homeier, D., & Freytag, B. 2011, in Astronomical Society of the Pacific Conference Series, Vol. 448, 16th Cambridge Workshop on Cool Stars, Stellar Systems, and the Sun, ed. C. Johns-Krull, M. K. Browning, & A. A. West, 91

Allende-Prieto, C. & Apogee Team. 2015, in American Astronomical Society Meeting Abstracts, Vol. 225, American Astronomical Society Meeting Abstracts #225, 422.07

Alonso-Santiago, J., Negueruela, I., Marco, A., et al. 2017, MNRAS, 469, 1330

Amôres, E. B., Lépine, J. R. D., & Mishurov, Y. N. 2009, MNRAS, 400, 1768

Anders, F., Cantat-Gaudin, T., Quadrino-Lodoso, I., et al. 2020, arXiv e-prints, arXiv:2006.01690

Anders, F., Khalatyan, A., Chiappini, C., et al. 2019, VizieR Online Data Catalog, I/349

Andrae, R., Fouesneau, M., Creevey, O., et al. 2018, A&A, 616, A8

Aparicio, A., Alfaro, E. J., Delgado, A. J., Rodriguez-Ulloa, J. A., & Cabrera-Cano, J. 1993, AJ, 106, 1547

Argast, D., Samland, M., Thielemann, F.-K., & Qian, Y.-Z. 2004, A&A, 416, 997

Asplund, M. 2005, ARA&A, 43, 481

Asplund, M., Grevesse, N., Sauval, A. J., & Scott, P. 2009, ARA&A, 47, 481

Ayres, T. R., Plymate, C., & Keller, C. U. 2006, ApJS, 165, 618

Bailer-Jones, C. A. L., Rybizki, J., Fouesneau, M., Mantelet, G., & Andrae, R. 2018, AJ, 156, 58

Balachandran, S. 1990, ApJ, 354, 310

Baratella, M., D'Orazi, V., Carraro, G., et al. 2020, A&A, 634, A34

Barbuy, B., Chiappini, C., & Gerhard, O. 2018, ARA&A, 56, 223

Barnes, S. A. 2007, ApJ, 669, 1167

Beane, A., Mac Low, M.-M., Sanderson, R., et al. 2019, in American Astronomical Society Meeting Abstracts, Vol. 233, American Astronomical Society Meeting Abstracts #233, 342.06

Bedell, M., Meléndez, J., Bean, J. L., et al. 2014, ApJ, 795, 23

Bellinger, E. P., Angelou, G. C., Hekker, S., et al. 2016, ApJ, 830, 31

Belokurov, V., Erkal, D., Evans, N. W., Koposov, S. E., & Deason, A. J. 2018, MNRAS, 478, 611

Belokurov, V., Zucker, D. B., Evans, N. W., et al. 2006, ApJ, 642, L137

Benjamin, R. A., Churchwell, E., Babler, B. L., et al. 2005, ApJ, 630, L149

Bensby, T., Feltzing, S., Gould, A., et al. 2017, A&A, 605, A89

Bensby, T., Feltzing, S., Lundström, I., & Ilyin, I. 2005, A&A, 433, 185

Bensby, T., Feltzing, S., & Oey, M. S. 2014, A&A, 562, A71

Bergemann, M., Huber, D., Adibekyan, V., et al. 2019, arXiv e-prints, arXiv:1903.03157

Bergemann, M., Lind, K., Collet, R., Magic, Z., & Asplund, M. 2012, MNRAS, 427, 27

Bergemann, M. & Nordlander, T. 2014, arXiv e-prints, arXiv:1403.3088

Bertelli Motta, C., Salaris, M., Pasquali, A., & Grebel, E. K. 2017, MNRAS, 466, 2161

Bessell, M. S., Castelli, F., & Plez, B. 1998, A&A, 333, 231

Blanco-Cuaresma, S. & Fraix-Burnet, D. 2018, A&A, 618, A65

Blanco-Cuaresma, S., Soubiran, C., Heiter, U., et al. 2015, A&A, 577, A47

Blanco-Cuaresma, S., Soubiran, C., Heiter, U., & Jofré, P. 2014, A&A, 569, A111

Bland-Hawthorn, J. & Gerhard, O. 2016, ARA&A, 54, 529

Blanton, M. R., Bershady, M. A., Abolfathi, B., et al. 2017, AJ, 154, 28

Bonatto, C., Kerber, L. O., Bica, E., & Santiago, B. X. 2006, A&A, 446, 121

Borucki, W. J., Koch, D., Basri, G., et al. 2010, Science, 327, 977

Bovy, J. 2015, ApJS, 216, 29

Bovy, J. 2016, ApJ, 817, 49

Bovy, J., Rix, H.-W., Liu, C., et al. 2012, ApJ, 753, 148

Bovy, J., Rix, H.-W., Schlafly, E. F., et al. 2016, ApJ, 823, 30

Boyle, W. S. & Smith, G. E. 1993, Charge coupled semiconductor devices (Bell System Technical Journal 1970), 475

Bragaglia, A. 2008, MnSAI, 79, 365

Bragaglia, A. & Tosi, M. 2006, AJ, 131, 1544

Brandt, T. D. & Huang, C. X. 2015, ApJ, 807, 24

Bravi, L., Zari, E., Sacco, G. G., et al. 2018, A&A, 615, A37

Bressan, A., Marigo, P., Girardi, L., et al. 2012, MNRAS, 427, 127

Brooke, J. S. A., Bernath, P. F., Schmidt, T. W., & Bacskay, G. B. 2013, JQSRT, 124, 11

Buckner, A. S. M. & Froebrich, D. 2014, MNRAS, 444, 290

Buder, S., Asplund, M., Duong, L., et al. 2018, MNRAS, 478, 4513

Busso, M., Gallino, R., Lambert, D. L., Travaglio, C., & Smith, V. V. 2001, ApJ, 557, 802

Busso, M., Gallino, R., & Wasserburg, G. J. 1999, ARA&A, 37, 239

Cantat-Gaudin, T. 2015, PhD thesis, Universita Degli Studi di Padova

Cantat-Gaudin, T. & Anders, F. 2020, A&A, 633, A99

Cantat-Gaudin, T., Anders, F., Castro-Ginard, A., et al. 2020, A&A, 640, A1

Cantat-Gaudin, T., Jordi, C., Vallenari, A., et al. 2018a, A&A, 618, A93

Cantat-Gaudin, T., Vallenari, A., Sordo, R., et al. 2018b, A&A, 615, A49

Cantat-Gaudin, T., Vallenari, A., Zaggia, S., et al. 2014, A&A, 569, A17

Carollo, D., Beers, T. C., Lee, Y. S., et al. 2007, Nature, 450, 1020

Carraro, G., Geisler, D., Villanova, S., Frinchaboy, P. M., & Majewski, S. R. 2007, A&A, 476, 217

Carraro, G., Janes, K. A., Costa, E., & Méndez, R. A. 2006, MNRAS, 368, 1078

Carrera, R. 2012, A&A, 544, A109

Carrera, R., Pasquato, M., Vallenari, A., et al. 2019, A&A, 627, A119

Carretta, E., Bragaglia, A., Gratton, R. G., et al. 2010, A&A, 516, A55

Carretta, E., Bragaglia, A., Gratton, R. G., & Tosi, M. 2005, A&A, 441, 131

Carretta, E., Gratton, R. G., & Sneden, C. 2000, A&A, 356, 238

Carroll, B. W. & Ostlie, D. A. 1996, An Introduction to Modern Astrophysics

Casali, G., Magrini, L., Frasca, A., et al. 2020a, A&A, 643, A12

Casali, G., Magrini, L., Tognelli, E., et al. 2019, A&A, 629, A62

Casali, G., Spina, L., Magrini, L., et al. 2020b, A&A, 639, A127

Casamiquela, L., Blanco-Cuaresma, S., Carrera, R., et al. 2019, MNRAS, 490, 1821

Casamiquela, L., Carrera, R., Balaguer-Núñez, L., et al. 2018, A&A, 610, A66

Castelli, F. & Kurucz, R. L. 2003, in IAU Symposium, Vol. 210, Modelling of Stellar Atmospheres, ed. N. Piskunov, W. W. Weiss, & D. F. Gray, A20

Castelli, F. & Kurucz, R. L. 2004, A&A, 419, 725

Castro-Ginard, A., Jordi, C., Luri, X., et al. 2020, A&A, 635, A45

Castro-Ginard, A., Jordi, C., Luri, X., et al. 2018, A&A, 618, A59

Chaplin, W. J., Basu, S., Huber, D., et al. 2014, ApJS, 210, 1

Chaplin, W. J., Serenelli, A. M., Miglio, A., et al. 2020, Nature Astronomy, 4, 382

Charbonnel, C. & Lagarde, N. 2010, A&A, 522, A10

Chen, L., Hou, J. L., & Wang, J. J. 2003, AJ, 125, 1397

Chen, Y. Q. & Zhao, G. 2020, MNRAS, 495, 2673

Chiappini, C. 2001, American Scientist, 89, 506

Chiappini, C., Anders, F., Rodrigues, T. S., et al. 2015, A&A, 576, L12

Chiappini, C., Matteucci, F., & Gratton, R. 1997, ApJ, 477, 765

Chiosi, C. 1980, A&A, 83, 206

Chubak, C., Marcy, G., Fischer, D. A., et al. 2012, arXiv e-prints, arXiv:1207.6212

Churchwell, E., Babler, B. L., Meade, M. R., et al. 2009, Publications of the ASP, 121, 213

Cignoni, M., Beccari, G., Bragaglia, A., & Tosi, M. 2011, MNRAS, 416, 1077

Cirasuolo, M., Afonso, J., Bender, R., et al. 2011, The Messenger, 145, 11

Collet, R., Asplund, M., & Thévenin, F. 2005, A&A, 442, 643

Collinder, P. 1931, Annals of the Observatory of Lund, 2, B1

Cosentino, R., Lovis, C., Pepe, F., et al. 2014, Society of Photo-Optical Instrumentation Engineers (SPIE) Conference Series, Vol. 9147, HARPS-N @ TNG, two year harvesting data: performances and results, 91478C

Cristallo, S., Piersanti, L., Straniero, O., et al. 2011, ApJS, 197, 17

Cui, X.-Q., Zhao, Y.-H., Chu, Y.-Q., et al. 2012, Research in Astronomy and Astrophysics, 12, 1197

Cutri, R. M., Wright, E. L., Conrow, T., et al. 2013, Explanatory Supplement to the AllWISE Data Release Products, Explanatory Supplement to the AllWISE Data Release Products

da Silva, R., Porto de Mello, G. F., Milone, A. C., et al. 2012, A&A, 542, A84

Dalton, G., Trager, S. C., Abrams, D. C., et al. 2012, Society of Photo-Optical Instrumentation Engineers (SPIE) Conference Series, Vol. 8446, WEAVE: the next generation wide-field spectroscopy facility for the William Herschel Telescope, 84460P

D'Antona, F., Ventura, P., Dotter, A., Ekström, S., & Tailo, M. 2019, IAU Symposium, 343, 314

Davies, G. R. & Miglio, A. 2016, Astronomische Nachrichten, 337, 774

de Jong, R. 2011, The Messenger, 145, 14

De Silva, G. M., Freeman, K. C., Asplund, M., et al. 2007a, AJ, 133, 1161

De Silva, G. M., Freeman, K. C., Bland-Hawthorn, J., Asplund, M., & Bessell, M. S. 2007b, AJ, 133, 694

De Silva, G. M., Freeman, K. C., Bland-Hawthorn, J., et al. 2015, MNRAS, 449, 2604

De Silva, G. M., Sneden, C., Paulson, D. B., et al. 2006, AJ, 131, 455

Degl'Innocenti, S. 2009, in American Institute of Physics Conference Series, Vol. 1111, Probing Stellar Populations Out to the Distant Universe: Cefalu 2008, Proceedings of the International Conference, ed. G. Giobbi, A. Tornambe, G. Raimondo, M. Limongi, L. A. Antonelli, N. Menci, & E. Brocato, 83–90

Delgado Mena, E., Israelian, G., González Hernández, J. I., et al. 2014, A&A, 562, A92

Delgado Mena, E., Moya, A., Adibekyan, V., et al. 2019, A&A, 624, A78

Dell'Omodarme, M., Valle, G., Degl'Innocenti, S., & Prada Moroni, P. G. 2012, A&A, 540, A26

Deng, L.-C., Newberg, H. J., Liu, C., et al. 2012, Research in Astronomy and Astrophysics, 12, 735

Dias, W. S., Alessi, B. S., Moitinho, A., & Lépine, J. R. D. 2002, A&A, 389, 871

Dias, W. S. & Lépine, J. R. D. 2005, ApJ, 629, 825

Domínguez, I., Cristallo, S., Straniero, O., et al. 2011, Astronomical Society of the Pacific Conference Series, Vol. 445, The Fruity Database: Chemical Features of Low-Mass AGB Stars, ed. F. Kerschbaum, T. Lebzelter, & R. F. Wing, 57

Donati, P., Bragaglia, A., Cignoni, M., Cocozza, G., & Tosi, M. 2012, MNRAS, 424, 1132

Donati, P., Cantat Gaudin, T., Bragaglia, A., et al. 2014, A&A, 561, A94

Donati, P., Cocozza, G., Bragaglia, A., et al. 2015, MNRAS, 446, 1411

Donor, J., Frinchaboy, P. M., Cunha, K., et al. 2020, AJ, 159, 199

Donor, J., Frinchaboy, P. M., Cunha, K., et al. 2018, AJ, 156, 142

D'Orazi, V., Oliva, E., Bragaglia, A., et al. 2020, A&A, 633, A38

Draine, B. T. 2011, Physics of the Interstellar and Intergalactic Medium

Dwek, E., Arendt, R. G., Hauser, M. G., et al. 1995, ApJ, 445, 716

Eggen, O. J., Lynden-Bell, D., & Sandage, A. R. 1962, ApJ, 136, 748

Eggenberger, P., Meynet, G., Maeder, A., et al. 2010, A&A, 519, A116

Eisenhauer, F., Genzel, R., Alexander, T., et al. 2005, ApJ, 628, 246

Epstein, C. R., Johnson, J. A., Dong, S., et al. 2010, ApJ, 709, 447

Fabbro, S., Venn, K., O'Briain, T., et al. 2020, in Astronomical Society of the Pacific Conference Series, Vol. 522, Astronomical Data Analysis Software and Systems XXVII, ed. P. Ballester, J. Ibsen, M. Solar, & K. Shortridge, 393

Feltzing, S., Fohlman, M., & Bensby, T. 2007, A&A, 467, 665

Feltzing, S., Howes, L. M., McMillan, P. J., & Stonkutė, E. 2017, MNRAS, 465, L109

Ferrini, F., Molla, M., Pardi, M. C., & Diaz, A. I. 1994, ApJ, 427, 745

Fishlock, C. K., Karakas, A. I., Lugaro, M., & Yong, D. 2014, ApJ, 797, 44

Fornal, B., Tucker, D. L., Smith, J. A., et al. 2007, AJ, 133, 1409

Franchini, M., Morossi, C., Di Marcantonio, P., et al. 2020, ApJ, 888, 55

Frasca, A., Alonso-Santiago, J., Catanzaro, G., et al. 2019, A&A, 632, A16

Frasca, A., Guillout, P., Marilli, E., et al. 2006, A&A, 454, 301

Frasca, A., Molenda-Żakowicz, J., De Cat, P., et al. 2016, A&A, 594, A39

Freeman, K. & Bland-Hawthorn, J. 2002, ARA&A, 40, 487

Friel, E. D., Donati, P., Bragaglia, A., et al. 2014, A&A, 563, A117

Friel, E. D., Jacobson, H. R., Barrett, E., et al. 2003, AJ, 126, 2372

Friel, E. D., Jacobson, H. R., & Pilachowski, C. A. 2005, AJ, 129, 2725

Friel, E. D. & Janes, K. A. 1993, A&A, 267, 75

Friel, E. D., Janes, K. A., Tavarez, M., et al. 2002, AJ, 124, 2693

Fujii, M. S. & Portegies Zwart, S. 2016, ApJ, 817, 4

Gaia Collaboration, Babusiaux, C., van Leeuwen, F., et al. 2018a, A&A, 616, A10

Gaia Collaboration, Brown, A. G. A., Vallenari, A., et al. 2018b, A&A, 616, A1

Gaia Collaboration, Brown, A. G. A., Vallenari, A., et al. 2016a, A&A, 595, A2

Gaia Collaboration, Prusti, T., de Bruijne, J. H. J., et al. 2016b, A&A, 595, A1

Gallino, R., Arlandini, C., Busso, M., et al. 1998, ApJ, 497, 388

Gao, X.-H. 2014, Research in Astronomy and Astrophysics, 14, 159

García, R. A. & Ballot, J. 2019, Living Reviews in Solar Physics, 16, 4

García Pérez, A. E., Allende Prieto, C., Holtzman, J. A., et al. 2016, AJ, 151, 144

Geller, A. M., Latham, D. W., & Mathieu, R. D. 2015, AJ, 150, 97

Gennaro, M., Prada Moroni, P. G., & Degl'Innocenti, S. 2010, A&A, 518, A13

Genzel, R., Schödel, R., Ott, T., et al. 2003, Nature, 425, 934

Gibson, B. K., Courty, S., Cunnama, D., & Mollá, M. 2013, Asociacion Argentina de Astronomia La Plata Argentina Book Series, 4, 57

Gilmore, G., Randich, S., Asplund, M., et al. 2012, The Messenger, 147, 25

Gilmore, G. & Reid, N. 1983, MNRAS, 202, 1025

Gilmore, G., Wyse, R. F. G., & Kuijken, K. 1989, ARA&A, 27, 555

Goriely, S. & Siess, L. 2018, A&A, 609, A29

Gould, A., Bahcall, J. N., & Flynn, C. 1996, ApJ, 465, 759

Gratton, R. G., Carretta, E., & Bragaglia, A. 2012, A&A Reviews, 20, 50

Gratton, R. G., Sneden, C., Carretta, E., & Bragaglia, A. 2000, A&A, 354, 169

Grevesse, N., Asplund, M., & Sauval, A. J. 2007, Space Science Reviews, 130, 105

Griffith, E., Johnson, J. A., & Weinberg, D. H. 2019, ApJ, 886, 84

Guerço, R., Cunha, K., Smith, V. V., et al. 2019, ApJ, 876, 43

Gustafsson, B., Edvardsson, B., Eriksson, K., et al. 2008, A&A, 486, 951

Harris, W. E. 1996, AJ, 112, 1487

Hartwick, F. D. A. 1987, in NATO Advanced Science Institutes (ASI) Series C, Vol. 207, NATO Advanced Science Institutes (ASI) Series C, ed. G. Gilmore & B. Carswell, 281

Hasselquist, S., Holtzman, J. A., Shetrone, M., et al. 2019, ApJ, 871, 181

Hatzidimitriou, D., Held, E. V., Tognelli, E., et al. 2019, A&A, 626, A90

Hayden, M. R., Bovy, J., Holtzman, J. A., et al. 2015, ApJ, 808, 132

Hayden, M. R., Recio-Blanco, A., de Laverny, P., Mikolaitis, S., & Worley, C. C. 2017, A&A, 608, L1

Hayes, C. R., Majewski, S. R., Shetrone, M., et al. 2018, ApJ, 852, 49

Haywood, M., Di Matteo, P., Lehnert, M. D., Katz, D., & Gómez, A. 2013, A&A, 560, A109

Haywood, M., Lehnert, M. D., Di Matteo, P., et al. 2016, A&A, 589, A66

Heiter, U., Jofré, P., Gustafsson, B., et al. 2015a, A&A, 582, A49

Heiter, U., Lind, K., Asplund, M., et al. 2015b, Physica Scripta, 90, 054010

Helmi, A. 2008, A&A Reviews, 15, 145

Helmi, A., Babusiaux, C., Koppelman, H. H., et al. 2018, Nature, 563, 85

Hetem, A. 2020, in Origins: From the Protosun to the First Steps of Life, ed. B. G. Elmegreen, L. V. Tóth, & M. Güdel, Vol. 345, 304–305

Hill, V., Lecureur, A., Gómez, A., et al. 2011, A&A, 534, A80

Holtzman, J. A., Shetrone, M., Johnson, J. A., et al. 2015, AJ, 150, 148

Houdek, G., Balmforth, N. J., Christensen-Dalsgaard, J., & Gough, D. O. 1999, A&A, 351, 582

Howell, S. B., Sobeck, C., Haas, M., et al. 2014, Publications of the ASP, 126, 398

Iben, I., J. & Renzini, A. 1982, ApJ, 259, L79

Jackson, R. J., Jeffries, R. D., Wright, N. J., et al. 2020, MNRAS, 496, 4701

Jacobson, H. R., Friel, E. D., Jílková, L., et al. 2016, A&A, 591, A37

Jacobson, H. R., Pilachowski, C. A., & Friel, E. D. 2011, AJ, 142, 59

Janes, K., Barnes, S. A., Meibom, S., & Hoq, S. 2013, AJ, 145, 7

Janes, K., Barnes, S. A., Meibom, S., & Hoq, S. 2014, AJ, 147, 139

Jofré, P., Heiter, U., Soubiran, C., et al. 2014, A&A, 564, A133

Jofré, P., Jackson, H., & Tucci Maia, M. 2020, A&A, 633, L9

Jørgensen, B. R. & Lindegren, L. 2005, A&A, 436, 127

Jurić, M., Ivezić, Ž., Brooks, A., et al. 2008, ApJ, 673, 864

Kaluzny, J. 1989, Acta Astronomica, 39, 13

Karakas, A. I. & Lattanzio, J. C. 2014, Publications of the Astron. Soc. of Australia, 31, e030

Karakas, A. I. & Lugaro, M. 2016, ApJ, 825, 26

Karakas, A. I., Lugaro, M., Carlos, M., et al. 2018, MNRAS, 477, 421

Kennicutt, Robert C., J. 1998a, ARA&A, 36, 189

Kennicutt, Robert C., J. 1998b, ApJ, 498, 541

Kharchenko, N. V., Piskunov, A. E., Röser, S., Schilbach, E., & Scholz, R. D. 2005, A&A, 440, 403

Kharchenko, N. V., Piskunov, A. E., Schilbach, E., Röser, S., & Scholz, R.-D. 2013, A&A, 558, A53

Khoperskov, S., Haywood, M., Di Matteo, P., Lehnert, M. D., & Combes, F. 2018, A&A, 609, A60

Kim, S. C., Kyeong, J., & Sung, E.-C. 2009, Journal of Korean Astronomical Society, 42, 135

Koppelman, H. H., Helmi, A., Massari, D., Price-Whelan, A. M., & Starkenburg, T. K. 2019, A&A, 631, L9

Kordopatis, G., Recio-Blanco, A., de Laverny, P., et al. 2011, A&A, 535, A106

Korobkin, O., Rosswog, S., Arcones, A., & Winteler, C. 2012, MNRAS, 426, 1940

Kos, J., de Silva, G., Buder, S., et al. 2018, MNRAS, 480, 5242

Kounkel, M. & Covey, K. 2019, AJ, 158, 122

Kratz, K.-L., Farouqi, K., Pfeiffer, B., et al. 2007, ApJ, 662, 39

Krause, M. G. H., Offner, S. S. R., Charbonnel, C., et al. 2020, Space Science Reviews, 216, 64

Krauss, L. M. & Chaboyer, B. 2003, Science, 299, 65

Kroupa, P., Tout, C. A., & Gilmore, G. 1993, MNRAS, 262, 545

Krumholz, M. R. & McKee, C. F. 2020, MNRAS, 494, 624

Kubryk, M., Prantzos, N., & Athanassoula, E. 2015, A&A, 580, A126

Kuhn, M. A., Hillenbrand, L. A., Sills, A., Feigelson, E. D., & Getman, K. V. 2019, ApJ, 870, 32

Kurucz, R. L. 2005, Memorie della Societa Astronomica Italiana Supplementi, 8, 14

Kyeong, J., Kim, S. C., Hiriart, D., & Sung, E.-C. 2008, Journal of Korean Astronomical Society, 41, 147

Lada, C. J. & Lada, E. A. 2003, ARA&A, 41, 57

Lagarde, N., Decressin, T., Charbonnel, C., et al. 2012, A&A, 543, A108

Lagarde, N., Reylé, C., Robin, A. C., et al. 2019, A&A, 621, A24

Lagarde, N., Robin, A. C., Reylé, C., & Nasello, G. 2017, A&A, 601, A27

Leão, I. C., Pasquini, L., Ludwig, H. G., & de Medeiros, J. R. 2019, MNRAS, 483, 5026

Lèbre, A., Palacios, A., Jasniewicz, G., et al. 2005, in IAU Symposium, Vol. 228, From Lithium to Uranium: Elemental Tracers of Early Cosmic Evolution, ed. V. Hill, P. Francois, & F. Primas, 399–400

Lebreton, Y. & Montalbán, J. 2009, in IAU Symposium, Vol. 258, The Ages of Stars, ed. E. E. Mamajek, D. R. Soderblom, & R. F. G. Wyse, 419–430

Lépine, J. R. D., Andrievky, S., Barros, D. A., Junqueira, T. C., & Scarano, S. 2014, in IAU Symposium, Vol. 298, Setting the scene for Gaia and LAMOST, ed. S. Feltzing, G. Zhao, N. A. Walton, & P. Whitelock, 86–91

Leung, H. W. & Bovy, J. 2019, MNRAS, 483, 3255

Li, C., Zhao, G., Zhai, M., & Jia, Y. 2018, ApJ, 860, 53

Lin, J., Dotter, A., Ting, Y.-S., & Asplund, M. 2018, MNRAS, 477, 2966

Lind, K., Primas, F., Charbonnel, C., Grundahl, F., & Asplund, M. 2009, A&A, 503, 545

Lindegren, L., Hernández, J., Bombrun, A., et al. 2018, A&A, 616, A2

Liu, F., Asplund, M., Yong, D., et al. 2016, MNRAS, 463, 696

Liu, L. & Pang, X. 2019, ApJS, 245, 32

LSST Science Collaboration, Abell, P. A., Allison, J., et al. 2009, arXiv e-prints, arXiv:0912.0201

Lugaro, M., Karakas, A. I., Stancliffe, R. J., & Rijs, C. 2012, ApJ, 747, 2

Maciejewski, G., Mihov, B., & Georgiev, T. 2009, Astronomische Nachrichten, 330, 851

Maciejewski, G. & Niedzielski, A. 2007, A&A, 467, 1065

Mackereth, J. T., Bovy, J., Schiavon, R. P., et al. 2017, MNRAS, 471, 3057

Magrini, L., Randich, S., Donati, P., et al. 2015, A&A, 580, A85

Magrini, L., Randich, S., Friel, E., et al. 2013a, A&A, 558, A38

Magrini, L., Randich, S., Friel, E., et al. 2013b, A&A, 558, A38

Magrini, L., Randich, S., Kordopatis, G., et al. 2017, A&A, 603, A2

Magrini, L., Randich, S., Romano, D., et al. 2014, A&A, 563, A44

Magrini, L., Sestito, P., Randich, S., & Galli, D. 2009, A&A, 494, 95

Magrini, L., Spina, L., Randich, S., et al. 2018, A&A, 617, A106

Maiorca, E., Magrini, L., Busso, M., et al. 2012, ApJ, 747, 53

Majewski, S. R., Schiavon, R. P., Frinchaboy, P. M., et al. 2017, AJ, 154, 94

Majewski, S. R., Zasowski, G., & Nidever, D. L. 2011, ApJ, 739, 25

Martell, S. L., Smith, G. H., & Briley, M. M. 2008, AJ, 136, 2522

Martig, M., Fouesneau, M., Rix, H.-W., et al. 2016, MNRAS, 456, 3655

Martínez-García, E. E. & Puerari, I. 2014, ApJ, 790, 118

Mashonkina, L., Gehren, T., Shi, J. R., Korn, A. J., & Grupp, F. 2011, A&A, 528, A87

Masseron, T. & Gilmore, G. 2015, MNRAS, 453, 1855

Masseron, T., Lagarde, N., Miglio, A., Elsworth, Y., & Gilmore, G. 2017, MNRAS, 464, 3021

Mathur, S., Huber, D., Batalha, N. M., et al. 2017, ApJS, 229, 30

Matteucci, F. 2014, The Origin of the Galaxy and Local Group, Saas-Fee Advanced Course, Volume 37. ISBN 978-3-642-41719-1. Springer-Verlag Berlin Heidelberg, 2014, p. 145, 37, 145

Matteucci, F. & Brocato, E. 1990, ApJ, 365, 539

Matteucci, F. & Francois, P. 1989, MNRAS, 239, 885

Matteucci, F. & Recchi, S. 2001, ApJ, 558, 351

Mayor, M., Pepe, F., Queloz, D., et al. 2003, The Messenger, 114, 20

McMahon, R. G., Banerji, M., Gonzalez, E., et al. 2013, The Messenger, 154, 35

McWilliam, A. 2016, Publications of the Astron. Soc. of Australia, 33, e040

McWilliam, A. & Zoccali, M. 2010, ApJ, 724, 1491

Meingast, S., Alves, J., & Fürnkranz, V. 2019, A&A, 622, L13

Meléndez, J., Asplund, M., Gustafsson, B., & Yong, D. 2009, ApJ, 704, L66

Meléndez, J., Dodds-Eden, K., & Robles, J. A. 2006, ApJ, 641, L133

Meléndez, J. & Ramírez, I. 2007, ApJ, 669, L89

Meléndez, J., Ramírez, I., Karakas, A. I., et al. 2014a, ApJ, 791, 14

Meléndez, J., Schirbel, L., Monroe, T. R., et al. 2014b, A&A, 567, L3

Melotte, P. J. 1915, Memoirs of the RAS, 60, 175

Mermilliod, J.-C., Clariá, J. J., Andersen, J., Piatti, A. E., & Mayor, M. 2001, A&A, 375, 30

Mermilliod, J. C., Mayor, M., & Udry, S. 2008, A&A, 485, 303

Michaud, G. 1986, ApJ, 302, 650

Michel, E., Baglin, A., Auvergne, M., et al. 2008, Science, 322, 558

Milone, A. P., Marino, A. F., Da Costa, G. S., et al. 2020, MNRAS, 491, 515

Milone, A. P., Piotto, G., Renzini, A., et al. 2017, MNRAS, 464, 3636

Minchev, I., Chiappini, C., & Martig, M. 2014, A&A, 572, A92

Mints, A. & Hekker, S. 2017, A&A, 604, A108

Mints, A. & Hekker, S. 2018, A&A, 618, A54

Molenda-Żakowicz, J., Brogaard, K., Niemczura, E., et al. 2014, MNRAS, 445, 2446

Montalbán, J. & Schatzman, E. 2000, A&A, 354, 943

Monteiro, H. & Dias, W. S. 2019, MNRAS, 487, 2385

Montes, D., López-Santiago, J., Gálvez, M. C., et al. 2001, MNRAS, 328, 45

Mucciarelli, A. & Bellazzini, M. 2020, Research Notes of the American Astronomical Society, 4, 52

Mucciarelli, A., Salaris, M., Lovisi, L., et al. 2011, MNRAS, 412, 81

Nataf, D. M., Udalski, A., Gould, A., Fouqué, P., & Stanek, K. Z. 2010, ApJ, 721, L28

Ness, M., Hogg, D. W., Rix, H. W., Ho, A. Y. Q., & Zasowski, G. 2015, ApJ, 808, 16

Netopil, M., Paunzen, E., Heiter, U., & Soubiran, C. 2016, A&A, 585, A150

Nissen, P. E. 2015, A&A, 579, A52

Nissen, P. E., Gustafsson, B., Edvardsson, B., & Gilmore, G. 1994, A&A, 285, 440

Nissen, P. E. & Schuster, W. J. 2010, A&A, 511, L10

Nissen, P. E., Silva Aguirre, V., Christensen-Dalsgaard, J., et al. 2017, A&A, 608, A112

Nordlund, A. 1982, A&A, 107, 1

Nordlund, Å., Stein, R. F., & Asplund, M. 2009, Living Reviews in Solar Physics, 6, 2

Nota, A. & Charbonnel, C. 2016, Nature, 529, 473

Ojha, D. K. 2001, MNRAS, 322, 426

Oliva, E., Origlia, L., Baffa, C., et al. 2006, Society of Photo-Optical Instrumentation Engineers (SPIE) Conference Series, Vol. 6269, The GIANO-TNG spectrometer, 626919

Önehag, A., Gustafsson, B., & Korn, A. 2014, A&A, 562, A102

Origlia, L., Dalessandro, E., Sanna, N., et al. 2019, A&A, 629, A117

Overbeek, J. C., Friel, E. D., Donati, P., et al. 2017, A&A, 598, A68

Pagel, B. E. J. & Portinari, L. 1998, MNRAS, 298, 747

Pakhomov, Y. V., Antipova, L. I., Boyarchuk, A. A., et al. 2009, Astronomy Reports, 53, 660

Pancino, E., Carrera, R., Rossetti, E., & Gallart, C. 2010, A&A, 511, A56

Pancino, E., Lardo, C., Altavilla, G., et al. 2017, A&A, 598, A5

Park, H. S. & Lee, M. G. 1999, MNRAS, 304, 883

Pasquini, L., Avila, G., Blecha, A., et al. 2002, The Messenger, 110, 1

Pasquini, L., Biazzo, K., Bonifacio, P., Randich, S., & Bedin, L. R. 2008, A&A, 489, 677

Phelps, R. L. & Janes, K. A. 1996, AJ, 111, 1604

Piatti, A. E., Angelo, M. S., & Dias, W. S. 2019, MNRAS, 488, 4648

Piatti, A. E., Clariá, J. J., Bica, E., Geisler, D., & Minniti, D. 1998, AJ, 116, 801

Pietrinferni, A., Cassisi, S., Salaris, M., & Castelli, F. 2004, ApJ, 612, 168

Pietrinferni, A., Cassisi, S., Salaris, M., & Castelli, F. 2006, ApJ, 642, 797

Pinsonneault, M. H., Deliyannis, C. P., & Demarque, P. 1992, ApJS, 78, 179

Pizzolato, N., Maggio, A., Micela, G., Sciortino, S., & Ventura, P. 2003, A&A, 397, 147

Placco, V. M., Holmbeck, E. M., Frebel, A., et al. 2017, ApJ, 844, 18

Posbic, H., Katz, D., Caffau, E., et al. 2012, A&A, 544, A154

Pouliasis, E., Di Matteo, P., & Haywood, M. 2017, A&A, 598, A66

Prantzos, N. 2016, Astronomische Nachrichten, 337, 953

Queiroz, A. B. A., Anders, F., Santiago, B. X., et al. 2018, MNRAS, 476, 2556

Ramírez, I., Meléndez, J., & Asplund, M. 2009, A&A, 508, L17

Ramírez, I., Meléndez, J., & Asplund, M. 2014a, A&A, 561, A7

Ramírez, I., Meléndez, J., Bean, J., et al. 2014b, A&A, 572, A48

Randich, S., Gilmore, G., & Gaia-ESO Consortium. 2013, The Messenger, 154, 47

Randich, S., Sestito, P., Primas, F., Pallavicini, R., & Pasquini, L. 2006, A&A, 450, 557

Randich, S., Tognelli, E., Jackson, R., et al. 2018, A&A, 612, A99

Rauer, H., Catala, C., Aerts, C., et al. 2014, Experimental Astronomy, 38, 249

Recio-Blanco, A., Bijaoui, A., & de Laverny, P. 2006, MNRAS, 370, 141

Recio-Blanco, A., de Laverny, P., Kordopatis, G., et al. 2014, A&A, 567, A5

Reddy, A. B. S., Giridhar, S., & Lambert, D. L. 2012, MNRAS, 419, 1350

Reddy, A. B. S., Lambert, D. L., & Giridhar, S. 2016, MNRAS, 463, 4366

Reid, M. J. 1993, ARA&A, 31, 345

Renzini, A., Gennaro, M., Zoccali, M., et al. 2018, ApJ, 863, 16

Renzini, A. & Voli, M. 1981, A&A, 500, 221

Rojas-Arriagada, A., Recio-Blanco, A., de Laverny, P., et al. 2017, A&A, 601, A140

Romano, D., Karakas, A. I., Tosi, M., & Matteucci, F. 2010, A&A, 522, A32

Rosén, L., Kochukhov, O., Hackman, T., & Lehtinen, J. 2016, A&A, 593, A35

Röser, S. & Schilbach, E. 2019, A&A, 627, A4

Ruprecht, J. 1966, Bulletin of the Astronomical Institutes of Czechoslovakia, 17, 33

Ryan, S. G. & Norris, J. E. 1991, AJ, 101, 1865

Sacco, G. G., Morbidelli, L., Franciosini, E., et al. 2014, A&A, 565, A113

Sacco, G. G., Randich, S., Bravi, L., Jeffries, R., & Rigliaco, E. 2017a, MnSAI, 88, 660

Sacco, G. G., Spina, L., Randich, S., et al. 2017b, A&A, 601, A97

Sagar, R. & Griffiths, W. K. 1998, MNRAS, 299, 777

Salaris, M., Chieffi, A., & Straniero, O. 1993, ApJ, 414, 580

Salaris, M., Pietrinferni, A., Piersimoni, A. M., & Cassisi, S. 2015, A&A, 583, A87

Salaris, M., Weiss, A., & Percival, S. M. 2004, A&A, 414, 163

Salpeter, E. E. 1955, ApJ, 121, 161

Samadi, R. & Goupil, M. J. 2001, A&A, 370, 136

Samadi, R., Goupil, M. J., & Lebreton, Y. 2001, A&A, 370, 147

Sbordone, L., Caffau, E., Bonifacio, P., & Duffau, S. 2014, A&A, 564, A109

Scalo, J. M. 1986, Fundamental Cosmic Physics, 11, 1

Schiappacasse-Ulloa, J., Tang, B., Fernández-Trincado, J. G., et al. 2018, AJ, 156, 94

Schlegel, D. J., Finkbeiner, D. P., & Davis, M. 1998, ApJ, 500, 525

Schmidt, M. 1959, ApJ, 129, 243

Schneider, P. 2015, Extragalactic Astronomy and Cosmology: An Introduction

Schönrich, R., Binney, J., & Dehnen, W. 2010, MNRAS, 403, 1829

Schultheis, M., Rojas-Arriagada, A., García Pérez, A. E., et al. 2017, A&A, 600, A14

Schwarzschild, M. 1958, Structure and evolution of the stars.

Searle, L. & Zinn, R. 1978, ApJ, 225, 357

Semenova, E., Bergemann, M., Deal, M., et al. 2020, arXiv e-prints, arXiv:2007.09153

Sharma, S., Pandey, A. K., Ogura, K., et al. 2006, AJ, 132, 1669

Shetrone, M., Tayar, J., Johnson, J. A., et al. 2019, ApJ, 872, 137

Shingles, L. J., Doherty, C. L., Karakas, A. I., et al. 2015, MNRAS, 452, 2804

Short, C. I. & Hauschildt, P. H. 2003, ApJ, 596, 501

Sim, G., Lee, S. H., Ann, H. B., & Kim, S. 2019, Journal of Korean Astronomical Society, 52, 145

Skrutskie, M. F., Cutri, R. M., Stiening, R., et al. 2006, AJ, 131, 1163

Slumstrup, D., Grundahl, F., Brogaard, K., et al. 2017, A&A, 604, L8

Smiljanic, R., Korn, A. J., Bergemann, M., et al. 2014, A&A, 570, A122

Smiljanic, R., Romano, D., Bragaglia, A., et al. 2016, A&A, 589, A115

Snaith, O., Haywood, M., Di Matteo, P., et al. 2015, A&A, 578, A87

Snaith, O. N., Haywood, M., Di Matteo, P., et al. 2014, ApJ, 781, L31

Sneden, C. 1973, ApJ, 184, 839

Sneden, C., Bean, J., Ivans, I., Lucatello, S., & Sobeck, J. 2012, MOOG: LTE line analysis and spectrum synthesis

Sneden, C., Cowan, J. J., & Gallino, R. 2008, ARA&A, 46, 241

Sneden, C., Lucatello, S., Ram, R. S., Brooke, J. S. A., & Bernath, P. 2014, ApJS, 214, 26

Soderblom, D. R. 2010, ARA&A, 48, 581

Soderblom, D. R., Hillenbrand, L. A., Jeffries, R. D., Mamajek, E. E., & Naylor, T. 2014, Protostars and Planets VI, 219

Soubiran, C., Jasniewicz, G., Chemin, L., et al. 2013, A&A, 552, A64

Souto, D., Allende Prieto, C., Cunha, K., et al. 2019, ApJ, 874, 97

Spada, F., Demarque, P., Kim, Y. C., Boyajian, T. S., & Brewer, J. M. 2017, ApJ, 838, 161

Sparke, L. S. & Gallagher, John S., I. 2007, Galaxies in the Universe: An Introduction

Spina, L., Meléndez, J., Casey, A. R., Karakas, A. I., & Tucci-Maia, M. 2018a, ApJ, 863, 179

Spina, L., Meléndez, J., Karakas, A. I., et al. 2018b, MNRAS, 474, 2580

Spina, L., Meléndez, J., Karakas, A. I., et al. 2016, A&A, 593, A125

Spina, L., Nordlander, T., Casey, A. R., et al. 2020, ApJ, 895, 52

Spina, L., Randich, S., Magrini, L., et al. 2017, A&A, 601, A70

Spitoni, E. & Matteucci, F. 2011, A&A, 531, A72

Spitoni, E., Matteucci, F., Recchi, S., Cescutti, G., & Pipino, A. 2009, A&A, 504, 87

Spitoni, E., Recchi, S., & Matteucci, F. 2008, A&A, 484, 743

Spitoni, E., Romano, D., Matteucci, F., & Ciotti, L. 2015, ApJ, 802, 129

Stassun, K. G., Oelkers, R. J., Pepper, J., et al. 2018, AJ, 156, 102

Stetson, P. B. & Pancino, E. 2008, Publications of the ASP, 120, 1332

Stetson, P. B., Vandenberg, D. A., & Bolte, M. 1996, Publications of the ASP, 108, 560

Stonkutė, E., Koposov, S. E., Howes, L. M., et al. 2016, MNRAS, 460

Subramaniam, A. 2003, Bulletin of the Astronomical Society of India, 31, 49

Surman, R., McLaughlin, G. C., Ruffert, M., Janka, H.-T., & Hix, W. R. 2008, ApJ, 679, L117

Swenson, F. J. & Faulkner, J. 1992, ApJ, 395, 654

Tadross, A. L. 2003, New Astronomy, 8, 737

Talon, S. & Charbonnel, C. 2005, A&A, 440, 981

Tang, B., Geisler, D., Friel, E., et al. 2017, A&A, 601, A56

Tautvaišienė, G., Drazdauskas, A., Mikolaitis, Š., et al. 2015, A&A, 573, A55

Thorsbro, B., Ryde, N., Rich, R. M., et al. 2020, ApJ, 894, 26

Ting, Y.-S., De Silva, G. M., Freeman, K. C., & Parker, S. J. 2012, MNRAS, 427, 882

Titarenko, A., Recio-Blanco, A., de Laverny, P., Hayden, M., & Guiglion, G. 2019, A&A, 622, A59

Tofflemire, B. M., Gosnell, N. M., Mathieu, R. D., & Platais, I. 2014, AJ, 148, 61

Tognelli, E., Prada Moroni, P. G., & Degl'Innocenti, S. 2011, A&A, 533, A109

Tognelli, E., Prada Moroni, P. G., & Degl'Innocenti, S. 2018, MNRAS, 476, 27

Trumpler, R. J. 1930, Lick Observatory Bulletin, 420, 154

Tsantaki, M., Sousa, S. G., Adibekyan, V. Z., et al. 2013, A&A, 555, A150

Tsikoudi, V. 1980, ApJS, 43, 365

Tucci Maia, M., Ramírez, I., Meléndez, J., et al. 2016, A&A, 590, A32

Twarog, B. A., Ashman, K. M., & Anthony-Twarog, B. J. 1997, AJ, 114, 2556

Ulrich, R. K. 1986, ApJ, 306, L37

Valenti, E., Zoccali, M., Renzini, A., et al. 2013, A&A, 559, A98

Valenti, J. A. & Piskunov, N. 1996, A&A, Supplement, 118, 595

Valentini, M., Borgani, S., Bressan, A., et al. 2019, MNRAS, 485, 1384

Valle, G., Dell'Omodarme, M., Prada Moroni, P. G., & Degl'Innocenti, S. 2013a, A&A, 549, A50

Valle, G., Dell'Omodarme, M., Prada Moroni, P. G., & Degl'Innocenti, S. 2013b, A&A, 554, A68

Villanova, S., Carraro, G., Bresolin, F., & Patat, F. 2005, AJ, 130, 652

Vincenzo, F., Spitoni, E., Calura, F., et al. 2019, MNRAS, 487, L47

Wanajo, S. 2013, ApJ, 770, L22

Warren, S. R. & Cole, A. A. 2009, MNRAS, 393, 272

Wheeler, J. C., Sneden, C., & Truran, James W., J. 1989, ARA&A, 27, 279

Woosley, S. E. & Weaver, T. A. 1995, ApJS, 101, 181

Worley, C. C. & Cottrell, P. L. 2010, MNRAS, 406, 2504

Worley, C. C., Cottrell, P. L., McDonald, I., & van Loon, J. T. 2010, MNRAS, 402, 2060

Wright, E. L., Eisenhardt, P. R. M., Mainzer, A. K., et al. 2010, AJ, 140, 1868

Wu, T., Li, Y., & Hekker, S. 2014, ApJ, 786, 10

Xiong, D. R. & Deng, L. 2009, MNRAS, 395, 2013

Yen, S. X., Reffert, S., Schilbach, E., et al. 2018, A&A, 615, A12

York, D. G., Adelman, J., Anderson, Jr., J. E., et al. 2000, AJ, 120, 1579

Yoshii, Y. 1982, Publications of the ASJ, 34, 365

Zasowski, G., Cohen, R. E., Chojnowski, S. D., et al. 2017, AJ, 154, 198

Zasowski, G., Johnson, J. A., Frinchaboy, P. M., et al. 2013, AJ, 146, 81

Zhang, B., Chen, X.-Y., Liu, C., et al. 2015, Research in Astronomy and Astrophysics, 15, 1197

Zhang, J., Zhao, J., Oswalt, T. D., et al. 2019, ApJ, 887, 84

Zhong, J., Chen, L., Wu, D., et al. 2020, A&A, 640, A127

Zinn, R. 1985, ApJ, 293, 424

Zoccali, M., Vasquez, S., Gonzalez, O. A., et al. 2017, A&A, 599, A12